

APPENDIX III
DETAILS OF CASK RESPONSE TO IMPACT ACCIDENTS

Table of Contents

III.1 Finite Element Analysis of the HI-STAR 100.....	244
III.1.1 Problem statement.....	244
III.1.2 Geometric Assumptions and Mesh.....	244
III.1.3 Material Properties.....	248
III.1.4 Criteria for Element Death.....	252
III.1.5. Analysis Results.....	253
III.1.6 Acknowledgements.....	262
III.2 Finite Element Analysis of the NAC-STC.....	262
III.2.1 Problem statement.....	262
III.2.2 Geometric Assumptions and Mesh.....	262
III.2.3 Material Properties.....	266
III.2.4 Criteria for Element Death.....	271
III.2.5 Analysis Results.....	272
III.2.6 Determination of Lid Gaps.....	278
III.2.7 Acknowledgements.....	291
III.3 Impacts onto Yielding Targets.....	291
III.3.1 Introduction.....	291
III.3.2 Method.....	292
III.3.3 Soil Targets.....	294
III.3.4 Concrete Targets.....	295
III.3.5 Hard Rock Targets.....	297
III.3.6 Results for Real Target Calculations.....	298
III.3.7 Impacts onto Water.....	298
III.4 Response of Spent Fuel Assemblies.....	298
III.4.1 Introduction.....	298
III.4.2 Description and Method.....	299
III.4.3 Finite Element Models.....	301
III.4.3 Discussion and Conclusions.....	317

List of Figures

Figure III-1. Half-symmetric mesh of HI-STAR 100 cask.....	245
Figure III-2. Impact limiter mesh.....	246
Figure III-3. Impact limiter mesh with honeycomb removed, showing the internal support structure.....	246
Figure III-4. Mesh of lid closure bolts and impact limiter attachment bolts	247
Figure III-5. Orientation of cask model for material property definitions.....	248
Figure III-6. HI-STAR 100 end impact at 193 KPH (120 MPH)	253
Figure III-7. HI-STAR 100 corner impact at 48 KPH (30 MPH).....	254
Figure III-8. HI-STAR 100 corner impact at 97 KPH (60 MPH).....	254
Figure III-9. HI-STAR 100 corner impact at 145 KPH (90 MPH).....	255
Figure III-10. HI-STAR 100 side impact at 193 KPH (120 MPH)	255
Figure III-11. Plastic strain in the interior welded canister of the HI-STAR 100 from the end impact at 48 KPH (30 MPH)	256
Figure III-12. Plastic strain in the interior welded canister of the HI-STAR 100 from the end impact at 97 KPH (60 MPH)	257
Figure III-13. Plastic strain in the interior welded canister of the HI-STAR 100 from the end impact at 145 KPH (90 MPH)	257
Figure III-14. Plastic strain in the interior welded canister of the HI-STAR 100 from the end impact at 193 KPH (120 MPH)	258
Figure III-15. Plastic strain in the interior welded canister of the HI-STAR 100 from the corner impact at 48 KPH (30 MPH)	258
Figure III-16. Plastic strain in the interior welded canister of the HI-STAR 100 from the corner impact at 97 KPH (60 MPH)	259
Figure III-17. Plastic strain in the interior welded canister of the HI-STAR 100 from the corner impact at 145 KPH (90 MPH)	259
Figure III-18. Plastic strain in the interior welded canister of the HI-STAR 100 from the corner impact at 193 KPH (120 MPH)	260
Figure III-19. Plastic strain in the interior welded canister of the HI-STAR 100 from the side impact at 48 KPH (30 MPH)	260
Figure III-20. Plastic strain in the interior welded canister of the HI-STAR 100 from the side impact at 97 KPH (60 MPH)	261
Figure III-21. Plastic strain in the interior welded canister of the HI-STAR 100 from the side impact at 145 KPH (90 MPH)	261
Figure III-22. Plastic strain in the interior welded canister of the HI-STAR 100 from the side impact at 193 KPH (120 MPH)	262
Figure III-28. NAC-STC end impact at 48 KPH (30 MPH).....	272
Figure III-29. NAC-STC end impact at 97 KPH (60 MPH).....	273
Figure III-30. NAC-STC end impact at 145 KPH (90 MPH).....	273
Figure III-31. NAC-STC end impact at 193 KPH (120 MPH).....	274

Figure III-32. NAC-STC corner impact at 48 KPH (30 MPH)	274
Figure III-33. NAC-STC corner impact at 97 KPH (60 MPH)	275
Figure III-34. NAC-STC corner impact at 145 KPH (90 MPH)	275
Figure III-35. NAC-STC corner impact at 193 KPH (120 MPH)	276
Figure III-36. NAC-STC side impact at 48 KPH (30 MPH)	276
Figure III-37. NAC-STC side impact at 97 KPH (60 MPH)	277
Figure III-38. NAC-STC side impact at 145 KPH (90 MPH)	277
Figure III-39. NAC-STC side impact at 193 KPH (120 MPH)	278
Figure III-40. Gap opening locations for end impact orientation	278
Figure III-41. Gap opening locations for corner impact orientation.....	279
Figure III-42. Gap opening locations for side impact orientation	279
Figure III-43. Gaps in the inner and outer lids of the NAC-STC cask from the end impact at 48 KPH (30 MPH)	280
Figure III-44. Gaps in the inner and outer lids of the NAC-STC cask from the end impact at 97 KPH (60 MPH)	281
Figure III-45. Gaps in the inner and outer lids of the NAC-STC cask from the end impact at 145 KPH (90 MPH)	282
Figure III-46. Gaps in the inner and outer lids of the NAC-STC cask from the end impact at 193 KPH (120 MPH)	283
Figure III-47. Gaps in the inner and outer lids of the NAC-STC cask from the corner impact at 48 KPH (30 MPH)	284
Figure III-48. Gaps in the inner and outer lids of the NAC-STC cask from the corner impact at 97 KPH (60 MPH)	285
Figure III-49. Gaps in the inner and outer lids of the NAC-STC cask from the corner impact at 145 KPH (90 MPH)	286
Figure III-50. Gaps in the inner and outer lids of the NAC-STC cask from the corner impact at 193 KPH (120 MPH)	287
Figure III-51. Gaps in the inner and outer lids of the NAC-STC cask from the side impact at 48 KPH (30 MPH)	288
Figure III-52. Gaps in the inner and outer lids of the NAC-STC cask from the side impact at 97 KPH (60 MPH)	289
Figure III-541. Force generated by the NAC-STC cask penetrating hard desert soil.....	295
Figure III-56. PWR fuel assembly	299
Figure III-57. Fuel rod schematic drawing	300
Figure III-58. Model used to test finite element codes	302
Figure III-59 Kinetic energy for code test models.....	303
Figure III-60. Kinetic energy for ABAQUS test model with different numbers of elements	304
Figure III-61. Beam Fuel Assembly finite element model	305
Figure III-62. Cross-section of 17x17 fuel assembly with guide tubes (in blue)	305
Figure III-63. Acceleration curves applied to fuel assembly beam model	306

Figure III-64 Spacer grid 100g analysis plastic strain	307
Figure III-65. Hexahedron test model for solid rod-to-rod contact in Abaqus/Explicit	308
Figure III-66. Test model for beam-to-beam contact in Abaqus/Explicit	308
Figure III-67. Comparison of contact forces between solid rod and beam element rod.....	309
Figure III-68. Comparison of contact forces as a function of impact velocity	309
Figure III-69. Continuum rod finite element model	310
Figure III-70. Kinetic energy for Analysis Case 1	313
Figure III-71. Maximum equivalent plastic strain versus time for four inter-spacer grid locations. The spacer grids are specified by the letters in the legend (cf. Figure III-74).....	313
Figure III-73. Maximum equivalent plastic strain versus time for three spacer grid locations The spacer grids are specified by the letters in the legend (cf. Figure III-74).....	314
Figure III-74. Schematic showing maximum equivalent plastic strain for spacer grid and inter-spacer-grid locations	315
Figure III-75. Maximum equivalent plastic strain field in cladding for Analysis Case 2	316
Figure III-76. Maximum equivalent plastic strain versus time for four inter-spacer grid locations. The spacer grids are specified by the letters in the legend (cf. Figure III-78).....	316
Figure III-77. Maximum equivalent plastic strain versus time for four spacer grid locations The spacer grids are specified by the letters in the legend (cf. Figure III-78).....	317
Figure III-78. Schematic showing maximum equivalent plastic strain for spacer grid and inter-spacer-grid locations, Analysis Case 2	317

List of Tables

Table III-1. Available areas for leakage from the NAC-STC cask.....	291
Table III-2. Peak contact force for the NAC-STC impacts onto an unyielding target (bold numbers are for the cases where there may be seal leaks).....	294
Table III-3. Equivalent velocities for NAC-STC impacts onto various targets, KPH.....	298
Table III-4. Properties of fuel assembly	301
Table III-5. Zircaloy-4 material parameters.....	306
Table III-6. Standard Material Properties	311
Table III-7. Load case parameter changes	311
Table III-8. Analysis Case Summary	318

APPENDIX III

DETAILS OF CASK RESPONSE TO IMPACT ACCIDENTS

III.1 Finite Element Analysis of the HI-STAR 100

III.1.1 Problem statement

Simulate impact of a loaded HI-STAR 100 cask onto an unyielding surface. Consider impact velocities of 48 kph (30 mph), 97 kph (60 mph), 145 kph (90 mph) and 193 kph (120 mph). Include end, side, and center-of-gravity (cg) over corner impact orientations. Results will be used to assess integrity of the containment boundary and to estimate the extent of any possible breach. Although the deformation and failure of the lid closure bolts is of interest, the ultimate question of containment breach can be determined by assessing the integrity of the inner container. Plastic strains in the stainless steel inner container will be used to predict possible breach of the cask.

III.1.2 Geometric Assumptions and Mesh

A finite element model of the HI-STAR 100 cask was developed for use with the Sierra Mechanics code Presto. Presto is a nonlinear transient dynamics finite element code developed at Sandia National Laboratories and used extensively for weapons qualification work. The HI-STAR 100 model was developed over several years with many changes along the way to work around limitations in Presto. The model was also required to include the most important geometric features without becoming so large that it couldn't be run on the available computational platforms. The final half-symmetric model consisted of 1.4 million solid hex elements. The drop event lasted approximately 0.5 seconds. The simulation of this drop event required approximately 6-8 days of run time on 256 processors of the Tbird high performance computer at Sandia.

An earlier version of the model used shell elements in areas of thin walled components. The code had difficulty with contact between hexes and embedded shells, and the boundary conditions between the shells and hexes required careful and complicated consideration. Ultimately, the shell elements were replaced by hex elements with 2 or 3 elements through the thickness. Although 2 elements through the thickness is insufficient to correctly predict bending response, these instances were limited to components where bending responses were not considered important. For example, the outer shell of the impact limiters was modeled with 2 hex elements through the thickness. The purpose of this outer layer is to provide constraint to the aluminum honeycomb that comprises the impact limiter. The details of how it bends and folds away from the honeycomb are not important, and not accurate with 2 elements through the thickness. The model details are shown in Figures III-1 to III-4.

Closure bolts were modeled with hex elements, with a minimum of 4 elements across the diameter of the bolt, as shown in Figure III-4.

The total weight of the cask was 364,700 lbs. This weight is high due to an incorrect density value for the aluminum honeycomb that was not discovered until after the runs were completed. The over-weight of the impact limiters results in a more severe loading environment because it increases the amount of kinetic energy that must be absorbed, making all results conservative.

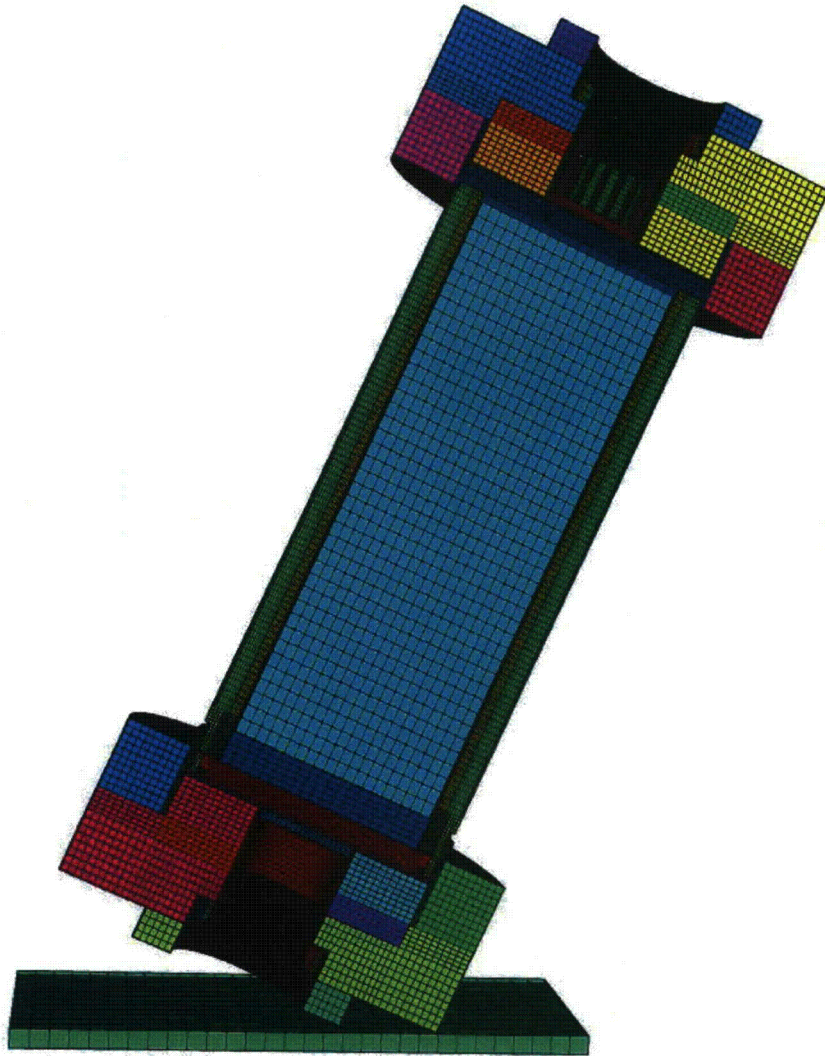


Figure III-1. Half-symmetric mesh of HI-STAR 100 cask

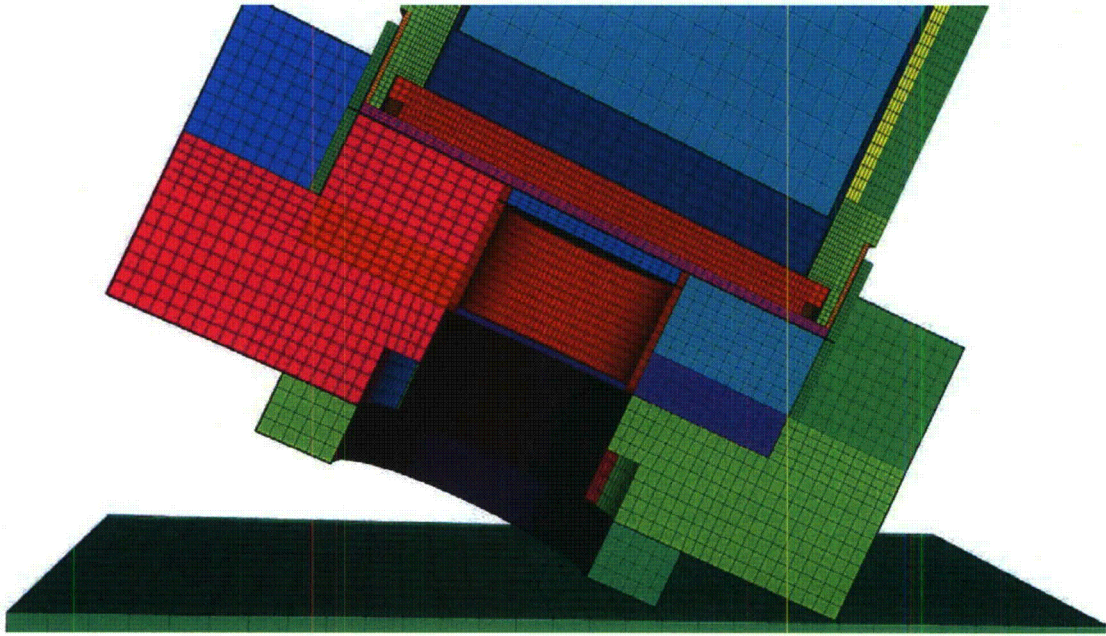


Figure III-2. Impact limiter mesh

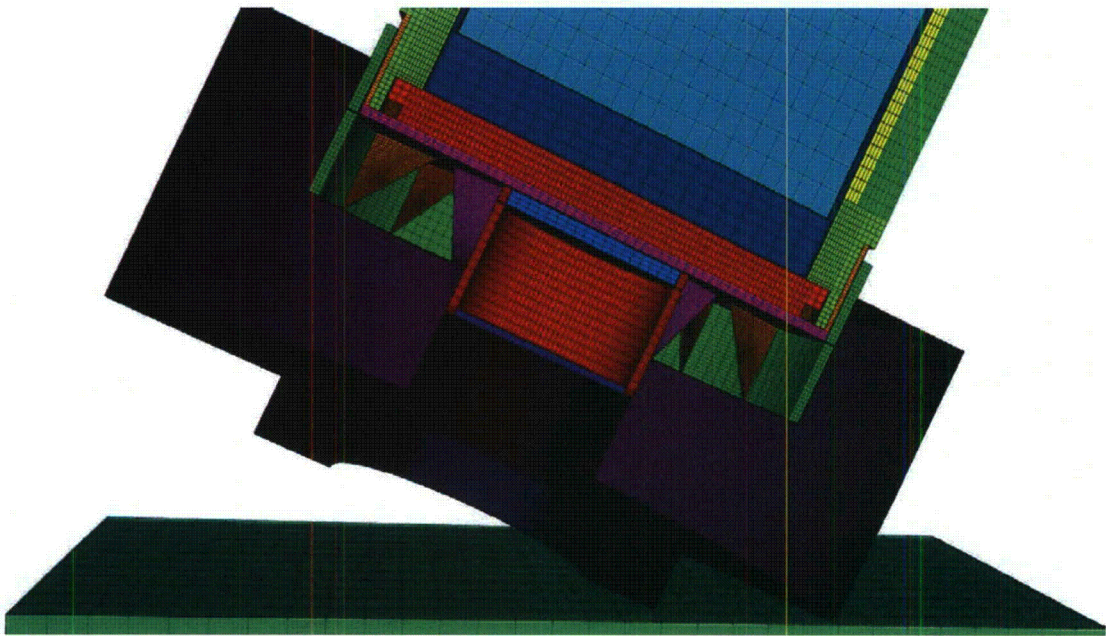


Figure III-3. Impact limiter mesh with honeycomb removed, showing the internal support structure

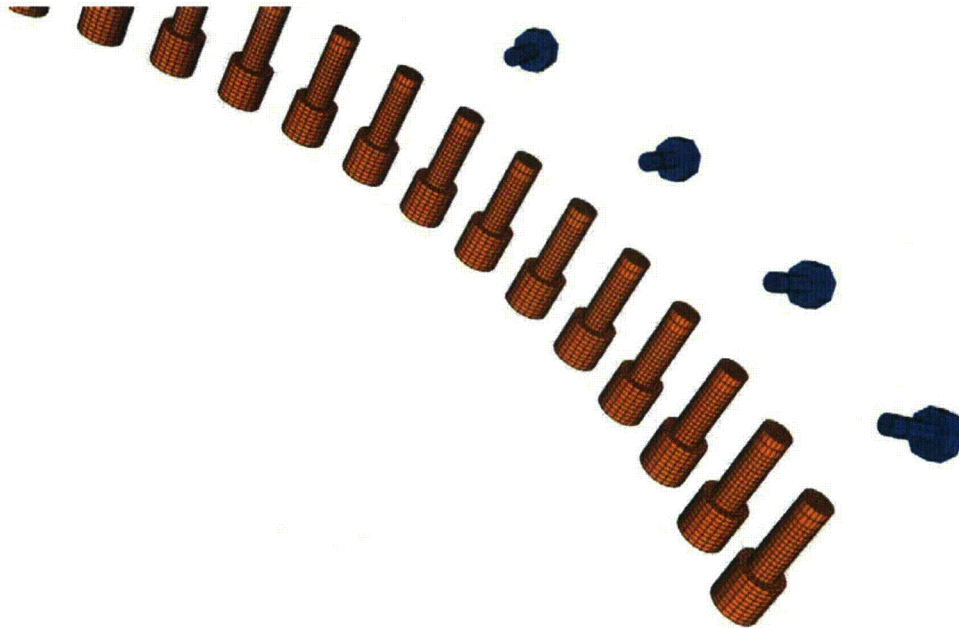


Figure III-4. Mesh of lid closure bolts and impact limiter attachment bolts

The orientation of the model is important to the definition of orthotropic material properties. The cask model is oriented as shown in Figure III-5, and the impact direction is changed for the three impact conditions. For an end drop, the initial velocity is in the +z direction. For a side drop, the initial velocity is in the -x direction. And for a c.g. over corner drop, the initial velocity is in a $-0.38269x + 0.92388z$ direction.



Figure III-5. Orientation of cask model for material property definitions

III.1.3 Material Properties

The response of the closure bolts was of primary importance in these analyses. The threaded ends of the bolts were modeled as fixed into their mating parts using equivalent nodes. The remainder of the bolt was allowed to slide in its through hole. Bolt failure was predicted by considering the equivalent plastic strain (eqps) required for failure. The value of eqps that constitutes failure was assessed using tensile test data and/or references. Details are given below.

The aluminum honeycomb in the impact limiters was assumed to be equally strong in the axial and radial directions, and weaker in the circumferential direction. Properties were not varied at 15 degree increments as specified by the design. Instead, properties were defined in the global x-y-z directions and aligned with the loading direction at the point of impact. The honeycomb was modeled with an orthotropic crush material model. The model has been used for many years in Presto and in the commercially available FEM code LSDyna. It is known to behave poorly at the transition to a fully compacted state, when the material transitions from a unidirectional compaction to an isotropic compression with Poisson's expansion. For lower impact velocities (30 and 60mph), this was not an issue. However, for the higher impact velocities the model became unstable at material lock-up. To allow the code to continue running, elements that behaved badly were deleted. Since they had already absorbed the energy of the impact and were

now just maintaining volume, their deletion was not considered important to the overall cask response.

Material properties are listed below along with the parameters required by Presto(SIERRA, 2009).

Material sa350lf3

Material SA350-LF3 low alloy steel (Holtec, 2001) used for top lid and cask bottom.

Density = 0.00074 lb-s²/in⁴
Material model ep_power_hard
Youngs Modulus = 28.0e6 psi
Poissons Ratio = 0.27
Yield Stress = 37.0e3 psi
Hardening Constant = 192746.0
Hardening Exponent = 0.748190
Luders Strain = 0.0

Material sa230e

Material SA203-E nickel alloy (Klamerus et al., 1996) used for the overpack outer wall.

Density = 0.00074 lb-s²/in⁴
Material model ep_power_hard
Youngs Modulus = 28.0e6 psi
Poissons Ratio = 0.27
Yield Stress = 40.0e3 psi
Hardening Constant = 192746
Hardening Exponent = 0.748190
Luders Strain = 0.0

Material sa516gr70

Material SA-516 Grade 70 (Klamerus et al., 1996), used for overpack external wall, buttress plates, and impact limiter gusset plates

Density = 0.00074 lb-s²/in⁴
Material model ep_power_hard
Youngs Modulus = 29.0e06 psi
Poissons Ratio = 0.3
Yield Stress = 53.097e3 psi
Hardening Constant = 0.131331E+06
Hardening Exponent = 0.479290
Luders Strain = 0.781E-02

Material testfoam

Material properties taken from typical aluminum honeycomb data as measured at Sandia National Labs (Hinnerichs et al., 2006). Properties used for holtite and impact limiter aluminum cross-ply honeycomb.

Density = 0.0003002 lb-s²/in⁴
Material model orthotropic_crush
Youngs Modulus = 4e6 psi
Poissons Ratio = 0.3
Yield Stress = 40000. psi
Ex = 5.00e04 psi
Ey = 5.00e04 psi
Ez = 5.00e04 psi
Gxy = 2.50e04 psi
Gyz = 2.50e04 psi
Gzx = 2.50e04 psi
Vmin = 0.70
Crush xx = 2300_T
Crush yy = 2300_T
Crush zz = 2300_L
Crush xy = 2300_T
Crush yz = 2300_T
Crush zx = 2300_T

Function 2300_L

0	1415.384615
0.05	2123.076923
0.1	2300
0.4	2300
0.5	1592.307692
0.6	3737.5
0.7	20000
0.9	20000

Function 2300_T

0	1415.384615
0.05	2123.076923
0.1	2300
0.4	2300
0.5	1592.307692
0.6	3737.5
0.7	20000
0.9	20000

Material internals

Used for cask contents inside of inner container.

Density = 0.00029 lb-s²/in⁴
 Material model Orthotropic_Crush
 Youngs Modulus = 0.5e6 psi
 Poissons Ratio = 0.3
 Yield Stress = 20000.0 psi
 Ex = 0.5e06 psi
 Ey = 0.5e06 psi
 Ez = 2.2e06 psi
 Gxy = 0.25e06 psi
 Gyz = 1.1e06 psi
 Gzx = 1.1e06 psi
 Vmin = 0.70
 Crush xx = 2300_T
 Crush yy = 700_W
 Crush zz = 2300_L
 Crush xy = foam_cross_1
 Crush yz = foam_cross_2
 Crush zx = foam_cross_1

Function foam_cross_1

0	1000
0.6	1000
0.7	10000
0.8	10000

Function foam_cross_2

0	500
0.6	500
0.7	5000
0.8	5000

Material sb637

Material SB637-N07718 (DOD, 199) used for lid closure bolts.

Density = 0.00074 lb-s²/in⁴
 Material model ml_ep_fail
 Youngs Modulus = 28.6e6
 Poissons Ratio = 0.3
 Yield Stress = 160000.
 Beta = 1.0
 Hardening Function = MLEP_Hardening
 Youngs Modulus Function = constant_one
 Poissons Ratio Function = constant_one
 Yield Stress Function = constant_one
 Critical Tearing Parameter = 0.13
 Critical Crack Opening Strain = 0.01

Material 304ss

Used for MPC, bottom impact limiter bolts, top impact limiter bolts and shell surrounding impact limiters (Hucek, 1986).

Density = 0.00074 lb-s²/in⁴
Material model ep_power_hard
Youngs Modulus = 53.3e06 psi
Poissons Ratio = 0.3
Yield Stress = 46.246e3 psi
Hardening Constant = 319.05e3
Hardening Exponent = 0.68
Luders Strain = 0.0

III.1.4 Criteria for Element Death

For all attachment bolts, elements failure is defined according to Presto (SIERRA, 2009) convention.

Criterion is element value of eqps > 1.12
Death on inversion = on

To account for instability in the orthotropic crush material model, elements are removed from the mesh if the following condition occurs, stated in the Presto element death convention.

Criterion is element value of solid_angle <= 0.05
Criterion is max nodal value of velocity(1) > 20000
Criterion is max nodal value of velocity(2) > 20000
Criterion is max nodal value of velocity(3) > 20000
Criterion is max nodal value of velocity(1) < -20000
Criterion is max nodal value of velocity(2) < -20000
Criterion is max nodal value of velocity(3) < -20000
Death on inversion = on

The impact limiter gusset plates and aluminum impact limiter honeycomb are in contact within the impact limiter. The honeycomb would likely fail before the gusset plates in an experiment. Due to the homogenized material modeling of the honeycomb and the relatively coarse mesh, the gusset plates are significantly deformed by the honeycomb. The failure of the gusset plates is defined according to Presto convention.

Criterion is element value of timestep < -0.01
Criterion is element value of volume <= 0.0
Death on inversion = on

III.1.5. Analysis Results

The deformed shape of the cask following each impact analysis is presented below.

Time = 0.05280



Figure III-6. HI-STAR 100 end impact at 193 KPH (120 MPH)

Time = 0.05680

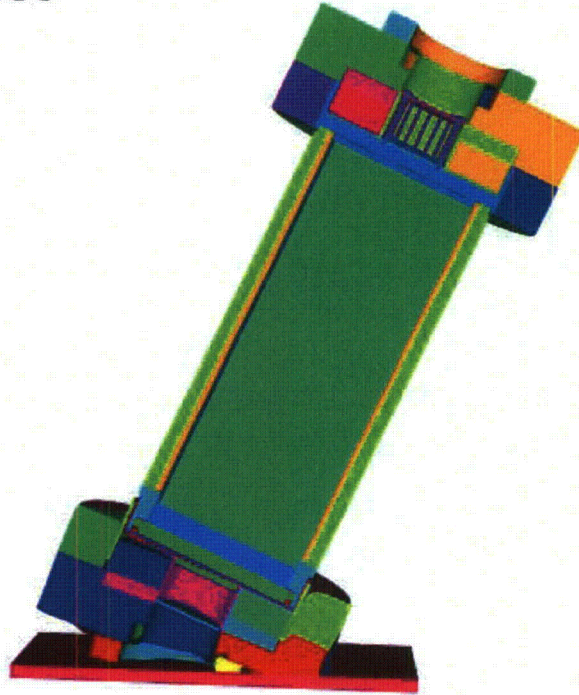


Figure III-7. HI-STAR 100 corner impact at 48 KPH (30 MPH)

Time = 0.06100



Figure III-8. HI-STAR 100 corner impact at 97 KPH (60 MPH)

Time = 0.04960

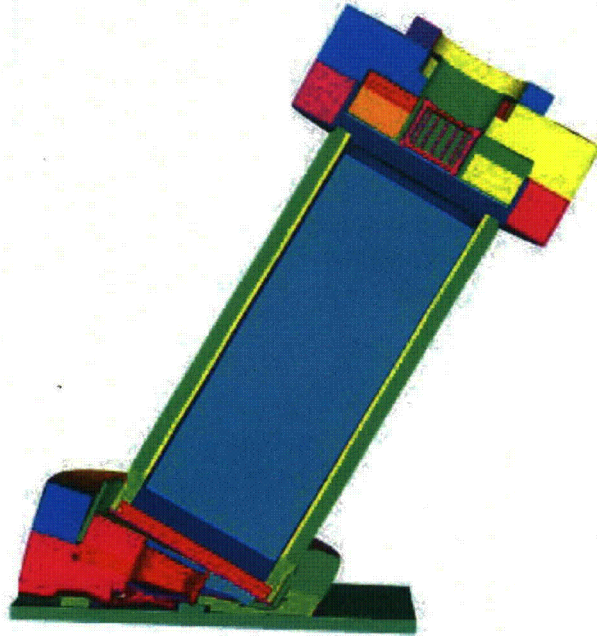


Figure III-9. HI-STAR 100 corner impact at 145 KPH (90 MPH)

Time = 0.03760

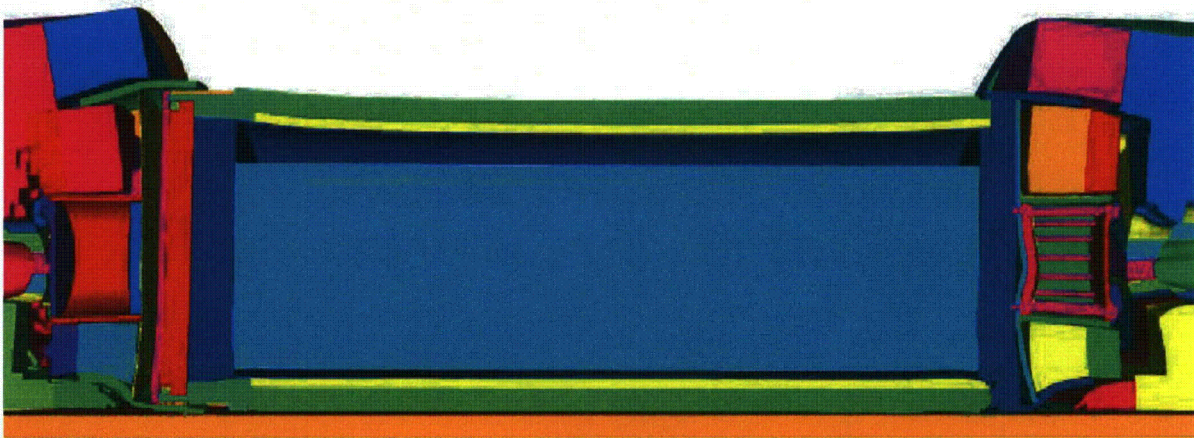


Figure III-10. HI-STAR 100 side impact at 193 KPH (120 MPH)

In the following sections the equivalent plastic strains in the welded inner canister are shown for each analysis case.

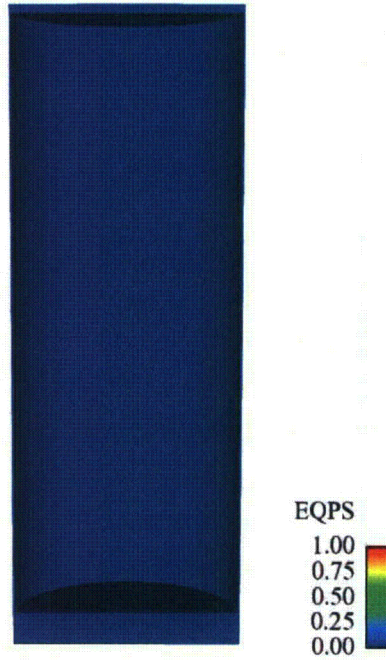


Figure III-11. Plastic strain in the interior welded canister of the HI-STAR 100 from the end impact at 48 KPH (30 MPH)

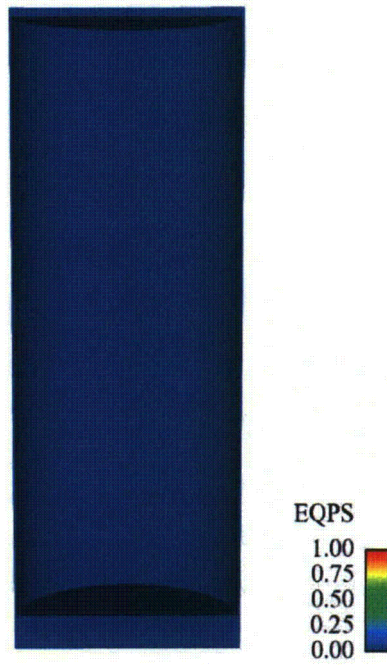


Figure III-12. Plastic strain in the interior welded canister of the HI-STAR 100 from the end impact at 97 KPH (60 MPH)

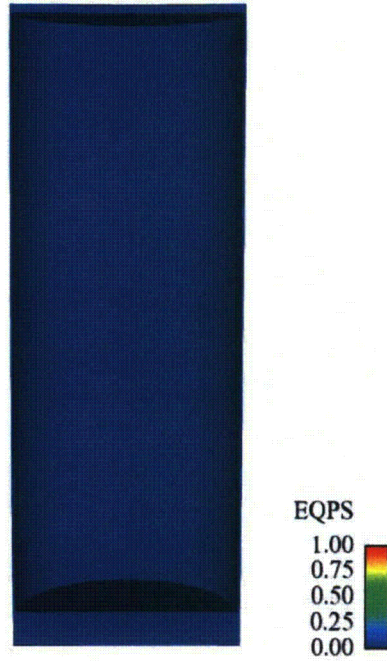


Figure III-13. Plastic strain in the interior welded canister of the HI-STAR 100 from the end impact at 145 KPH (90 MPH)

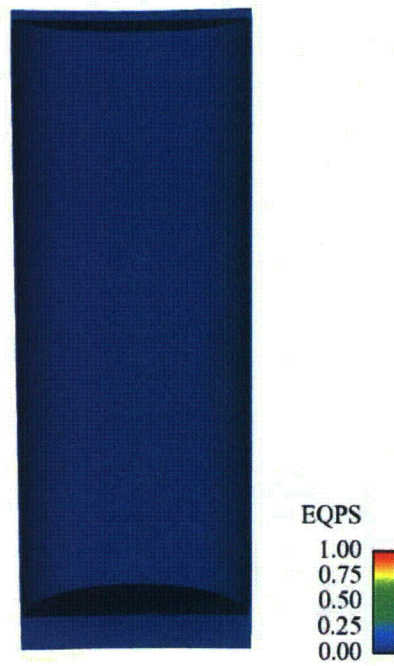


Figure III-14. Plastic strain in the interior welded canister of the HI-STAR 100 from the end impact at 193 KPH (120 MPH)

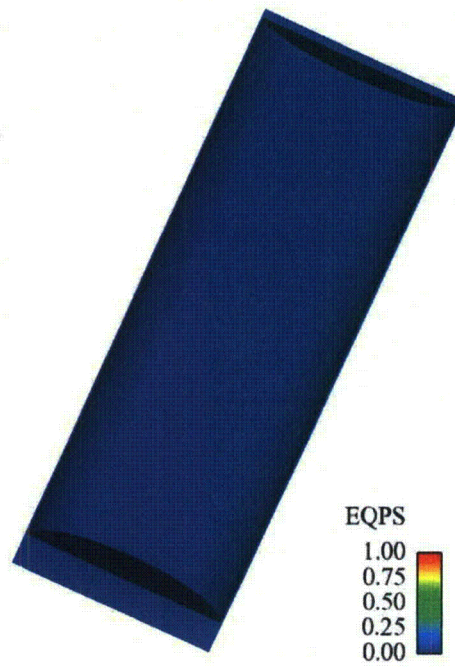


Figure III-15. Plastic strain in the interior welded canister of the HI-STAR 100 from the corner impact at 48 KPH (30 MPH)



Figure III-16. Plastic strain in the interior welded canister of the HI-STAR 100 from the corner impact at 97 KPH (60 MPH)

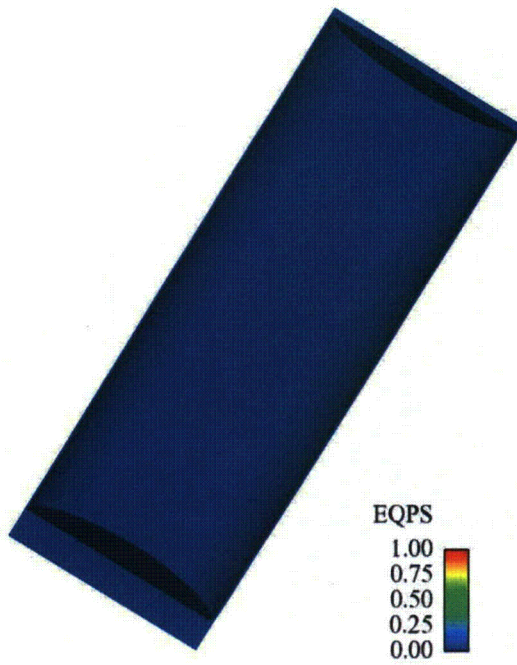


Figure III-17. Plastic strain in the interior welded canister of the HI-STAR 100 from the corner impact at 145 KPH (90 MPH)



Figure III-18. Plastic strain in the interior welded canister of the HI-STAR 100 from the corner impact at 193 KPH (120 MPH)



Figure III-19. Plastic strain in the interior welded canister of the HI-STAR 100 from the side impact at 48 KPH (30 MPH)



Figure III-20. Plastic strain in the interior welded canister of the HI-STAR 100 from the side impact at 97 KPH (60 MPH)



Figure III-21. Plastic strain in the interior welded canister of the HI-STAR 100 from the side impact at 145 KPH (90 MPH)



Figure III-22. Plastic strain in the interior welded canister of the HI-STAR 100 from the side impact at 193 KPH (120 MPH)

III.1.6 Acknowledgements

A number of people at Sandia contributed to the development of this model, including Jeff Smith, Bob Kalan, Lili Akin, and Chris Clutz. Nathan Crane was instrumental in finally getting it to run in Presto.

III.2 Finite Element Analysis of the NAC-STC

III.2.1 Problem statement

Simulate impact of a loaded NAC-STC cask onto an unyielding surface. Consider impact velocities of 48 kph (30 mph), 97 kph (60 mph), 145 kph (90 mph) and 193 kph (120 mph). Include end, side, and c.g. over corner impact orientations. Results will be used to assess integrity of the containment boundary and to estimate the extent of any possible breach. Estimate the deformation and failure of the lid closure bolts and any resulting gap between the lids and the cask. Also estimate the maximum lead slump distance.

III.2.2 Geometric Assumptions and Mesh

A finite element model of the NAC-STC cask was developed for use with the Sierra Mechanics code Presto(SIERRA, 2009). Presto is a nonlinear transient dynamics finite element code developed at Sandia National Laboratories and used extensively for weapons qualification work. The finite element model was built primarily of hex elements. Shell elements used for the thin stainless steel skin that wraps around the impact limiters. The final half-symmetric model

consisted of 750000 elements. The drop event lasted approximately 0.5 seconds. The simulation of this drop event required approximately 36-60 hours of run time on 64 processors of the RedSky high performance computer at Sandia.

The model details are shown in Figures III-23 to III-26.

Closure bolts were modeled with hex elements, with a minimum of 4 elements across the diameter of the bolt, as shown in Figure III-26.

The total weight of the cask was 247300 lbs.

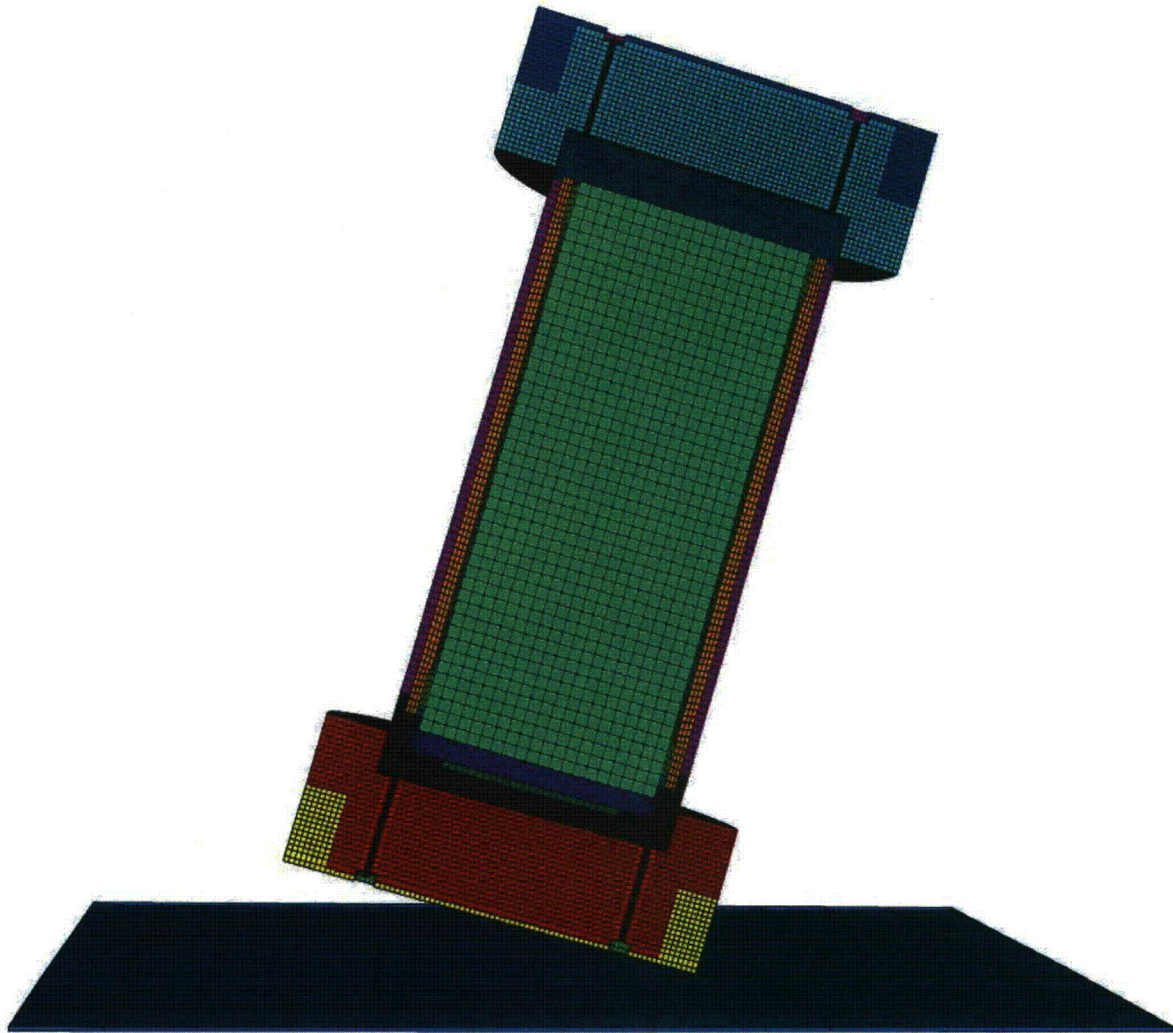


Figure III-23. Half-symmetric mesh of NAC-STC cask

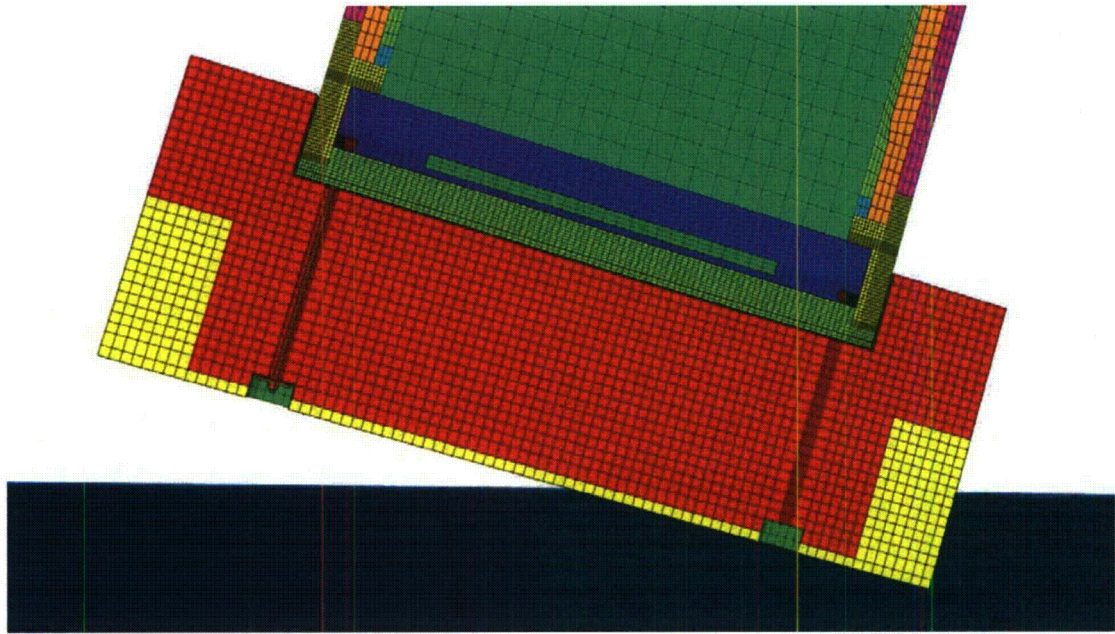


Figure III-24. Impact limiter mesh

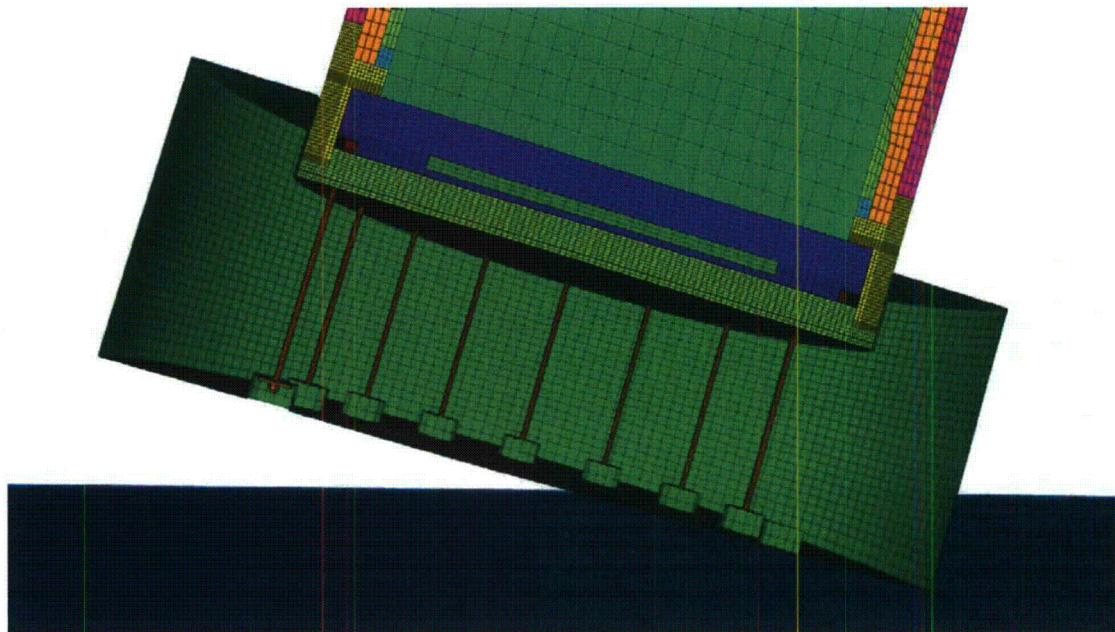


Figure III-25. Impact limiter mesh with wood removed

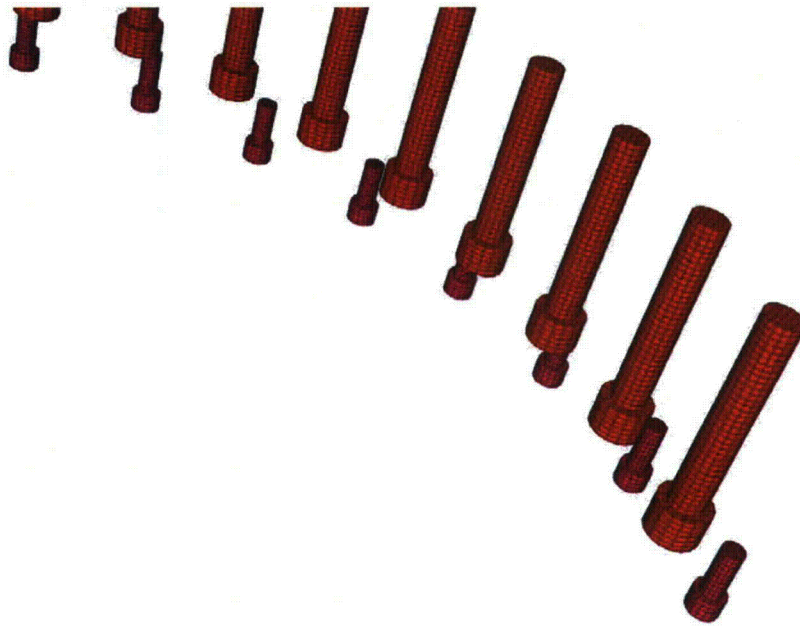


Figure III-26. Mesh of inner and outer lid closure bolts

The orientation of the model is important to the definition of orthotropic material properties. The cask model is oriented as shown in Figure III-27, and the impact direction is changed for the three impact conditions. For an end drop, the initial velocity is in the -y direction. For a side drop, the initial velocity is in the -x direction. And for a c.g. over corner drop, the initial velocity is in a $0.169912x - 0.98546y$ direction.

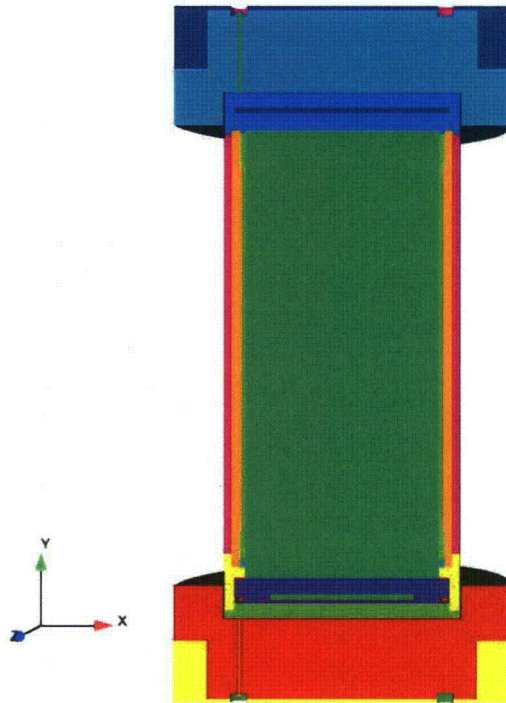


Figure III-27. Orientation of cask model for material property definitions

III.2.3 Material Properties

Material redwood

Used for top and bottom impact limiter

Density = $5.682e-5$ lb-s²/in⁴
 Material model orthotropic_crush
 Young's Modulus = $1.5e6$ psi
 Poisson's Ratio = 0.3
 Yield Stress = 20000 psi
 Vmin=0.9
 Ex = $1.5e6$ psi
 Ey = $0.3e6$ psi
 Ez = $1.5e6$ psi
 Gxy = $0.2e6$ psi
 Gyz = $0.2e6$ psi
 Gzx = $0.2e6$ psi
 Crush xx = redwood_strong
 Crush yy = redwood_weak
 Crush zz = redwood_strong
 Crush xy = redwood_shear
 Crush yz = redwood_shear
 Crush zx = redwood_shear

Function redwood_strong

strain stress (psi)

0. 2000.
0.14 4200.
0.28 5100.
0.42 5430.
0.57 6100.
0.71 10100.
0.80 15000.
0.90 20000.

Function redwood_weak

strain stress (psi)

0. 400.
0.14 986.
0.28 1200.
0.42 1275.
0.57 1432.
0.71 2371.
0.80 3521.
0.90 4690.

Function redwood_shear

strain stress (psi)

0.0 1000.
0.60 1000.
0.70 10000.
0.90 10000.

Material balsa

Used for outer corner of top and bottom impact limiters

Density = $1.5e-5$ lb-s²/in⁴

Material model orthotropic_crush

Young's Modulus = $1.5e6$ psi

Poisson's Ratio = 0.3

Yield Stress = 20000 psi

Vmin = 0.9

Ex = $1.5e6$ psi

Ey = $0.3e6$ psi

Ez = $1.5e6$ psi

Gxy = $0.2e6$ psi

Gyz = $0.2e6$ psi

Gzx = $0.2e6$ psi

Crush xx = balsa_strong

Crush yy = balsa_weak

Crush zz = balsa_strong

Crush xy = balsa_shear

Crush yz = balsa_shear

Crush zx = balsa_shear
 Function balsa_strong
 strain stress (psi)
 0. 2000.
 0.14 4200.
 0.28 5100.
 0.42 5430.
 0.57 6100.
 0.71 10100.
 0.80 15000.
 0.90 20000.

Function balsa_weak
 strain stress (psi)
 0. 400.
 0.14 986.
 0.28 1200.
 0.42 1275.
 0.57 1432.
 0.71 2371.
 0.80 3521.
 0.90 4690.

Function balsa_shear
 strain stress (psi)
 0.0 1000.
 0.60 1000.
 0.70 10000.
 0.90 10000.

Material 304 ss

Properties for 304 stainless steel were obtained from tensile tests conducted at Sandia National Labs.

Elastic values match NAC-STC SAR (NAC, 2004), but complete response curve is used for plasticity.

Used for inner and outer cask wall, shell surrounding impact limiters, and impact limiter attachment bolts.

Density = 7.48e-4 lb-s²/in⁴
 Material model ml_ep_fail
 Youngs Modulus = 28.0e6 psi
 Poissons Ratio = 0.27
 Yield Stress = 33.0e3 psi
 Beta = 1.0
 Youngs Modulus Function = 304_SS_YM
 Poissons Ratio Ffunction = 304_SS_PR
 Yield stress Function = 304_SS_YS

Hardening Function = 304_SS_H
Critical Tearing Parameter = 7.779
Critical Crack Opening Strain = 0.20

Function 304_SS_H

strain	stress (psi)
0.0	0.
0.0395	23.4e3
0.0782	34.9e3
0.1151	45.1e3
0.1509	54.0e3
0.1857	61.7e3
0.2197	68.5e3
0.2527	74.7e3
0.2848	80.5e3
0.3165	86.0e3
0.3470	91.2e3
0.3767	96.4e3
0.4077	101.5e3
0.4378	106.4e3
0.4690	111.4e3
0.5209	119.1e3
0.5797	128.4e3
0.6595	140.6e3
0.7520	156.5e3
0.8639	176.3e3
1.0129	204.2e3
1.2049	242.9e3
1.4476	298.5e3
1.7499	382.8e3
2.1246	519.1e3
2.5960	754.3e3
3.1689	1161.6e3
3.7371	1624.0e3
6.0	3465.5e3

Material filler

Used for internals

Density = $2.92e-4$ lb-s²/in⁴
Material model elastic
Youngs Modulus = 122.0e3 psi
Poissons Ratio = 0.30

Material 17 4 ss

Properties for 17-4 stainless steel were obtained from tensile tests conducted at Sandia National Labs.

Elastic values match NAC-STC SAR (NAC, 2004), but complete response curve is used for plasticity.

Used for outer lid and outer lid bolts.

Density = $7.48e-4$ lb-s²/in⁴
Material model ml_ep_fail
Youngs Modulus = 28.0e6 psi
Poissons Ratio = 0.28
Yield Stress = 100000. psi
Beta = 1.0
Youngs Modulus Function = 304_SS_YM
Poissons Ratio Function = 304_SS_PR
Yield Stress Function = 304_SS_YS
Hardening Function = 17_4_SS_H
Critical Tearing Parameter = 10.0
Critical Crack Opening Strain = 0.20

Function 17_4_SS_H

strain	stress (psi)
0	100000.0
0.00407825	136477.69
0.00879119	153992.02
0.01402863	161193.41
0.01969711	164727.25
0.02677325	166808.60
0.03772328	168627.66
0.12541256	176332.05
0.24107482	183114.13
0.37338829	196318.29
0.51621765	212319.68
0.67105461	234527.78
0.84082846	261327.83
1.03088417	297249.64
1.24626188	344040.44
1.49347177	408459.72
1.78071924	499087.83
2.13871929	625460.64

Material SB637

Material SB-637 Grade N07718 Nickel Alloy Steel (NAC, 2004) used for inner lid bolts

Density = $7.324e-4$ lb-s²/in⁴
Material model elastic_plastic
Youngs Modulus = 2.9e7 psi
Poissons Ratio = 0.32
Yield Stress = 1.508e5
Hardening Modulus = 5.314e5 psi

Beta = 1.0

Material Pb

Lead (Hoffman and Attaway, 1991), used for mid cask wall

Density = $1.06e-3 \text{ lb-s}^2/\text{in}^4$
Material model elastic_plastic
Youngs Modulus = $2.0e6 \text{ psi}$
Poissons Ratio = 0.3
Yield Stress = $1700. \text{ psi}$
Hardening Modulus = $2000. \text{ psi}$
Beta = 1.

Material ns4fr

Solid synthetic polymer NS-4-FR used for neutron shielding inserts in top and bottom lids

The neutron shielding material was developed by BISCO Products, Inc. and is now supplied by Genden Engineering Services and Construction Company.

NS-4-FR is an epoxy resin that contains boron

Density = $1.571e-4 \text{ lb-s}^2/\text{in}^4$
Material model elastic
Youngs Modulus = $5.61e5$
Poissons Ratio = 0.3

III.2.4 Criteria for Element Death

To account for instability in the orthotropic crush material model, elements are removed from the mesh if the following condition occurs, stated in the Presto (SIERRA, 2009) element death convention.

Criterion is max nodal value of velocity(1) > 20000
Criterion is max nodal value of velocity(2) > 20000
Criterion is max nodal value of velocity(3) > 20000
Criterion is max nodal value of velocity(1) < -20000
Criterion is max nodal value of velocity(2) < -20000
Criterion is max nodal value of velocity(3) < -20000
Death on inversion = on

For the impact limiter attachment bolts, elements failure is defined according to Presto convention. This means that failure occurs when the critical tearing parameter (Wellman and Salzbrenner, 1992) is reached, as defined for 304 stainless steel.

Material criterion = ml_ep_fail

Failure of the outer lid and outer lid bolts was defined according to Presto convention when a maximum value of eqps was reached in 17-4 stainless steel. This value of eqps was established

using an analysis of a tensile test specimen, and defining failure approximately midway between maximum stress and the final stress. The conservative value was chosen to compensate for the relatively coarse mesh in the bolt.

Criterion is element value of eqps > 1.5

Failure of the inner lid bolts was defined according to Presto convention when a maximum value of eqps was reached in SB-637 Grade N07718 Nickel Alloy Steel.

Criterion is element value of eqps > 0.1

III.2.5 Analysis Results

The deformed shape of the cask following each impact analysis is presented below.

Time = 0.03480



Figure III-28. NAC-STC end impact at 48 KPH (30 MPH)

Time = 0.03480

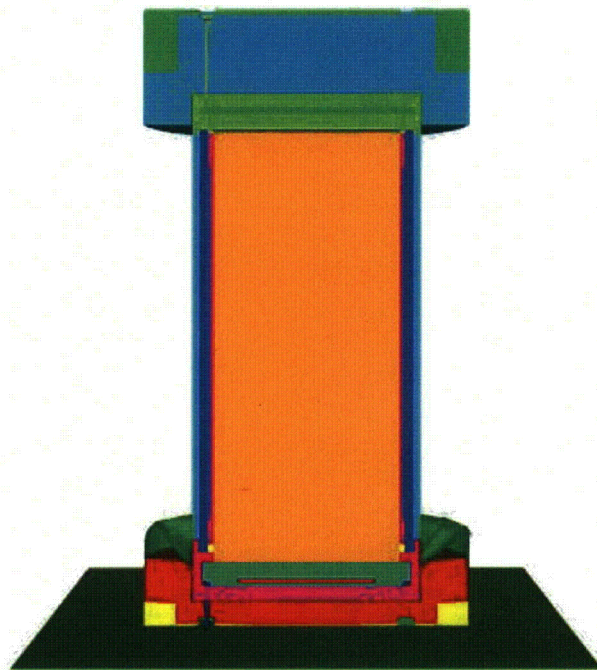


Figure III-29. NAC-STC end impact at 97 KPH (60 MPH)

Time = 0.03480



Figure III-30. NAC-STC end impact at 145 KPH (90 MPH)

Time = 0.03480

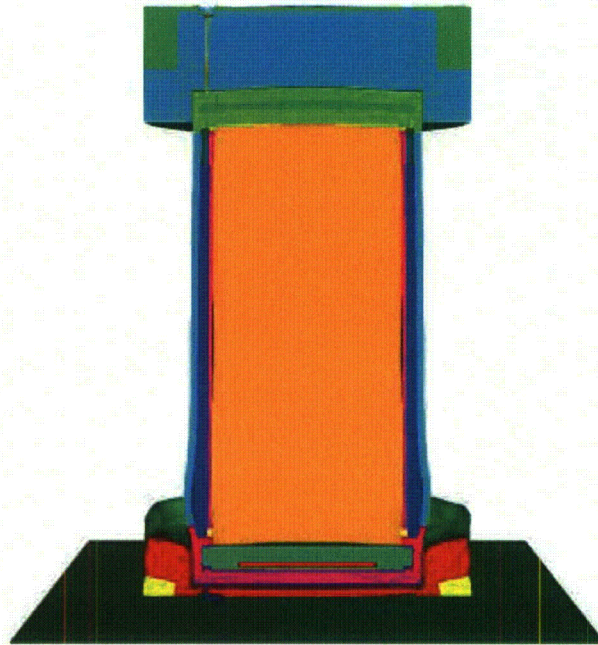


Figure III-31. NAC-STC end impact at 193 KPH (120 MPH)

Time = 0.06420

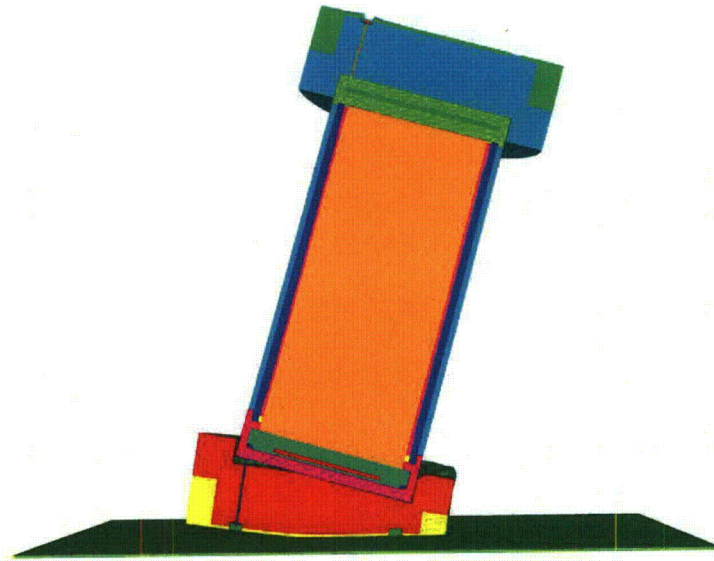


Figure III-32. NAC-STC corner impact at 48 KPH (30 MPH)

Time = 0.05040

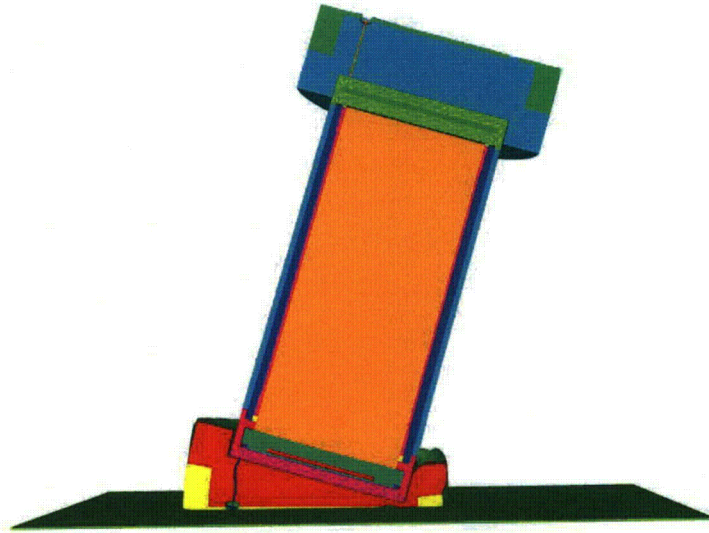


Figure III-33. NAC-STC corner impact at 97 KPH (60 MPH)

Time = 0.03500

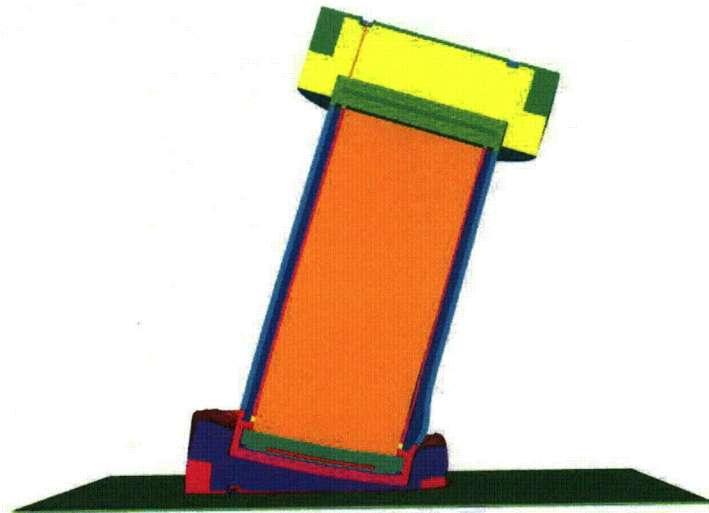


Figure III-34. NAC-STC corner impact at 145 KPH (90 MPH)

Time = 0.03500

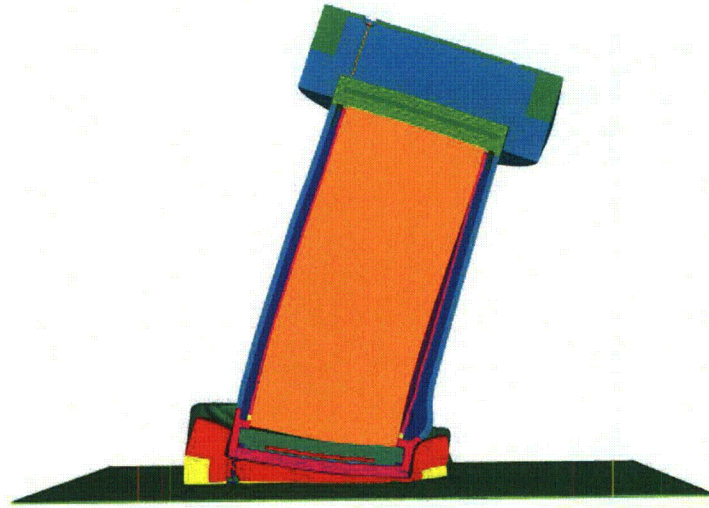


Figure III-35. NAC-STC corner impact at 193 KPH (120 MPH)

Time = 0.03000



Figure III-36. NAC-STC side impact at 48 KPH (30 MPH)

Time = 0.03000



Figure III-37. NAC-STC side impact at 97 KPH (60 MPH)

Time = 0.02400



Figure III-38. NAC-STC side impact at 145 KPH (90 MPH)

Time = 0.01800

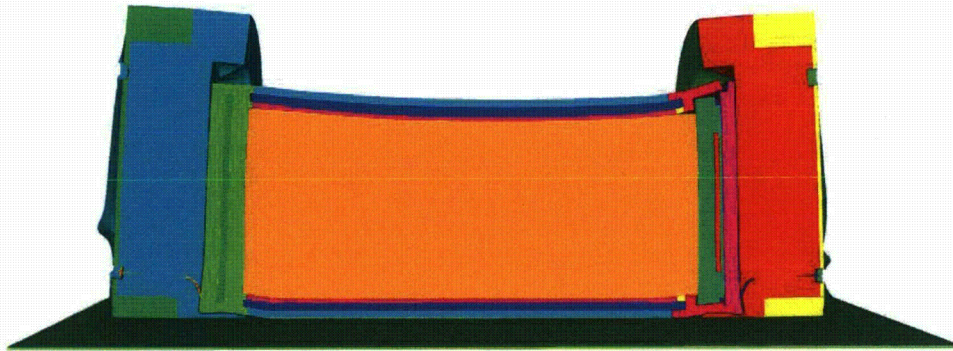


Figure III-39. NAC-STC side impact at 193 KPH (120 MPH)

III.2.6 Determination of Lid Gaps

Possible gaps between the lids and the cask were extracted from the final drop results. The longitudinal orientation of the cask was along the y-direction, so the difference in y-direction displacement between the lid and the cask gave a measure of the gap. A node on the cask was paired with the nearest node on the lid for this gap calculation. The nodes did not align exactly in the xz plane. Two gap values were calculated for the end drop orientation since the deformations were axisymmetric. For side down and cg over corner orientations, gap values were calculated at 5 equally spaced locations around the half-circumference of the cask, as shown in Figures III-40 to III-42.

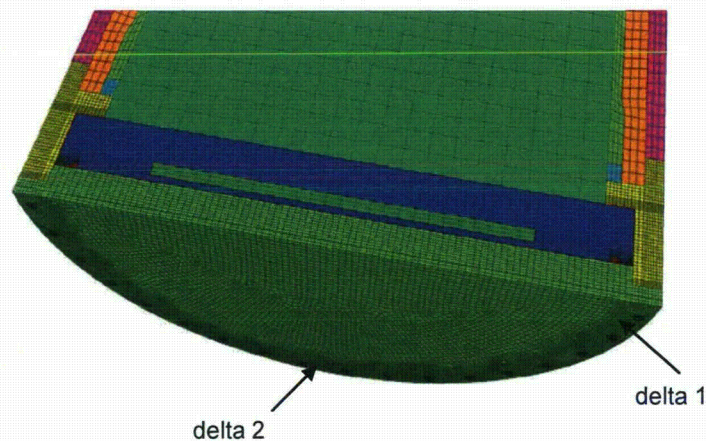


Figure III-40. Gap opening locations for end impact orientation

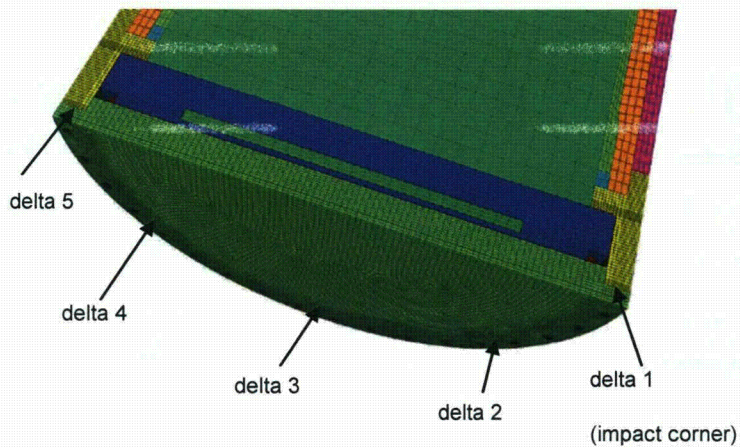


Figure III-41. Gap opening locations for corner impact orientation

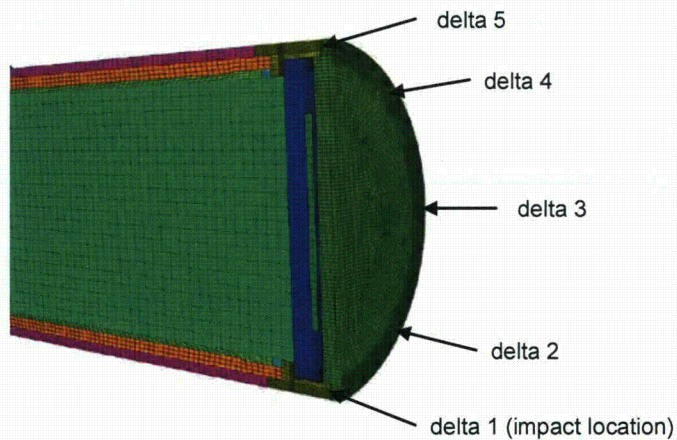


Figure III-42. Gap opening locations for side impact orientation

The next set of figures show plots of the gap sizes as a function of time for the inner and outer lid for each analysis case. All of the gaps calculated are somewhat conservative because the bolts did not include any pre-load. Pre-load decreased the gap size because the bolts do not start to elongate until the pre-load is overcome. As an example, if the 7.1-inch long inner lid bolts are pre-loaded to 50% of their yield strength ($0.5 * 150.8 = 75.4$ ksi) the elastic elongation is 0.018 inches. This indicates the calculated gap for the inner lid is probably overestimated by this amount.

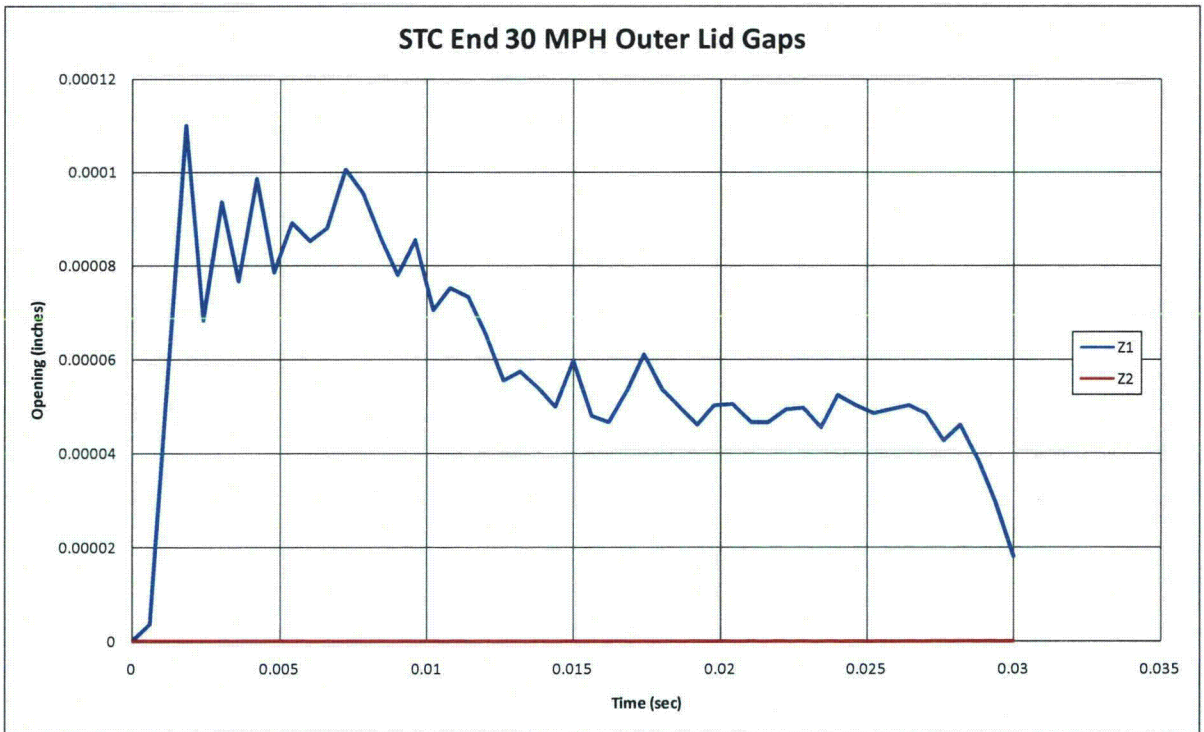
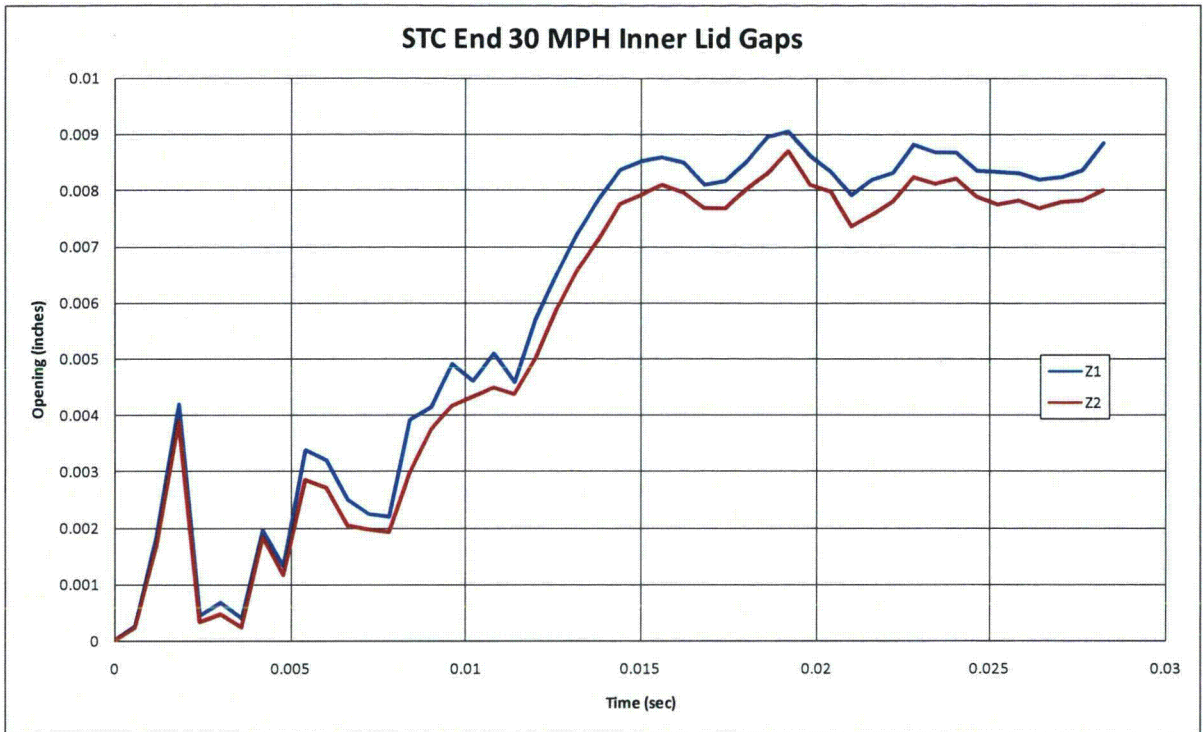


Figure III-43. Gaps in the inner and outer lids of the NAC-STC cask from the end impact at 48 KPH (30 MPH)

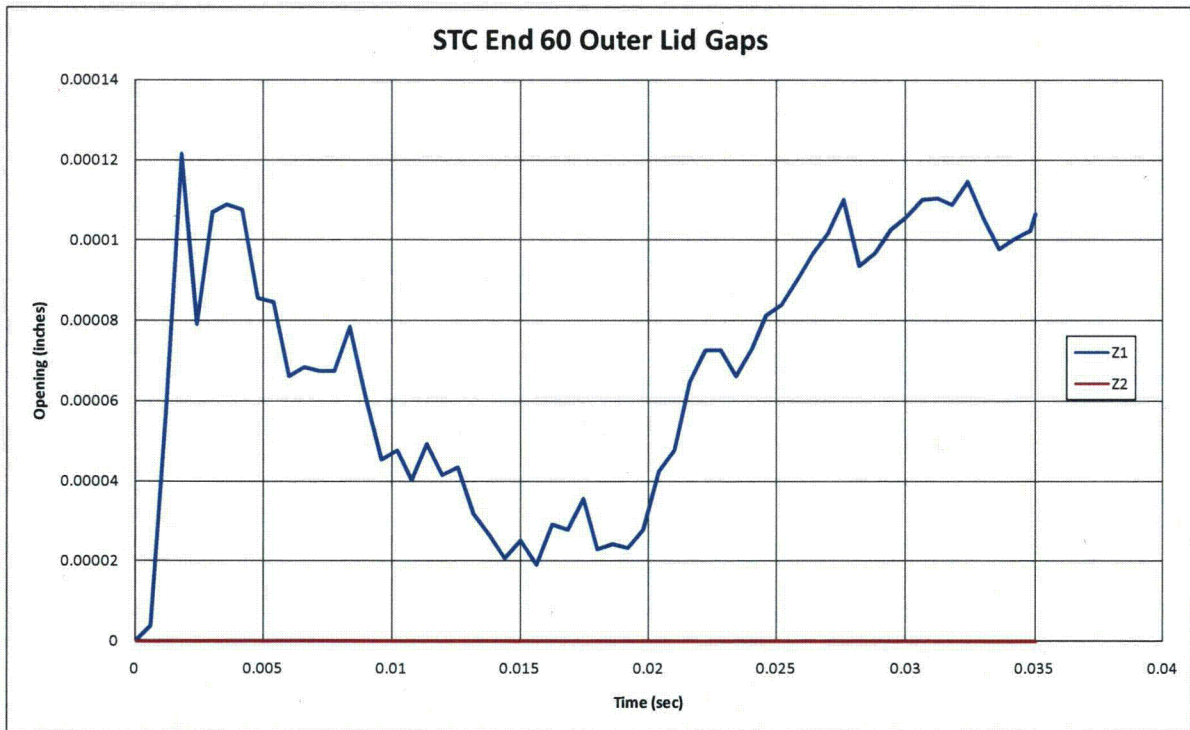
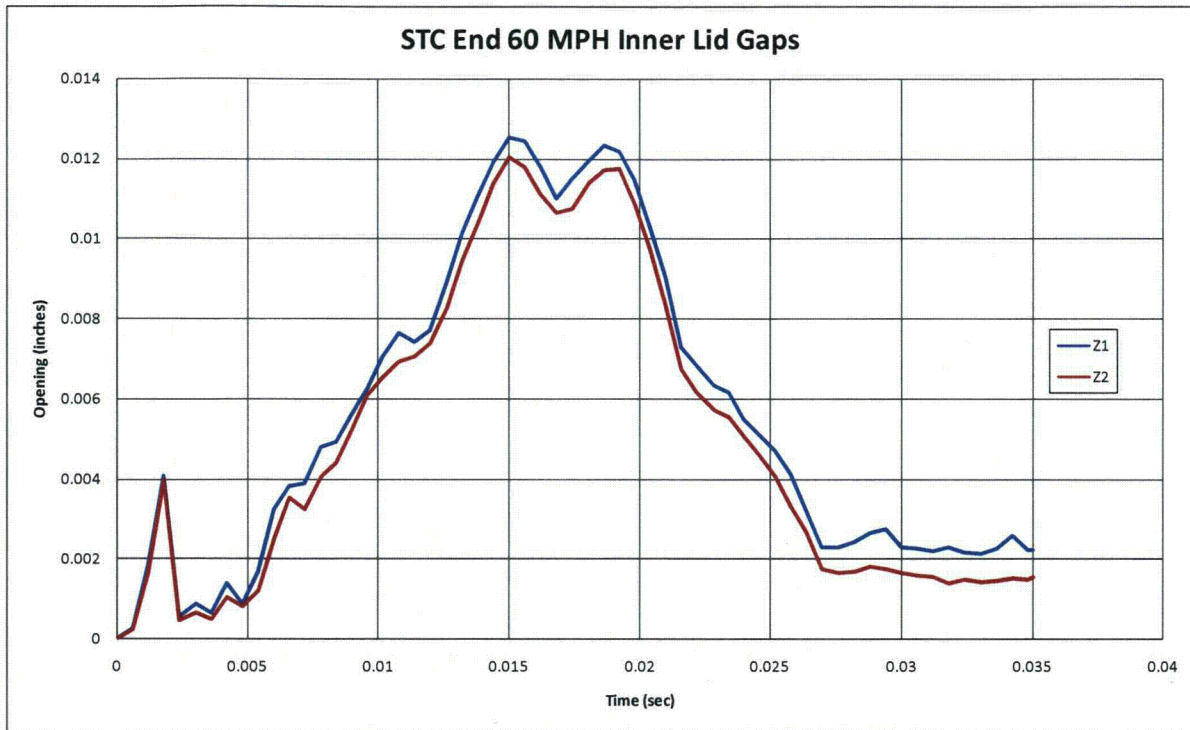


Figure III-44. Gaps in the inner and outer lids of the NAC-STC cask from the end impact at 97 KPH (60 MPH)

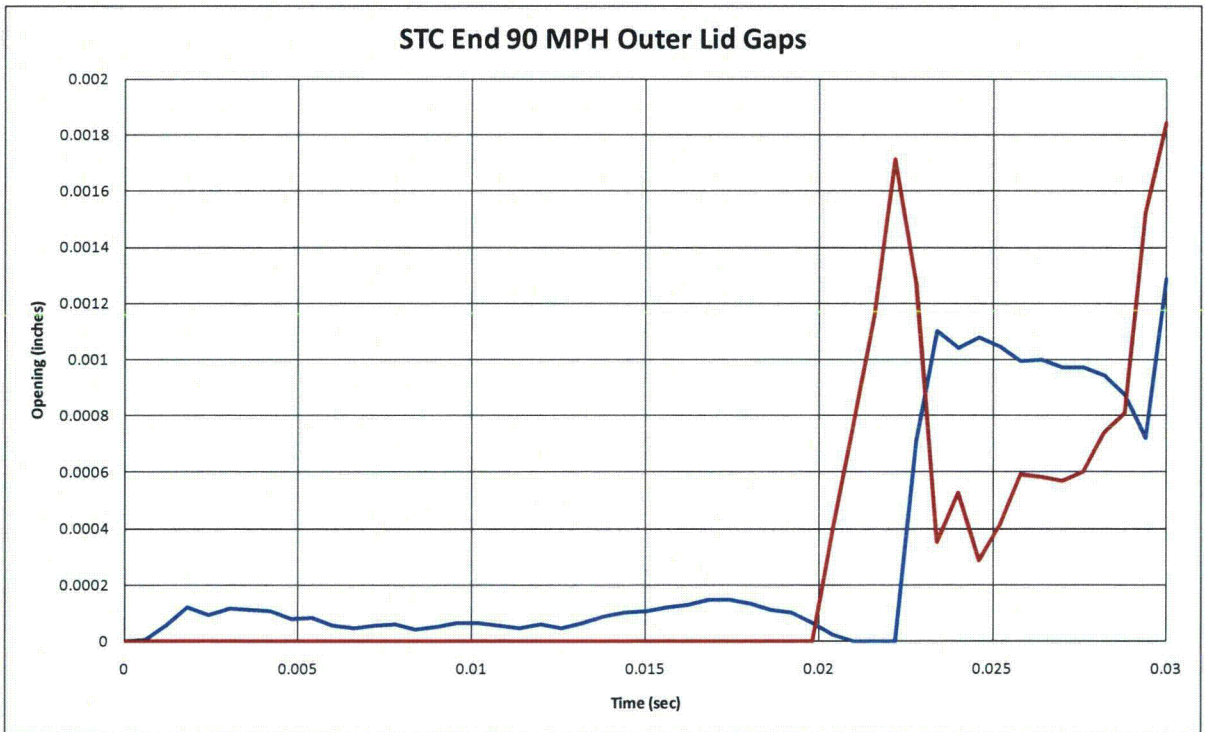
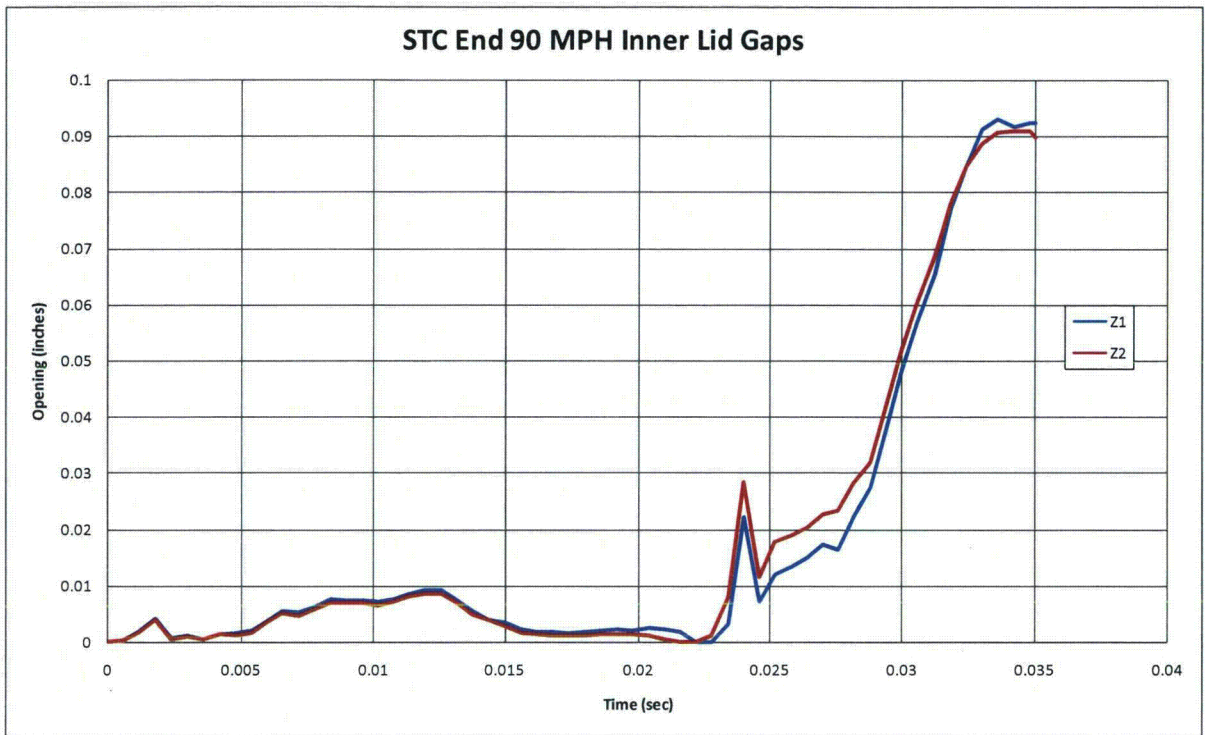


Figure III-45. Gaps in the inner and outer lids of the NAC-STC cask from the end impact at 145 KPH (90 MPH)

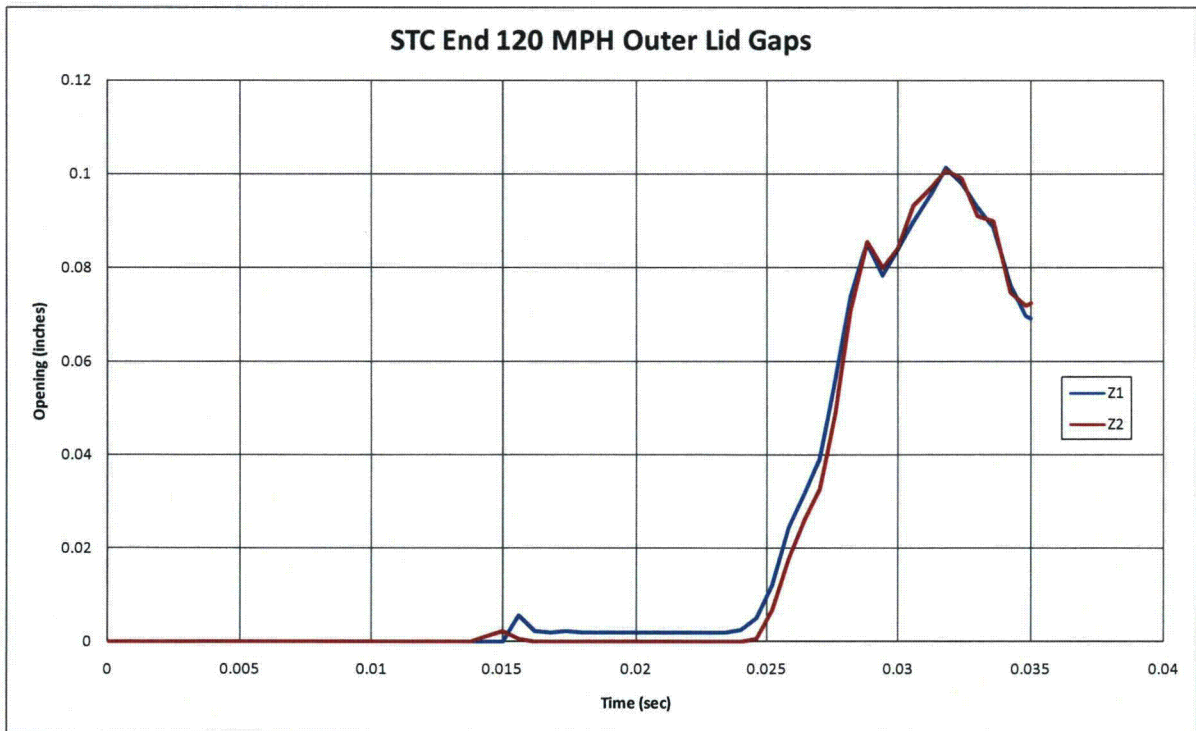


Figure III-46. Gaps in the inner and outer lids of the NAC-STC cask from the end impact at 193 KPH (120 MPH)

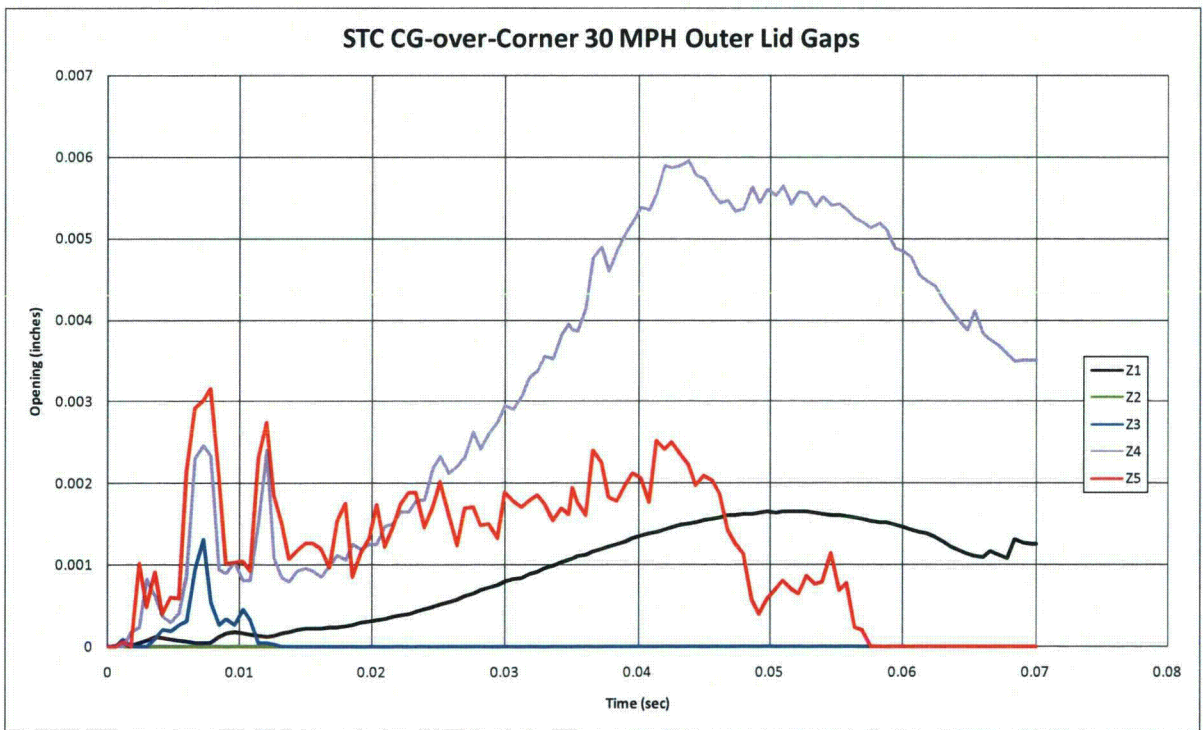
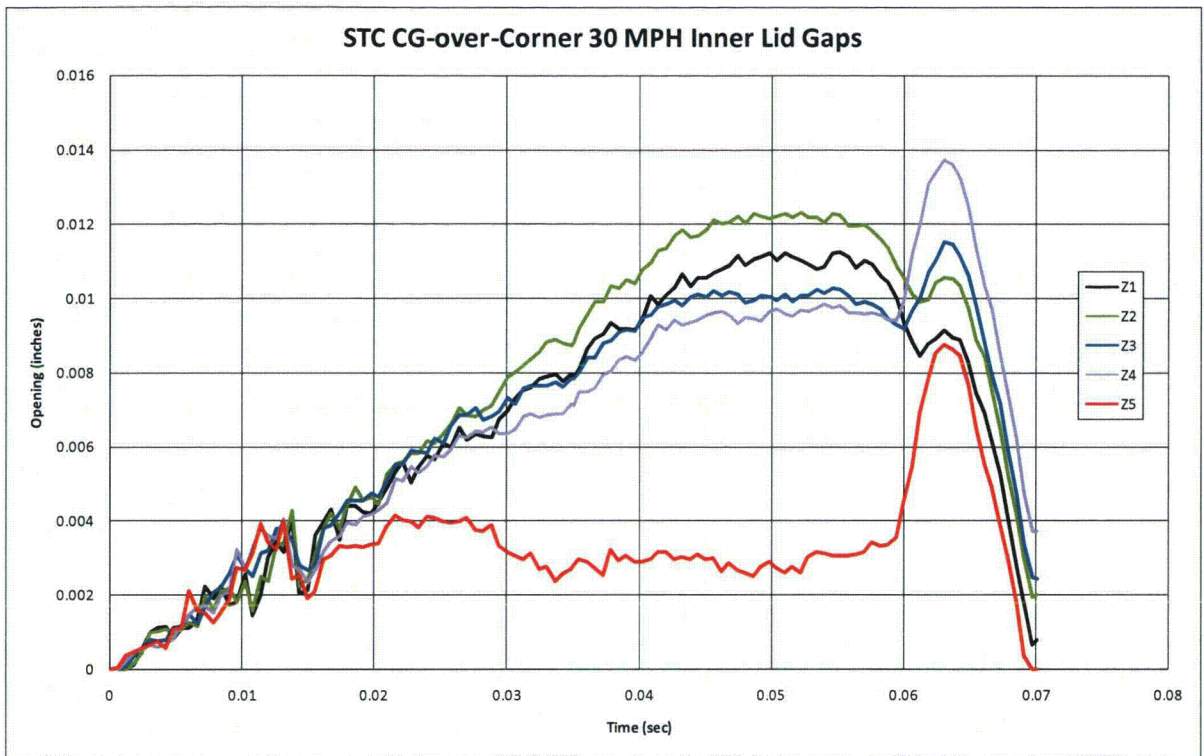


Figure III-47. Gaps in the inner and outer lids of the NAC-STC cask from the corner impact at 48 KPH (30 MPH)

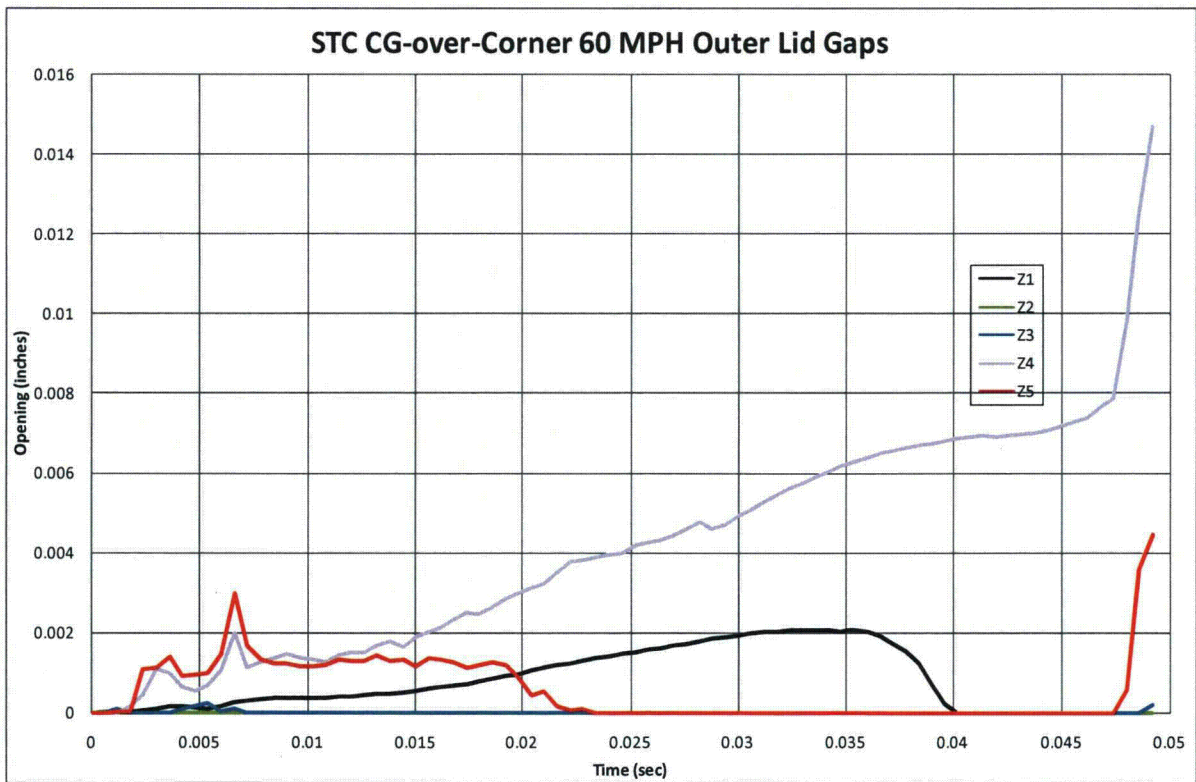
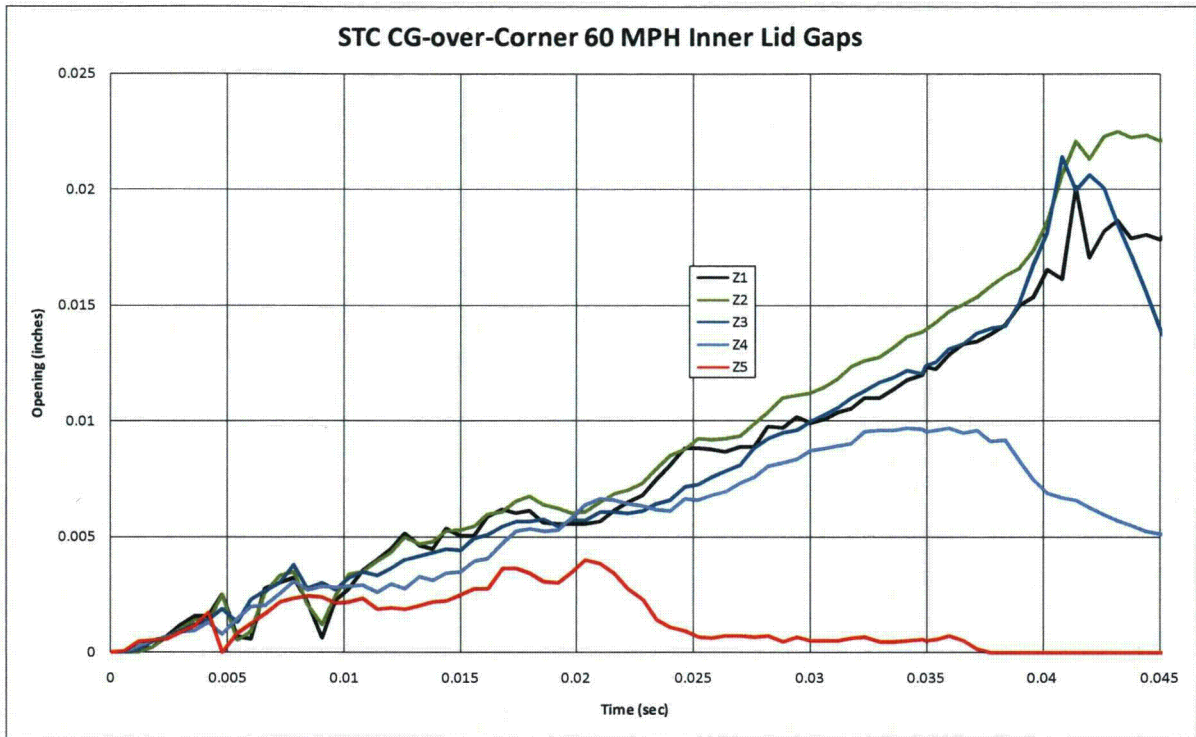


Figure III-48. Gaps in the inner and outer lids of the NAC-STC cask from the corner impact at 97 KPH (60 MPH)

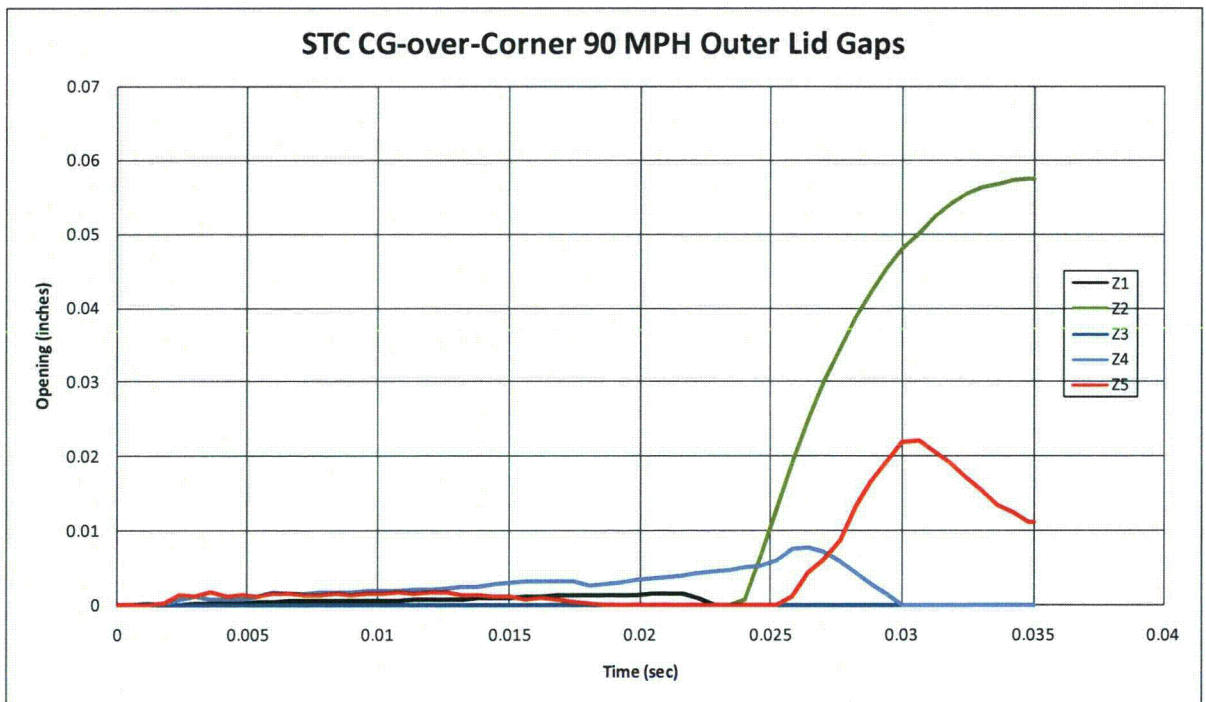
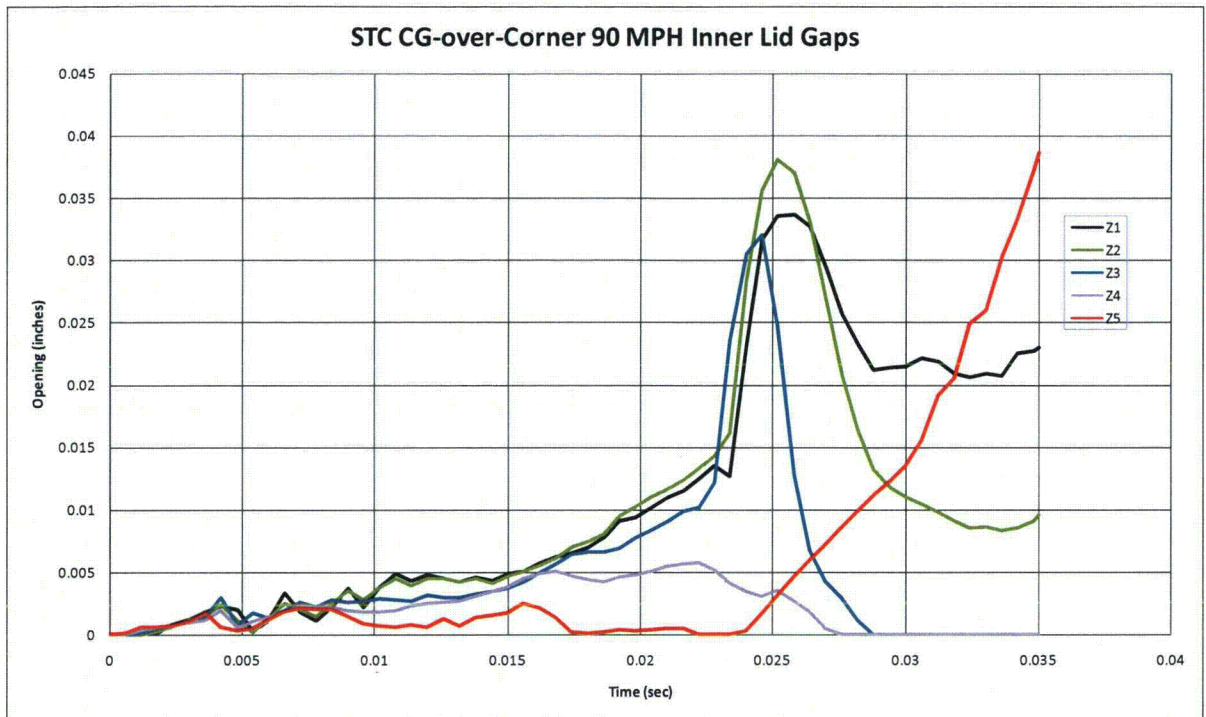


Figure III-49. Gaps in the inner and outer lids of the NAC-STC cask from the corner impact at 145 KPH (90 MPH)

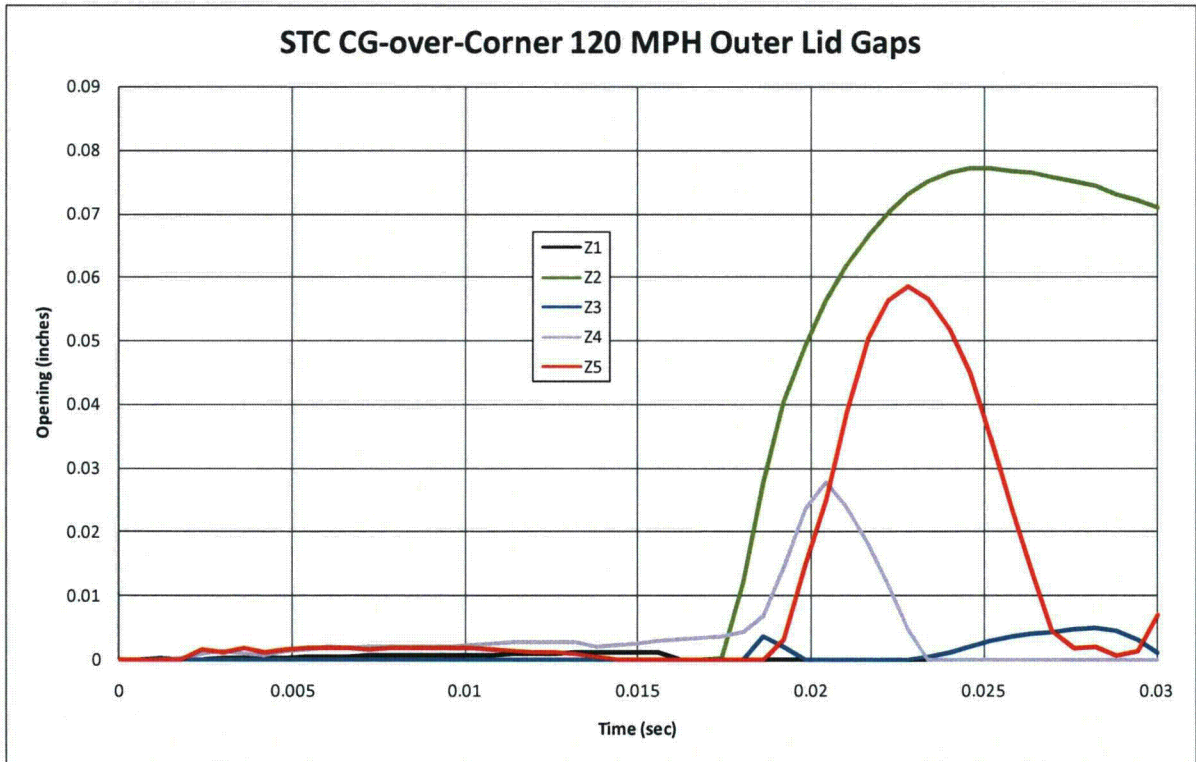
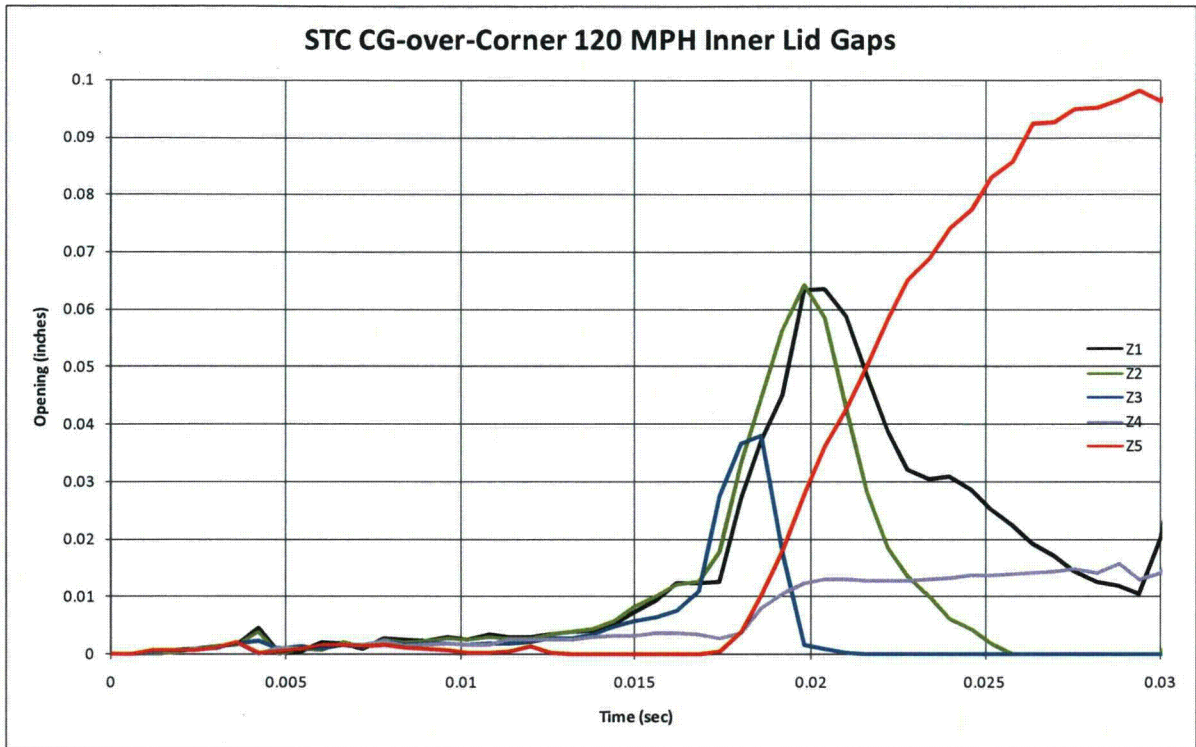


Figure III-50. Gaps in the inner and outer lids of the NAC-STC cask from the corner impact at 193 KPH (120 MPH)



Figure III-51. Gaps in the inner and outer lids of the NAC-STC cask from the side impact at 48 KPH (30 MPH)

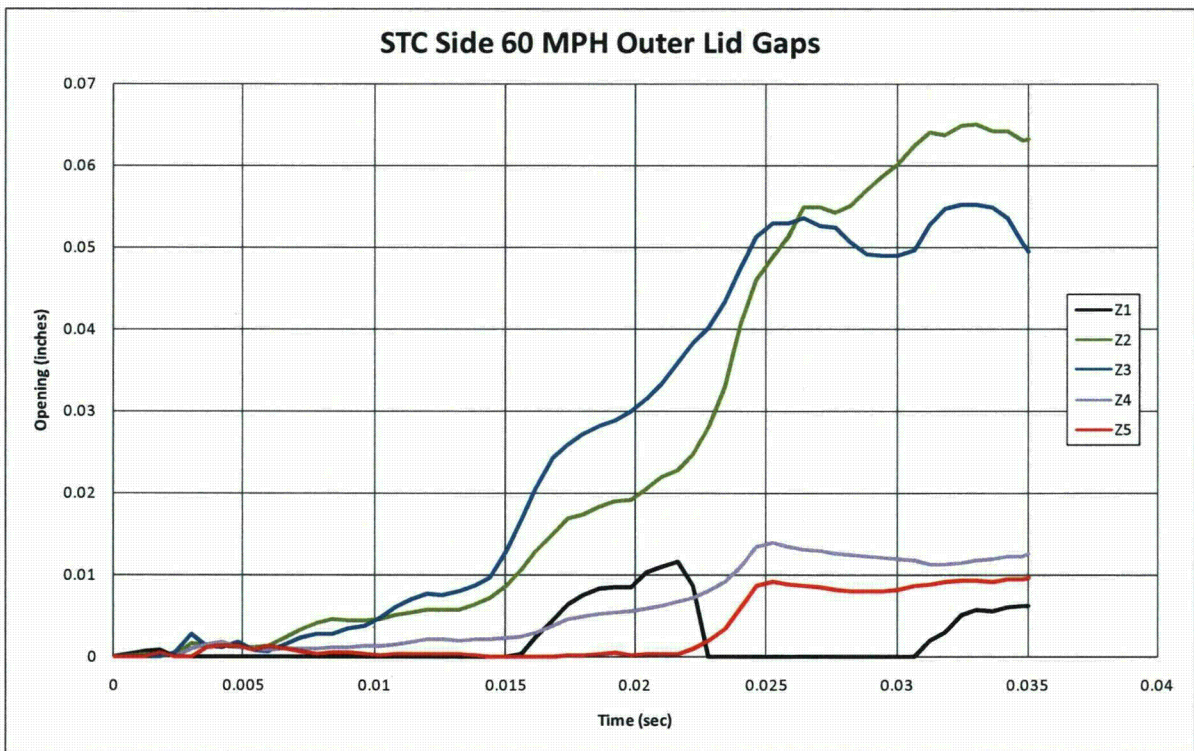
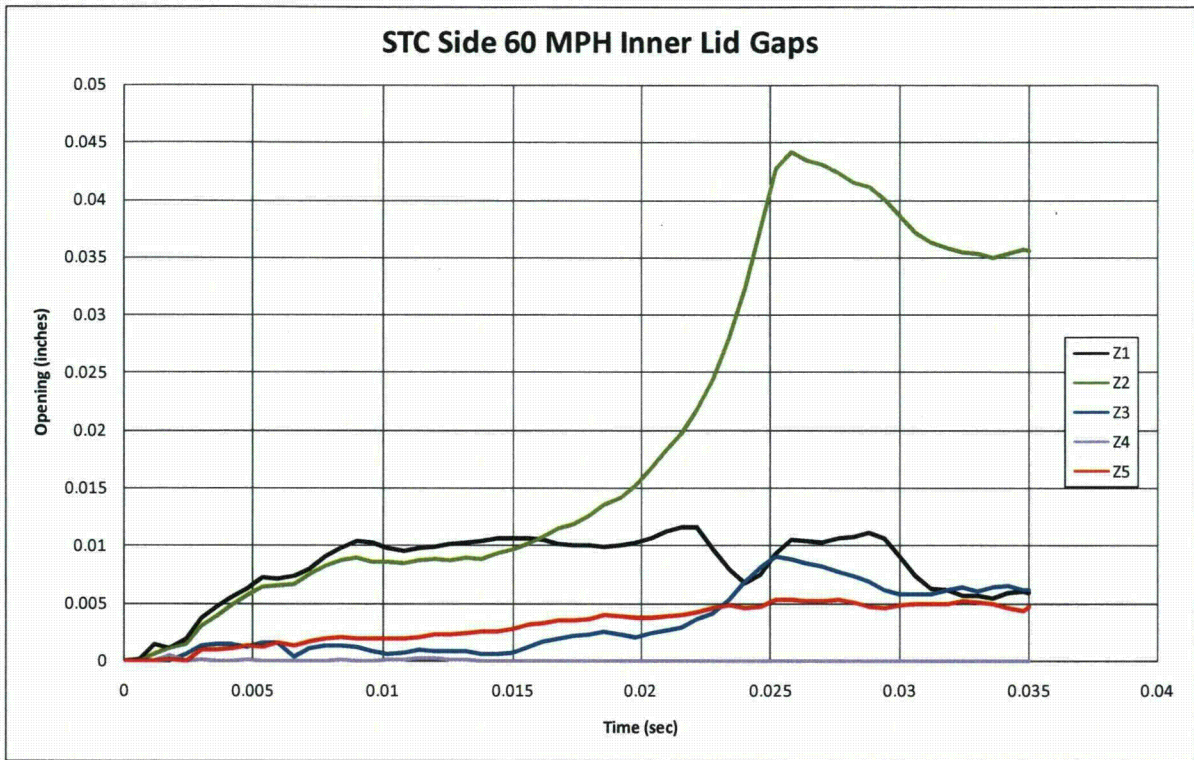


Figure III-52. Gaps in the inner and outer lids of the NAC-STC cask from the side impact at 97 KPH (60 MPH)

To calculate any leak size based upon the gaps the compliance of the o-rings had to be taken into account. The NAC-STC can be sealed with either elastomeric o-rings or metallic o-rings. Elastomeric o-rings can typically maintain a seal when the opening between the mating surfaces opens by 2.5 mm (0.10 in.), and this number is used as the compliance for the cases with elastomeric o-rings. Metallic o-rings are much less tolerant to gaps, and a value of 0.25 mm (0.010 in.) is used as the compliance for the cases with metallic o-rings. For the end impact analyses the gap size is uniform for the entire circumference of the seal, and the hole size is calculated by subtracting the compliance of the o-ring from the gap and multiplying by the circumference. If either the inner seal or the outer seal has a gap less than the compliance, then there is no leak area. For end impacts the only case where there is any leakage is for the 193 KPH (120 MPH) impact with metallic o-rings.

For the corner and side impacts the amount of gap varies around the circumference of the seal, and a more complicated algorithm is needed to calculate the hole size. As in the end impact, the compliance of the seal is subtracted from the gap and a trapezoidal area between measurement locations is assumed. In the corner impact, none of the gaps is large enough to overcome the compliance of elastomeric o-rings, but there would be some leakage for the 97, 145, and 193 KPH (60, 90, and 120 MPH) impacts. The calculated hole sizes for these three cases are 65, 599, and 1716 mm², respectively. In the side impact at 97 KPH (60 MPH) the gaps are not sufficient to cause a leakage with elastomeric seals, but with metallic seals a hole size of 799 mm² is calculated. In the 145 and 193 KPH (90 and 120 MPH) analyses there are a number of failed bolts and very large openings between the lids and the cask body. In these cases both the elastomeric and metallic seals fail and the resulting hole size is more than 10,000 mm². Table III-1 gives the gap and hole sizes for each of the analyses.

Table III-1. Available areas for leakage from the NAC-STC cask

Orientation	Speed (KPH)	Location	Lid Gap (mm)	Seal Type	Hole Size (mm ²)
End	48	Inner	0.226	Metal	none
		Outer	0	Elastomer	none
	97	Inner	0.056	Metal	none
		Outer	0.003	Elastomer	none
	145	Inner	2.311	Metal	none
		Outer	0.047	Elastomer	none
	193	Inner	5.588	Metal	8796
		Outer	1.829	Elastomer	none
Corner	48	Inner	0.094	Metal	none
		Outer	0.089	Elastomer	none
	97	Inner	0.559	Metal	65
		Outer	0.381	Elastomer	none
	145	Inner	0.980	Metal	599
		Outer	1.448	Elastomer	none
	193	Inner	2.464	Metal	1716
		Outer	1.803	Elastomer	none
Side	48	Inner	0.245	Metal	none
		Outer	0.191	Elastomer	none
	97	Inner	0.914	Metal	799
		Outer	1.600	Elastomer	none
	145	Inner	8*	Metal	>10000
		Outer	25*	Elastomer	>10000
	193	Inner	15*	Metal	>10000
		Outer	50*	Elastomer	>10000

III.2.7 Acknowledgements

Jim Bean at Sandia contributed significantly to the development of this model.

III.3 Impacts onto Yielding Targets

III.3.1 Introduction

The finite element results discussed in the previous section are all for impacts onto a rigid target. For this type of impact, the entire kinetic energy of the impact is absorbed by the cask. For finite element analyses a rigid target is easily implemented by enforcing a no displacement boundary condition at the target surface. In real life, the construction of a rigid target is impossible, but it is possible to construct a target that is sufficiently rigid that increasing its rigidity does not increase the amount of damage to the cask. This is because in real impacts there is a sharing of energy absorption between the cask and the target. If the target is much weaker than the cask, the target will absorb most of the energy. If the target is much stronger than the cask, most of the energy will be absorbed by the cask. In this section the partitioning of the drop energy between the four generic casks and several “real-world” targets will be developed in order to obtain

impact speeds onto real surfaces that give the same damage as impacts onto rigid targets. Impacts onto hard desert soil, concrete highways, and hard rock are considered. Impacts onto water surfaces are not explicitly treated, but are discussed. In addition, the probability of puncture of the cask caused by impact against a non-flat surface (or impact by a puncture probe) is developed.

III.3.2 Method

For each finite element calculation for impact onto a rigid target the total kinetic energy of the finite element model is output at 100 time-steps through the analysis. The total kinetic energy is one half of the sum of the mass associated with each node times the velocity of that node squared. Figure III-53 shows kinetic energy time-histories for the steel-lead-steel truck cask for each orientation from the 120-mph impact analyses with pre-crushed impact limiters. From the time-history of kinetic energy, a velocity time history is derived. The rigid-body velocity for each time-step is calculated assuming that all of the kinetic energy of the model is caused by velocity in the direction of the impact. Equation III-1 shows this mathematically.

$$v_t = \sqrt{\frac{2KE_t}{\sum m_i}} \quad (\text{Eq. III-1})$$

where v_t is the velocity at time t , KE_t is the kinetic energy at time t , m_i is the mass associated with node i , and the summation is over all of the nodes in the finite element model.

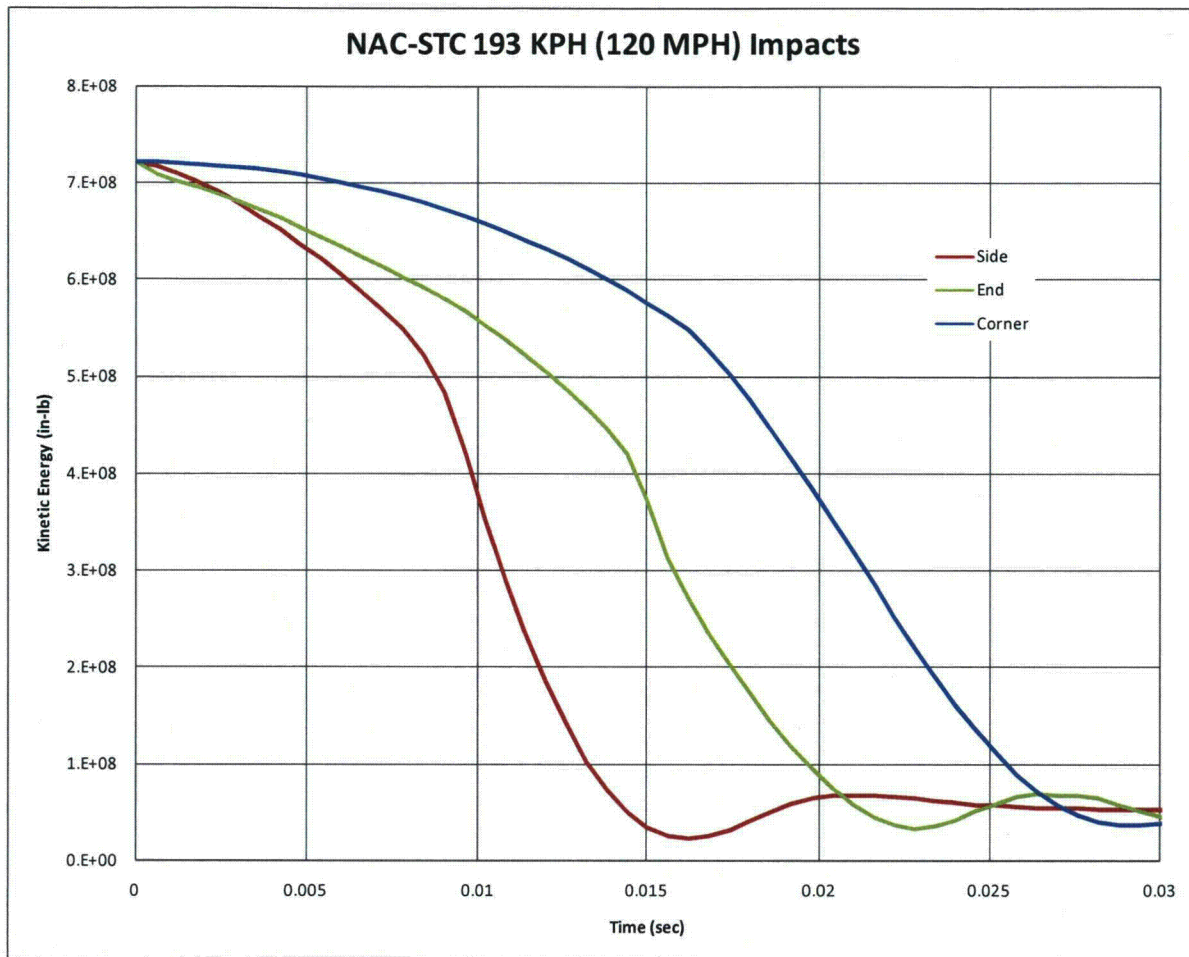


Figure III-53. Kinetic energy time histories for the NAC-STC cask from 193 KPH (120 MPH) impact analyses in the end, side, and corner orientations

For each analysis the peak contact force is determined. Table III-2 lists these forces. For an impact onto a real target to be as damaging to the cask as the impact onto the rigid target, the target must be able to impart a force equal to this peak force to the cask.

The energy absorbed by the target in developing this force is added to the initial kinetic energy of the cask. This total absorbed energy is used to calculate an equivalent velocity by replacing KE_t in Equation III-1 with the total energy.

Table III-2. Peak contact force for the NAC-STC impacts onto an unyielding target (bold numbers are for the cases where there may be seal leaks)

Orientation	Speed (KPH)	Accel. (G)	Contact Force (Millions of Pounds)	Contact Force (MN)
End	48	58.5	14.6	65.0
	97	111.6	27.9	123.9
	145	357.6	89.3	397.1
	193	555.5	138.7	616.8
Corner	48	36.8	9.2	40.9
	97	132.2	33.0	146.8
	145	256.7	64.1	285.1
	193	375.7	93.8	417.2
Side	48	76.1	19.0	84.5
	97	178.1	44.5	197.8
	145	411.3	102.7	456.7
	193	601.1	150.0	667.4

III.3.3 Soil Targets

The force that hard desert soil imparts onto a cask following an impact was derived from results of impact tests performed by Gonzales [5-13], Waddoups [5-14], and Bonzon and Schamaun [5-15]. The tests by Gonzales and Waddoups used casks that were comparable to NAC-STC, but much smaller. The tests by Bonzon and Schamaun were with casks that were less stiff than the NAC-STC. This large amount of test data was used to develop an empirical soil target force-deflection equation that is a function of impactor area. Figure III-54 shows the force-deflection curves for impact of the NAC-STC onto a soil target. Corner impacts were assumed to have the same contact area on the soil target as the end impacts, so only two curves are shown. Similar curves were developed for each of the other casks. Comparison of Figure III-54 with the forces in Table III-2 show that many of the impacts will result in very large soil penetrations. This is consistent with the results seen in Waddoups' tests, where casks were dropped 2,000 feet from a helicopter. Penetration depths for these impacts were up to 8 feet, and the equivalent rigid target impact velocity was less than 30 mph. Integration of the force-deflection curve up to the peak contact force determines the amount of energy absorbed by the target.

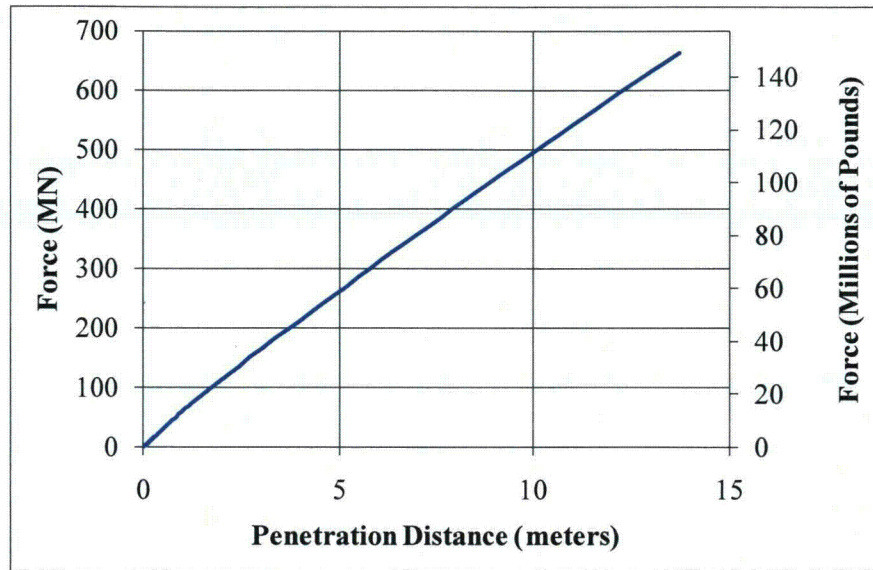


Figure III-541. Force generated by the NAC-STC cask penetrating hard desert soil

III.3.4 Concrete Targets

The force imparted to a cask by impact onto a concrete target is derived from test results by Gonzales [5-13]. In his series of tests, a cask-like test unit was impacted onto two types of concrete targets, one 12 inches thick and one 18 inches thick, at velocities from 30 to 60 mph. All of the impacts were in an end-on orientation. Based upon the results of these tests and engineering mechanics, an empirical relationship between the force and energy absorbed was derived. For impacts onto concrete slab targets there are two mechanisms that produce large forces onto the cask. The first is the generation of a shear plug in the concrete. The force required to produce this shear plug is linearly related to the impact velocity, the diameter of the impacting body, and the thickness of the concrete. Equation III-2 gives the empirical equation for the force required to produce the shear plug.

$$F_s = C_s v_e d_i t_c \quad (\text{Eq. III-2})$$

where F_s is the force required to produce the shear plug, C_s is an empirical constant (16.84), v_e is the equivalent impact velocity, d_i is the diameter of the impactor, and t_c is the thickness of the concrete slab.

The energy absorbed in producing this shear plug is linearly related to the cask diameter, the square of the impact velocity, and the fourth root of the slab thickness. Equation III-3 gives the empirical equation for the energy required to produce the shear plug.

$$E_s = C_e d_i v_e^2 t_c^{0.25} \quad (\text{Eq. III-3})$$

where E_s is the energy required to produce the shear plug and C_e is an empirical constant (0.00676).

After the shear plug is formed, further resistance to penetration is achieved by the behavior of the subgrade and soil beneath the concrete. This material is being penetrated by the cask and the shear plug. Generally, the shear plug forms with 45-degree slopes on the side. Therefore, the diameter of the soil being penetrated is equal to the cask diameter plus twice the slab thickness. The behavior of the subgrade and soil is assumed to be the same as the hard desert soil used for the soil target impacts. Figure III-55 shows a comparison of the empirical relationship with one of Gonzales' tests. For corner and side impacts an equivalent diameter is calculated to fit with the empirical equations. For each case the diameter is calculated by assuming the shear plug forms when the concrete target has been penetrated two inches. The area of the equivalent diameter is equal to the area of the concrete in contact with the cask when the penetration depth is two inches. To calculate the equivalent velocity for concrete targets the force required to generate the shear plug must be compared to the peak contact force for the impact onto the rigid target. The velocity required to produce this force can be calculated from Equation III-2. The kinetic energy associated with this velocity is absorbed by a combination of producing the shear plug, penetration of the subgrade and soil beneath the concrete, and deformation of the cask. The energy absorbed in producing the shear plug is calculated by Equation III-3, the energy absorbed by the cask is equal to the kinetic energy of the rigid target impact, and the energy absorbed by the subgrade and soil is calculated in a manner similar to that for the soil impact discussed above. If the amount of energy to be absorbed by the soil is sufficiently high, the force in the soil will be higher than the force required to produce the shear plug. In this case, an iterative approach is necessary to derive an equivalent velocity so that the maximum force generated in penetrating the subgrade and soil beneath the concrete is equal to the peak contact force for the rigid target impact.

Gonzales Impacts onto Highway Targets

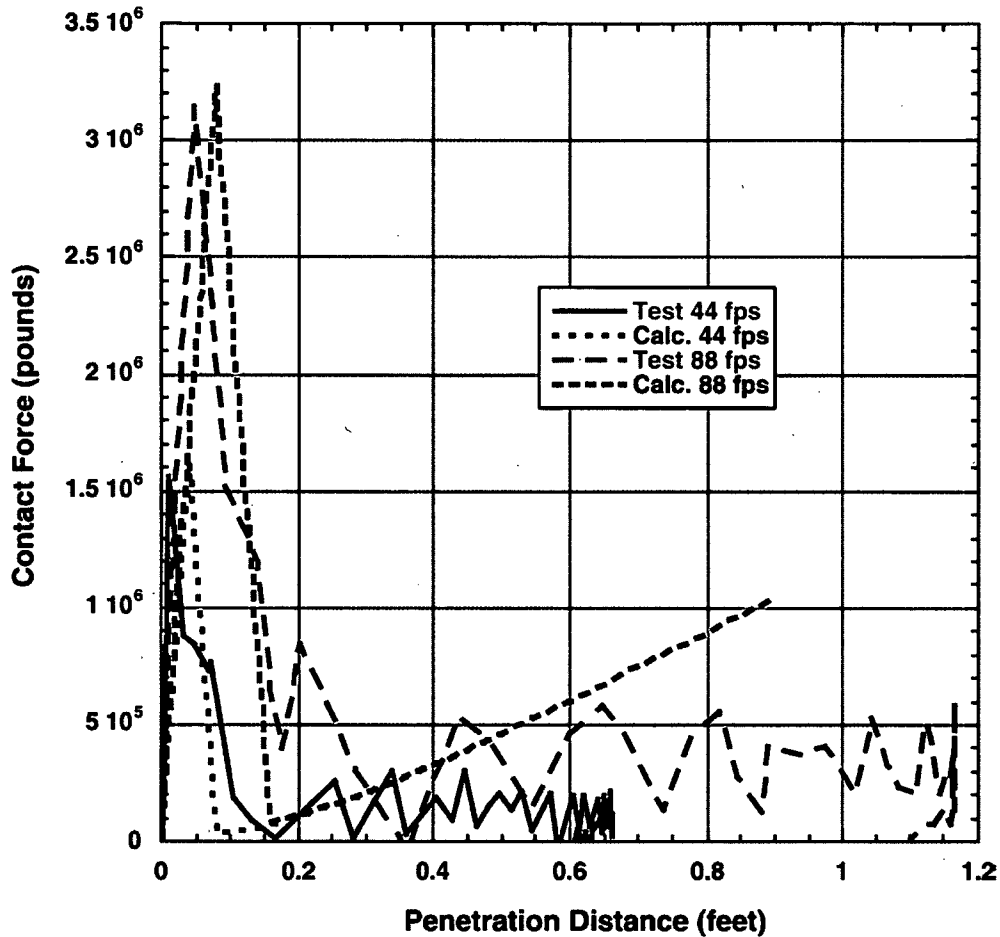


Figure III-55. Comparison of test force-deflection curves with those derived from the empirical equations.

The only orientation of impacts onto concrete targets where test data is available is for end impacts. In this orientation the contact area between the cask and the concrete does not increase with increasing penetration distance. In order to use the empirical relationships developed for end impacts with other impact orientations, an equivalent diameter must be determined. For both the side and corner impacts, the equivalent diameter was calculated to have an area equal to the area of the cask two inches above the contact point. For side impact orientations, this area is a rectangle. For corner impact orientations this area is a truncated parabola.

III.3.5 Hard Rock Targets

For impacts onto hard rock targets the target is assumed to be a semi-infinite half plane. The force and energy absorbed by the target is determined by the volumetric behavior of the rock. For hard rock surfaces this behavior is sufficiently stiff that very little energy is absorbed by the target. For this reason these impacts are treated as rigid target impacts.

III.3.6 Results for Real Target Calculations

Table III-3 gives the results for impacts onto soil and concrete targets.

Table III-3. Equivalent velocities for NAC-STC impacts onto various targets, KPH

Orientation	Rigid	Soil	Concrete
End	48	102	71
	97	205	136
	145	>250	>250
	193	>250	>250
Corner	48	73	70
	97	236	161
	145	>250	>250
	193	>250	>250
Side	48	103	79
	97	246	185
	145	>250	>250
	193	>250	>250

III.3.7 Impacts onto Water

Equivalent velocities for impacts onto water targets for velocities greater than the regulatory impact are assumed to be above the range of possible impact velocities (150 mph). The incompressible nature of water makes perfectly flat impacts quite severe. As the impact velocity increases smaller deviations from the perfectly flat orientation are sufficient to cause the lack of shear strength in water to dominate the response. Because perfectly flat impacts are very improbable, this approach is justified.

III.4 Response of Spent Fuel Assemblies

III.4.1 Introduction

The response of spent power reactor fuel assemblies to impact accidents is not well understood. While this area has been investigated in the past (Sanders et al. 1992), those models tended to be relatively crude and imprecise. In addition, there is a renewed interest on the part of utility companies in shipping higher burnup spent fuel. Therefore, determining a more accurate response of spent fuel assembly to impact loads that may be the result of transportation or handling accidents or malevolent acts is essential. Sandia National Laboratories has performed a series of computational analyses to predict the structural response of a spent nuclear fuel assembly that is subjected to a hypothetical regulatory impact accident, as defined in 10 CFR71.73. This study performs a structural analysis of a typical pressurized water reactor (PWR) fuel assembly using the Abaqus/Explicit finite element analysis code. The configuration of the pellet/cladding interface and the material properties of the pellet have been varied in the model to account for possible variations in actual spent fuel assemblies.

III.4.2 Description and Method

A typical PWR fuel assembly is shown in Figure III-56. The assembly consists of a series of fuel pins, or rods, grouped together in a square array. The fuel rods are held in place by a series of equally spaced grids. Within the array of fuel tubes are a series of guide tubes in which control rods are placed for controlling the fission reaction during operation. The guide tubes are attached to endplates, nozzles or end fittings, which provide rigidity for handling.

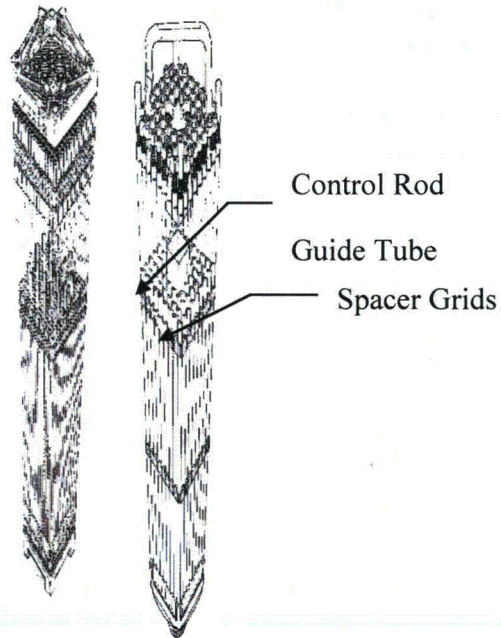
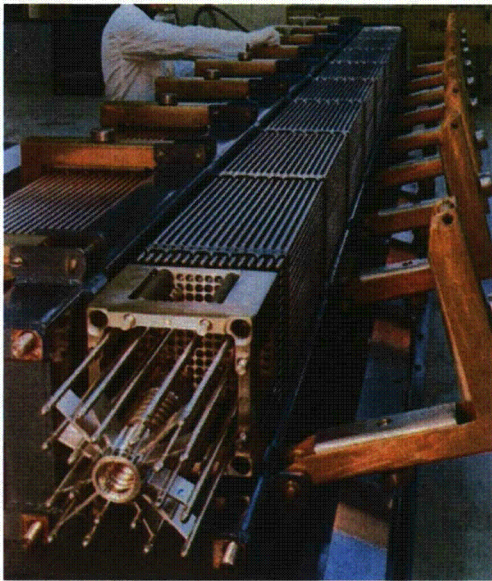


Figure III-56. PWR fuel assembly

An individual fuel rod is shown schematically in Figure III-57. It is constructed by stacking a series of Uranium Dioxide (UO_2) pellets inside a Zirconium tube, placing a spring on the top of the pellet stack and welding on end caps. A plenum is added at the top of the assembly to provide a sufficient volume to collect released fission gases.

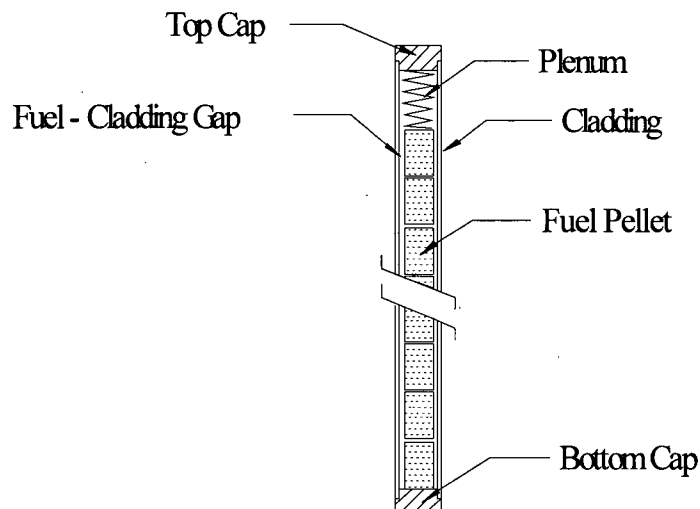


Figure III-57. Fuel rod schematic drawing

The working environment of a reactor is extremely harsh. The fuel rods are subjected to neutron radiation, large thermal gradients, large stress due to external water pressure and large local stress from contact between the pellet and the cladding. Upon the first power cycle, the uranium pellet cracks into pie shaped pieces due to the large radial temperature gradients across the pellet. Over a short period of time (months), the pellets shrink as fine porosity in the fuel is removed by radiation densifications. The cladding slowly creeps down onto the pellet due to its high operating temperature and the external pressure of the coolant. The pellet also begins to expand due to fission product swelling. Over a period of 1-2 years the initial gap between the fuel rod and the pellet is eliminated. However, the contact between the cladding and the fuel pellet is not necessarily circular and uniform. This leads to local increases in the cladding stress. In addition, zirconium is one of the few elements that react with both oxygen and hydrogen. This can lead to a reaction between the ZrO_2 layers on the inner cladding surface and the fuel pellet to form a bonding interface of $(U,Zr)O_2$ between the fuel pellet and the cladding. In essence, bonding the pellet to the cladding wall. In addition, hydride precipitants can also form in the Zircaloy cladding wall.

Upon the removal from the reactor, the state of the spent fuel assembly at any future time depends on the spent fuel's environmental history as well as its condition upon removal from the reactor. The internal gas pressure in a fuel rod having been removed from the reactor now provides a tensile hoop stress on the cladding. This stress along with changes in cladding temperature may allow hydrogen to precipitate out and possibly reform along the circumferential directions (direction of highest stress). Plastic creep in the cladding may cause a gap to develop between the cladding and the fuel pellet and the development of void spaces in the crack pellets. The current material conditions and stress state of any particular rod at the time of an accident is complex and unknown. Therefore, the current material properties and geometric configuration

will be varied over a small range to attempt to account for the actual unknown material and geometric variations.

Table III-4 lists the material properties and nominal dimensions of a 17x17 PWR fuel assembly. Due to the large number of rods and the large ratio between the fuel assembly length and the fuel rod diameter, modeling a complete assembly using the finite element method is challenging. To build the entire model using continuum and structural shell elements with a high enough resolution in each fuel rod would produce a model with so many degrees of freedom as to be computationally intractable. Therefore, the current analysis will be broken down into three steps. In the first step, the entire assembly will be modeled using structural beam and shell elements. Then in the second step, the loads from the highest loaded rod in the full assembly model will be transferred to a single rod model constructed of continuum and structural shell elements. This model will provide the detailed stress field necessary to determine the integrity of the fuel rod. Due to the severe nature of the reactor environments there are significant material and geometric changes in the fuel rods. Very little if any test data is available for the Zircaloy-4 material under high irradiation conditions, therefore as a third step, a series of parametric analyses were conducted with the continuum model to determine the sensitivity of the model to changes in the rod geometry and the pellet and cladding material properties.

Table III-4. Properties of fuel assembly

Assembly Type 17 x 17	
Cladding Material	Zircaloy-4
Assembly Cross-section (in)	8.43-8.54
Number of Fuel Rods per Assembly	264
Fuel Rod OD (in)	0.374 to 0.379
Minimum Cladding Thickness	0.023
Pellet Diameter (in)	0.3225 to 0.3232
Maximum Active Fuel Length (in)	144

III.4.3 Finite Element Models

Two major models have been developed in this analysis. The first of these is the beam fuel assembly model which is a structural model consisting of beam and shell elements. This model is used to determine the overall response of the fuel assembly. Using data from this model a

detailed continuum model of a single rod is developed to determine a more detailed response of the most highly loaded rod. Several parametric analyses are conducted with the latter model to determine the effect of variations of rod material properties and geometry. In addition to these models, several smaller models have been developed to aid in the overall analysis. Initial models were developed to test the capabilities of the finite element codes. Small models were also developed when problems arose in the analyses. All of these models along with the final rod analysis are discussed in the following section.

Code Testing Models

Beam-to-beam contact is a capability not currently supported by the two Sandia finite element codes, PRONTO3D and PRESTO. However, two commercial codes, Abaqus/Explicit [3] and LS-DYNA [4], have recently implemented this capability into their codes. Small models were constructed representing spent fuel assemblies to test this capability in each code.

A small three-beam model with three cells representing spacer grid members is shown in Figure III-58. The model was developed to test the two commercial finite element codes. The beam elements have a circular cross-section and are modeled as unirradiated Zircaloy-4 material. The spacer grid segments are modeled using shell elements made of the same Zircaloy-4 material. The beam elements are given an initial velocity in the negative-Y direction and the bottom of the spacer grid cells are fixed in all degrees of freedom.

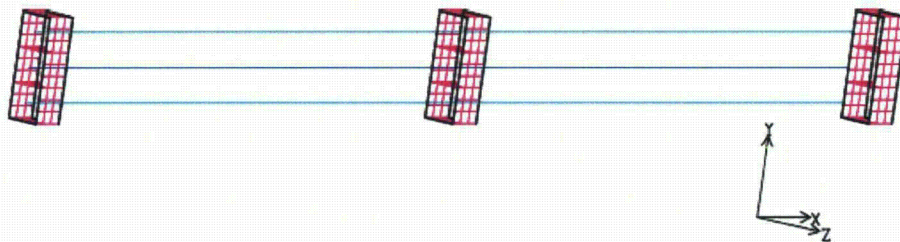


Figure III-58. Model used to test finite element codes

The General Contact algorithm was used in the Abaqus/Explicit code and the Contact Automatic Single Surface and Contact Automatic General algorithms were used with the LS-DYNA code. The calculated kinetic energies for these three models are shown in Figure III-59, with each model having 24 beam elements along the length of each beam member.

From the kinetic energy plots in Figure III-59, it is clear that there is a problem with the beam contact algorithms in LS-DYNA. For the case using the Automatic Single Surface algorithm, the kinetic energy spikes from the initial value of 200 in-lbs to a value of 1000 in-lbs, which is beyond the range shown in the graph. For the LS-DYNA model using the Contact Automatic General algorithm, which was recommended for beam and shell contact by an LS-DYNA instructor, the kinetic energy initially decreases but then spikes beyond the original value of 200 in-lbs to other very large values several times later. For this reason, the LS-DYNA code was not used to model the fuel assembly.

Initially, the Abaqus/Explicit code using the General Contact algorithm looked much better. The kinetic energy plot for the test model indicated an initial drop with a small rebound and a final tapering off. However, further analyses of the same model with different numbers of elements also showed a spike in kinetic energy. These results are presented in Figure III-60. For the model containing six elements along the beam length, there is a huge rebound in the kinetic energy to over 3000 in-lbs. Consultation with Abaqus personnel resulted in them finding a bug in the code and sending out a new version of their code to Sandia.

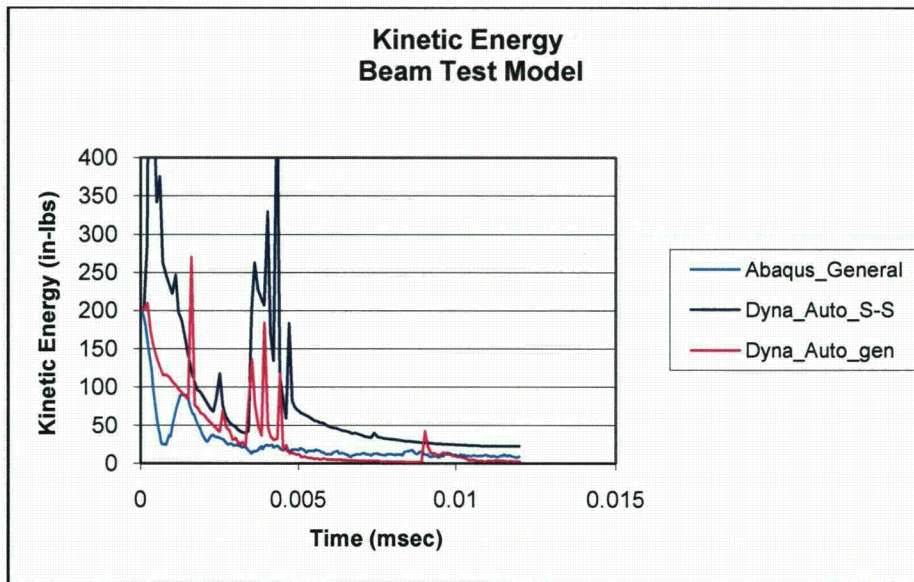


Figure III-59 Kinetic energy for code test models

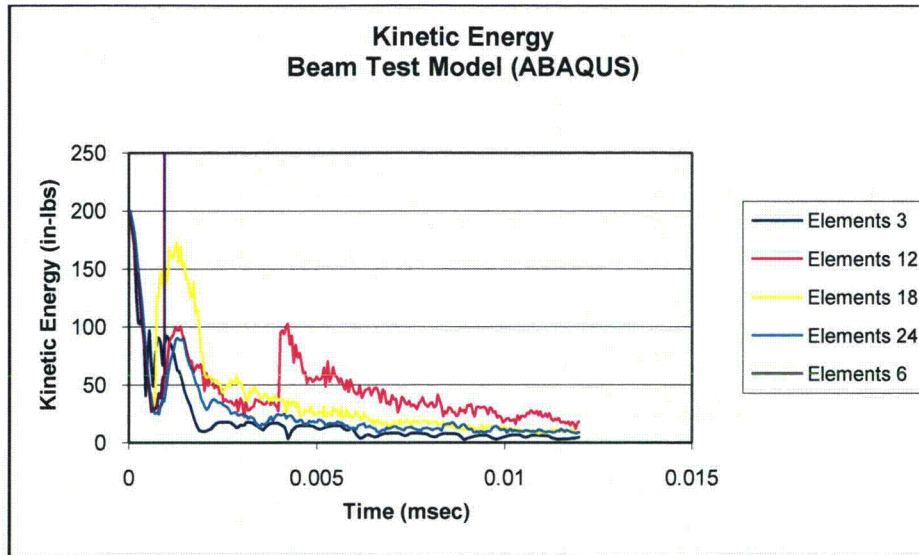


Figure III-60. Kinetic energy for ABAQUS test model with different numbers of elements

Fuel Assembly Finite Element Model

Using the latest version of the Abaqus/Explicit finite element code, a complete fuel assembly model (shown in Figure III-61) was constructed and analyzed. It incorporates 3D beam elements for the fuel pins and control rods, and shell elements for the spacer grid assemblies and the support plates representing the basket walls. The endplates are modeled as solid plates using hexahedron elements so that the support rod beam elements can be attached. The model contains 265 fuel pins and 24 tie rods. There are a total of 129,440 elements, with 41,616 beam elements. There are 144 beam elements along the length of each fuel rod and support rod. The location of the guide tubes in the cross-section of the fuel assembly is presented in Figure III-62.

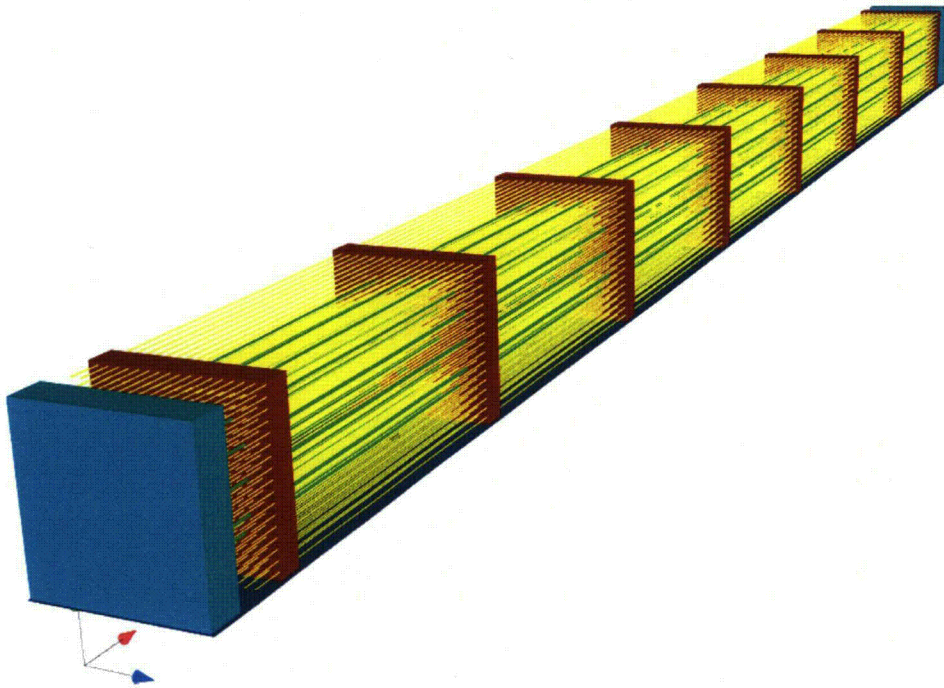


Figure III-61. Beam Fuel Assembly finite element model

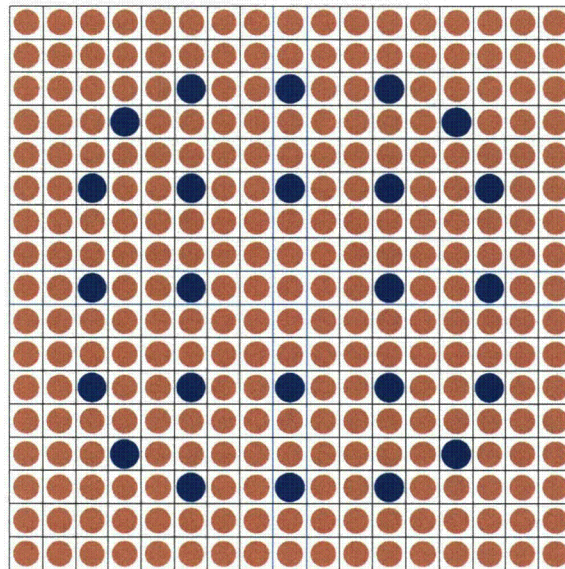


Figure III-62. Cross-section of 17x17 fuel assembly with guide tubes (in blue)

The fuel assembly model was loaded using acceleration curves developed from experimental data of a side impact drop test. The full-scale data for the analysis was calculated from the ¼ scale test data. A plot of the full-scale data is presented in Figure III-63. An additional curve was generated from the full-scale data to yield a maximum acceleration of 100 g's, while maintaining the same total impulse. The fuel rods are given an initial velocity of 528 in/sec, which corresponds to a 9-meter drop test. The acceleration is applied to the lower plate, which represents the side of the fuel basket.

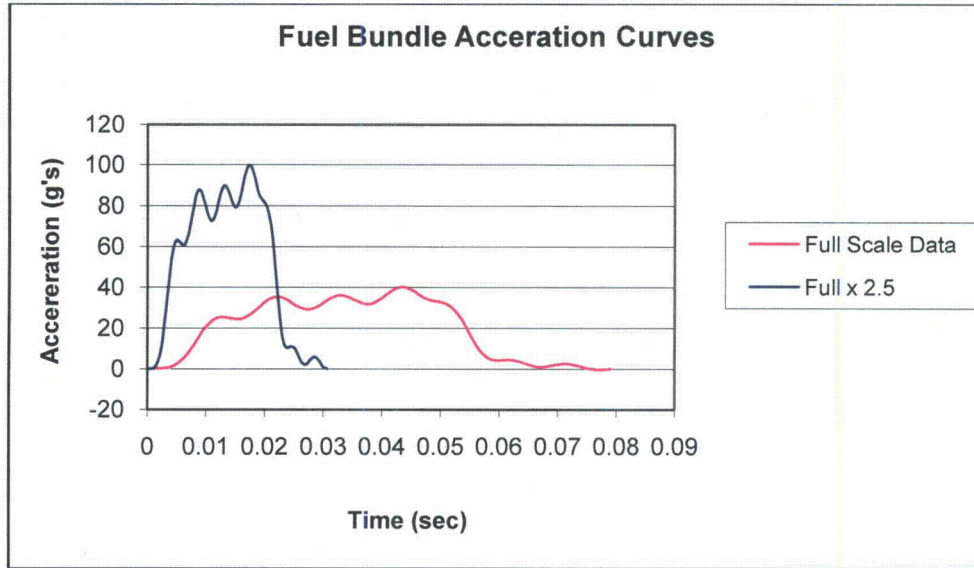


Figure III-63. Acceleration curves applied to fuel assembly beam model

The fuel rod material is modeled as unirradiated Zircaloy-4, using a power law hardening constitutive model fit to test data from the literature, Pierron et al. [5] The calculated material parameters are shown in Table III-5. These material properties are used for the fuel pins, the ties rods, and the support grid. In this analysis, the fuel pins and tie rods are modeled as solid beams with a circular cross-section.

Table III-5. Zircaloy-4 material parameters

Elastic Modulus	13.0 E3 ksi
Yield Stress	65 ksi
Luder Strain	0.00
Hardening Constant	103.5 ksi
Hardening Exponent	0.845

Fuel Assembly Model Results

For the lower acceleration curve given in Figure III-63, which represents a rail cask, there is no plastic deformation in the fuel rods or the spacer grids. The entire model remains elastic. For the analysis with the higher acceleration curve, there is no plastic deformation in the fuel rods and some plastic deformation in the spacer grids. Figure III-64 shows the most highly strained spacer grid. The lower three sections of the spacer grid buckle and a maximum plastic strain of 28% is calculated.

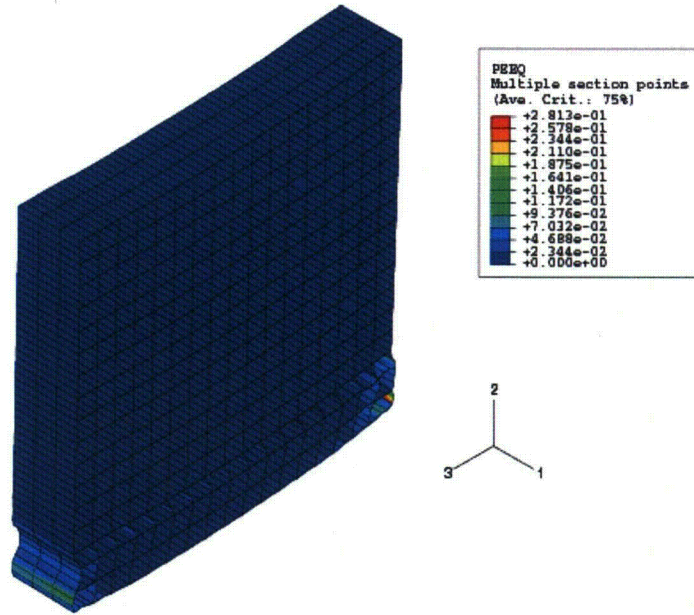


Figure III-64 Spacer grid 100g analysis plastic strain

The contact forces from the beam fuel assembly model will be used as input to a single rod continuum model. Since these forces occur over very short durations during the analysis, it was necessary to obtain data points at each time step in the fuel assembly model. Therefore, contact forces at a total of 20,349 time steps were obtained from the fuel assembly analysis.

Beam Element Versus Solid Element Contact

In processing the contact forces from the beam fuel assembly model, it was observed that the forces calculated during beam-to-beam contact were very large and acted over very short durations. They were much larger than the forces calculated in the model for the beam-to-shell contact. To investigate this difference in the magnitude and duration of the contact forces, two additional models were developed. The first, shown in Figure III-65, is a model of two impacting rods modeled with hexahedron elements. The second, shown in Figure III-66, is a model of two impacting rods modeled using beam elements. Since the beam elements in the beam fuel assembly model remain elastic, these models were evaluated for impact using elastic material properties.

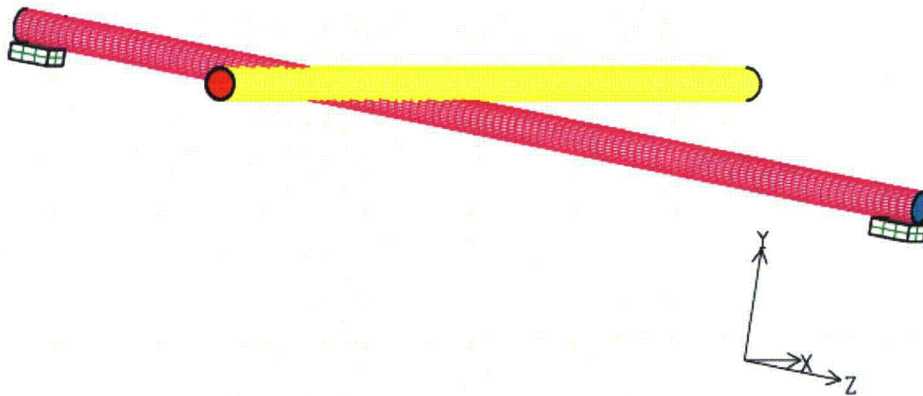


Figure III-65. Hexahedron test model for solid rod-to-rod contact in Abaqus/Explicit

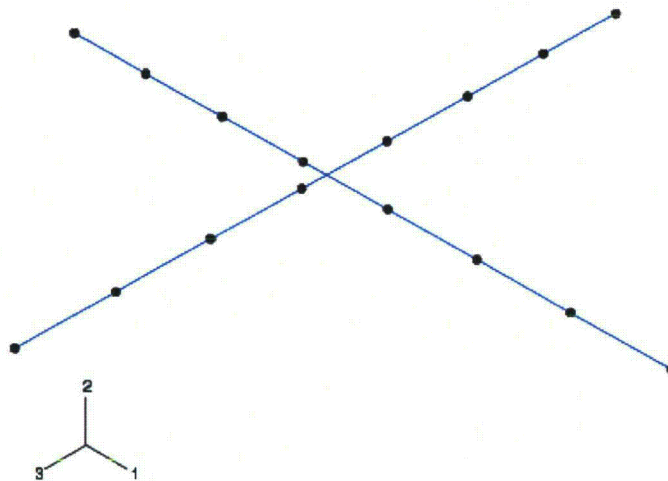


Figure III-66. Test model for beam-to-beam contact in Abaqus/Explicit

The results from the two finite element rod models are shown in Figure III-67 and Figure III-68. For the same mass, impact velocity and cross-sectional geometry, the two models generate two different sets of contact forces. As shown in Figure III-67, the beam element impact forces are much larger and shorter in duration than those generated from the hex rod model. The magnitudes of the forces differ by about a factor of five. An additional check was made comparing the hexahedron Abaqus/Explicit model to a similar model run in the Sandia code PRONTO3D. Both codes generated similar contact and reaction forces. Therefore, it is presumed that the beam element contact algorithm in Abaqus/Explicit is in error. Abaqus personnel were contacted and they are investigating the problem, but no resolution has been reached. Continued evaluation of the two models generated the curves shown in Figure III-68. For the velocity range of interest there is a good linear fit for each curve. Therefore, in transferring the loads between the beam

fuel assembly model and the continuum beam model the magnitude of the forces were scaled in accordance with the curves in Figure III-68. The length of each beam element impulse was increased to keep the integral of the curve the same. That is, the total impulse was maintained to conserve the change in momentum.

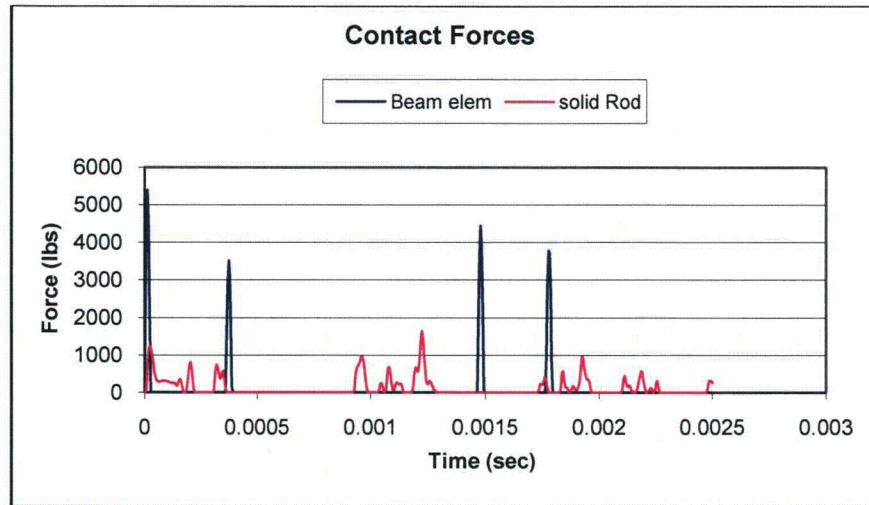


Figure III-67. Comparison of contact forces between solid rod and beam element rod

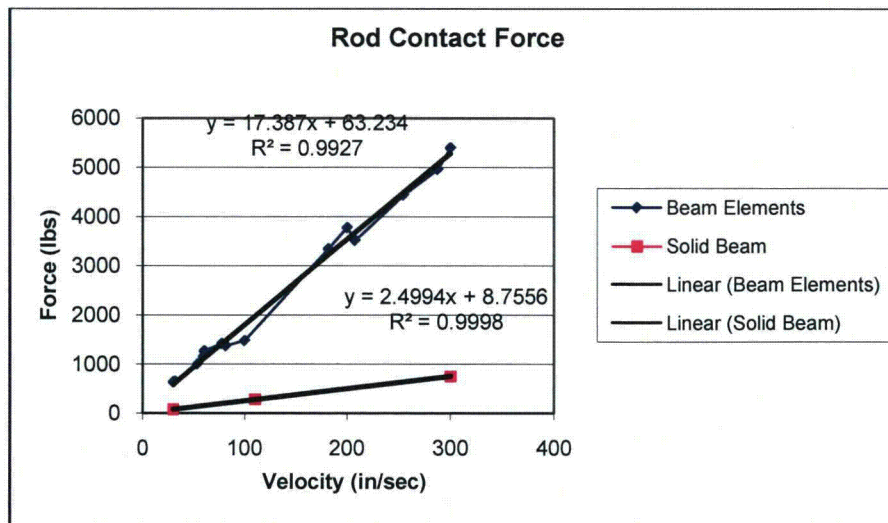


Figure III-68. Comparison of contact forces as a function of impact velocity

Continuum Rod Model

A continuum model was constructed using shell and hexahedral elements. The mesh is shown in Figure III-69, with a blowup of the end region showing the mesh density. The magenta colored regions represent the locations of the spacer grids. There is a plane of symmetry along the longitudinal axis of the beam. The symmetric model contains 162,000 elements, with 139,000 hexahedron elements used to model the UO_2 core and 23,000 shell elements used to model the Zircaloy-4 cladding. The hexahedron core has 16 elements across the diameter and there are 16 shell elements around the semicircular arc of the cladding.

The contact forces obtained from the beam fuel assembly model for the 100g loading are applied to a set of shell nodes running along the top and bottom of the symmetry plane. There are 1,446 nodes along each surface. Positive contact forces are applied to the bottom set of nodes and negative forces are applied to the upper nodes. As noted in the previous section the forces from the beam fuel assembly model that result from beam-to-beam contact are scaled according the curves in Figure III-68 and the duration of the load is then increased to conserve the change in momentum. In the region of the spacer grid where there is beam-to-shell contact, the loads are not scaled. The new load curves are then interpolated from the element nodes in the beam fuel assembly model to a larger number of element nodes in the continuum model. The rod model is given the same initial velocity as the beam fuel assembly model, 528 in/sec.

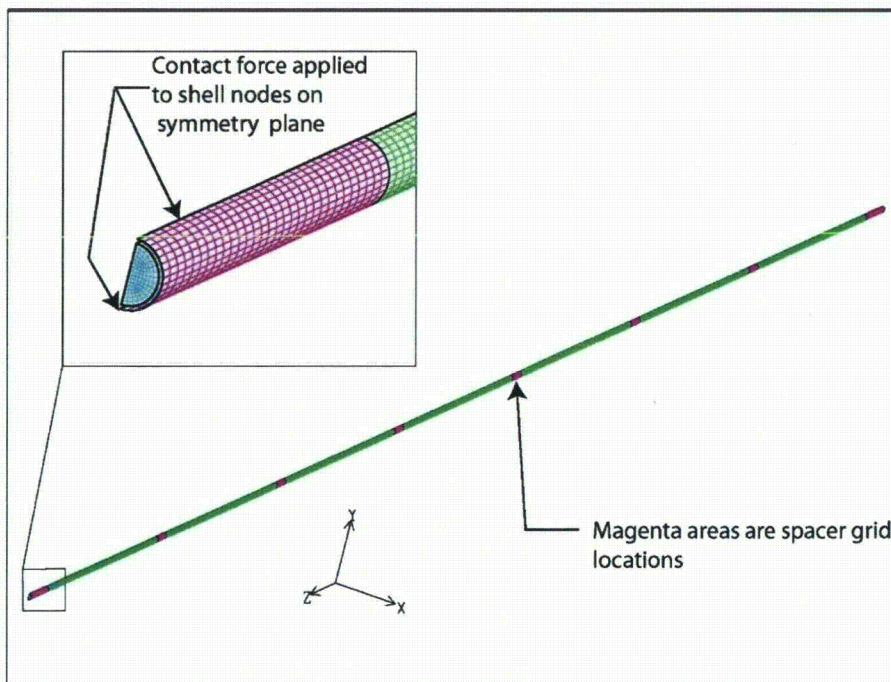


Figure III-69. Continuum rod finite element model

The rod materials are also modeled using a power-law hardening model. The parameters are presented in Table III-6. The model was run for two different load cases as shown in Table III-7. In the first case, the outside diameter of the UO₂ core and the inside diameter of the cladding are the same, the Zircaloy-4 material is modeled as unirradiated fuel and the UO₂ is also assumed to be pristine. In the second load case, the cladding material is assumed unirradiated, while the modulus of the UO₂ is decreased by an order of magnitude to simulate a softer, crumbled material, which has been irradiated. The results from both of these analyses are presented in the following section.

Table III-6. Standard Material Properties

	Zircaloy	Uranium Oxide
Elastic Modulus	13.0 E3 ksi	28.0 E3 ksi
Yield Stress	65 ksi	21.6 ksi
Luder Strain	0.00	0.00
Hardening Constant	103.5 ksi	103.5 ksi
Hardening Exponent	0.845	0.845

Table III-7. Load case parameter changes

Load Case parameters			
Case	Cladding Yield Strength (psi)	UO ₂ Modulus (psi)	Cladding Gap (inches)
Case 1	65,250	28 x 10 ⁶	None
Case 2	65,250	28 x 10 ⁵	None

Continuum Rod Results

Analysis Case 1

The first analysis case models unirradiated Zircaloy-4 material with no gap between the UO₂ rod and the cladding. The resulting kinetic energy plot for this analysis case is presented in Figure III-70. Almost all of the kinetic energy is lost from the rod; this indicates that the load impulse applied in the continuum model matches the impulse generated in the beam fuel assembly model. There is a large decrease in the kinetic energy at approximate 5.2 msec. This

corresponds to the large loads applied to the rod due to beam-beam contact forces at locations between the spacer grids. These impacts are illustrated in Figure III-71, which show the maximum equivalent plastic strain (EQPS) in the rod cladding as a function of time for three inter-grid locations. A maximum plastic strain of 1.5% is observed between spacer grid locations G and H. A detailed contour plot of this region is presented in Figure III-72.

The plastic strain in the rods at several spacer grid locations is presented in Figure III-73. These strains are approximately an order of magnitude smaller than inter-grid strains. This indicates that the spacer grids contact is much softer than beam-to-beam contact.

Figure III-74 shows the distribution of plastic strains along the length of the rod. The peak equivalent plastic strains are at the inter-rod locations between spacer grids G and H and between grids D and E. Strain at most of spacer grid locations along the rod remain elastic. The maximum plastic strain in the rod at a spacer grid is 0.06% at spacer grid C.

A close examination of the strain distribution in Figure III-74 shows that they are not symmetric about the center of the beam, although the initial beam fuel assembly finite element model and its loading were symmetric. This artifact is a result of the beam contact algorithm in Abaqus. As shown in Figure III-67, the impulses calculated for beam-to-beam contact are only a few microseconds long or roughly equal to three analysis time increments. Since the resolution of the impulse and the analysis time step are of the same order of magnitude, any accumulative numerical error on the position of the beam element nodes may result in a change in the time of contact and therefore the magnitude of the contact force and the subsequent position and velocity of the nodes. This results in a slight asymmetry in the calculated beam forces in the beam fuel assembly model. These forces are subsequently applied to the continuum model and result is the asymmetry of the strain fields shown in Figure III-74.

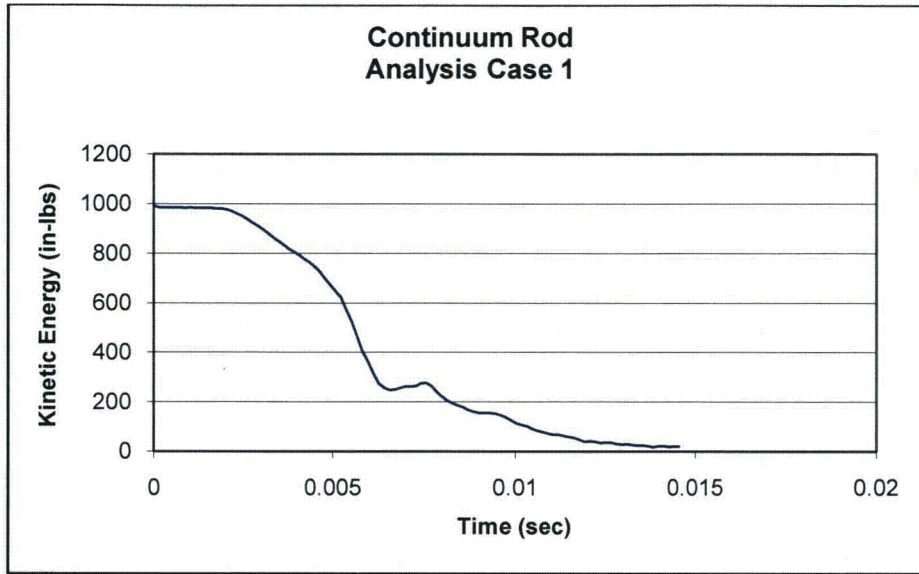


Figure III-70. Kinetic energy for Analysis Case 1

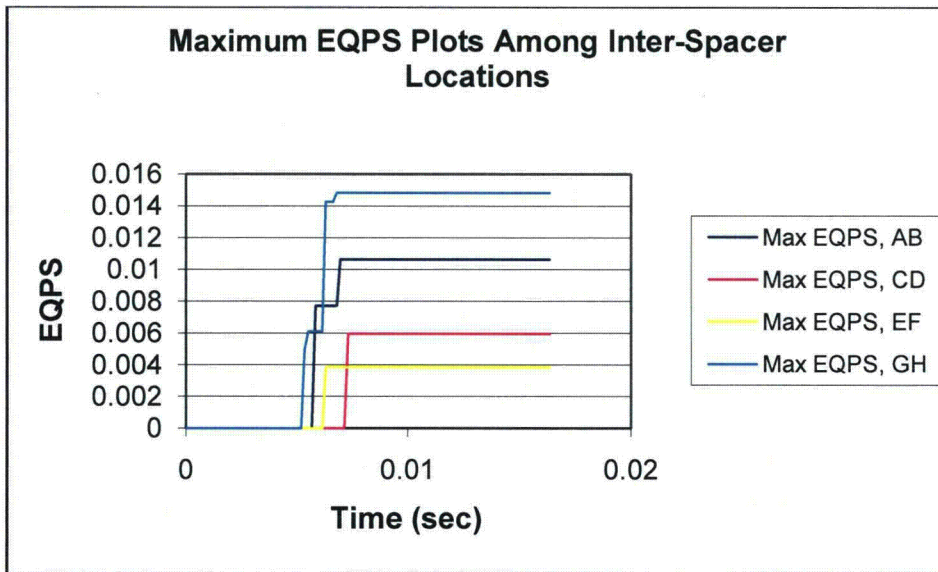


Figure III-71. Maximum equivalent plastic strain versus time for four inter-spacer grid locations. The spacer grids are specified by the letters in the legend (cf. Figure III-74)

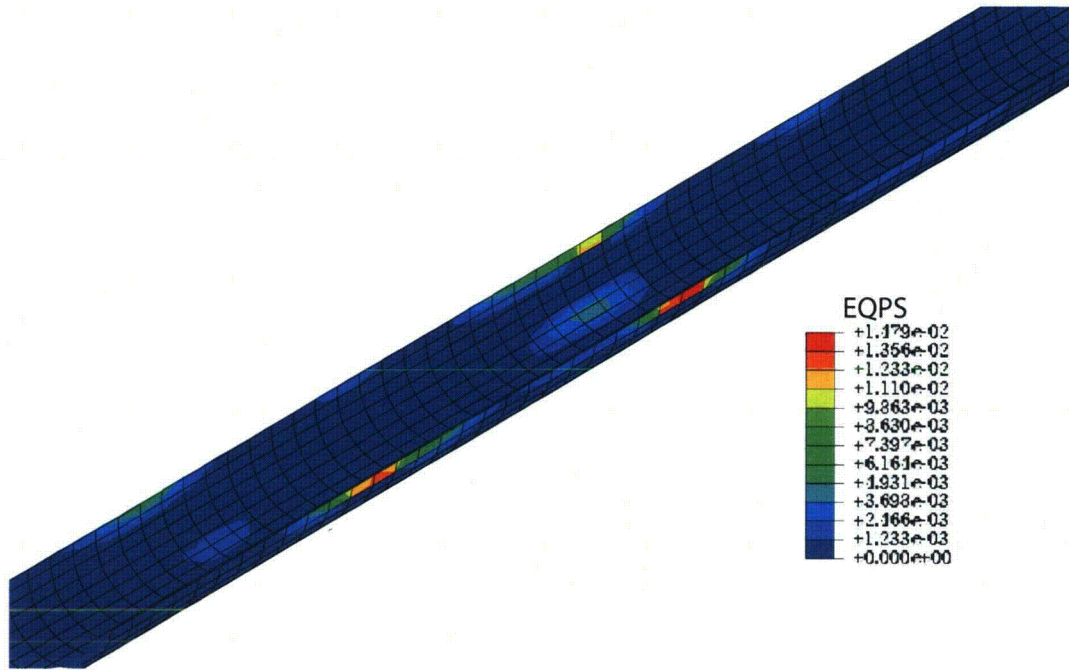


Figure III-72. Maximum equivalent plastic strain field in cladding for Analysis Case 1

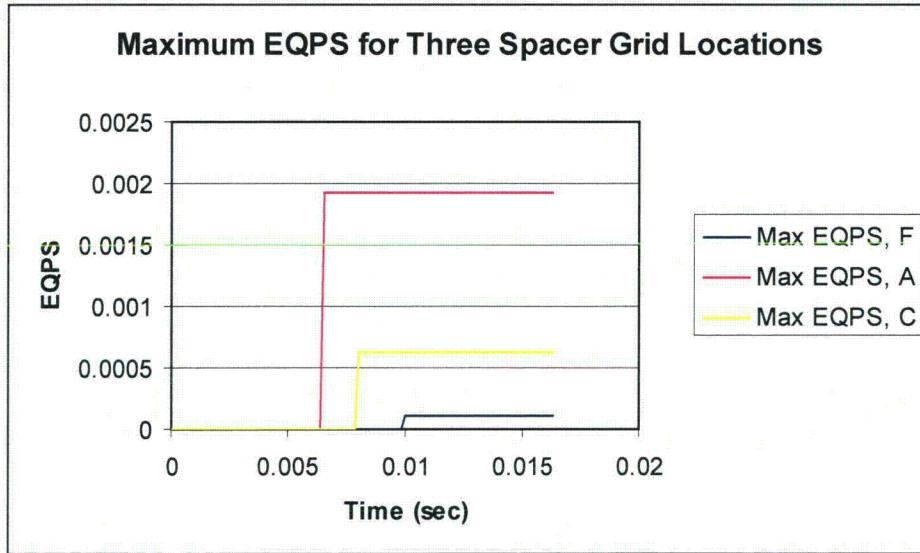


Figure III-73. Maximum equivalent plastic strain versus time for three spacer grid locations The spacer grids are specified by the letters in the legend (cf. Figure III-74).

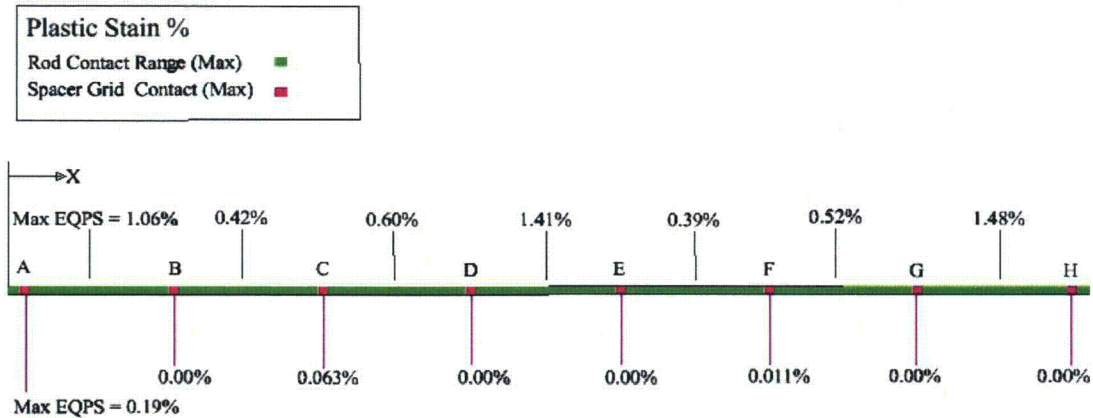


Figure III-74. Schematic showing maximum equivalent plastic strain for spacer grid and inter-spacer-grid locations

Analysis Case 2

For the second analysis case, the Zircaloy material properties remain the same, but the modulus of the UO_2 is decreased by an order of magnitude to provide a probable overestimation of the softness in the post-reactor UO_2 . This softness is engendered by the large cracks that develop in the fuel pellets during its in-core lifetime. The largest plastic strains for this configuration are about one-third higher than those in the previous case of an unirradiated (pristine) UO_2 core. The maximum EQPS is reached between spacer grids A and B and has a value of 1.98%. A contour plot of this region is presented in Figure III-75, which shows an axial region about 2 inches long with strain between 1% and 2%. The maximum EQPS at four inter-spacer locations as a function of time is shown in Figure III-76 and the maximum EQPS for four spacer grid locations is shown in Figure III-77. These curve are similar in shape to those in Analysis Case 1 where large strains occur at 5.2 msec. For this configuration there are plastic strains in the rod at all but one of the spacer grid locations and the maximum value of plastic strain for a spacer grid location is 0.67% at spacer grid C. A distribution of plastic strain over the entire rod is presented in Figure III-78.

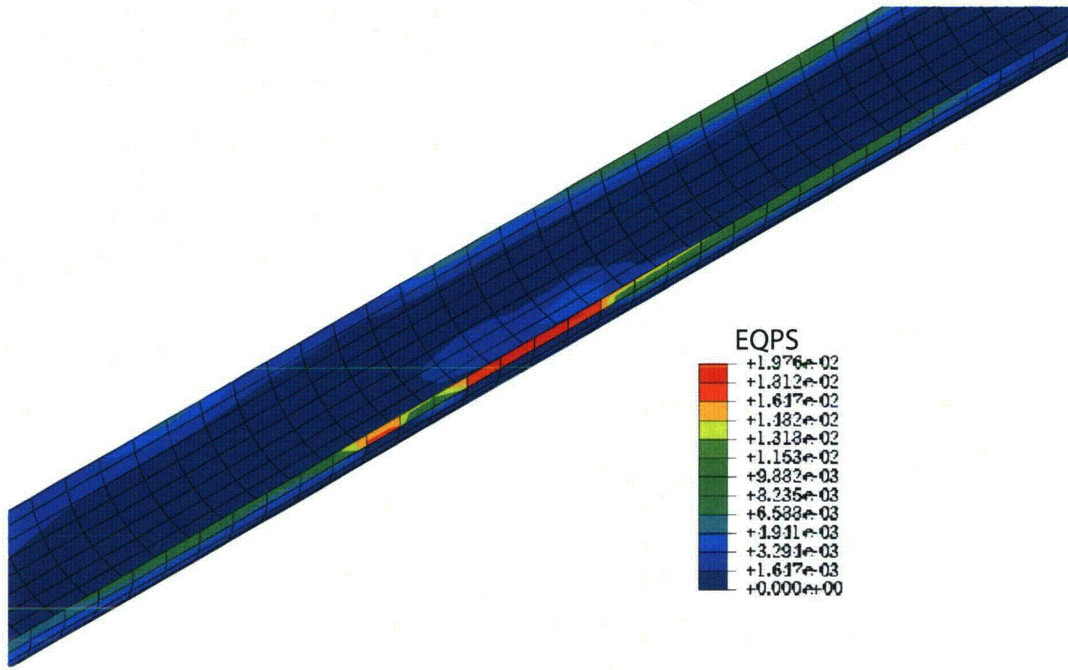


Figure III-75. Maximum equivalent plastic strain field in cladding for Analysis Case 2

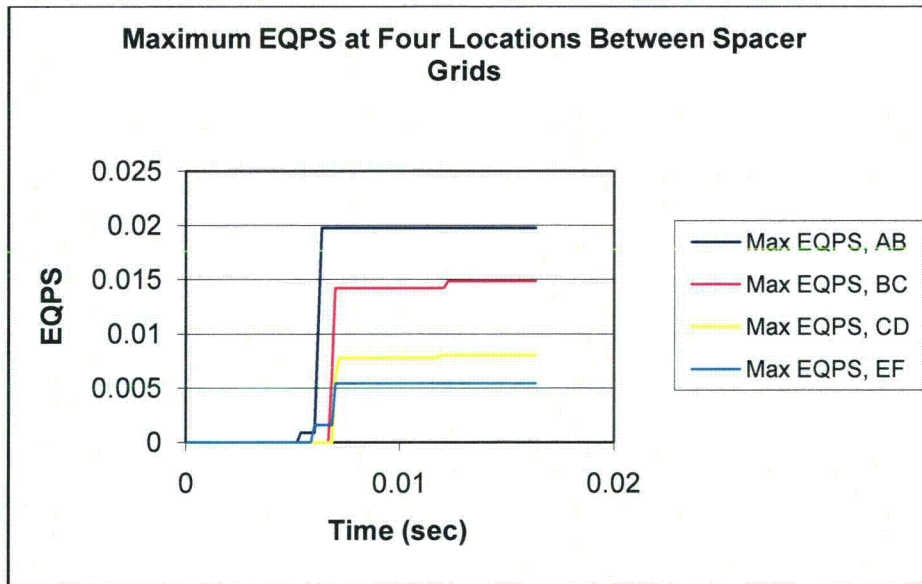


Figure III-76. Maximum equivalent plastic strain versus time for four inter-spacer grid locations. The spacer grids are specified by the letters in the legend (cf. Figure III-78)

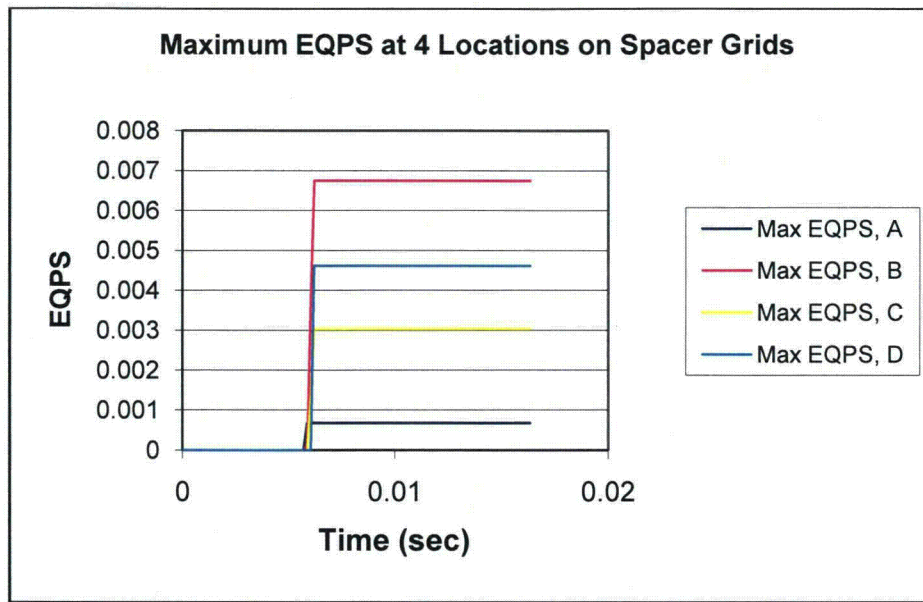


Figure III-77. Maximum equivalent plastic strain versus time for four spacer grid locations
The spacer grids are specified by the letters in the legend (cf. Figure III-78)

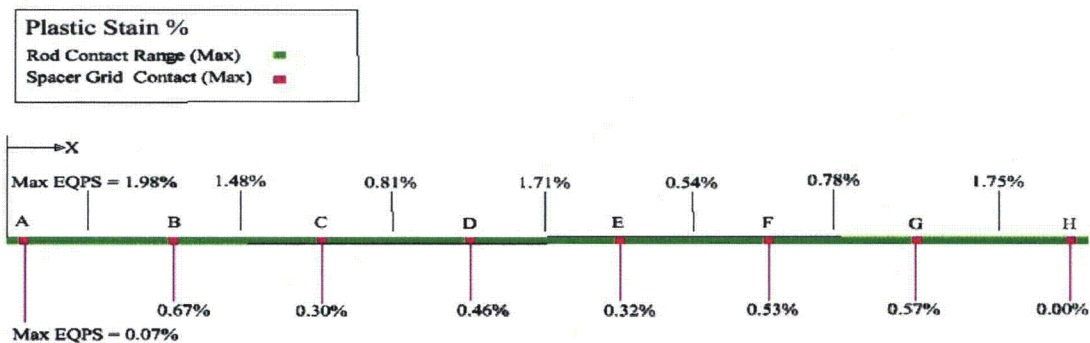


Figure III-78. Schematic showing maximum equivalent plastic strain for spacer grid and inter-spacer-grid locations, Analysis Case 2

III.4.3 Discussion and Conclusions

In this study explicit dynamic finite element analyses of a pressurized water reactor fuel assembly were conducted using two separate finite element models. The first model consisted of structural beam and shell elements and was used to determine the overall response of the complete fuel assembly to a regulatory side impact. Loading data from this analysis was applied to a continuum model of a single fuel pin to determine the localized stress and strain fields. It

was observed that during impact the largest loads on the rods were generated from beam-to-beam contact.

Due to the lack of experimental data and the variability in properties of stored spent fuel rods, a series of analyses were conducted with variations in the stiffness of the UO₂ core material and the gap size between the fuel pellet and the cladding material. A summary of the parameters used in each analysis and the maximum plastic strain calculated in the cladding wall is presented in Table 5. From Table 5 it can be concluded that an order of magnitude change in the stiffness of the pellet material results in a 30% increase in the maximum plastic strain in the rod, while the existence of a 0.010 inch gap results in an increase in the plastic strain by about a factor of nine. Clearly the existence of any gap between the pellet and the cladding would have a significant effect on the response of the rod. However, the materials in this study were modeled as isotropic and homogeneous using an elastic plastic power-law hardening model. It is not clear that this approximation accurately models the response of the UO₂ pellets. It is more likely that the initial response would not be a steep linear response as modeled, but would be nonlinear, with a soft initial reaction that would increase in stiffness as the pellet is squeezed. This type of behavior in the pellet may result in cladding strain values closer to those calculated using an initial gap even if one is not actually present. Since these values quickly approach a level that would fail the rod, a more accurate material characterization of irradiated fuel rods is required and this must entail experimental studies. Any attempt to estimate the nonlinear response of the pellet at this point would be pure conjecture.

Table III-8. Analysis Case Summary

Case	Cladding Yield Strength (psi)	UO ₂ Modulus (psi)	Cladding Gap (inches)	Max EQPS (%)
Case 1	65,250	28 x 10 ⁶	None	1.5
Case 2	65,250	28 x 10 ⁵	None	1.96

APPENDIX IV
DETAILS OF CASK RESPONSE TO FIRE ACCIDENTS

Table of Contents

IV.1 Introduction.....	6
IV.2 CAFE Finite Volume Domain and Boundary Conditions	7
IV.3 The Rail-Steel Cask	9
IV.3.1 Geometric Consideration	9
IV.3.2 Rail-Steel Thermal Behavior and Model Assumptions.....	17
IV.3.3 Rail-Steel Materials and Thermal Properties	19
IV.3.4 Rail-Steel P-Thermal Finite Element Model and Boundary Conditions.....	27
IV.3.5 Rail-Steel Thermal Analysis Results.....	30
IV.4 Rail-Pb	30
IV.4.1 Geometry Considerations.....	41
IV.4.2 Rail-Pb Thermal Behavior and Model Assumptions	44
IV.4.3 Rail-Pb Materials and Thermal Properties	47
IV.4.4 Rail-Pb P-Thermal Finite Element Model	51
IV.4.5 Rail-Pb Thermal Analysis Results	51
IV.5 CAFE Benchmark	63

List of Figures

Figure IV-1. CAFE three-dimensional domain: (a) CAFE regulatory fire, (b) cask on ground and at the center of the pool, (c) cask on the ground and 3m (10ft) from the edge of the pool, (d) cask on the ground and 18.3m (60ft) from the edge of the pool.....	9
Figure IV-2. Rail-Steel cask: (a) assembly of MPC and overpack, and (b) cask with limiters....	10
Figure IV-3. Rail-Steel overpack: (a) cross-sectional view through the center of the cask, (b) cross-sectional view through the mid-plane of the overpack.....	11
Figure IV-4. Rail-Steel MPC: (a) cross-sectional view through the axis of the cask, (b) cross-sectional through the midplane of the overpack.	12
Figure IV-5. Fuel assembly (a) and fuel rod (b).	14
Figure IV-6. Fuel-basket region (left) and equivalent fuel-basket region (right).	15
Figure IV-7. Rail-Steel upper (a) and lower (b) impact limiters.	16
Figure IV-8. Rail-Steel finite element mesh.	29
Figure IV-9. Rail-Steel Regulatory Uniform Heating Results (P-Thermal).....	31
Figure IV-10. Rail-Steel CAFE regulatory fire.	33
Figure IV-11. Rail-Steel CAFE fire with cask on ground and at the pool center.....	35
Figure IV-12. Rail-Steel CAFE fire with cask on ground 3.0m (10ft) from the edge of the pool.	37
Figure IV-13. Rail-Steel CAFE fire with cask on ground 18.3m (60ft) from the edge of the pool.	39
Figure IV-14. Rail-Pb components with the direct loaded fuel basket shown to the right.....	42
Figure IV-15. Cross-section view of the Rail-Pb with the directly loaded fuel basket.	42
Figure IV-16. Axial burn up profile for the directly loaded fuel basket.....	45
Figure IV-17. Three-dimension, quarter section of the directly loaded basket. The helium material is not shown.	46
Figure IV-18. The Rail-Pb mesh.....	52
Figure IV-19. Rail-Pb Regulatory Uniform Heating Results	53
Figure IV-20. Rail-Pb CAFE Regulatory Fire.....	55
Figure IV-21. Rail-Pb cask on ground at the pool center.	57
Figure IV-22. Rail-Pb cask on ground 3.0m (10ft) from the edge of the pool.	59
Figure IV-23. Rail-Pb cask on ground 18.3m (60ft) from the edge of the pool.	61
Figure IV-24. Large calorimeter fire test: (a) test setup and (b) fire fully engulfing the calorimeter.	64
Figure IV-25. Side view (looking from the north) of calorimeter and test setup. Note: the calorimeter is centered with the pool. This drawing is not to scale.	64
Figure IV-26. CAFE benchmark results using fully engulfed large calorimeter: (a) temperatures average along the 0, 90, 180, and 270 degree side looking at the calorimeter from the negative z-direction, and (b) temperatures averaged over each ring starting from Ring 1 located on the positive side of the z-axis.....	65

Figure IV-27. CAFE benchmark results using a small calorimeter 1.5m (4.9ft) from the edge of the fire. 66

List of Tables

Table IV-1. Axial burn up profile in the active fuel region.....	17
Table IV-2. Thermal conductivities for the Rail-Steel materials.....	21
Table IV-3. Specific heat for the Rail-Steel materials.....	21
Table IV-4. Densities for the Rail-Steel materials.....	22
Table IV-5. Emissivity for some of the Rail-Steel materials and paints.	22
Table IV-6. Effective thermal conductivity for the fuel-basket region.	24
Table IV-7. Effective thermal conductivity of the aluminum heat conduction elements.	25
Table IV-8. Effective thermal conductivity of the intermediate shells in the in-plane directions.	26
Table IV-9. Effective conductivity of the neutron shield region.	27
Table IV-10. Thermal conductivities for the Rail-Pb materials.	48
Table IV-11. Specific heat for the Rail-Pb materials.....	48
Table IV-12. Densities for the Rail-Pb materials.....	48
Table IV-13. Emissivity for some of the Rail-Pb materials.....	48
Table IV-14. Effective thermal properties of the directly loaded fuel basket.	51
Table IV-15. Effective thermal conductivities for the neutron shield region of the Rail-Pb.....	52

APPENDIX IV

DETAILS OF CASK RESPONSE TO FIRE ACCIDENTS

IV.1 Introduction

A thermal analysis of Rail-Steel and Rail-Pb cask types is performed to obtain the thermal response of these casks. The approach used to model the Rail-Steel and the Rail-Pb is similar to the ones used in the HI-STAR 100 and NAC-STC Safety Analysis Reports (SARs) (Holtec International, 2004, Nuclear Acceptance Corporation International, 2004), a combination of thermal resistor network analysis and finite element modeling. The thermal resistor network method is used to obtain effective thermal properties for several regions of the casks. These homogenized regions are then added to the finite element model with equivalent effective properties. This process eliminated some of the geometric redundancies and/or discretization complexities inherent in the models, while at the same time keeping the essential thermal response of the casks.

For the Rail-Steel, assumptions and results reported in the Rail-Steel SAR (Holtec International, 2004) are used, but modified where necessary to reflect the current study. The approach used to model the Rail-Pb is similar to the approach used in the Rail-Pb SAR (Nuclear Acceptance Corporation International, 2004). The only exception is in how the contents of the cask are modeled. In the Rail-Pb SAR, the fuel-basket region and the rest of the overpack are modeled explicitly using a three-dimensional, quarter-section of the cask to obtain a steady-state solution. The maximum temperature difference between the center of the fuel-basket region and the inner wall of the overpack obtained in the steady-state solution is then used to calculate the fuel-basket cladding temperature for the regulatory uniform heating flux (see 10CFR71.73), which did not include a fuel-basket region. Here, a quarter section of the fuel basket is used to obtain effective thermal properties for the basket. The fuel-basket region is replaced in the full-scale, finite element model using effective properties for the homogenized basket region. As in the Rail-Steel analysis, assumptions and results in the Rail-Pb SAR are used to obtain the thermal response of this cask; again, with minor changes to reflect the current study. Values taken from the Rail-Steel and the Rail-Pb SARs are checked where possible—using formulas taken directly from these reports or derived from independent analysis—to assess the validity of assumptions and to verify results; no significant errors are found.

In general, boundary conditions and material properties are slightly different from those used in the Rail-Steel and Rail-Pb SARs. The intent of this thermal analysis is to determine the temperature of critical components during and after a hypothetical fire accident using material properties and boundary conditions that closely resemble the conditions in a real fire accident. Since realistic boundary conditions are sometimes difficult to implement using available data and/or current analysis tools, some simplifications had to be made. For example, NS-4-FR, the

insulation material used in the both cask neutron shields, is assumed to decompose completely when its operational temperature limit is reached. In such cases, conservative assumptions are made to maximize heat input to the casks, as is done in both SARs cited above. In the case of material properties, those presented in the SARs are preferred, followed by those in standard thermal textbooks and journals. For some materials, like NS-4-FR, properties are available but only over a limited temperature range. In such cases, the value available at the highest temperature is used throughout the rest of the temperature range.

As mentioned in Chapter 4, MSC PATRAN-Thermal (P-Thermal) (MSC, 2008) is the finite element heat transfer code used to solve the internal thermal response of the Rail-Steel and Rail-Pb in the regulatory uniform heating scenario. This scenario effectively simulates fire conditions using a spatially uniform radiation flux over the external surfaces of the casks as established in 10 CFR 71.73. CAFE (Container Analysis Fire Environment) is the computational fluid dynamics (CFD) code used to generate the fire environment for the CAFE regulatory and CAFE non-regulatory scenarios described in Chapter 4. For these scenarios, CAFE and P-Thermal are coupled together to obtain the thermal response of the Rail-Steel and Rail-Pb casks. CAFE generates more realistic fire conditions on the external surfaces of the casks, as opposed to spatially uniform heating conditions. P-Thermal uses CAFE-predicted, external conditions to calculate the internal thermal response of the casks.

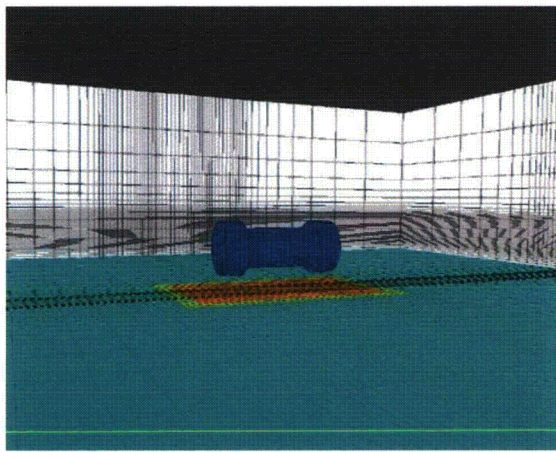
In the following sections, the geometry, material properties, and boundary conditions used to model the Rail-Steel and the Rail-Pb are described, and results that supplement discussions in Chapter 4 are shown. The three-dimensional domain and the boundary conditions used in the CAFE runs are described first, followed by the geometry and boundary conditions used in the Rail-Steel and Rail-Pb P-thermal finite element models. Finally, results from two CAFE benchmark runs are presented.

IV.2 CAFE Finite Volume Domain and Boundary Conditions

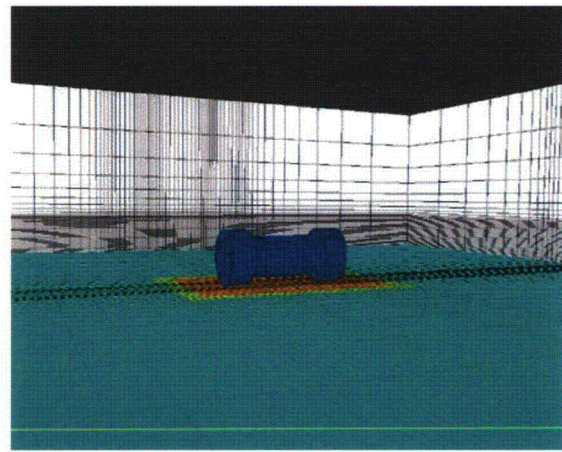
CAFE (Suo-Antilla et al., 2005) uses the finite volume approach with orthogonal Cartesian discretization to solve: (1) the three momentum equations for predicting the velocity and momentum field, (2) the mass continuity equation, (3) the energy equation for predicting the temperature field, (4) the equation of state, (5) a number of scalar transport equations for tracking the flow of species, and (2) two transport equation to solve thermal radiation within and outside the fire. CAFE uses a variable density PISO algorithm to obtain a velocity field which satisfies both the momentum and continuity equations. CAFE has a number of turbulence models, but for this study a large eddy simulation formulation is used. Thermal radiation transport within and near the fires is split into two types: diffusive radiation inside the flame zone and clear air radiation outside the flame zone. Diffusive thermal radiation transport is modeled with the Rosseland approximation. Clear air radiation outside the flame zone is modeled using view factor methods.

CAFE is coupled to P-Thermal through a set of user subroutines that are responsible for passing temperature and thermal heat flux data between both codes. CAFE uses a specialized scheme to map the temperature and heat fluxes to the exterior surfaces of the finite element model (Suo-Antilla et al., 2005). MSC PATRAN is the front end code employed to generate the material database, the finite element discretization, and the boundary conditions used by P-Thermal. It is through a special boundary condition, setup in PATRAN, that CAFE and P-Thermal are able to exchange data.

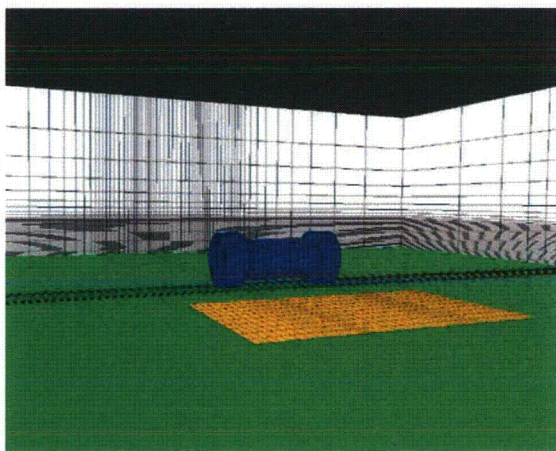
Figure IV-1 illustrates the domain configurations used in the CAFE fire scenarios discussed in Chapter 4. Figure IV-1a shows the computational fluid dynamics domain used for the CAFE regulatory run, and Figures IV-1b through IV-1d show the domain for the CAFE non-regulatory runs. As explained in Chapter 4, all non-regulatory CAFE runs were determined based on the severity and likelihood of the scenario. A square pool is used to assure the specifications from 10CFR71.73 are met in the case of regulatory fires. For consistency the pool remained a square in all other cases. The pool area is 9.25x13.80m (30.35x45.28ft) in the Rail-Steel configurations,



(a)



(b)



(c)



(d)

Figure IV-1. CAFE three-dimensional domain: (a) CAFE regulatory fire, (b) cask on ground and at the center of the pool, (c) cask on the ground and 3m (10ft) from the edge of the pool, (d) cask on the ground and 18.3m (60ft) from the edge of the pool.

and 9.14x12.42m (29.99x40.75ft) in the Rail-Pb configurations. These pool areas corresponded to a fully-loaded rail tank car burning over a period of 3 hours, the maximum burn time based on 113.6m³ (30,000 gallons) of fuel. The pool edges remained 3m (9.8ft) away from the casks in all runs.

An appropriate domain size is determined from del Valle et. al. (2007) and from del Valle (2009), both thermal analyses conducted with CAFE using a calorimeter the size of a rail cask. In these studies, results of CAFE runs are compared to experiments and showed good agreement. In the current study, the ground dimensions varied between cases since a larger domain is required for the cask offset cases, but are at least 25x15x25m (82x49x82ft), about the size of the domain used in del Valle et. al. (2007) and del Valle (2009). A mesh refinement study is conducted to assess the sensitivity of the cask external temperatures to mesh size and to determine an appropriate mesh size. Approximately 145000 finite volumes are used in this study for both casks. Slightly hotter temperatures are observed on the bottom of the cask when finer grids are used, but the differences are not sufficient to outweigh the extra computational expense. As observed in Figure IV-1, the mesh is finer in the region near the pool. All CAFE scenarios used calm wind conditions; the velocity at the boundaries and inside the domain are originally set to zero, but are allowed to float as the fire develops.

IV.3 The Rail-Steel Cask

The Rail-Steel cask is a packaging system designed for transportation of a variety of nuclear spent fuel assemblies and is intended to fit horizontally in a rail cask bed. Therefore, the Rail-Steel system is assumed to be in the horizontal position in all CAFE runs (see Figure IV-1), as it would be after derailment if the flatbed rail car overturns or if the cask is ejected from rail car. Only the thermally relevant components of the Rail-Steel are considered in this thermal analysis. As stated in the introduction, some results reported in the Rail-Steel SAR (Holtec International, 2004) are used in this analysis. Values taken from this report are checked where possible to assess validity of assumptions and to verify results.

IV.3.1 Geometric Consideration

The Rail-Steel cask consists of an overpack, a multipurpose canister (MPC), and two impact limiters; these components fit together as shown in Figure IV-2. The MPC stores the nuclear spent fuel material, and is sealed tight to prevent the contents from leaking into the overpack inner cavity. The MPC is the first containment barrier in the Rail-Steel cask. The overpack is designed to attenuate both the heat, and the neutron and gamma rays generated inside the MPC. The overpack is also sealed tight to prevent the contents from a breached canister from further leaking into the external environment; thus, the overpack forms the second containment barrier in the Rail-Steel. During transportation, the overpack ends are fitted with impact limiters that,

besides absorbing most of the impact energy during an impact, add an additional thermal insulation layer to the extreme ends of the overpack when intact.

IV.3.1.1 The Overpack

The Rail-Steel overpack is a multilayered cylindrical vessel approximately 2.11 m (83.3 in) in diameter and 5.16 m (203.1 in) in length. The inner cavity of the overpack is approximately 1.75 m (64.7 in) in diameter and 4.85 m (191.1 in) in length. The inner cavity is formed by (1) welding a thick wall cylinder, called the inner shell, to a metal base cup at the bottom and to a large diameter vacuum flange at the top, and (2) bolting a closure plate onto the flange as shown in Figure IV-3. Five thin wall cylinders, tightly fitted to one another and to the inner shell, form the next structural layer of the overpack, strengthening the overpack against puncture or penetration. These cylinders are jointly referred to as the intermediate shells and act as the gamma shield. Channels welded to the outermost intermediate shell extend radially outward and delimit the last layer of the overpack. These channels act as fins enhancing conduction to the periphery of the overpack. Plates welded between the ends of each successive channel complete the outer enclosure shell of the overpack. The cavities formed between the channel walls, and between the outermost intermediate shell and the outer enclosure plates are filled with a neutron shield material which provides thermal insulation in addition to neutron attenuation. The outermost intermediate shell, the neutron shield region, and the outer enclosure shell effectively extend the diameter of the overpack an additional 32.3 cm (12.7 in) beyond the perimeter of the flange and the metal base cup.

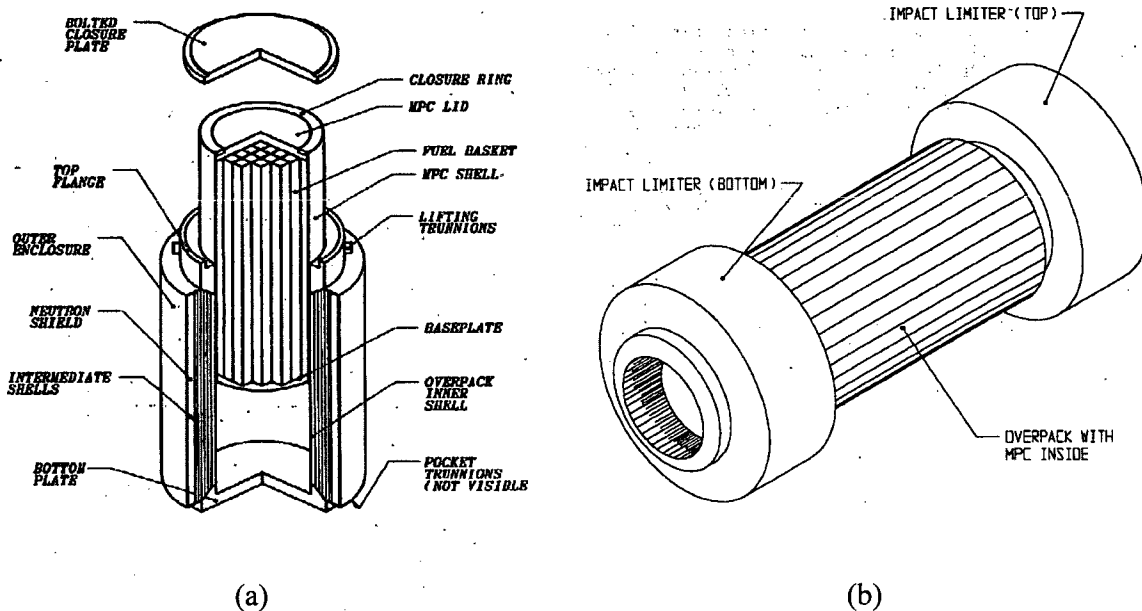


Figure IV-2. Rail-Steel cask: (a) assembly of MPC and overpack, and (b) cask with limiters.

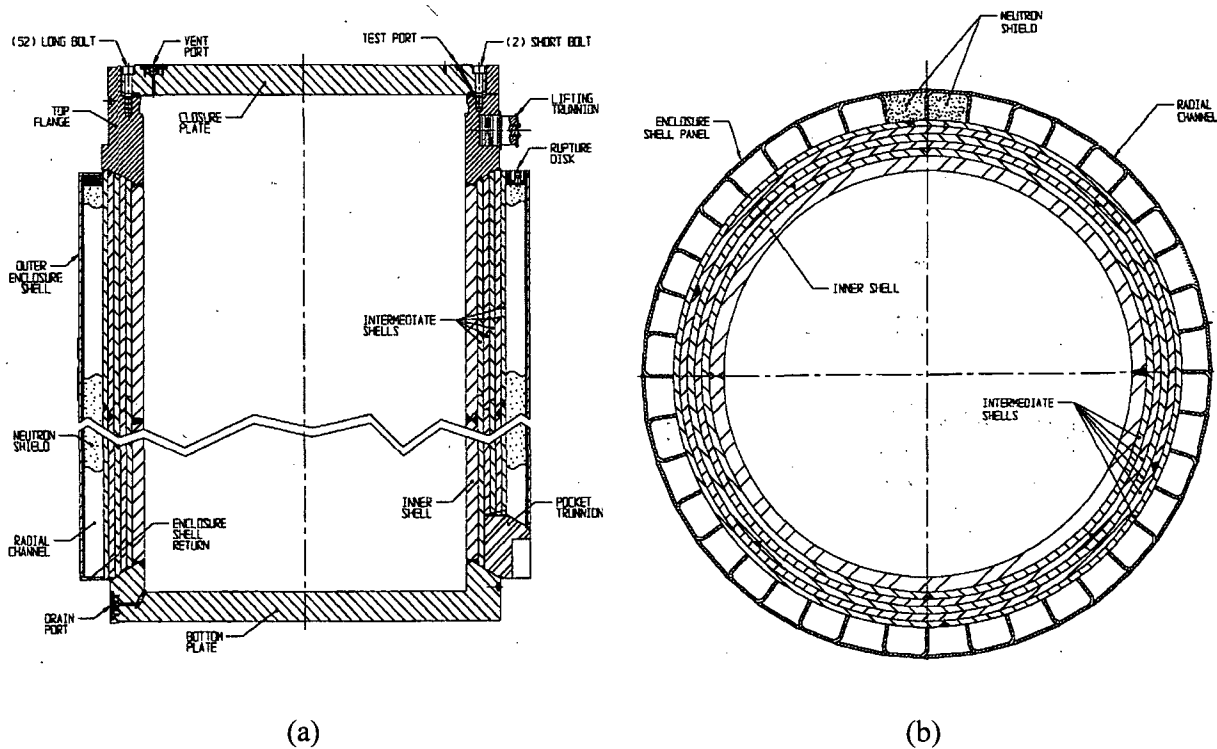


Figure IV-3. Rail-Steel overpack: (a) cross-sectional view through the center of the cask, (b) cross-sectional view through the mid-plane of the overpack.

The overpack shells, metal base cup, vacuum flange, closure plate, and neutron shield region are the major components of the overpack and together comprise most of its volume. The overpack shells, metal base cup, vacuum flange, and closure plate are represented explicitly in the thermal model with minor alterations to simplify the solid modeling and meshing process. The most significant change is extending the length of the overpack shells through the length of the neutron shell region. Note these length changes are expected to have a minor effect on the overall thermal response of the overpack, and only in the radial direction. The intermediate shells and the neutron shield region are each represented as a single volume also to minimize geometric complexity; however, their thermal properties are properly accounted for in the thermal model using the techniques described in Sections IV.3.3.3 and IV.3.3.4.

The overpack contains additional components used to service the overpack during normal operations or designed to function only during abnormal ambient conditions such as fires. These features include seals, gas ports, rupture disks, and lifting and pocket trunnions as observed in Figure IV-3. These components are not included in the model because their effects are assumed: (1) negligible due to their small volume and mass relative to the other components in the overpack, (2) highly localized with no effect to the overall thermal performance of the package at locations of interest, or (3) both.

IV.3.1.2 *Multipurpose Canister*

The MPC is a cylindrical vessel approximately 1.73m (68.3in) in diameter (outside) and 4.83m (190.3in) in length. The MPC is made from a cylindrical shell 1.2cm (0.5in) thick and 4.76m (187.4in) in length, a circular baseplate 6.35cm (2.5in) thick, and a circular plate lid 24.1cm (9.5in) thick (see Figure IV-4a). The baseplate is welded to the bottom of the MPC shell, and this shell is intern welded to the exterior surface of the lid. At the top, the MPC shell is flushed against a large groove on the end perimeter of the circular plate lid. An annular closure ring welded on the groove and to the top of the shell seals the contents of the MPC. In the horizontal position, the shell and the base plate rest on the inner shell of the overpack. Drain and vent ports on the MPC lid are used to evacuate and filled the MPC with a known gas. With the exception of the closure ring and drain ports, all these components are modeled explicitly. The closure ring is assumed to be part of the lid.

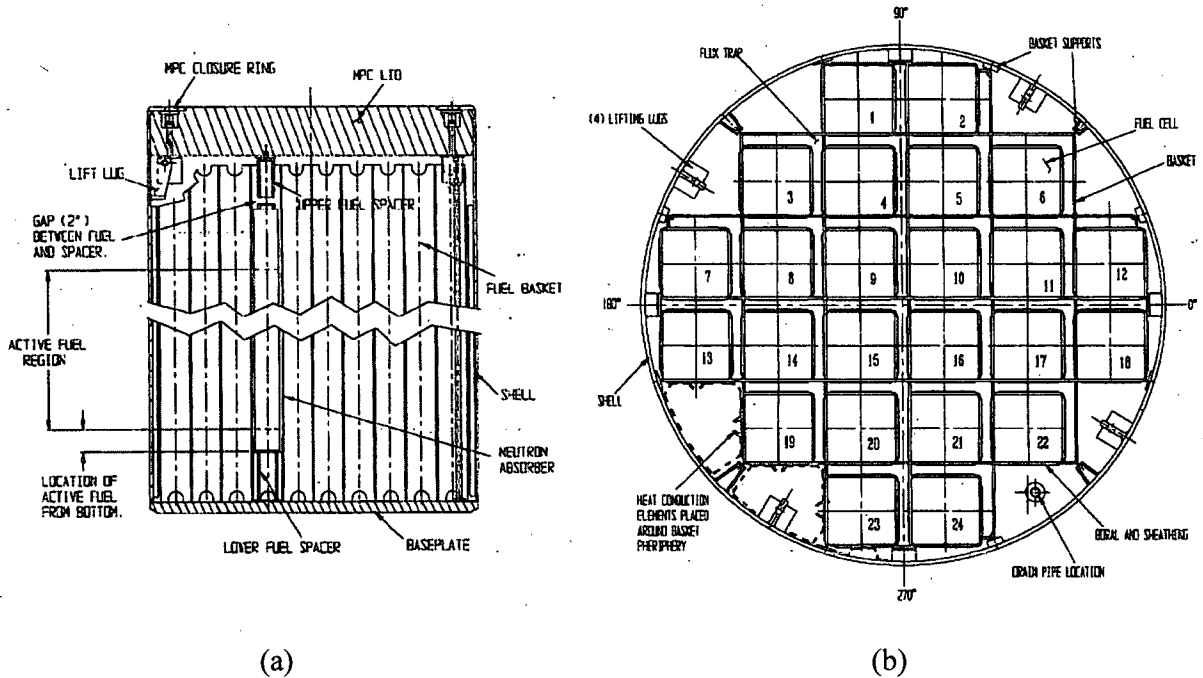


Figure IV-4. Rail-Steel MPC: (a) cross-sectional view through the axis of the cask, (b) cross-sectional through the midplane of the overpack.

The nuclear spent fuel material is stored in a fuel basket inside the MPC (see Figure IV-4b). The fuel basket is made by welding a series of perpendicular and parallel plates to form an array of storage cells. Each storage cell contains a single fuel assembly. The MPC is designed to carry two types of fuel baskets: (1) the MPC-24, which contains a maximum of 24 PWR fuel assemblies; and (2) the MPC-68, which contains a maximum of 68 BWR assemblies. Both fuel baskets are similar in design; however, the MPC-24 is designed to carry a greater heat load. For this reason, attention is focused on the MPC-24. In the MPC-24, the fuel cells are physically

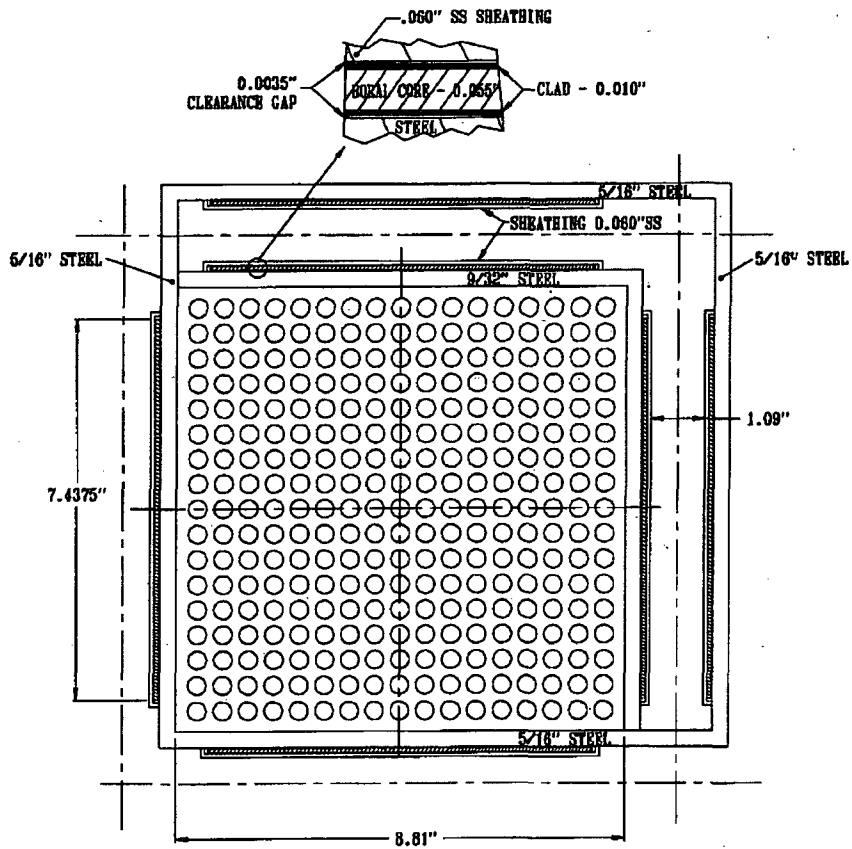
separated from one another by a gas pocket called the flux trap. The length of the fuel basket is approximately 4.48m (176.5in). The fuel assembly may not extend this length; in such cases, spacers are installed on the baseplate and on the MPC lid to hold the fuel assemblies in place (see Figure IV-4a).

A single fuel assembly consists of an array of fuel rods, each rod separated by a gas space as shown in Figure IV-5a. The total number of rods per assembly varies with fuel assembly design. Each fuel rod however consists of a number of cylindrical fuel pellets fitted into a thin walled pipe, called the fuel cladding. The fuel cladding, inner diameter is slightly larger than the diameter of the pellets as shown in Figure IV-5b. The fuel pellets are held tightly against each other using the force of a spring. The radial dimensions of the rod components vary between fuel rod designs. In general, the length of the fuel column is only a fraction of the total length of the fuel rod and marks the active fuel region. The total length of the fuel rod is approximately the same as the length of the fuel assembly. Additional supports are added to the ends of the fuel assembly and at regular intervals along the length of the assembly for structural integrity, to maintain spacing between the rods, and for handling purposes.

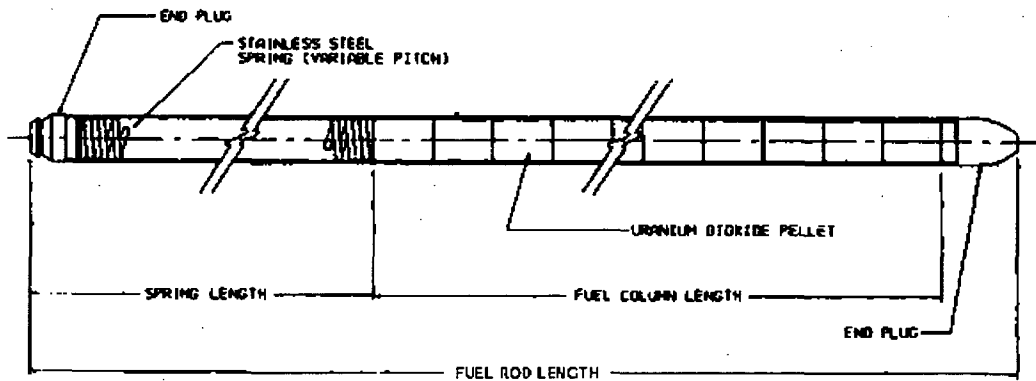
The Rail-Steel system is designed to carry a number of PWR fuel rods; it's impractical to analyze the Rail-Steel system with all these fuel rod designs. Similarly, it's impractical to model the MPC contents with all the components described above because: (1) the wide range of component length scales creates additional meshing complexities, and (2) alternative methods have been employed in the SAR literature and in this study to obtain equivalent thermal properties for the MPC internal contents with good results (see Section IV.4.4). Hence, the fuel-basket region, which includes the fuel assembly, basket walls, and flux trap gaps, is not represented explicitly in the Rail-Steel model.

The MPC shell contains support structures that help keep the fuel basket laterally in place and lift logs which are used during loading and unloading operations. Some slots between the periphery of the fuel basket and the MPC shell wall contain thin wall heat conduction elements. These conduction elements extend the full length of the basket and provide an effective heat conduction path between the MPC basket and MPC shell. With the exception of the heat conduction elements, all other structural elements in the fuel-basket periphery region are ignored for the same reason cited in Section IV.3.1.1. The fuel heat conduction elements are not represented explicitly, but their thermal effect is included through the use of a simplified analytical model explained in the Rail-Steel SAR.

To simplify the modeled geometry, the fuel-basket region and fuel-basket periphery region are modeled as two concentric cylindrical regions extending the length of the fuel assembly (see Figure IV-6). The diameter of the equivalent fuel-basket region (Zone 1) is calculated in Holtec International (1997) using the hydraulic diameter of the fuel-basket periphery region



(a)



(b)

Figure IV-5. Fuel assembly (a) and fuel rod (b).

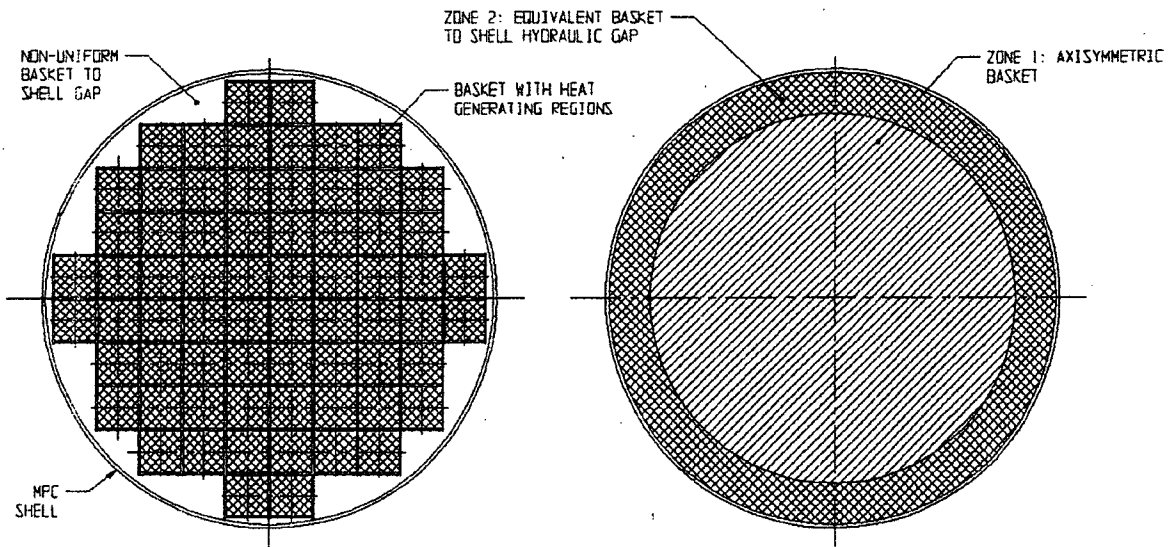


Figure IV-6. Fuel-basket region (left) and equivalent fuel-basket region (right).

(Zone 2). The hydraulic diameter takes into account the perimeter of the fuel basket and MPC inner shell wall, and the average basket-to-shell gap length—indirectly obtained from total surface area between the perimeter of the fuel basket and MPC inner wall—through which heat transfer occurs. For the MPC-24 basket, the hydraulic diameter is approximately 12.7cm (5in) (Holtec International, 1997). The hydraulic diameter is also equal to the inner diameter of the MPC shell minus the inner diameter of the equivalent fuel-basket cylinder region; in this way the equivalent fuel-basket cylinder diameter and periphery annulus gap length may be obtained.

IV.3.1.3 Rail-Steel Impact Limiters

The impact limiters are relatively low density cylindrical components that are not only designed to absorb energy during impact but also serve as insulators during fires in the uncrushed state. The main body of the impact limiter has a maximum diameter of 3.25m (128in) and a maximum length of 1.52m (60in) Figure IV-6.

Most of the impact limiter is honeycomb material enclosed in a thin shell metal wall. The honeycomb material and outer shell walls are supported in the interior of the limiter by a large-diameter circular plate welded (1) on one side to a small-diameter, thin-wall, cylinder and (2) on the perimeter to a large-diameter, thick wall, cylinder. The small- and large-diameter cylinders extend axially outward from the large-diameter plate into the interior of the limiter a distance of approximately 54.9cm (21.6in) and 34.6cm (13.5in), respectively. The small diameter cylinder forms the smallest diameter cavity in the impact limiter, on the side facing the external environment. This air-filled cavity is covered with a circular plate. In the upper limiter, the large

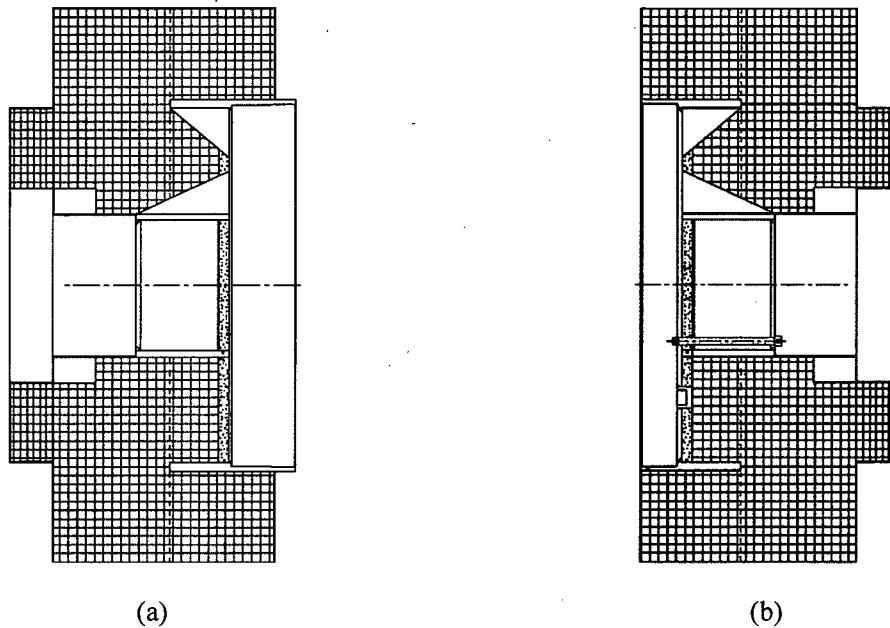


Figure IV-7. Rail-Steel upper (a) and lower (b) impact limiters.

diameter cylinder also extends in the opposite direction a distance of 36.8cm (14.5in) from the large-diameter plate, protruding beyond the surface of the limiter facing the overpack. In the lower limiter, the large-diameter cylinder only extends from the large-diameter plate to the surface of the limiter. Triangular channels are welded to the large-diameter plate and to the large- and small-diameter cylinders at regular angular intervals in the interior of the impact limiter. Each impact limiter contains a circular segment of neutron shielding, 6.35m (2.5in) thick, next to the large-diameter plate and between the triangular channels. This neutron shield provides axial neutron attenuation and serves as a heat barrier between the impact limiter body and the overpack ends. The neutron shield is covered at the other end by a thin shell wall.

The overpack fits into the cavity formed by the large diameter cylinder and the large diameter plate. The top upper limiter bolts into the sides of the vacuum flange through the protruding ends of the large diameter cylinder. The lower limiter is secured into the metal base cup using bolts that extend from the circular plate to just past inner surface of the large diameter plate as shown in Figure IV-7b.

The overpack limiters are assumed to stay intact after the hypothetical accident scenarios described in Chapter 4. This assumption is reasonable since the height of the flatbed rail car is approximately that of the diameter of the overpack. This height precludes any significant damage to the impact limiter during an accident scenario involving, for example, the overturn of the rail car flatbed, or the Rail-Steel falling off the flatbed. Since the limiters are assumed to stay intact, they are modeled in their original shape. The impact limiter, shell walls are not considered. The neutron shield material in the limiters is retained since it serves as a heat barrier between the

main body of the limiter and the overpack. Only the large-diameter, thick-wall, cylinder is explicitly modeled since it serves as a direct conduction path from the exterior to the interior of the limiter.

IV.3.2 Rail-Steel Thermal Behavior and Model Assumptions

The MPC-24 is designed to carry a maximum heat load of 20kW (0.833kW per fuel assembly). This heat generation rate is non-uniform along the length of the active fuel region. Table IV-1 shows the normalized, axial heat generation rate distribution for a typical Rail-Steel, PWR assembly (Holtec International, 2004). This table is used in Holtec International (1997) to calculate the heat generation rate through the active length of the basket (i.e., in the axial direction). The Rail-Steel system is designed to reject heat passively to the environment under normal conditions of transport. Thus, heat is dissipated from the fuel rods to the exterior surfaces of the cask only by a combination of conduction, convection, and radiation heat transfer modes.

Table IV-1. Axial burn up profile in the active fuel region.

Axial Distance from Bottom of Active Fuel (% of Active Fuel Length)	Normalized Value
0% to 4-1/6%	0.548
4-1/6% to 8-1/3%	0.847
8-1/3% to 16-2/3%	1.077
16-2/3% to 33-1/3%	1.105
33-1/3% to 50%	1.098
50% to 66-2/3%	1.079
66-2/3% to 83-1/3%	1.050
83-1/3% to 91-2/3%	0.960
91-2/3% to 95-5/6%	0.734
95-5/6% to 100%	0.467

For normal transportation conditions, the external temperature is higher than the internal temperature of the cask; therefore, heat will be dissipated outwardly starting from the fuel rods. Inside the fuel rods, heat is dissipated outward by (1) conduction through the gas space between rods; and (2) by radiation exchange between the fuel rods, and between the fuel rods and the walls of the basket. Convection is assumed negligible in this region since radiation effects dominate at high temperatures. Heat is then dissipated by conduction through the gas space in the flux traps, and by radiation between the basket walls. Convection is also assumed negligible in flux trap region. In the fuel-basket periphery, heat is dissipated to the MPC shell (1) by conduction through the heat conduction elements and the gas; and (2) by radiation between the walls of the fuel basket and the MPC, and between the inner walls of the heat conduction elements. In this region, convection enhances heat transfer between the inner walls of the heat conduction elements through the Rayleigh effect; this effect is taken into account through the

results provided in the Rail-Steel SAR. There a two-dimensional, finite element model is used to determine the heat convection coefficient for this region of the basket.

Heat transfer from the MPC shell to the overpack inner shell occurs through a MPC-overpack non-concentric gap. In the horizontal position the MPC makes contact with the overpack at the bottom. This contact gap is approximately 0.5 mm (0.02in) across. In this region, heat is also dissipated by conduction through the variable gas-filled gap, and by radiation between the outer and inner walls of the MPC and overpack, respectively. A two-dimensional, analytical model is used in the Rail-Steel SAR to obtain an effective conductivity through the variable length gap and is discussed in Section IV.3.3.2. Heat transfer through the inner and intermediate shells occurs by conduction through the shell material and through the contact gaps between the shells. These contact gaps are assumed to be five microns (2000 μ -in) across as in the Rail-Steel SAR. Conduction in the neutron shield region occurs in parallel through the radial connectors and the neutron shield material. A simple thermal resistor network is used to calculate the effective thermal conductivity through intermediate shells and through neutron shield region (see Sections IV.3.3.3 and IV.3.3.4).

The Rail-Steel cask system is designed to maintain the temperature of components below their operational temperature limits¹ for normal conditions of transport, and for a 30-minute, fully-engulfing, regulatory fire and subsequent cool down period (10CFR71). For longer-period, fully-engulfing fires, such as the ones depicted in this study, a significant amount of heat may be transferred to the interior of the Rail-Steel cask, raising the temperature of some of its components above their operational temperature limits. This is expected to occur in the neutron shield region. The operational temperature limit of the neutron shield insulation is 149°C (300°F). In our model, the neutron shield material is assumed to decompose completely shortly after it reaches this temperature limit, immediately triggering thermal radiation exchange between the overpack enclosure shell and the outermost intermediate shell. The assumption used here is a significant departure from what is assumed in the SAR, but is conservative in that heat from the fire is transferred more efficiently to the interior layers of the overpack. More will be said in Section IV.3.3 regarding this topic. As with the neutron shield, the aluminum honeycomb is expected to reach temperatures beyond the operational temperature limits. However, the honeycomb material is not expected to completely melt. Given the results in Pierce et. al. (2003), the regression rate of the honeycomb material is expected to be minimal over a three hour period and have only a local effect.

Heat dissipation through the cross section (i.e., in the axial direction) of the MPC and overpack, and through the limiters is assumed to occur mostly by conduction. Heat conduction occurs in parallel through each of the materials that comprise this cross section. Thermal radiation in the axial direction is possible; however, since view factors tend to diminish with the distance square

¹ The term operational temperature limit does not necessarily mean melting point. Operational temperature limits are given in the Rail-Steel SAR.

and angle of view, and the temperature gradients are weak along the axis compared to on the in-plane, as observed in contour results presented in Chapter 4, these effects are neglected in the basket region. Thus, radiation effects are assumed to be mostly in the radial direction except near the lateral ends of the MPC. Thermal radiation exchange occurs between the MPC outer surface and the overpack inner lid and between the MPC outer surface and the overpack bottom plate. In the limiters, the thin metal shell covering the neutron shield radiates to the small diameter plate located directly across the air-gap that fills the small diameter cylinder (see Figure IV-7 and the description in Section IV.3.1.3).

With the exception of the contact gaps already mentioned (e.g., between intermediate shell layers and between MPC and overpack), all contact gaps in the Rail-Steel cask are assumed perfect. This assumption is conservative in that heat is allowed to penetrate the Rail-Steel cask with reduced thermal resistance.

IV.3.3 Rail-Steel Materials and Thermal Properties

The Rail-Steel system is made from a variety of steel and aluminum alloys. The overpack inner shell is made from SA203-E cryogenic steel, and the metal base cup, vacuum flange, and closure plate are made from SA350-LF3 cryogenic steel. The intermediate shells are made from SA516-70 carbon steel, and the radial channels and enclosure plates from SA515-70 carbon steel. The neutron shield material is Holtite-A, a synthetic neutron-absorbing polymer with one percent boron carbide sold commercially under the trade name NS-4-FR (Holtec International, 2004). The variable-length gap between the MPC and overpack is filled with helium.

The MPC shell, lid, and baseplate, and the basket, fuel-cell walls are made from alloy X, a generic term used in various SARs that usually stands for one of the following stainless steel metals: SA304, SA304LN, SA316, or SA316LN (Holtec International, 2004). The thermal properties of SA304 are assumed for these components. Very little difference in thermal properties is found between SA304 and the other stainless steel materials already mentioned. On one side of each fuel cell wall is a thin layer of Boral sandwiched between the fuel cell wall and thin stainless steel sheathing. Boral is a neutron absorber made of boron carbide and aluminum alloy 1100 (Holtec International, 2004). The Boral layer and stainless steel sheathing extend the length of the active fuel region. The MPC-24 is designed to carry intact zircaloy and stainless steel clad fuel assemblies. In this study, the fuel rods are assumed to be made from zircaloy cladding as done in the Rail-Steel cask for conservative results. The fuel pellets are uranium dioxide (UO₂). The MPC heat conduction elements are made from aluminum alloy 1100. All void spaces inside the MPC are filled with helium (Holtec International, 2004).

The honeycomb in the impact limiter is made from aluminum 5052, and the large-diameter, cylinder from carbon steel (SA516). The neutron shield segments are also made from Holtite-A.

Table IV-2 provides the thermal conductivity for materials used in the Rail-Steel at several temperatures. For aluminum 1100 and the various carbon steels, data from Rail-Steel SAR is

available only over a limited temperature range since the analysis in that report showed cask temperatures within a limited range due to the limited 30 minute fire exposure and subsequent cool down. For these materials, the data trend is decreasing; therefore, the thermal conductivity value at the highest temperature is used at higher temperatures, a conservative assumption since the thermal conductivity values used are higher than what they should be. Note also that Holtite-A is replaced with air once the temperature of the neutron shield region reached the operational temperature limit of that material. In reality, only a fraction of the Holtite-A decomposes. Some of the gases generated in the shield region outgas through the neutron shield rupture disks at high pressures. Up to 90% of these gases come from moisture in the Holtite-A (Federal Register, 2000). Experiments show that up to fifty percent (by weight) of the NS-4-FR eventually degrades by the time temperature of the material reaches 800°C, leaving behind charred remains (Soo-Haeng et. al., 1996), and these are not expected to combust (Soo-Haeng et. al., 1996; Federal Register, 2000). The thermal conductivity of helium varies with pressure in addition to temperature; however, the pressure dependency is much weaker over the range of 101 to 689kPa (14 to 100lb/in²) (Petersen, 1970).

Table IV-3 provides the specific heat for these same materials at several temperatures. Temperature dependent values are given only for those materials which exhibited large variation in temperature. With the exception of stainless steel, aluminum 5052, and carbon steel, the specific heat of most materials used in the Rail-Steel is fairly constant. Note however that limited data is available for Holtite-A. The specific heat of Holtite-A is assumed remain constant from 92°C to its operational temperature limit. Recall that air properties are used beyond this limit. The specific heat of carbon steel increases significantly over the stated range. Most of the change is slow at low temperatures, but then is sudden between 450 and 727°C (842 and 1340°F) (Incropera and Dewitt, 1996, Yafei, 2009) and reaches a peak at around 1010°C (1850°F), the Curie temperature. The specific heat quickly drops after reaching the Curie temperature. This behavior is associated with changes in the magnetic state of these materials and has been observed for a great number of carbon steel materials with various carbon contents (Yafei, 2009).

Table IV-4 provides densities for stainless steel, carbon steel, zircaloy, and UO₂ at 92°C (200°F), and for air and helium at various temperatures. Since the density of most metals changes very little with temperature, only the values at 92°C (200°F) are used. The density of Holtite-A is assumed not to vary significantly from 92°C to its operational temperature limit. Recall that air properties are used above this limit to replace Holtite-A.

Table IV-2. Thermal conductivities for the Rail-Steel materials.

Material	Thermal Conductivity W/m-°C (Btu/ft-hr-°F)				
	92°C (200°F)	226°C (450°F)	377°C (700°F)	477°C (900°F)	726°C (1340°F)
Air [§]	0.026 (0.015)	0.040 (0.023)	0.050 (0.028)	0.055 (0.031)	0.067 (0.038)
Stainless Steel [§]	14.5 (8.3)	18.3 (10.5)	20.4 (11.8)	21.9 (12.6)	25.4 (14.6)
Aluminum Alloy 1100*	228 (131)	212 (122)	—	—	—
Aluminum-Honeycomb [‡]	3.5 (2.0)	4.1 (2.4)	4.8 (2.8)	5.2 (3.0)	—
Boral (B ₄ C)*	83.3 (48.2)	83.1 (48.0)	81.3 (47.0)	80.5 (46.5)	—
Carbon Steel- Int. Shells*	42.3 (24.5)	41.7 (24.1)	38.8 (22.4)	—	—
Carbon Steel-N. Shield*	50.7 (29.3)	49.1 (28.4)	42.6 (24.6)	—	—
Cryogenic Steel*	41.1 (23.8)	41.0 (23.7)	38.5 (22.3)	—	—
Helium [§]	0.17	0.22 (0.12)	0.26 (0.15)	0.29 (0.16)	0.35 (0.20)
Holtite-A*	0.65 (0.37)	—	—	—	—
UO ₂ *	6.0 (3.4)	6.0 (3.4)	5.1 (2.9)	—	—
Zircaloy*	13.5 (1.78)	14.6 (8.4)	16.2 (9.3)	17.8 (10.2)	—

[§]Incropera and Dewitt, 1996

*Holtec International, 2004

[‡]Thermophysical Properties Research Laboratory Inc., 2001

Table IV-3. Specific heat for the Rail-Steel materials.

Material	Specific Heat J/kg-°C (Btu/lbm-°F)				
	92°C (200°F)	226°C (450°F)	377°C (700°F)	477°C (900°F)	726°C (1340°F)
Air [§]	1010	—	—	—	—
Stainless Steel [§]	482 (0.11)	535 (0.12)	563 (0.13)	575 (0.13)	611 (0.14)
Aluminum [§]	903 (0.21)	—	—	—	—
Aluminum-Honeycomb [‡]	890 (0.21)	976 (0.23)	1057	1100	—
Carbon Steel [§]	434 (0.10)	505 (0.12)	590 (0.14)	653 (0.15)	1169
Boral (B ₄ C)*	2478	—	—	—	—
Helium [§]	5193 (1.2)	—	—	—	—
Holtite-A*	1632	—	—	—	—
UO ₂ *	234	—	—	—	—
Zircaloy*	304	—	—	—	—

Table IV-4. Densities for the Rail-Steel materials.

Material	Density kg/m ³ (lbm/ft ³)				
	92°C (200°F)	226°C (450°F)	377°C (700°F)	477°C (900°F)	726°C (1340°F)
Air [§]	0.98	0.69	0.54	0.46	0.35
Stainless Steel [§]	7900 (493)	—	—	—	—
Aluminum [§]	2702 (168)	—	—	—	—
Aluminum-Honeycomb [‡]	526 (32)	—	—	—	—
Carbon Steel [§]	7854 (490)	—	—	—	—
Boral (B ₄ C) [*]	544 (34)	—	—	—	—
Helium [§]	0.14	0.10	0.077	0.065	0.048
Holtite-A [*]	1681 (105)	—	—	—	—
UO ₂ [*]	10956	—	—	—	—
Zircaloy [*]	6551 (409)	—	—	—	—

Table IV-5 shows the emissivity values obtained from Rail-Steel SAR. The exterior surface of the Rail-Steel cask is coated with Carboline 890 paint and the overpack inner surfaces with Thermaline 450 paints, but these coats are only good up to 216°C (422°F) and 262°C (505°F), respectively (Holtec International, 2004). Note also the internal surfaces of the heat conduction elements are sandblasted to increase radiation between opposite sides of the heat conduction elements.

Table IV-5. Emissivity for some of the Rail-Steel materials and paints.

Material	Emissivity
Zircaloy	0.8
Painted Surface	.85
Rolled Carbon Steel	.66
Stainless Steel	.36
Sandblasted Aluminum	.40

IV.3.3.1 Effective Thermal Properties of Fuel Basket and Fuel-basket Periphery

Thermal properties for the fuel-basket region and fuel-basket periphery are obtained from the Rail-Steel SAR. In that report, the fuel basket and the fuel-basket periphery cross sections were replaced with two concentric cylinders each with equivalent effective thermal properties as described in Section IV.3.1.2. The procedure used to obtain the in-plane thermal conductivities

of the fuel basket and fuel-basket periphery as a function of temperature is described in this Rail-Steel SAR but is summarized here for completeness.

First, the cross section of the fuel assembly is modeled using a detailed two-dimensional, finite element model of the cross-section of a 17x17OAF fuel assembly rod arrangement (see Figure IV-5a), a uniform heat generation rate over each fuel rod, and a uniform temperature applied to the periphery of the fuel assembly. The 17x17OAF assembly used was determined to be the most resistive assembly design (Holtec International, 2004). The finite element model takes into account radiation between the rods and conduction across the helium gap. The effective thermal conductivity is obtained from the following equation:

$$k_{eff} = \frac{0.29468(q_g a^2)}{\Delta T}$$

where q_g is the heat generation rate per fuel cell per unit length, a is half the length of one side of the fuel cell, and ΔT is the maximum temperature difference in the fuel assembly (Sanders et. al., 1992). Since radiation is not linearly dependent on temperature, the model is run several times, each time with increasing uniform temperature near on the edge of the fuel assembly, to obtain effective properties at various temperatures. The detail fuel assembly is thus replaced with a homogenized fuel cell region (see Figure IV-6)

Second, the in-plane thermal conductivity of the basket storage wall, Boral, and stainless steel sheathing are replaced with an equivalent thermal conductivity using the thermal resistor network described in Rail-Steel SAR. The representative network takes into account the thermal resistances perpendicular to the wall and along the wall.

Third, the cross section of the MPC is modeled using a two-dimensional, finite element representation of the homogenized, fuel-basket walls, with a uniform heat generation rate applied over each homogenized fuel assembly, and a uniform temperature applied over the perimeter of the MPC shell. The model in the Rail-Steel SAR took into account: (1) conduction through the homogenized fuel assemblies, the helium gas in the flux traps, and the basket periphery, (2) radiation between homogenized basket walls, and (3) convection due to Rayleigh effects in the basket periphery. The effective conductivities of the basket region (k_b) and periphery region (k_p) are given by (Holtec International, 1999):

$$(k_b)_{eff} = \frac{Nq_g}{4\pi\Delta T_{bm}}$$

$$(k_p)_{eff} = \frac{Nq_g W}{A_s \Delta T_{pb}}$$

where

$$\Delta T_{pb} = \Delta T_{pm} - \Delta T_{bm}$$

Here ΔT_{bm} is the maximum temperature difference in the basket, ΔT_{pm} is maximum temperature difference in the MPC cross section, A_s is the surface area per unit length, W is basket periphery annular gap length. The equivalent fuel-basket thermal conductivities are given in Table IV-6. The effective axial thermal conductivities of the fuel basket are obtained in the Rail-Steel SAR using the resistor method which reduces to an area weighted average since the basket length (L) in the resistance (L/kA) is equal across all materials. The specific heat and density are obtained using a mass and volume weighted average, respectively. Near the ends of the basket, the fuel rods are filled with gas, decreasing the in-plane and axial thermal conductivity of the basket slightly, since the thermal conductivity of helium is smaller than the UO_2 pellets. Note that the temperature conductivities vary very little in temperature.

The properties in Table IV-6 are used over the length of the basket. For consistency, temperature varying properties are implemented in the thermal model.

Fuel spacers separate the ends of the fuel assembly from the MPC lid and MPC bottom plate. In these regions, conduction is predominately through the helium gas, but thermal radiation occurs between the walls of the basket and the fuel spacers where the spacers overlap the fuel basket. Thus, outside the fuel rod region, the in-plane, thermal conductivity is bounded by the thermal conductivity of helium and the effective conductivity of the active fuel-basket region. The in-plane, thermal conductivity is assumed to be the average of the helium conductivity and the fuel-basket region, homogenized conductivities. This in-plane, thermal conductivity is varied to assess the sensitivity of this assumption; very little differences are found, and did not have an impact at regions of interest (e.g., seals, cladding temperature, etc.) The axial thermal conductivity is obtained using an area weighted average using the dimensions of the basket, the fuel spacers, and the helium void. Dimensions for these components are provided in the Rail-Steel SAR. The specific heat and density in this region is obtained from a mass and volume weighted average, respectively, using the same components.

Table IV-6. Effective thermal conductivity for the fuel-basket region.

Effective Thermal Properties	92°C (200°F)	226°C (450°F)	377°C (700°F)	477°C (900°F)	726°C (1340°F)
In-Plane Thermal Conductivity W/m-°C (Btu/ft-hr-°F)	1.9 (1.1)	2.6 (1.5)	3.4 (1.9)	—	—
Axial Thermal Conductivity W/m-°C (Btu/ft-hr-°F)	3.4 (1.9)	3.8 (2.2)	4.3 (2.5)	4.6 (2.6)	—
Specific Heat J/kg-°C (Btu/lbm-°F)	305 (0.073)				
Density kg/m ³ (lbm/ft ³)	2688 (168)				

Fourth, the thermal conductivity in the basket periphery is further enhanced to account for heat dissipation through heat conduction elements. The equivalent resistor network through the heat conduction elements is obtained using a two-dimensional, analytical model explained in the Rail-Steel SAR. This resistance is added in parallel with the resistance obtained from the two-dimensional, finite element model for the basket periphery region. The fuel-basket periphery, in-plane conductivity is given in Table IV-7.

Table IV-7. Effective thermal conductivity of the aluminum heat conduction elements.

Effective Thermal Properties	92°C (200°F)	226°C (450°F)	377°C (700°F)	477°C (900°F)	726°C (1340°F)
In-Plane Thermal Conductivity W/m-°C (Btu/ft-hr-°F)	0.43 (0.25)				
Axial Thermal Conductivity W/m-°C (Btu/ft-hr-°F)	10 (5.8)				
Specific Heat J/kg-°C (Btu/lbm-°F)	964 (0.23)				
Density kg/m ³ (lbm/ft ³)	132 (8.25)				

The axial thermal conductivity is obtained from an area weighted average using aluminum 1100 and helium properties. The area of the periphery region is given in Holtec International (1997). The area of the heat conduction elements is estimated at 3.5 times the fuel-basket, cell pitch (27.3cm [10.7in]), multiplied by the thickness of the elements (3.175mm [0.125in]) and the total number of aluminum inserts (8) (Holtec International, 1999). The specific heat and density of the fuel-basket periphery is obtained from an area and mass weighted average, respectively, again considering only aluminum 1100 and helium.

Heat transfer through the periphery region is further enhanced by radiation between the inner walls of the heat conduction elements and the walls of the MPC and fuel basket. The emissivity of stainless steel and sandblasted aluminum are not very different as observed in Table IV-6.

IV.3.3.2 Effective Thermal Properties of MPC-Overpack Helium Gap

In the horizontal position, the MPC rests on the overpack forming a non-concentric, variable-length, helium gap. This gap is not modeled explicitly. Instead, a two-dimensional, analytical model derived in Holtec International (1997) is used to obtain an effective conductivity through the variable-length gap. This model included the effects of the contact region as explained below.

To account for radial heat dissipation through the variable-length, helium gap and through the metal-to-metal contact area, equations for the overall heat conducted through these regions are summed and then equated to the overall heat conducted through a concentric gap to obtain an effective thermal conductivity for a constant-length helium gap (i.e., concentric gap). The

following equation taken from the Rail-Steel SAR is used to obtain the effective thermal conductivity across the gap (k_{gap}):

$$\frac{(k_{gap})_{eff}}{k_{gas}} = \frac{t}{\pi} \int_0^{\pi} \frac{1}{t(1 - \cos \theta) + \varepsilon \cos \theta} d\theta$$

where k_{gas} is the conductivity of the gas, t is the thickness of the concentric gap and ε (0.5mm [0.02in]) is the metal-to-metal, contact area width. Results reported in the SAR show the effective conductivity through the equivalent concentric gap is twice the conductivity of helium.

IV.3.3.3 Effective Thermal Properties of Overpack Intermediate Shells

The Rail-Steel consists of a series of shell-gas layers between the inner shell wall and the outermost intermediate shell of the overpack. The contact gaps are assumed to be 0.05 mm (0.002in) across (Holtec International, 2004). No radiation is assumed through these gaps since radiation accounts for less than five percent of the effective conductivity for gaps of this size. The in-plane thermal conductivity is obtained by adding the resistances across each shell and gap in series. The axial and circumferential conductivities are assumed to be that of the shell layer material since the thermal conductivity of air and the gap area of air contribute very little. Similarly, the specific heat and density of the intermediate shell layers are assumed to be equal to the intermediate shell material.

Table IV-8. Effective thermal conductivity of the intermediate shells in the in-plane directions.

Effective Thermal Properties	92°C (200°F)	226°C (450°F)	377°C (700°F)	477°C (900°F)	726°C (1340°F)
In-Plane Thermal Conductivity W/m-°C (Btu/ft-hr-°F)	13.2 (7.6)	15.6 (9.0)	17.0 (9.8)	18.6 (10.7)	22.1 (12.7)

IV.3.3.4 Effective Thermal Properties of Neutron Shield Region

The neutron shield region consists of the Holtite-A inside the cavities formed between the outermost intermediate shell and the outer enclosure shell, and between the radial channels. Note the outer enclosure shell is not included here since it is modeled explicitly. The neutron shield region includes the Holtite-A material and the radial sections of the channel (2 per channel for a total of 40). This region is also modeled as a single volume with homogenized thermal properties.

Table IV-9 shows the effective properties in the neutron shield region. The effective thermal conductivity in the in-plane and axial direction are obtained by summing the resistance through the radial channels and through the neutron shield material in parallel. Since both the Holtite-A

and radial channels extend the same length in the axial direction, the resistance equation in the axial direction reduces to an area weighted average of the individual material conductivities.

Table IV-9. Effective conductivity of the neutron shield region.

Effective Thermal Properties	92°C (200°F)	226°C (450°F)	377°C (700°F)	477°C (900°F)	726°C (1340°F)
In-Plane Thermal Conductivity W/m-°C (Btu/ft-hr-°F)	4.3 (2.4)	3.5 (2.0)	3.2 (1.8)	3.1 (1.8)	2.7 (1.5)
Axial Thermal Conductivity W/m-°C (Btu/ft-hr-°F)	3.6 (2.0)	3.3 (1.9)	3.0 (1.7)	3.0 (1.7)	2.6 (1.5)
Specific Heat J/kg-°C (Btu/lbm-°F)	1315 (0.31)	505 (0.12)	590 (0.14)	653 (0.15)	1170 (0.28)
Density kg/m ³ (lbm/ft ³)	2113	552 (34)			

The thermal conductivity in the circumferential direction is assumed to be that of Holtite-A since the total thickness of the radial channels in this direction is small compared to the total circumferential length of the Holtite-A. Note that this is a conservative assumption in the sense that heat dissipated through the neutron shield region is preferentially in the in-plane and axial directions as a result of the latter assumption. This assumption does not have an impact in the uniform heating run, but it does have impact the CAFE-fire runs, where heat input around the circumference of the cask varies. In this case, heat will be dissipated more readily through the in-plane direction; thus giving higher temperatures in the interior of the cask.

The specific heat and density of the neutron shield region are obtained using a mass and area weighted average, respectively. Holtite-A is expected to reach its temperature limit during the early transient period of a fire. When this happens, Holtite-A partially decomposes leaving char residue behind. Most of the excess gas generated in Holtite-A outgases through the rupture disks when the pressure inside the neutron shield region reaches the disks design limits. In the thermal model, when Holtite-A temperature limit is reached, Holtite-A is replaced with air, and radiation is activated by setting the emissivity to an appropriate value. Note that air effectively lowers the specific heat and density of the neutron shield region. The effective specific heat of the neutron shield region is greatly influenced by the specific heat values of carbon steel since the density of air in the mass weighted average is very small compare to carbon steel.

IV.3.4 Rail-Steel P-Thermal Finite Element Model and Boundary Conditions

A steady-state case is run to obtain the initial conditions of the Rail-Steel cask and to compare results against those provided in the Rail-Steel SAR and in Adkins et. al. (2006). The steady-state model consisted of the Rail-Steel cask being exposed to a 37.8°C (100°F) ambient temperature, radiation boundary condition. This boundary condition is applied over the entire outer surface of the package using an emissivity of 0.85. In addition, insulation is applied over

the outer curved surfaces of the package (193.8W/m^2 [$34.1\text{ Btu/ft}^2\text{-hr-}^\circ\text{F}$]) and over the flat ends of the package (96.9W/m^2 [$17.0\text{ Btu/ft}^2\text{-hr-}^\circ\text{F}$]) as specified in (ASTM E 2230). A convection boundary condition is also applied to the outer surface of the package using a heat transfer coefficient of 3W/m^2 ($5\text{ Btu/ft}^2\text{-hr-}^\circ\text{F}$). This value is obtained from a set of correlations described in the Rail-Steel SAR—assuming turbulent flow—and is within the same order of magnitude as values obtained from correlations in (Incropera and Dewitt, 1996).

In general steady-state results are slightly higher than those presented in the Rail-Steel SAR, but lower than those reported in Adkins et. al. (2006). For example, the current study found a maximum fuel cladding temperature of 376°C (710°F), compared to 372°C (701°F) in the Rail-Steel SAR and 392°C (738°F) in Adkins et. al. (2006). The largest differences are observed in the extreme ends of the overpack, where temperatures in the Rail-Steel are lower (by $\sim 25^\circ\text{C}$) than reported here and significantly lower ($\sim 50^\circ\text{C}$) than what is reported in Adkins et. al. (2006). These differences are attributed to dissimilarities in modeling assumptions and approaches, and boundary conditions. For example, in Adkins et. al. (2006) a gap is assumed between the overpack and the limiters. Overall, however, the temperatures obtained from these three studies showed similar spatial trends and good agreement given the differences cited above.

The steady-state case is used to assess the suitability of the mesh. The mesh is initially 169600 elements; this corresponded to a nominal element size of 10.2cm (4in). This value is decreased to 5.1cm (2in) and then increased to 15.2cm (6in) to study the effects of element size on temperatures at locations of interest (as shown in the results of Chapter 4 and later in this Appendix). Results of the 15.2cm, element-size mesh showed some difference in the temperatures in the interior of the package when compared to those of the 10.2cm, element-size mesh. This is expected since large cells are created in the interior of the package. Near the exterior of the overpack, small geometric features resulted in small size elements. Results of the 5.1cm, element-size mesh showed very little difference when compared to the 10.2cm element mesh. The 5.1cm, element-size mesh had smaller elements in the interior and about the same near the exterior of the overpack. Therefore a third case is run, this time using the 10.2cm mesh, with a refined mesh in the near the exterior of the overpack. Results from this mesh showed some difference (less than 5 degrees in the neutron shield region), but not enough to justify the extra computational time needed to run this mesh. Figure IV-8 shows the final mesh used to run the five scenarios described in Chapter 4.

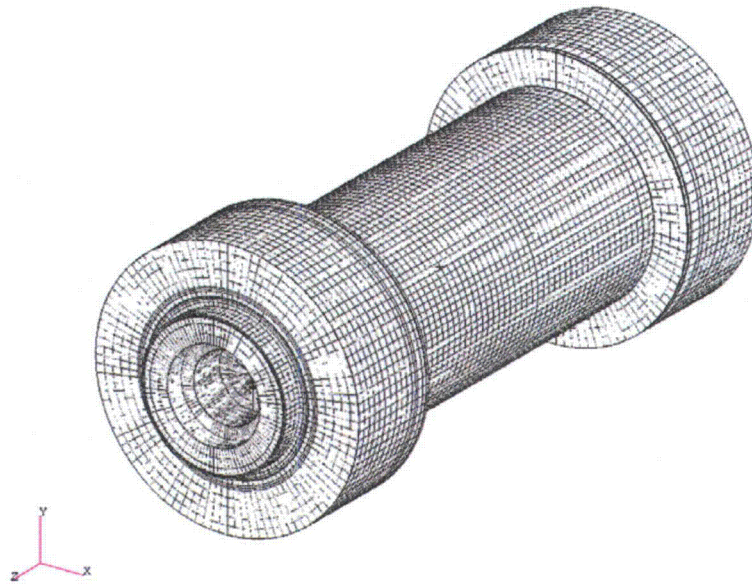


Figure IV-8. Rail-Steel finite element mesh.

The uniform heating case described in Chapter 4 is run initially to verify the Rail-Steel FE model. This exercise gave an additional measure of confidence in the Rail-Steel model. The boundary conditions for this case consisted of the Rail-Steel cask being exposed to an 800°C (1472°F) ambient-temperature, radiation boundary condition. This boundary condition is applied over the entire outer surface of the package using an emissivity of 0.9. A convection boundary condition is also applied to the outer surface of the package using a heat transfer coefficient of 85W/m² (15.2 Btu/ft²-hr-°F). This value is obtained in the Rail-Steel SAR from a set of correlations described there and assuming a 15m/s (49ft/s) vertical flame speed, a value significantly higher than what is specified in Nakos (2005) but nevertheless conservative in that it will result in a higher heat input to the cask. Convection accounts for about 10-20% of the total heat input for large objects inside a fire, the rest is through thermal radiation (Nicolette and Larson, 1989).

The uniform heating case is run for 30 minutes, followed by an 11.5 hour transient cool down. During the cool down period, the boundary conditions are set back to their steady-state case values, except for the emissivity of the outer cask which remained the same to simulate what happens in actual fires—a blanket of soot covers the cask. Also, the neutron shield region is assumed to contain air with radiation interaction between the outer enclosure shell and the outermost intermediate shell.

Overall, maximum temperatures obtained using the model developed here and in the Rail-Steel SAR show some differences during the 30 minute fire and during the cool down period—6% or less lower through the cask cross section, and 20% lower in the closure plate seal region. This

difference can be attributed to significant differences in boundary conditions. During the fire, the impact limiters are assumed to have been crushed. This effectively reduces the lateral dimension of the cask and increases the thermal conductivity through the limiters. Moreover, during the cool down period, a smaller emissivity value is assumed and no credit is taken for conduction through the neutron shield material (i.e., Holtite-A region). In this study, the most realistic boundary conditions are used, which were not necessarily the most conservative in terms of heat input. Only when reliable data was not available, or when current tools did not allow for effective implementation of realistic boundary conditions are conservative assumptions applied.

For the remaining cases, the external boundary conditions are obtained from CAFE, the computational fluid dynamics code coupled to P-Thermal. As is mentioned in Section IV.2, a boundary condition is setup in PATRAN that allowed CAFE results to be communicated to P-Thermal and vice-versa. The cool down period for these cases also used the steady-state case, boundary conditions.

IV.3.5 Rail-Steel Thermal Analysis Results

Pages 31 through 39 show results for the five scenarios already described in Chapter 4. These results are not discussed here, but are presented to supplement results discussed in Chapter 4. Figure IV-9 shows results for the regulatory uniform heating case cited in the previous section. This is the P-Thermal only run. Figure IV-10 shows results for the regulatory CAFE fire and together with Figure IV-9 may be useful in determining the differences between uniform and non-uniform fire conditions. The effect that large objects have on fires and their implications to modeling large packages in fires has been discussed in Nicolette and Larson (1989). Figure IV-11 shows results for the fully engulfing CAFE fire with the cask on the ground, and Figures IV-12 and IV-13 show results for the cask on ground but outside the fire. The last three cases are for a three hour fire and subsequent cool down period.

IV.4 Rail-Pb

The Rail-Pb (Nuclear Acceptance Corporation International, 2004) is also certified to transport spent nuclear fuel material in rail cars. This cask is chosen because it presents quite a different design philosophy from the Rail-Steel cask. The Rail-Pb cask uses lead for the gamma shield. Moreover, the Rail-Pb cask is able to carry spent fuel without the need for a MPC canister. As in the Rail-Steel analysis, the Rail-Pb is assumed to be in the horizontal configuration, as it would be during transportation, and most likely after an accident scenario. Only the thermally relevant components of the Rail-Pb are considered to estimate the thermal response of this cask.

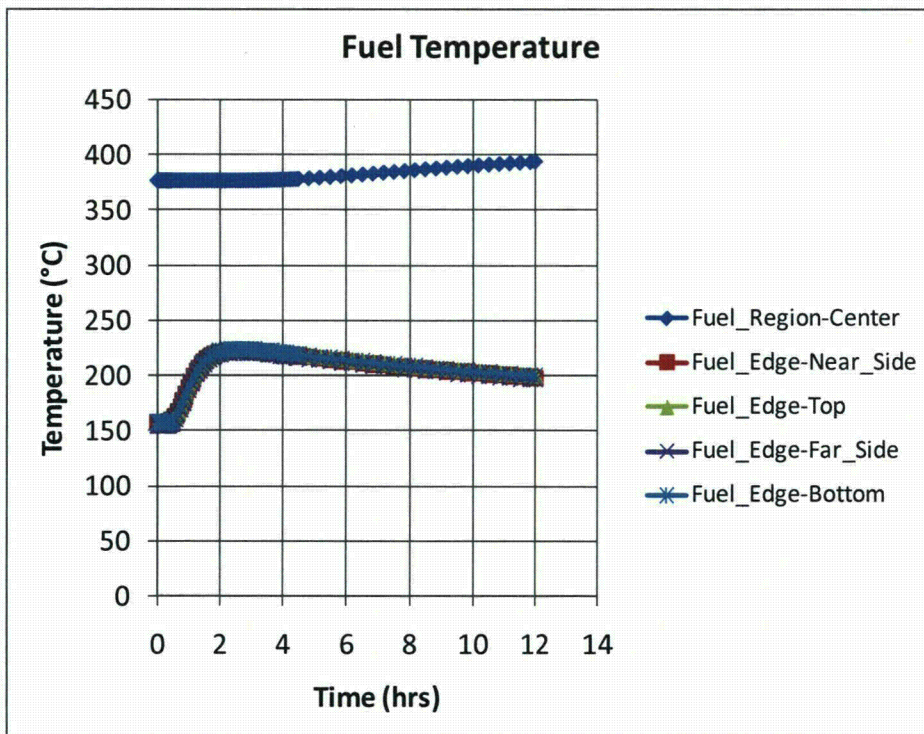
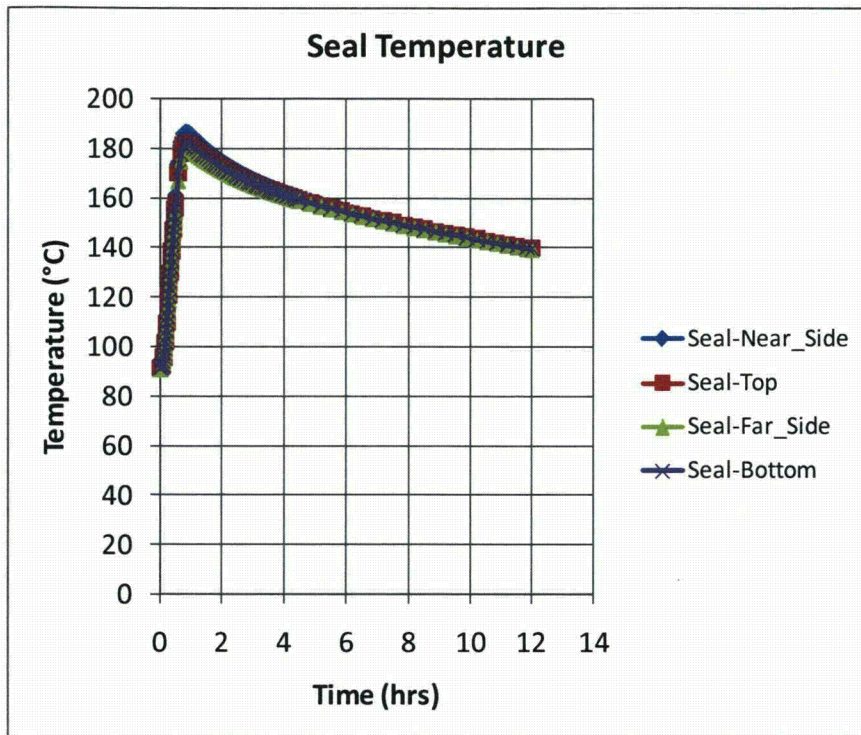
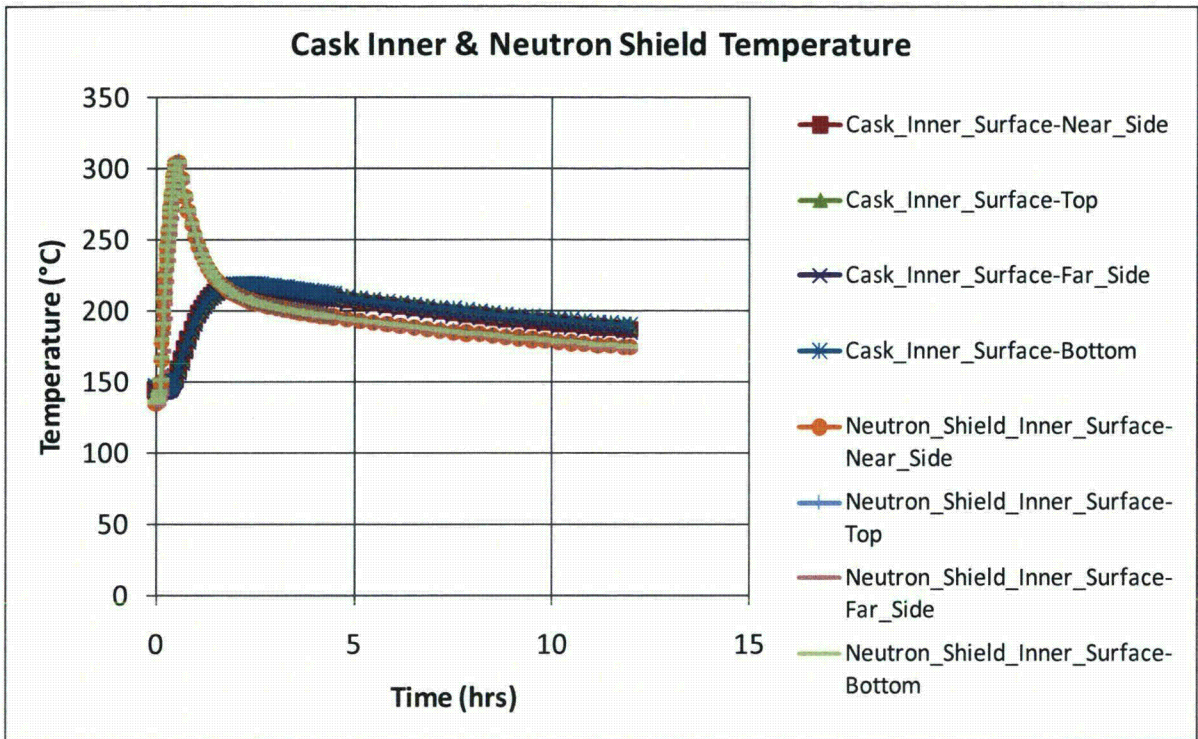


Figure IV-9. Rail-Steel Regulatory Uniform Heating Results (P-Thermal)



S

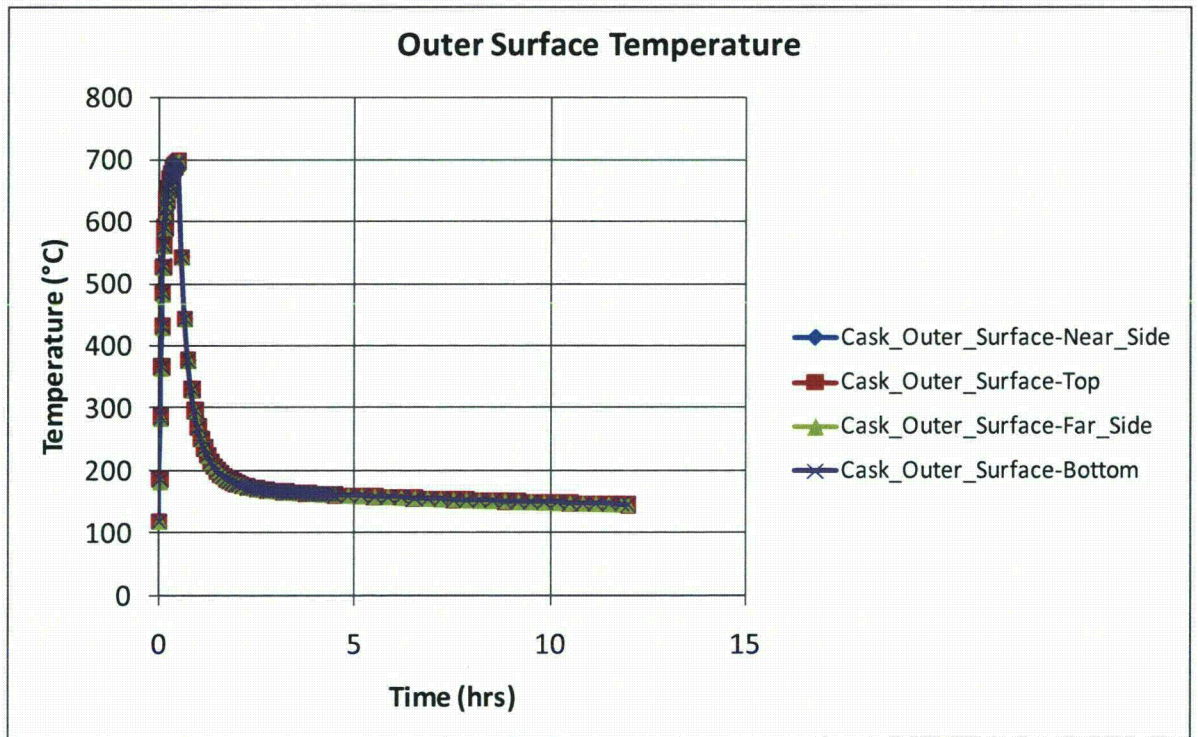


Figure IV-9. Rail-Steel Regulatory Uniform Heating Results (P-Thermal) – Continue

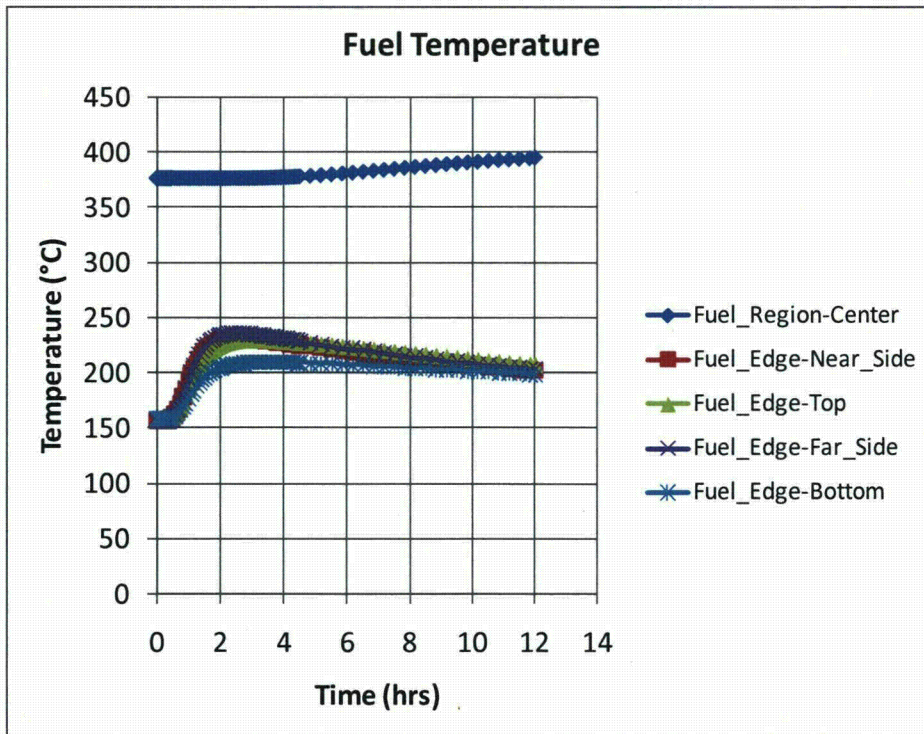
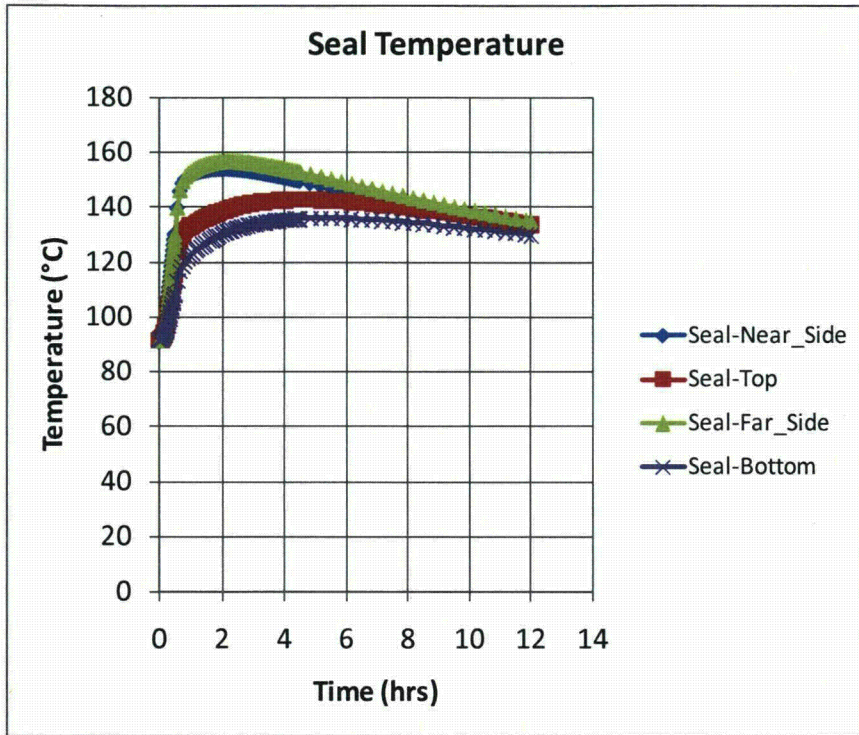


Figure IV-10. Rail-Steel CAFE regulatory fire.

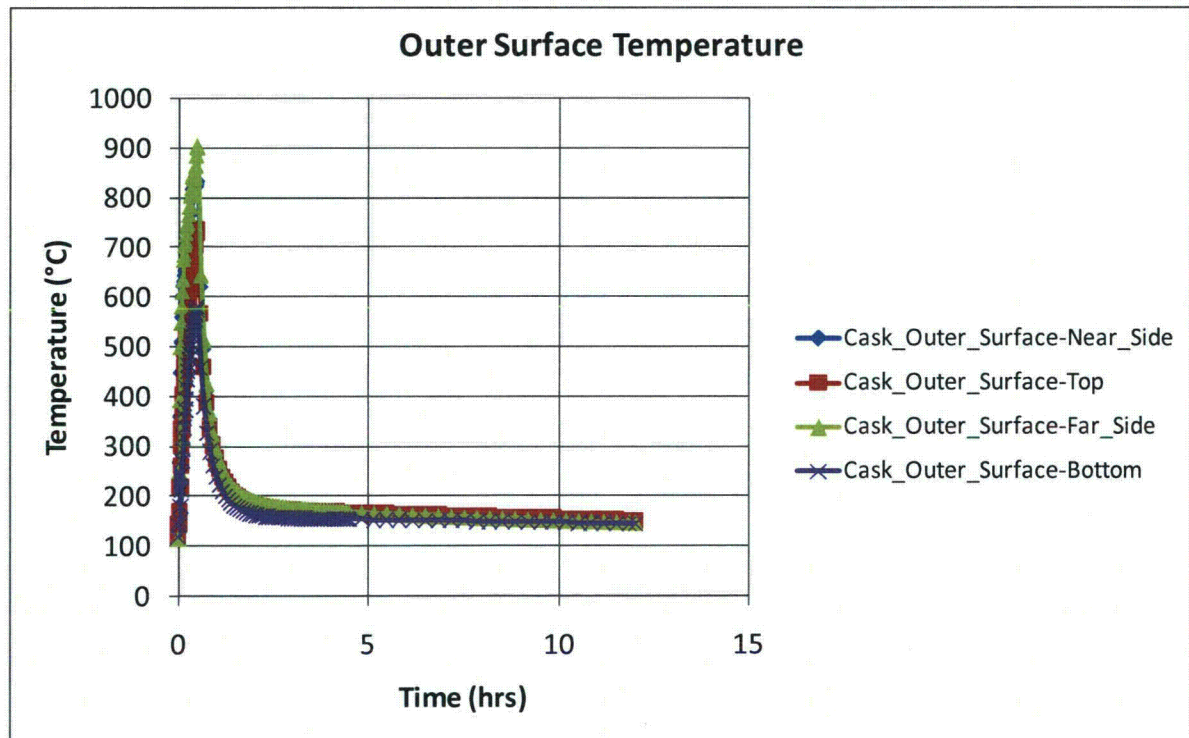
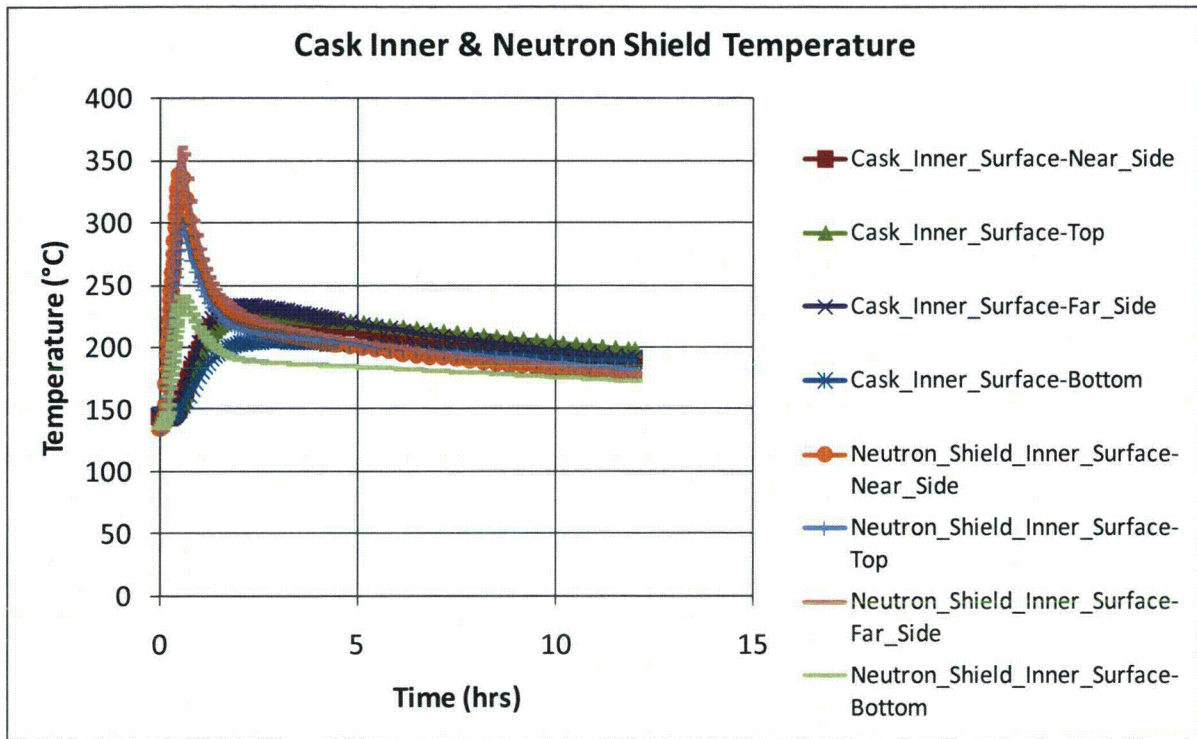


Figure IV-10. Rail-Steel CAFE regulatory fire. – Continue

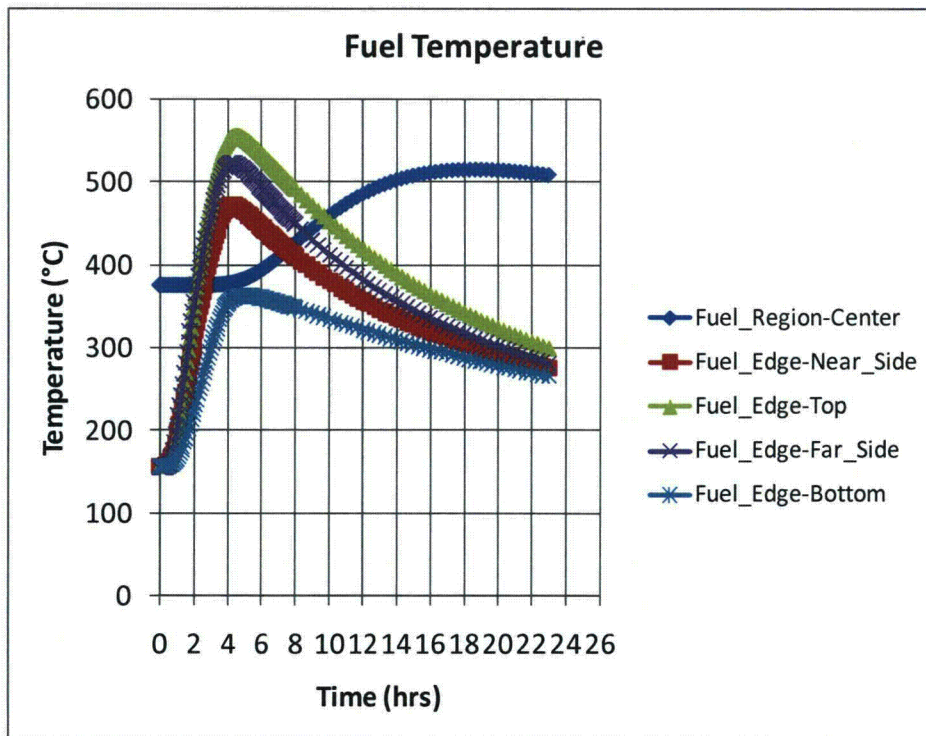
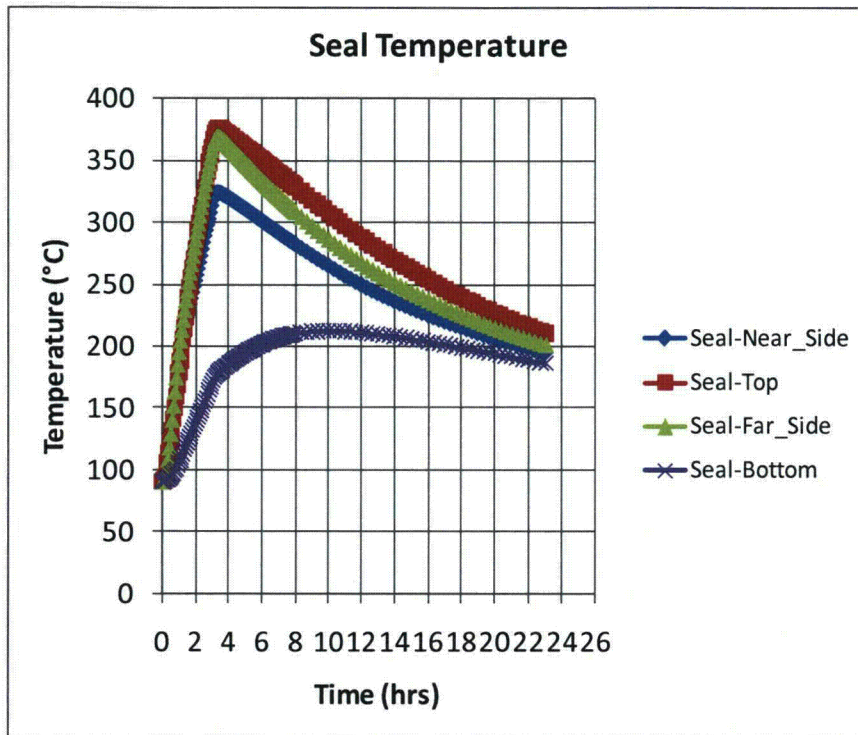


Figure IV-11. Rail-Steel CAFE fire with cask on ground and at the pool center.

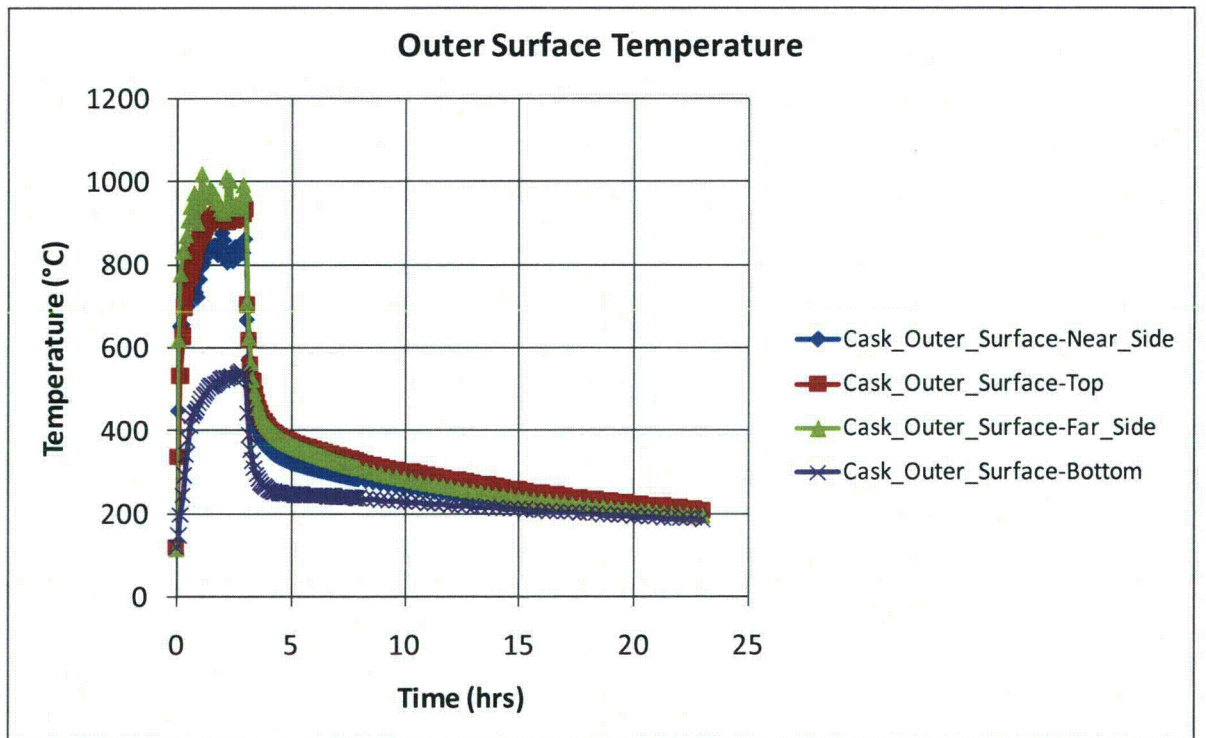
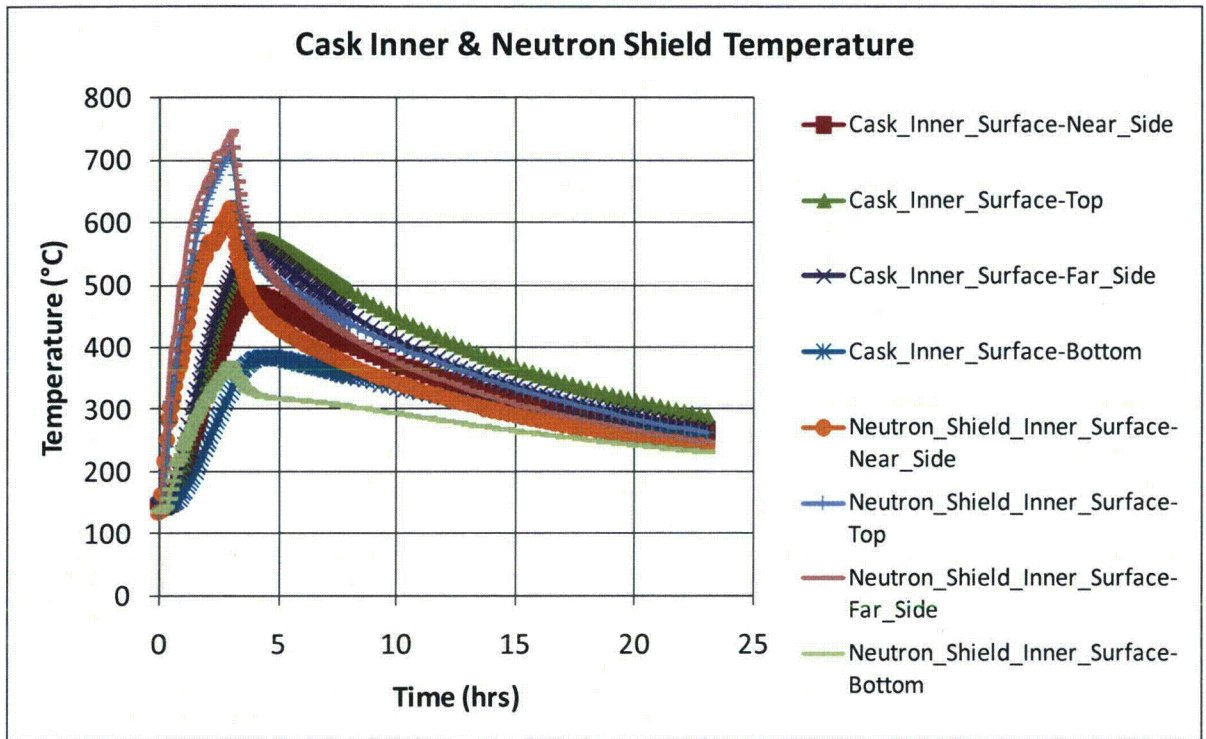


Figure IV-11. Rail-Steel CAFE fire with cask on ground and at the pool center. – Continue

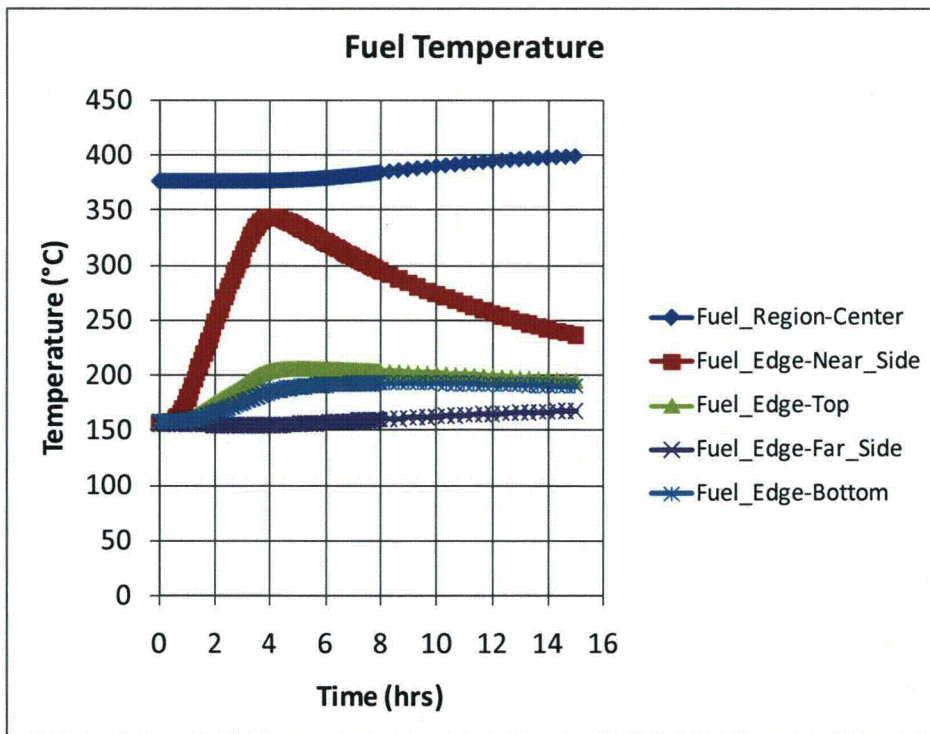
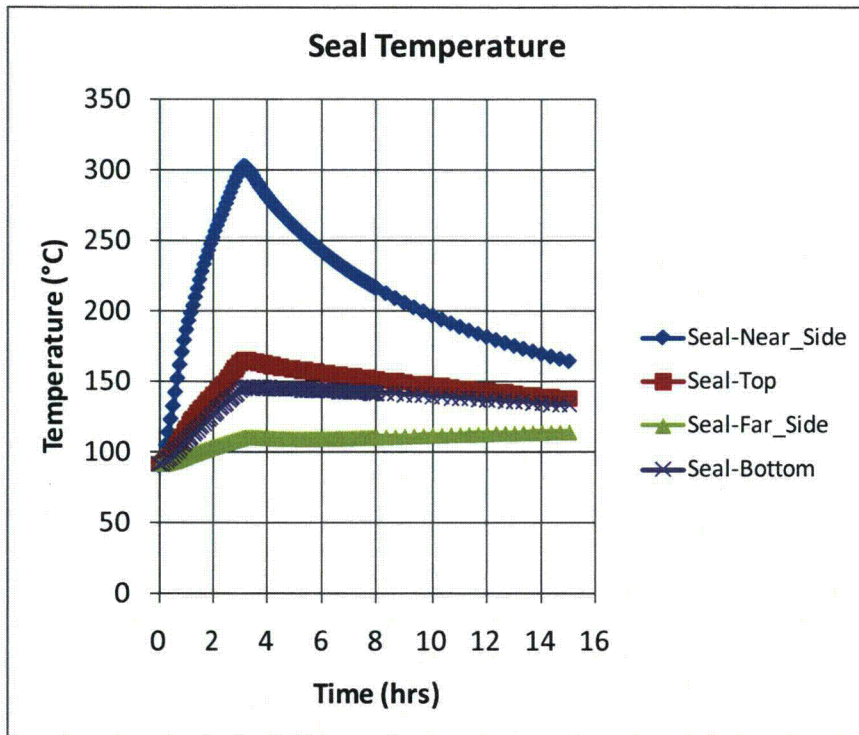


Figure IV-12. Rail-Steel CAFE fire with cask on ground 3.0m (10ft) from the edge of the pool.

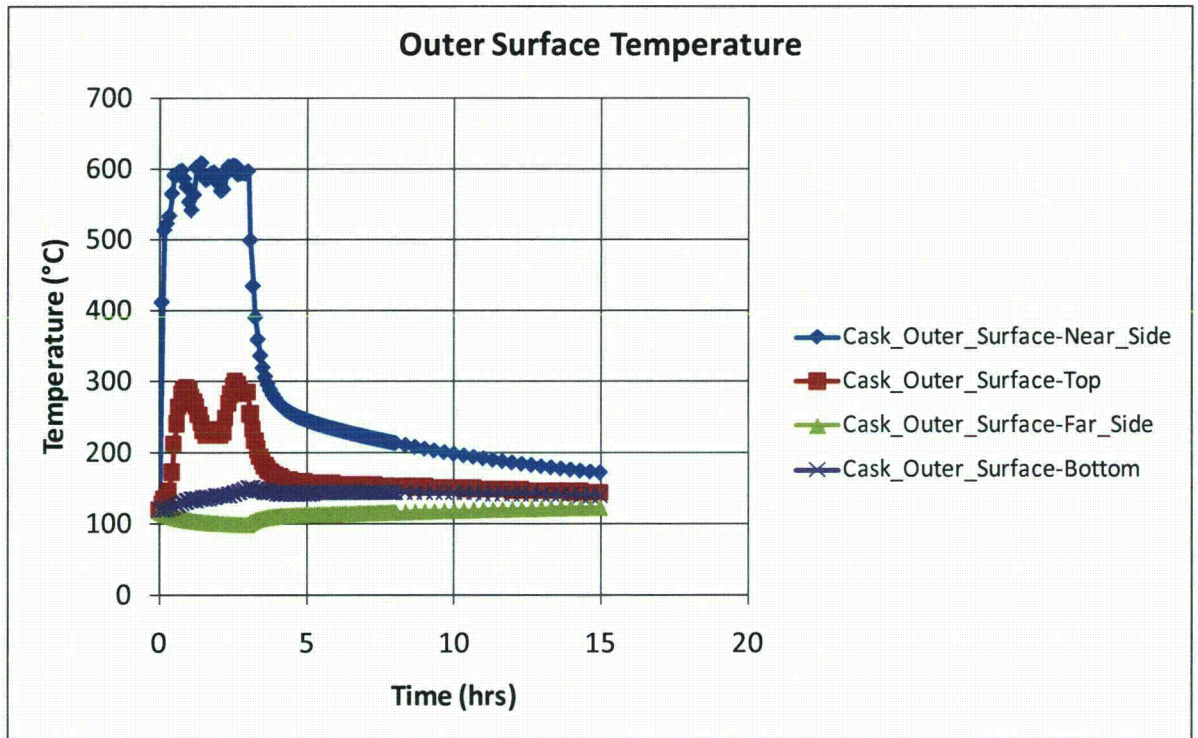
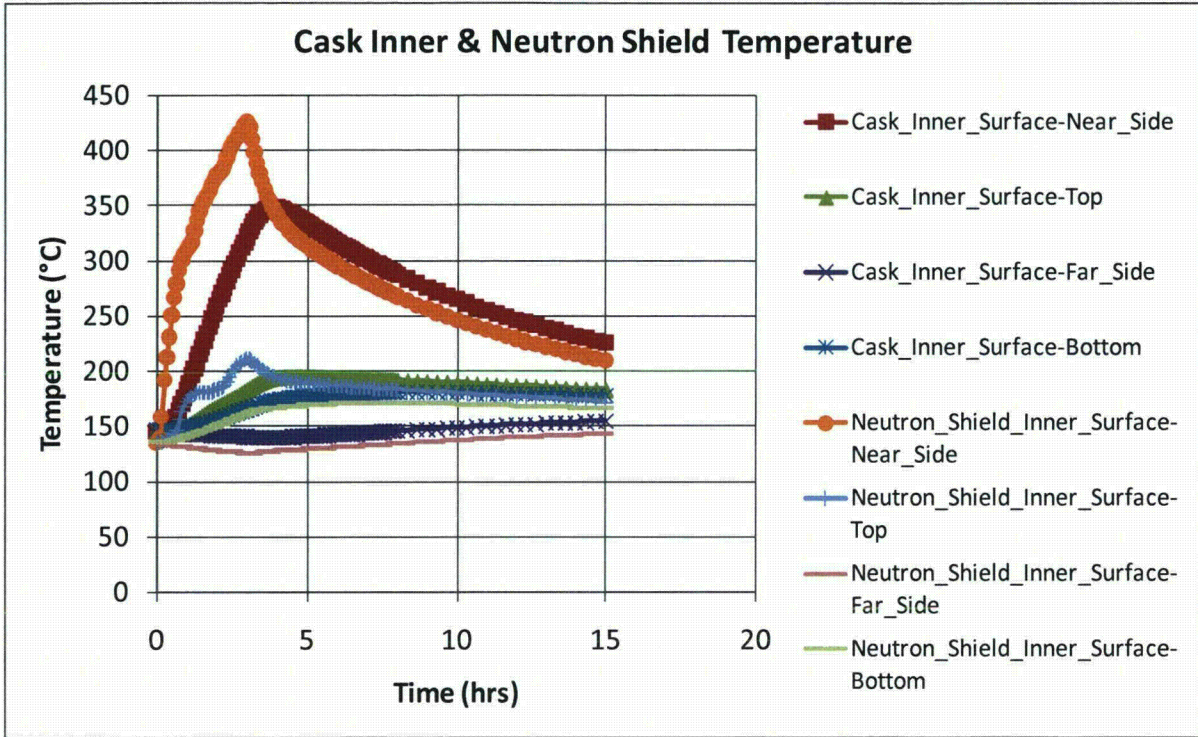


Figure IV-12. Rail-Steel CAFE fire with cask on ground 3.0m (10ft) from the edge of the pool. - Continue

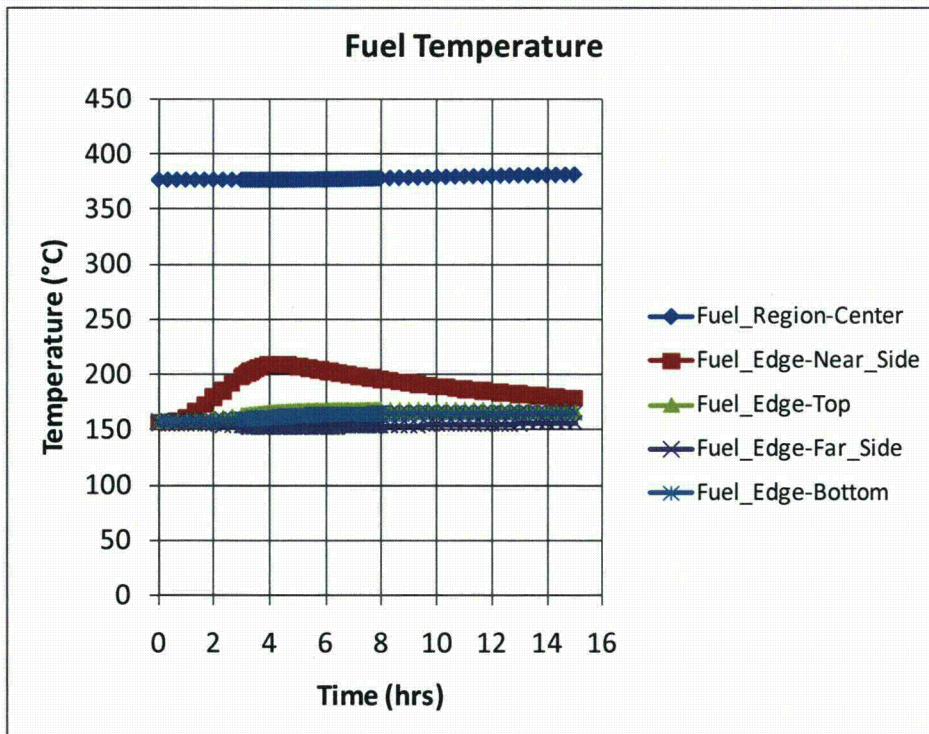
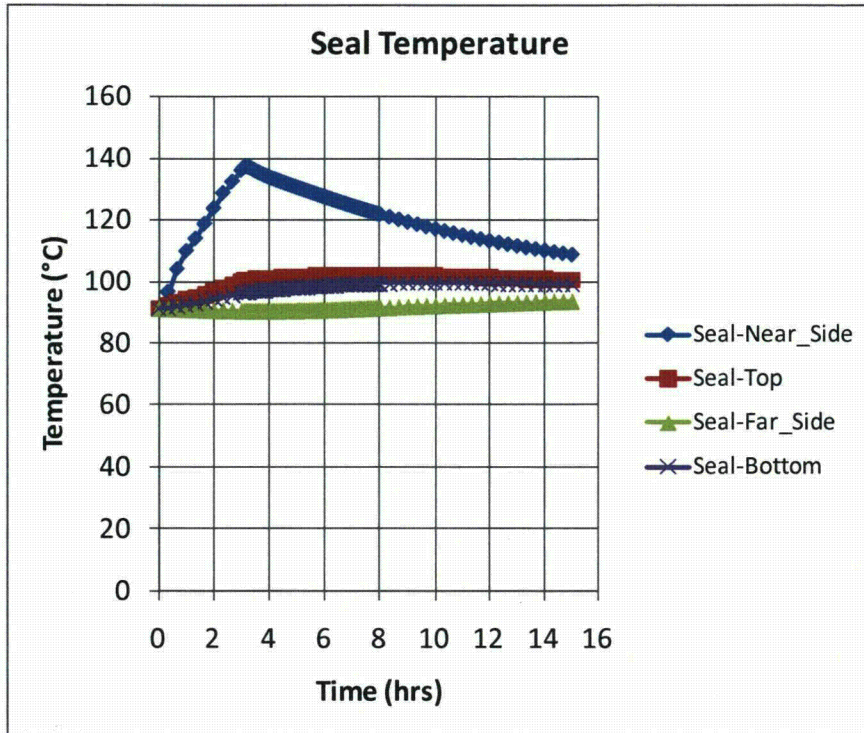


Figure IV-13. Rail-Steel CAFE fire with cask on ground 18.3m (60ft) from the edge of the pool.

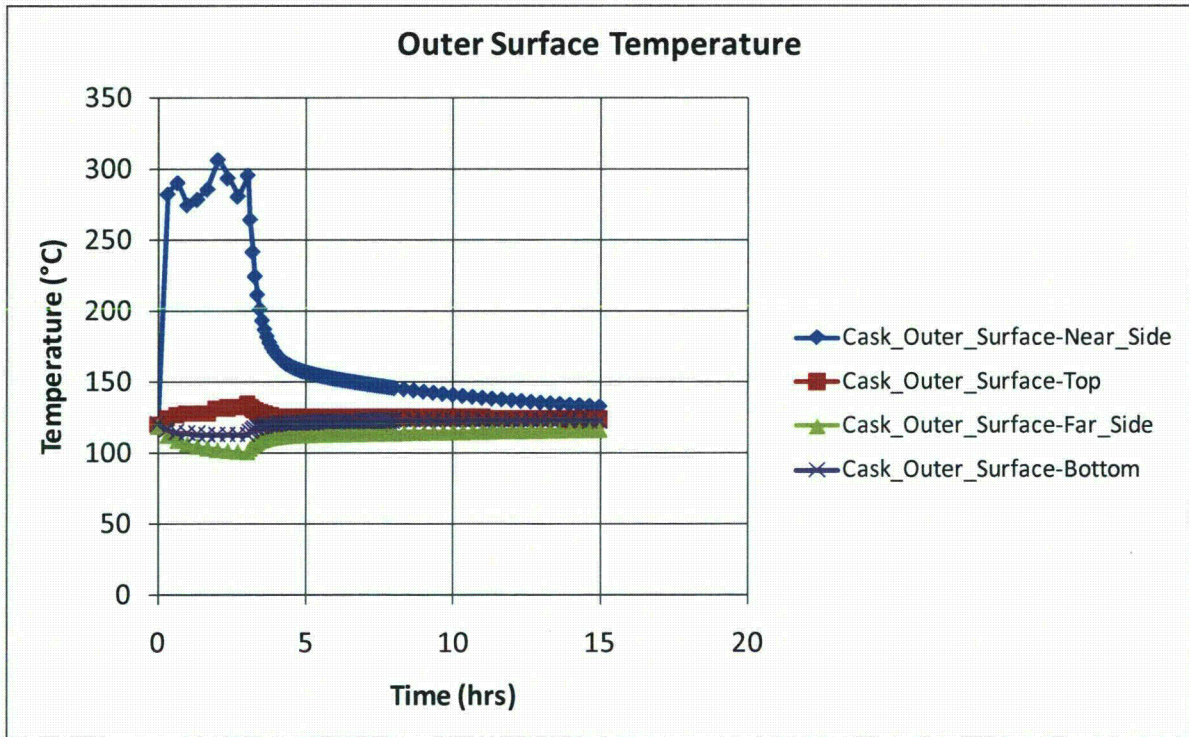
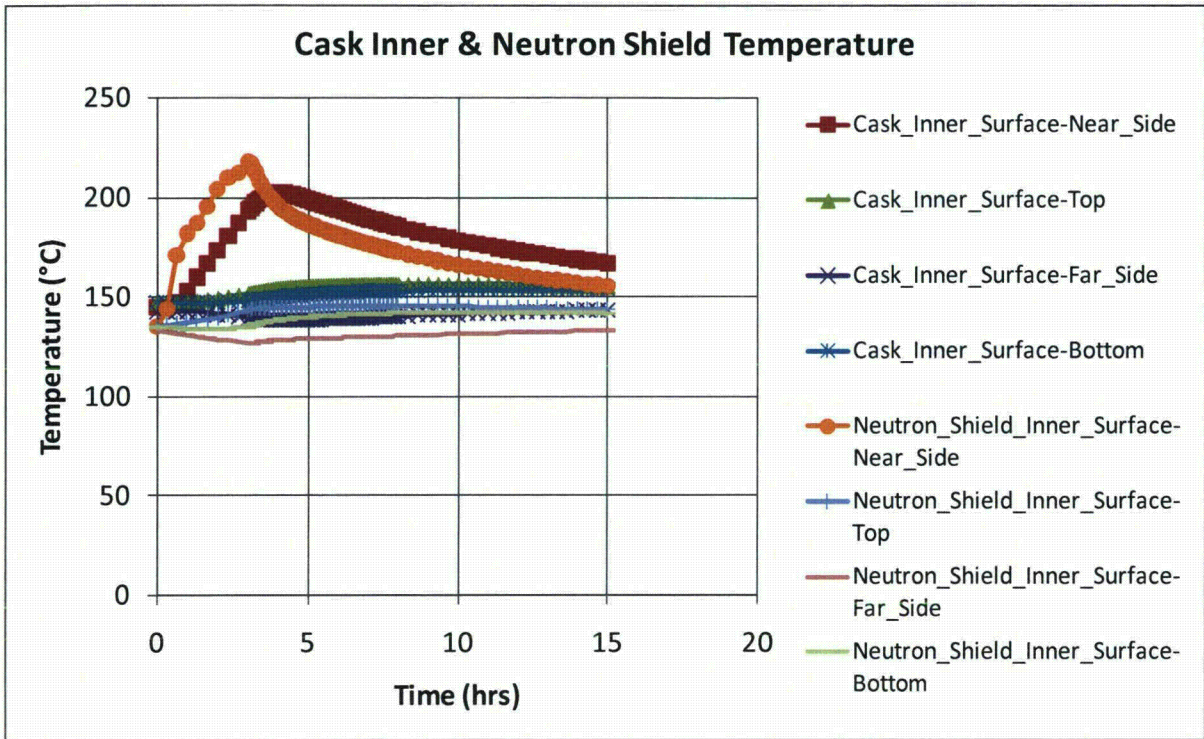


Figure IV-13. Rail-Steel CAFE fire with cask on ground 18.3m (60ft) from the edge of the pool. – Continue

The Rail-Pb cask uses a single lead gamma shield as opposed to a multilayer carbon steel gamma shield like the one used in the Rail-Steel cask. This lead shield melts at relatively low temperatures, but remains in the overpack in molten form until the temperature is low enough to change back to the solid state. This process has an impact of the cask ability to attenuate gamma rays as described in Chapter 5 and Appendix V. One unique feature of the Rail-Pb cask is that it can store the spent nuclear fuel in a directly loaded fuel basket in addition to inside an MPC as is seen in the Rail-Steel. The directly loaded configuration is a significant design departure from the MPC configuration since there is no barrier between the fuel assemblies and the inner walls of the overpack. For this reason, this analysis focuses on the directly loaded configuration. Finally, the Rail-Pb uses wood filled impact limiters as oppose to an aluminum honeycomb, a minor difference from the thermal analysis point of view, but nevertheless important to point out.

In most cases, results reported in the Rail-Pb SAR (Nuclear Acceptance Corporation International, 2004) are used but modified where necessary as is done with the Rail-Steel analysis. The only significant departure is how the interior of overpack is treated in the Rail-Pb SAR as explained in the introduction of this Appendix. Unlike the method used that SAR, the directly loaded basket is replaced with a cylinder having equivalent effective thermal properties using a simple, three-dimensional, finite element model and the thermal resistor network method. As is done in the Rail-Steel analysis, the neutron shield region is replaced with an equivalent thermal region using the thermal resistor network method. The impact limiters are also modeled in the uncrushed state for the same reasons cited in Section IV.3.1.3.

IV.4.1 Geometry Considerations

The directly loaded Rail-Pb cask consists of an overpack, a fuel basket, and limiters at each end of the basket as shown in Figure IV-14. The directly loaded fuel basket is an open fuel container designed to fit snug within the overpack interior cavity. The overpack is designed to attenuate both the heat, and the neutron and gamma rays generated inside the fuel basket. The overpack contains two lids, each fitted with seals that completely seal the contents inside the overpack from the outside environment. This double lid design essentially forms a double containment barrier. The total length of the Rail-Pb, including the limiters, is approximately 6.5m (256 in).

IV.4.1.1 Overpack

The Rail-Pb overpack is also a multilayer cylindrical vessel approximately 2.20m (86.7in) in diameter and 4.90m (193in) in length (see Figure IV-14). The inner cavity of the overpack is approximately 1.80m (71in) in diameter and 4.19m (165in) in length. The cross section of the overpack vessel is made of three shells layers arranged in following order starting from the center of the overpack: an inner shell, a lead shell, and an outer shell (see Figure IV-15). As in the Rail-Steel cask, these shells are tightly coupled to each other and are welded to the overpack bottom plate and top flange. The lead shell acts as the gamma shield in this design. The thickness of the inner shell wall is not constant throughout, but tapers in slightly through most of the overpack side wall. That allows the thickness of the lead shell to increase slightly through the

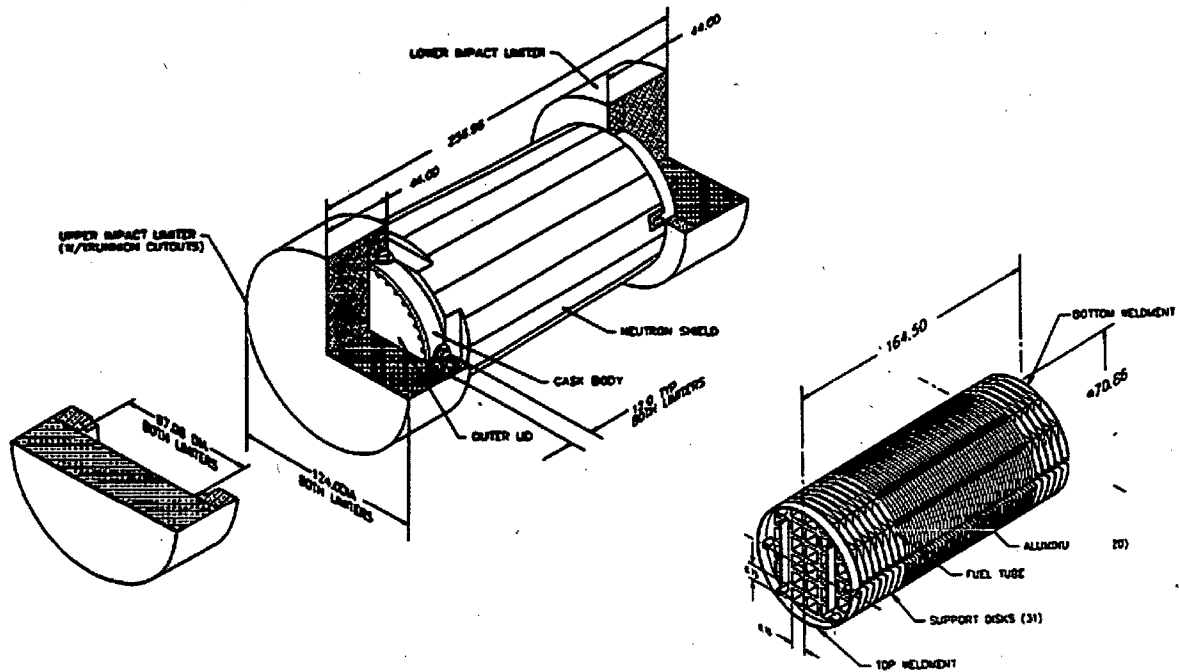


Figure IV-14. Rail-Pb components with the direct loaded fuel basket shown to the right.

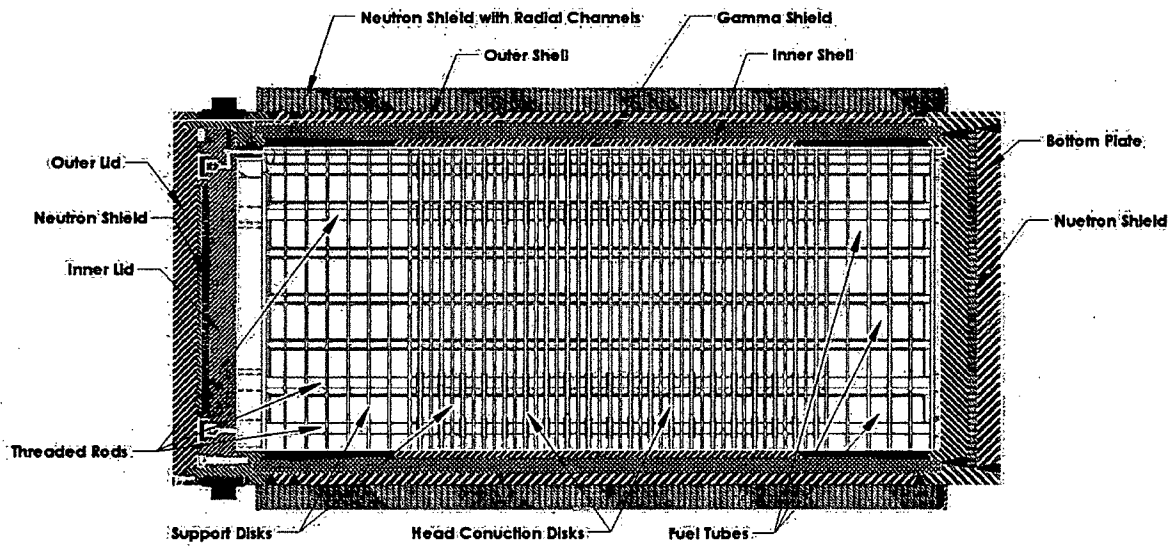


Figure IV-15. Cross-section view of the Rail-Pb with the directly loaded fuel basket.

same section of the overpack, where the gamma shielding is most needed. Radial channels are also welded to the outer shell to enhance heat transfer through the neutron shield region. The outer enclosure shell is formed the same way as in the Rail-Steel. Similarly, the cavities formed by the outer enclosure shell, the radial channels, and the outer enclosure shell are filled with a neutron shield material. The neutron shield region increases the diameter of the overpack an additional 29.2cm (11.5in). Unlike the Rail-Steel, the overpack contains inner and outer lids that fit into the vacuum flange and complete the double containment barrier. Both the inner lid and bottom plate contain 5cm (2in) thick cylindrical layer of neutron shield within them.

The inner, outer, and lead shells, the vacuum flange, the inner and outer lids, and the bottom plate are represented explicitly in the thermal model with minor alterations to simplify the model. The most significant change is making the thickness of the inner shell and lead shell constant throughout. Their thickness is kept equal to the corresponding thicknesses in the middle section of the overpack. As in the Rail-Steel model, the neutron shield region is represented as a single volume to minimize geometric complexity. As with the Rail-Steel, the Rail-Pb overpack contains a number of features that serve a special purpose. These features are omitted from the model as is done in the Rail-Steel model and for the same reasons: (1) negligible due to their small volume and mass relative to the other components in the overpack, (2) highly localized with no effect to the overall thermal performance of the package at locations of interest, or both.

IV.4.1.2 Directly Loaded Fuel Basket

In the Rail-Pb, the nuclear spent fuel is stored in a directly loaded basket (see Figure IV-14). In this configuration, the fuel basket can store up to 26 PWR fuel assemblies. The total length of the fuel basket is 4.18m (164.5in) and the diameter is a little less than the inner diameter of the overpack. The fuel basket consists of thirty-one support disks and twenty heat transfer disks, aligned parallel to each other, and each precisely separated using six threaded rods and spacer nuts. The heat transfer disks are placed between the support disks in the region where the heat decay rate is at a maximum. Except for the end support disks, all support disks are the same thickness; the end support disks are twice as thick. Except for the end support disks, all heat transfer disks are slightly thicker. Both disk types contain twenty-six square holes spaced at regular intervals, and aligned between disks. Each square hole fits a thin walled, square, fuel tube which extends almost the length of the basket. These tubes are welded to the disks and accommodate the fuel assemblies. The fuel assemblies extend almost the entire length of the fuel basket. The basket active fuel region is assumed to be 3.66m (144in) in length as suggested in the Rail-Pb SAR. Additional plates and a short length cylinder are welded to the end support disks for extra support and complete the fuel-basket design. The fuel basket fits within the inner cavity of the overpack, but there are a small gap between the basket disks and the inner wall of the overpack, and between the ends of the basket, and the lid and bottom plate walls.

As in the Rail-Steel, each fuel assembly consists of an array of fuel rods, each separated by a helium gas space. The total number of rods in the fuel assembly, the dimensions of each rod, and

the type of fuel cladding vary between assembly designs. A more complete description of the fuel assembly and fuel rods is given in Section IV.3.1.2.

The fuel basket and fuel assemblies are not explicitly included in the model. Instead, a separate three-dimensional model is generated to obtain the effective properties of the basket in the in-plane and axial directions. Since the basket support disks, gas regions, and heat transfer disks repeat at regular intervals in the active fuel region, a three-dimensional, quarter solid model of a section comprising two support disk, heat transfer disk, and the gas and fuel tubes between them is generated to obtain the effective properties of the basket in the in-plane and axial directions. The diameter of the support and heat transfer disks is assumed the same to simplify the solid modeling and mesh process. The same model is used for the portion of the fuel basket without the heat transfer disk. In this case, the material properties and boundary conditions for the heat transfer disk are replaced with those of the gas region.

IV.4.1.3 Impact Limiters

The impact limiters in the Rail-Pb are cylindrical wood-filled structures also encased in a thin metal shell. Each impact limiter is 3.15m (124in) in diameter and 1.12m (44in) in length (see Figure IV-14). The depth of the cap where the overpack fits is 30.5cm (12in.). These limiters serve the same purpose as the impact limiters in the Rail-Steel (see Section IV.3.1.3). Since the impact limiters are mostly wood and have very little metal structures, they are modeled as two coupled solid wood structures, retaining their volume and shape.

IV.4.2 Rail-Pb Thermal Behavior and Model Assumptions

The Rail-Pb is also designed to release heat by passive means under normal conditions of transport. In the direct loaded configuration, the basket is designed to generate at most 22.1kW (0.85kW per fuel assembly). Figure IV-16 shows the normalized, axial heat generation rate distribution for a typical Rail-Pb PWR assembly. As with the Rail-Steel, heat is dissipated from the fuel rods to the exterior surfaces of the Rail-Pb by a combination of conduction, convection, and radiation heat transfer modes.

The fuel assembly design in the Rail-Pb is conceptually the same as in the Rail-Steel model; therefore, the same heat transfer mechanisms are present as described in Section IV.3.2. The approach described in Section IV.3.3.1 is also used in Rail-Pb SAR to obtain the effective thermal conductivity of the fuel assembly in radial direction. Values presented in the Rail-Pb SAR are used in this study and are not much different from what is used in the Rail-Steel SAR, as expected. Heat from generated in the assembly is dissipated by conduction through the fuel tube walls. From the tubes, heat is then radially dissipated by conduction through the support and heat transfer disks, and through the gas in the void formed between the tubes and the inner wall of the overpack; and by radiation to the adjacent tubes and disks, and to the inner wall of the overpack. Convection due to Rayleigh effects is also possible in the gas void. As in the Rail-Steel fuel basket, convection is limited to a few regions around the basket perimeter. However, unlike the HI-STAR configuration, the convective cells in the Rail-Pb basket are confined to the

gas void between adjacent disks. Moreover, heat dissipated from the adjacent disks through this void tends to decrease the temperature gradient across this void region, reducing temperature gradient induced flow. In the Rail-Pb model, convection is neglected in this region since it is not expected to be significant given the Nusselt values presented in the Rail-Steel SAR for a similar void configuration.

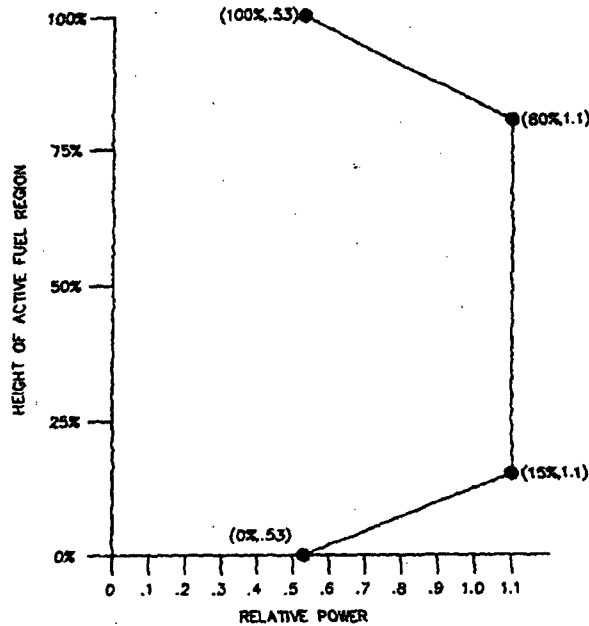


Figure IV-16. Axial burn up profile for the directly loaded fuel basket.

Heat is dissipated radially by conduction and radiation through the gap between the disks and the overpack inner wall. This gap is assumed to be 1.65mm (0.065in) across as stated in the Rail-Pb SAR. As mentioned before, a three-dimensional, quarter section of the fuel basket is generated to obtain effective thermal conductivities in the in-plane and axial directions (see Figure IV-17). The small gap between the disks and the inner wall of the overpack is included (not clearly visible in Figure IV-17). Except for convection, all modes of heat transfer are accounted for in this model, and included radiation between the tubes, between the tubes and the disks, between the tubes and the inner shell (also not shown), between the disks, and between the disks and the inner shell. In the horizontal position, the disks make contact with the inner shell wall. To account for conduction through the contact area between the disks and the inner shell wall, the same model derived in Holtec International (1997) is employed to enhance conductivity through the equivalent concentric gap (see Section IV.3.3.2). Note that both the support and heat transfer disk diameters are assumed to be the same after thermal expansion.

Heat transfer through the inner, lead, and outer shell of the overpack occurs by conduction through the shell materials. These are modeled explicitly. As in the Rail-Steel, conduction in the neutron shield region occurs in parallel through the radial connectors and the neutron shield material.

Heat transfer from the cross section of the direct loaded basket and overpack to the axial ends of the overpack is assumed to occur by conduction and radiation. Heat conduction occurs in parallel through each of the connecting materials that comprise the basket and overpack. The effective thermal properties are obtained in the same manner as in the Rail-Steel model. Radiation is assumed to occur between the end disks of the basket to the interior wall of the inner lid and bottom plate of the overpack.

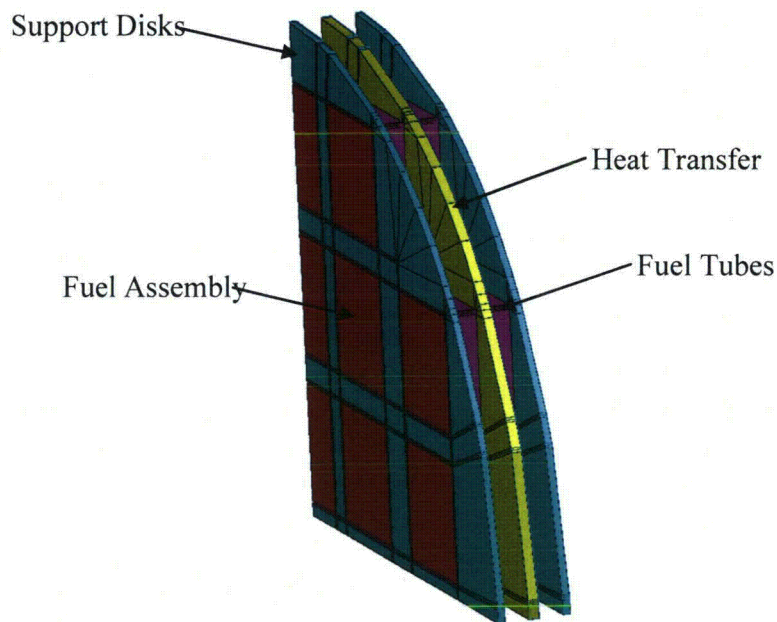


Figure IV-17. Three-dimension, quarter section of the directly loaded basket. The helium material is not shown.

The Rail-Pb system is also designed to maintain the temperature of critical components below their design limits during and after a 30 minute, fully engulfing, fire accident scenario. For longer period, fire accident scenarios a significant amount of heat may be transferred to the interior of the cask. As in the Rail-Steel, the temperature of the neutron shield is expected to reach temperatures beyond the temperature limits. Heat then is dissipated by conduction through the gas layer in the neutron shield and by radiation between the outer wall of the intermediate shell layer and the outer enclosure shell. Similarly, the lead shell is expected to melt since its melting point is around 321°C (611°F). The impact limiters are made of wood encased in a thin metal layer and are sealed to prevent moisture from deteriorating the wood over long periods of

time. Since the impact limiters are assumed to stay intact (i.e., with the content sealed) after the initial accident event (e.g., derailment), the wood is not expected to char significantly. Charring is therefore not taken into account in this model.

IV.4.3 Rail-Pb Materials and Thermal Properties

The Rail-Pb is made of stainless steel, lead, copper, aluminum, NS-4-FR, Boral neutron absorber and helium. The inner and outer shell, the outer enclosure shell, the bottom plate, the vacuum flange, and the inner lid of the overpack are made from stainless steel, type 304. The gamma shield is made from copper-lead, and the outer lid from stainless steel, type 630. The radial channels are made from a combination of stainless steel, type 304, copper, and a small section of carbon steel. The stainless steel in the channel serves as the main support component while the copper enhances conduction through the channels. The overpack neutron shield is made from NS-4-FR. The impact limiters are redwood and balsa layers encased in a thin steel shell.

In the fuel basket, the support disks, threaded rods, and spacer nuts are made from stainless steel, type 630, and the top and bottom support plates, short length cylinder, and fuel tubes from stainless steel, type 304. The heat transfer support disks are made from aluminum alloy 6061. As with the Rail-Steel, adjacent to each fuel tube wall is a layer of Boral sandwiched between the tube wall and a thin layer of stainless steel sheathing. The fuel rods are made from zircaloy or stainless steel cladding, but are assumed to be zircaloy as in the Rail-Steel analysis. The pellets are made from UO_2 . The empty gas space, which encompasses most of the volume inside the overpack cavity, is filled with helium.

Tables IV-10 through IV-13 provide the thermal conductivity, specific heat, density, and emissivity for those materials used in the Rail-Pb which are different from the Rail-Steel, or for which the properties are significantly different (see Table IV-2 through Table IV-5 for additional properties). The properties of NS-4-FR reported in the Rail-Pb SAR are marginally different from those reported for Holtite-A, as expected. The thermal conductivity of redwood and balsa vary depending on the direction of the grain. For balsa, temperature dependent data is not found; therefore, values from MSC Patran material database are used and compared well with values in Incropera and Dewitt (1996). The MSC Patran database references are given in Tables IV-10. NUREG-0361 (1978) gives values through and along the grain for redwood; however, since the Rail-Pb SAR does not specifically describe the arrangement of the wood layers in the limiters, average properties (along and through the grain) are assumed. The specific heat and density of copper-lead provided in the Rail-Pb SAR are slightly lower and higher, respectively, than for plain lead (Incropera and Dewitt, 1996); properties from MSC Patran database are used instead since data is readily available above the melting temperature and included the specific latent heat of fusion (23.9kJ/kg [10.3Btu/lbm]). The specific heat of lead increases up to the melting point (by a factor of 1.07), but then remains approximately the same. Since these changes are small, the value at 92°C is used throughout the rest of the temperature range.

Table IV-10. Thermal conductivities for the Rail-Pb materials.

Material	Thermal Conductivity W/m-°C (Btu/ft-hr-°F)				
	92°C (200°F)	226°C (450°F)	377°C (700°F)	477°C (900°F)	726°C (1340°F)
Aluminum 6061*	171 (98.8)	176	176		
Copper [§]	402 (232.4)	386	376	369	352
Balsa [¶]	0.050	—	—	—	—
Lead [‡]	33.9 (19.6)	29.3 (16.9)	16.7 (9.7)	15.3 (8.8)	14.7 (8.5)
Redwood [€]	3.6 (2.0)	5.5 (3.1)	—	—	—
Stainless Steel Type	17.5 (9.9)	18.3 (10.6)	20.7 (12.0)	24.6 (14.2)	—

*Nuclear Acceptance Corporation International, 2004

[§]Incropera and Dewitt, 1996

[¶]McAdams, 1954; Perry, 1963; Weast, 1966

[‡]Kelley, 1960; Schorsch, 1966; Weast, 1966

[€]NUREG-0361, 1978

Table IV-11. Specific heat for the Rail-Pb materials.

Material	Specific Heat J/kg-K (Btu/lbm-F)				
	92°C (200°F)	226°C (450°F)	377°C (700°F)	477°C (900°F)	726°C (1340°F)
Copper [§]	390 (0.093)	406 (0.097)	422 (0.101)	431 (0.103)	451 (0.108)
Balsa [¶]	2302 (0.55)	—	—	—	—
Lead [‡]	131 (0.031)	—	—	—	—
Redwood [€]	2386 (0.57)	3898 (0.93)	—	—	—

Table IV-12. Densities for the Rail-Pb materials.

Material	Density kg/m ³ (lbm/ft ³)				
	92°C (200°F)	226°C (450°F)	377°C (700°F)	477°C (900°F)	726°C (1340°F)
Aluminum	2823 (176)	—	—	—	—
Copper [§]	8933 (558)	—	—	—	—
Balsa [¶]	130 (8.1)	—	—	—	—
Lead [‡]	11350 (709)	—	—	—	—
Redwood [€]	352 (22)	—	—	—	—

Table IV-13. Emissivity for some of the Rail-Pb materials.

Material	Emissivity
Aluminum 6061	0.22
Stainless Steel Type 630	0.58

With the exception of the basket and neutron region, all components are modeled explicitly. The impact limiters are modeled in their intact state, with properties of redwood and balsa since the outer shell volume is significantly smaller than the total wood volume. Contact gap effects are assumed negligible. As in the Rail-Steel model, NS-4-FR is replaced with air when the former reached its temperature limit, but only in the neutron shield region of the overpack. Radiation is activated in this region by setting the emissivity to the appropriate value.

IV.4.3.1 Directly Fuel Loaded Basket

In the Rail-Pb SAR, fuel rods are evaluated to determine a representative fuel rod configuration. The fuel assembly is then modeled explicitly to obtain an equivalent in-plane thermal conductivity for the homogenized fuel assembly, as described in Section IV.3.3.1. The fuel assembly axial conductivity is next obtained with an area weighted average using the thermal conductivities of the individual components of the fuel rods and helium. The directly loaded basket is then included explicitly in the normal condition run, but is not included in the subsequent regulatory fire accident run. Instead, the maximum temperature difference between the fuel basket and the inner wall of the overpack calculated in the normal condition run is added to the inner wall temperature of the overpack calculated in the regulatory fire run to obtain an estimate of the temperature of the center of the fuel basket for the regulatory run. A different approach is used here.

The directly loaded fuel basket is replaced with a homogenized cylinder having equivalent effective thermal conductivities in the in-plane and axial directions. As described in Section IV.4.2, two variations of the same three-dimensional, quarter section, finite element model are generated. The first model included a support disk, a heat transfer disk, and the fuel tubes and helium space between the disks (see Figure IV-17). The second model did not include the heat transfer disk; instead, it is replaced with helium and the boundary conditions are modified to reflect this change.

The in-plane and axial thermal conductivity of the fuel basket are replaced with an equivalent thermal conductivities using the following four step procedure borrowed from the Rail-Steel SAR and modified here to address this particular model. First, the detail cross section of the fuel assembly is replaced with a homogenized fuel region having equivalent thermal properties. This analysis is done in the Rail-Pb SAR, as explained above, and the analysis results are included in this study. As expected, the thermal conductivity reported in the Rail-Pb SAR are close to those reported in Rail-Steel SAR for similar fuel assemblies, which served as a check. Second, the fuel

tube, Boral, and stainless steel sheathing are replaced with a homogenized wall having an equivalent thermal conductivity as described in the Rail-Pb SAR.

Third, the two, three-dimensional, quarter section models described above are used to obtain the in-plane and axial effective thermal conductivities. Both these models are evaluated with two sets of boundary conditions:

- (1) a uniform circumferential temperature applied across the circumferential wall of the model; adiabatic conditions over the axial ends; and uniform heat generation in the homogenized fuel assemblies; and
- (2) a uniform temperature over one axial end; a uniform heat flux over the other axial end; and adiabatic conditions over the circumference.

In the first case, the in-plane thermal conductivity is obtained using the same procedure described in Section IV.3.3.1. In the second case, the axial thermal conductivity is obtained using the standard relationship:

$$k_{eff} = \frac{qA}{L(T_q - T_t)}$$

Here A is the cross sectional area of the basket; L is the thickness across the modeled section; q is the uniform heat flux applied over one of the cross sectional area, axial ends; and T_t is the uniform temperature applied over the other cross sectional area, axial end. T_q is the average temperature where uniform heat flux is applied and is calculated using the simulation results. A second option is to apply constant temperatures at both axial ends of the basket, then calculate the total heat flow (qA) through the basket using the simulation results, and lastly calculate the effective axial conductivity using the above equation. To obtain temperature dependent thermal conductivities, this third step is repeated a number of times using a wide range of uniform circumferential temperatures and applied heat fluxes.

Fourth, the thermal conductivities obtained in the previous step are added using an equivalent thermal resistor network model to obtain in-plane and axial thermal conductivities, respectively, over the entire fuel basket.

Table IV-14 shows the thermal properties used for the basket. These properties are applied to the homogenized fuel-basket cylinder. The equivalent specific heat and density are obtained using a mass and volume weighted average, respectively, over the individual component properties. The volume of each component in the fuel basket (i.e., support disks, heat transfer disks, fuel tubes, etc.) is given in the Rail-Pb SAR.

Table IV-14. Effective thermal properties of the directly loaded fuel basket.

Effective Thermal Properties	92°C (200°F)	226°C (450°F)	377°C (700°F)	477°C (900°F)	726°C (1340°F)
Radial Thermal	3.2 (1.8)	3.8 (2.1)	4.3 (2.4)	5.0 (2.8)	5.9 (3.4)
Axial Thermal Conductivity	2.4 (1.4)	3.2 (1.8)	3.8 (2.1)	4.5 (2.6)	5.8 (3.3)
Specific Heat	332 (0.079)				
Density	2450 (153)				

IV.4.3.2 Neutron Shield Region

The neutron shield region is model using the same approach used in the SARs (Nuclear Acceptance Corporation International, 2004, Holtec International, 2004). Both reports used the thermal resistor network method to obtain the in-plane and axial effective thermal conductivities (see Section IV.3.3.4). In the case of the Rail-Pb, there are fewer radial channels than in the Rail-Steel; however, as will be demonstrated shortly, this shortcoming is compensated by adding copper in the neutron shield region. Table IV-15 shows the thermal properties used for the neutron shield region in the Rail-Pb. The circumferential thermal conductivity is assumed to be that of NS-4-FR. As before, the specific heat and density are obtained from a mass and area weighted average. Note the thermal conductivity is slightly higher than in the Rail-Steel even though the Rail-Pb contains fewer channels. This is expected since the neutron shield in the Rail-Pb contains copper which has a much higher thermal conductivity than carbon steel.

IV.4.4 Rail-Pb P-Thermal Finite Element Model

The following description is short since most of the details are similar to the Rail-Steel analysis described in Section IV.3.4. In the Rail-Pb runs, the cask model had 109662 elements (see Figure IV-18); this corresponds to a nominal element size of 10.2cm (4in). The element count is less than in the Rail-Steel since the Rail-Pb is smaller and has fewer features which add to the element count. A mesh refinement study is also conducted with the Rail-Pb model with a similar outcome. The boundary conditions for the normal condition, steady-state run, the regulatory uniform heating run, and the CAFE fire runs are the same as discussed in Sections IV.2 and IV.3.4. They are not repeated here.

IV.4.5 Rail-Pb Thermal Analysis Results

The following figures (see pages 53 through 61) show additional results for the Rail-Pb not provided in Chapter 4. Figure IV-19 shows results for the regulatory uniform heating case. Recall this is a P-Thermal only run. Figure IV-20 shows results for the regulatory CAFE fire; Figure IV-21 shows results for the fully engulfing CAFE fire run with the cask on the ground; and Figures IV-22 and IV-23 show results for the CAFE fire runs with the cask on the ground and outside the pool area. As with the Rail-Steel, the last three cases are run for a total of three hours. A discussion of these results and their implications is provided in Chapter 4.

Table IV-15. Effective thermal conductivities for the neutron shield region of the Rail-Pb.

Effective Thermal Properties	92°C (200°F)	226°C (450°F)	377°C (700°F)	477°C (900°F)	726°C (1340°F)
In-Plane Thermal Conductivity W/m-°C	8.1 (4.6)	7.9 (4.5)	7.7 (4.4)	7.7 (4.4)	7.4 (4.2)
Axial Thermal Conductivity W/m-°C (Btu/ft-hr-°F)	7.6 (4.3)	7.3 (4.2)	7.3 (4.2)	7.2 (4.1)	6.9 (3.9)
Specific Heat J/kg-°C (Btu/lbm-°F)	1406 (0.33)	535 (0.12)	563 (0.13)	575 (0.13)	611 (0.14)
Density kg/m ³ (lbm/ft ³)	1983	380 (23)			

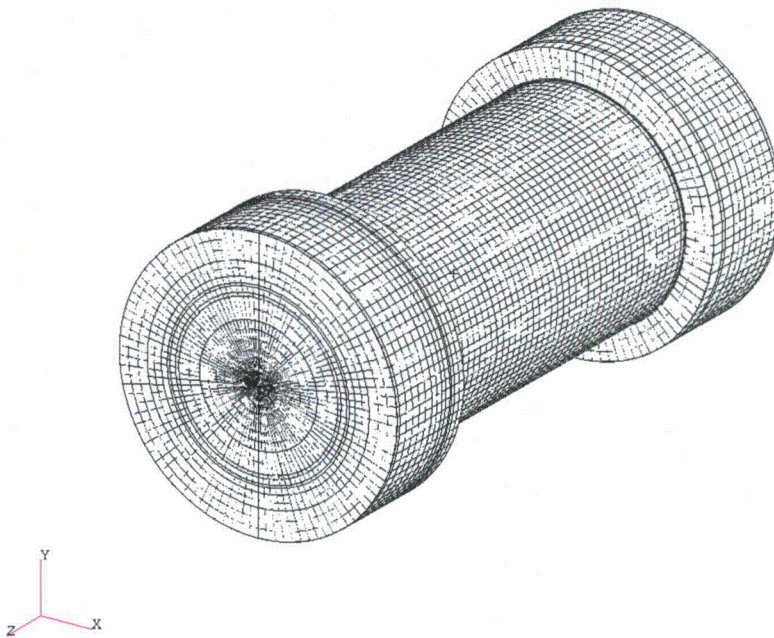


Figure IV-18. The Rail-Pb mesh.

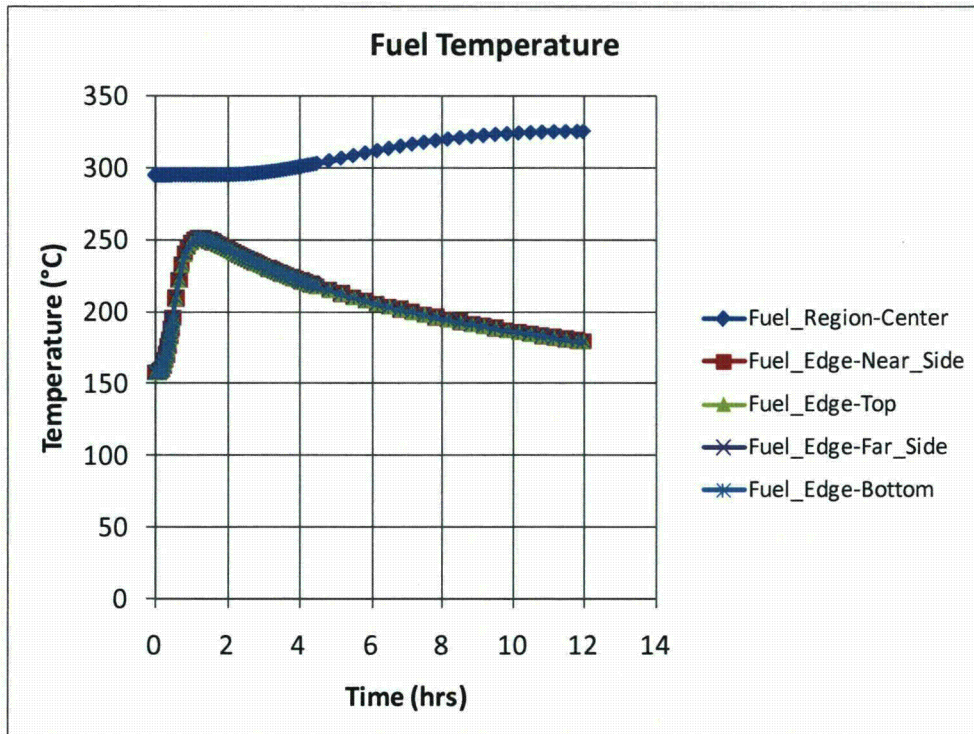
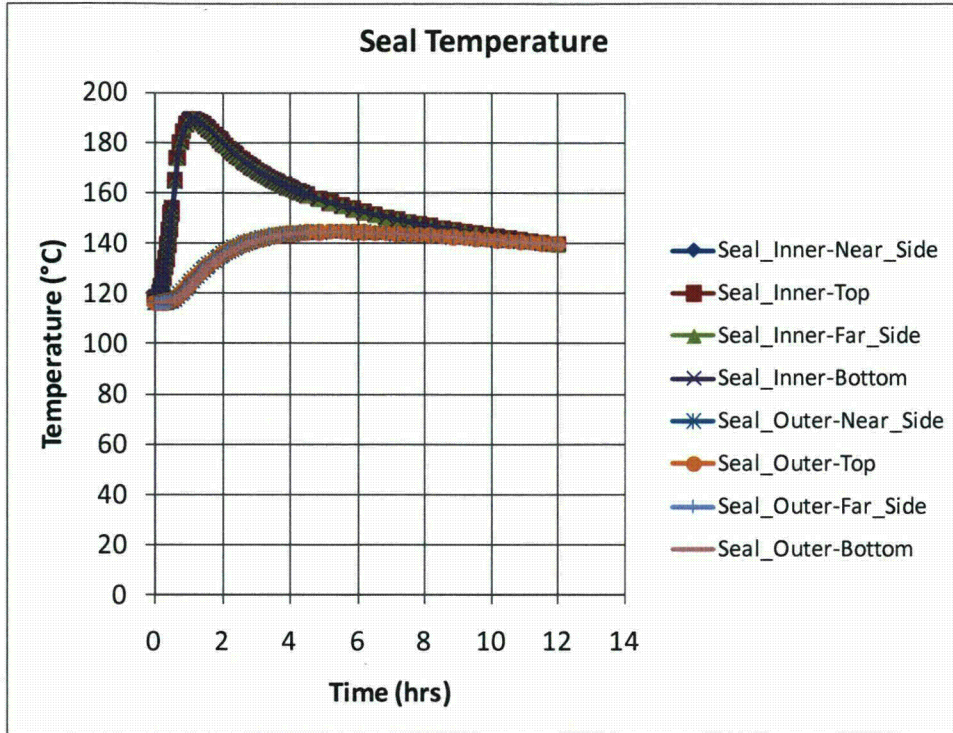


Figure IV-19. Rail-Pb Regulatory Uniform Heating Results

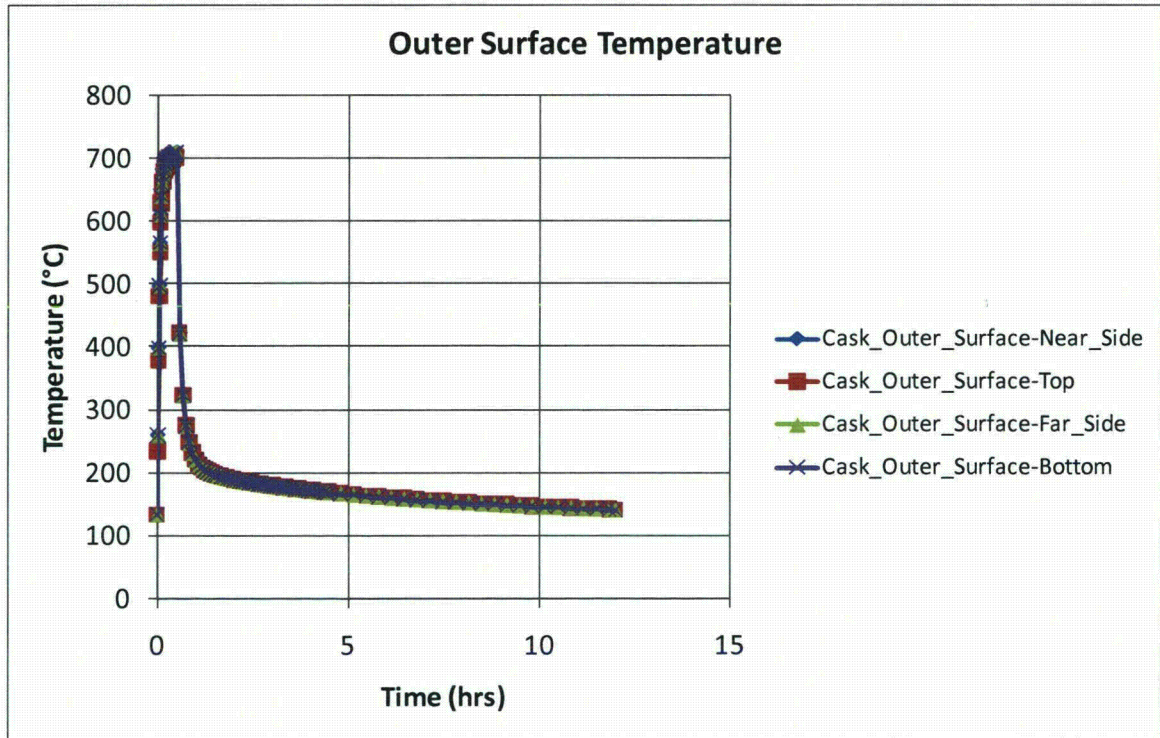
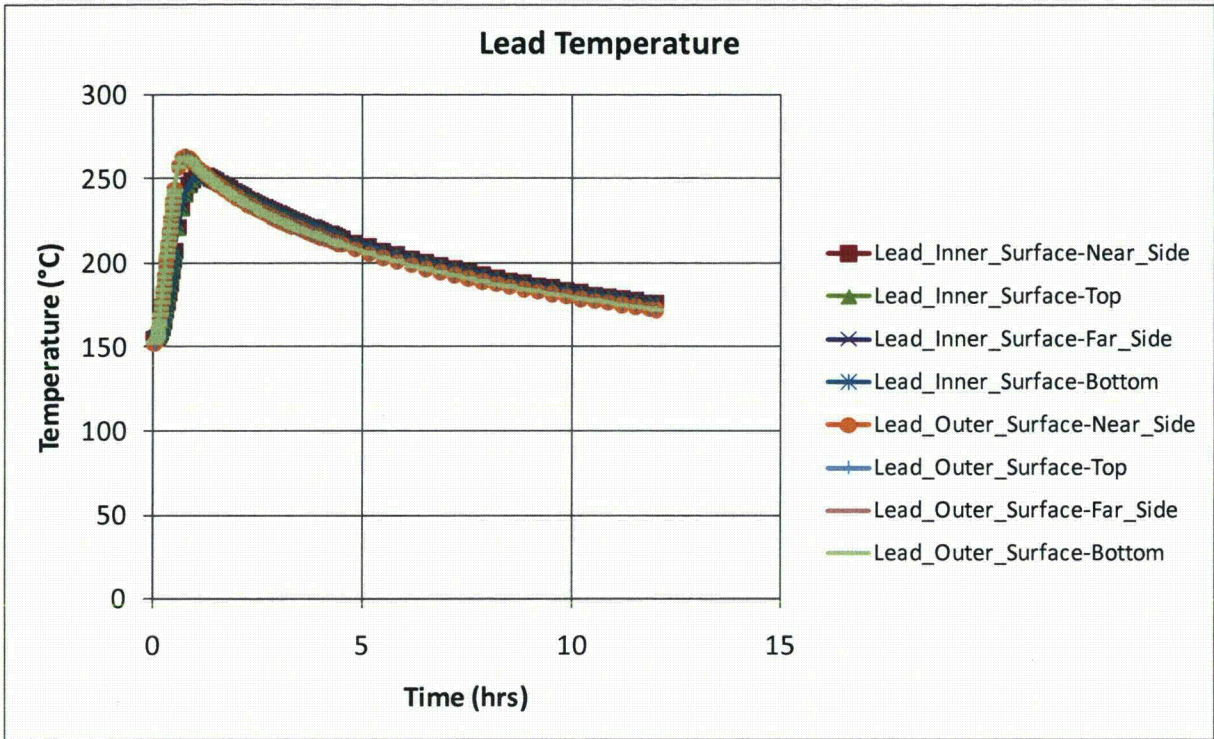


Figure IV-19. Rail-Pb Regulatory Uniform Heating Results - Continue

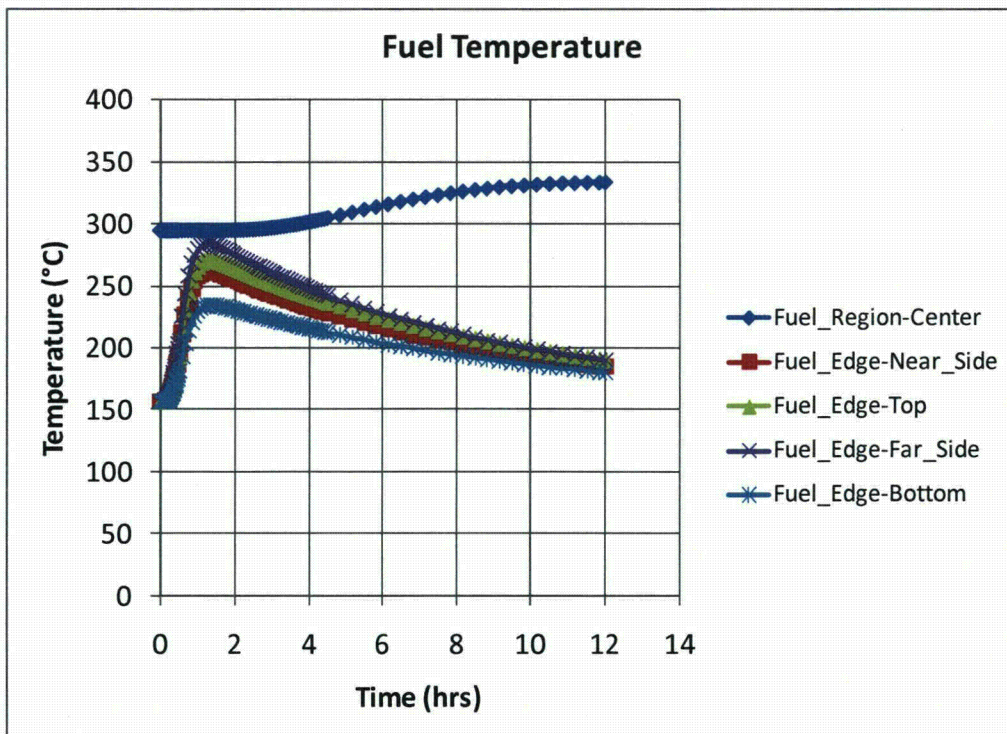
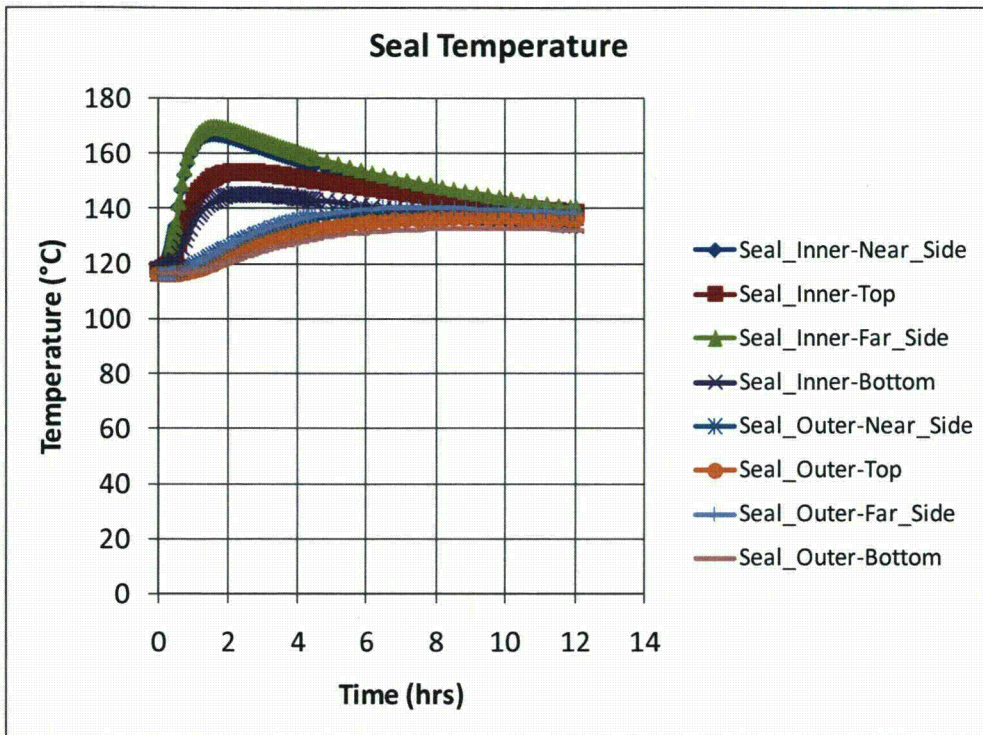


Figure IV-20. Rail-Pb CAFE Regulatory Fire

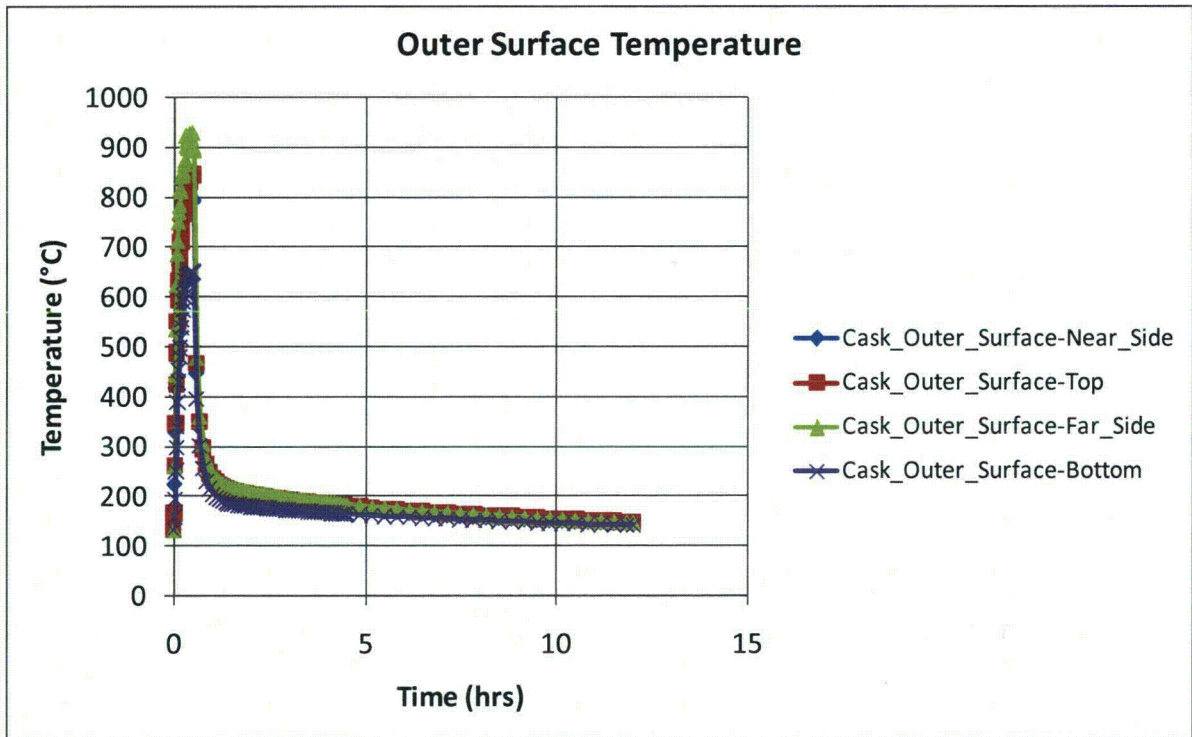
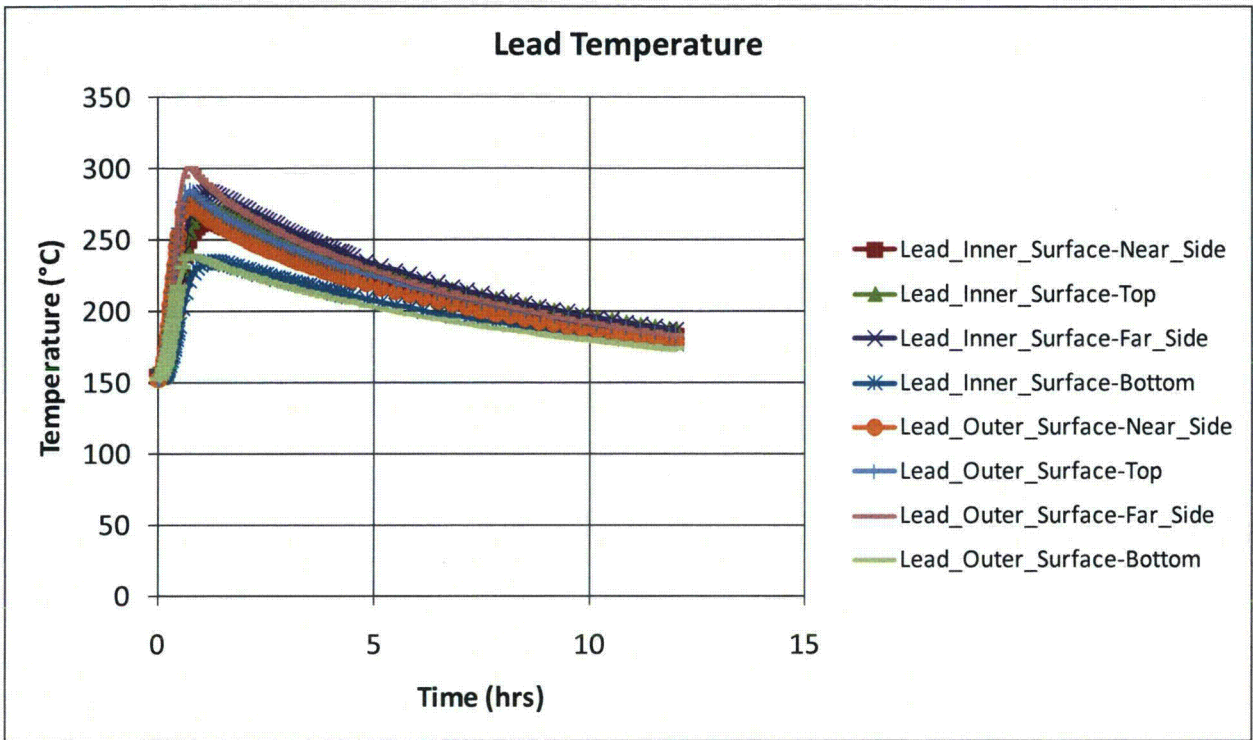


Figure IV-20. Rail-Pb CAFE Regulatory Fire - Continue

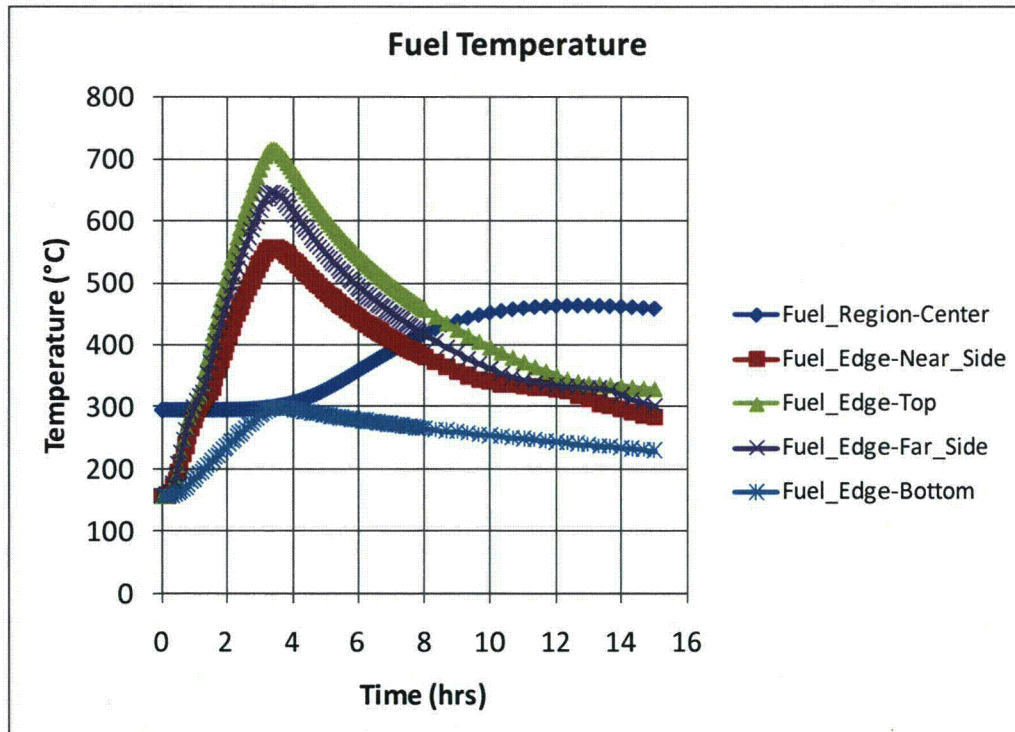
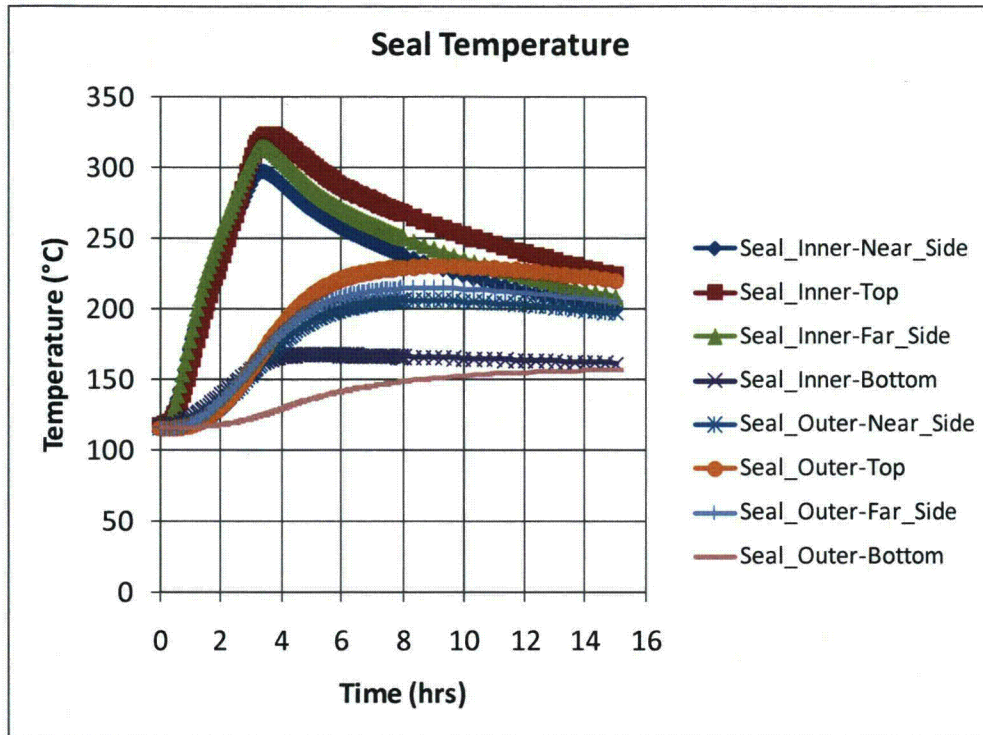


Figure IV-21. Rail-Pb cask on ground at the pool center.

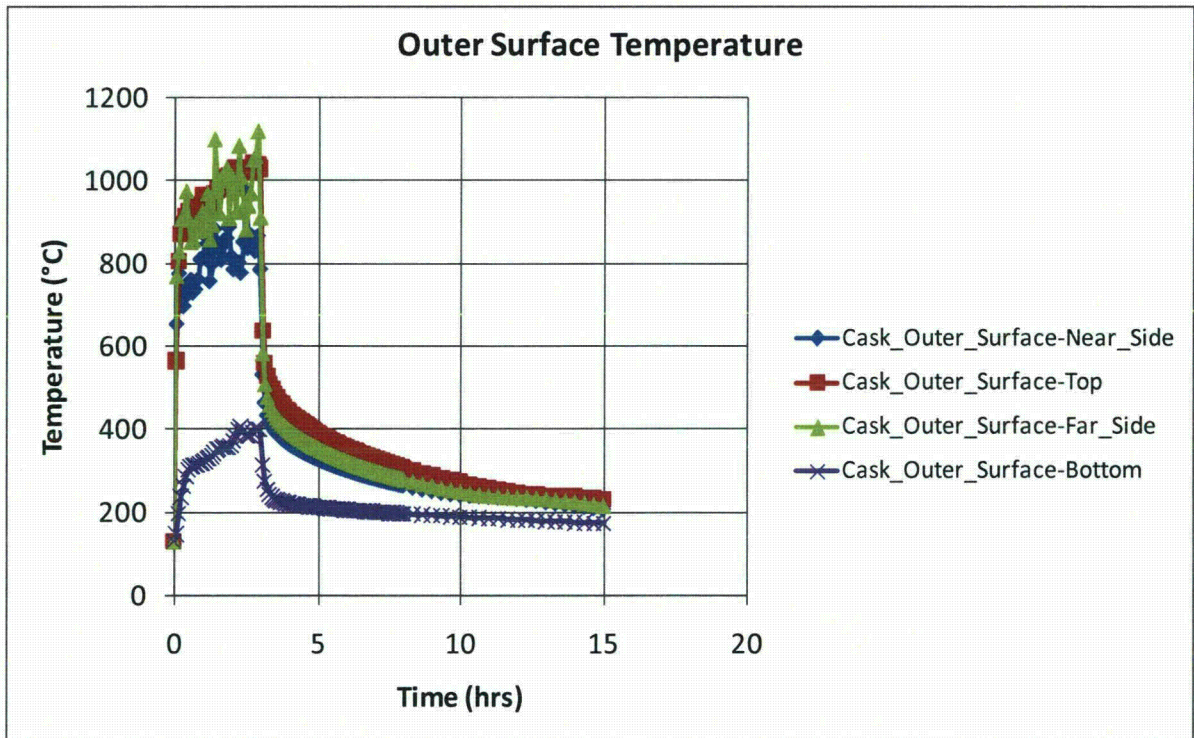
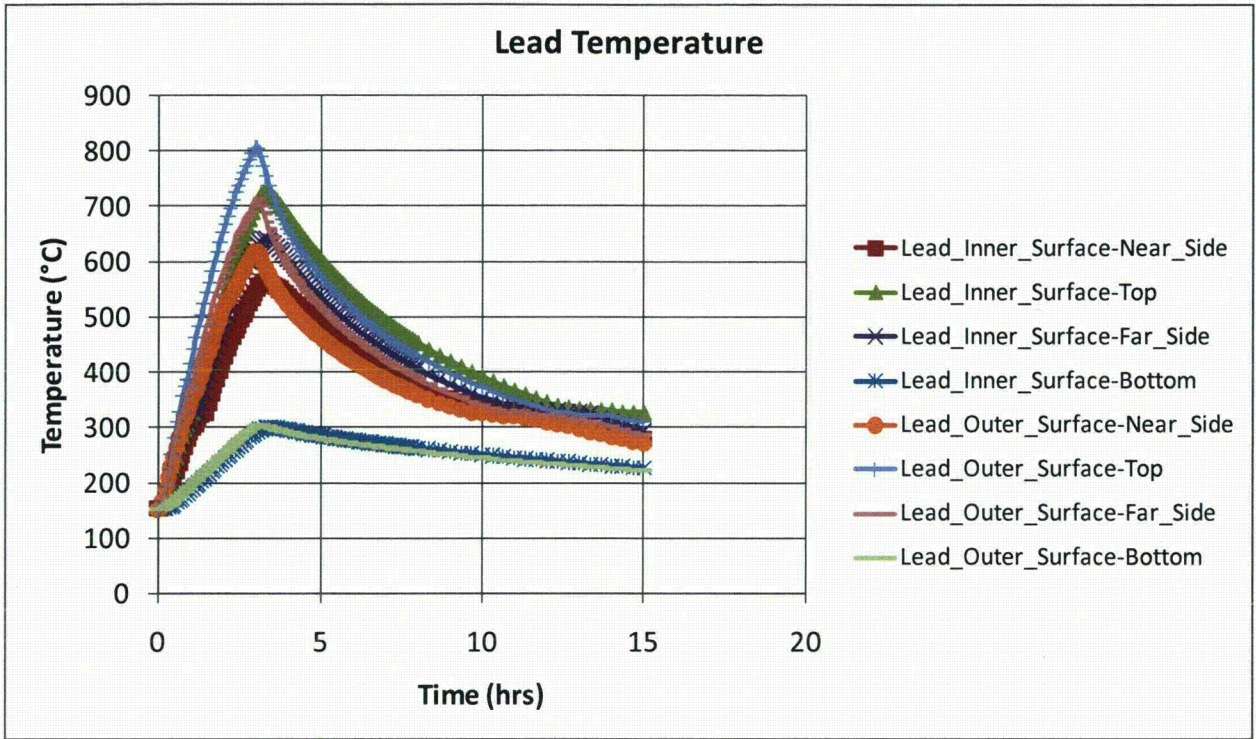


Figure IV-21. Rail-Pb cask on ground at the pool center. - Continue

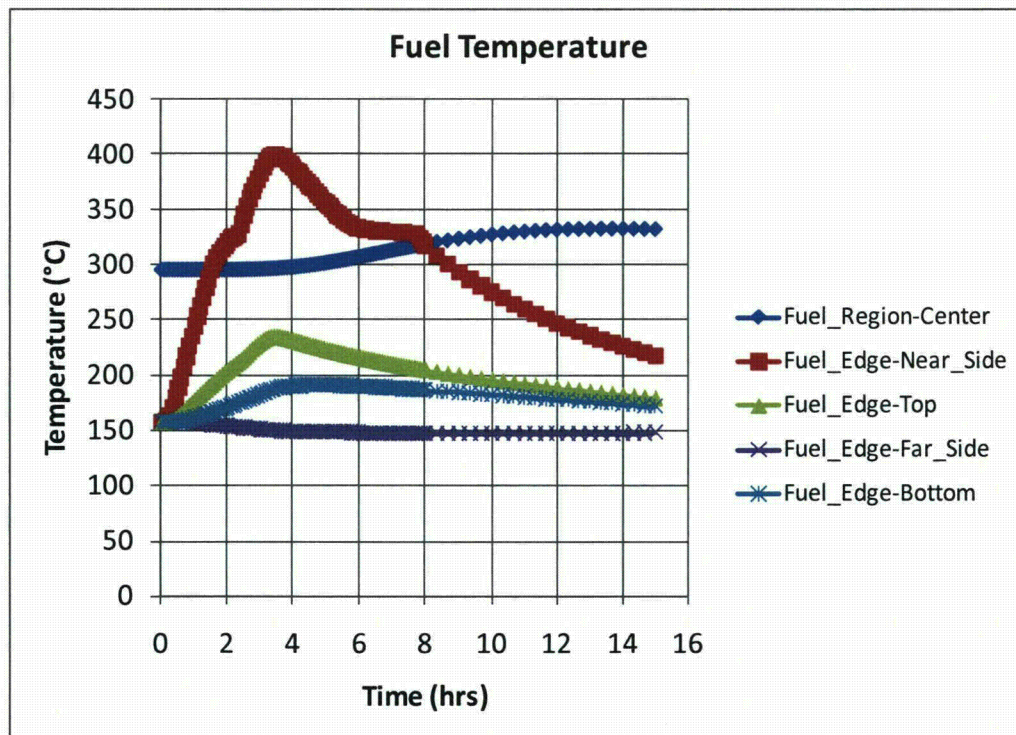
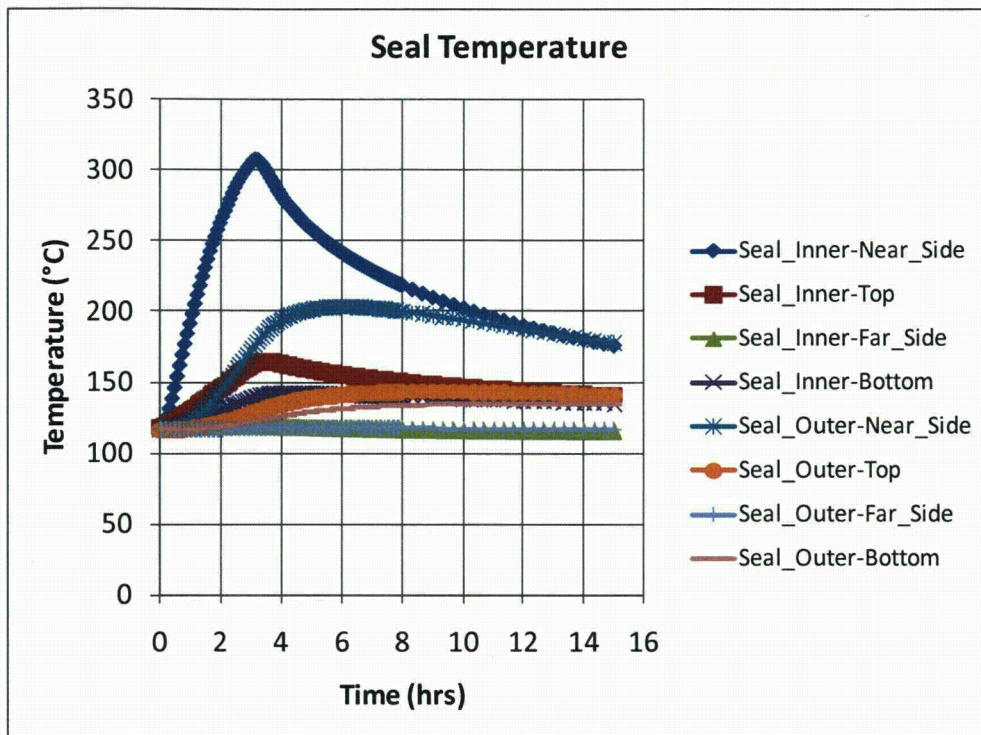


Figure IV-22. Rail-Pb cask on ground 3.0m (10ft) from the edge of the pool.

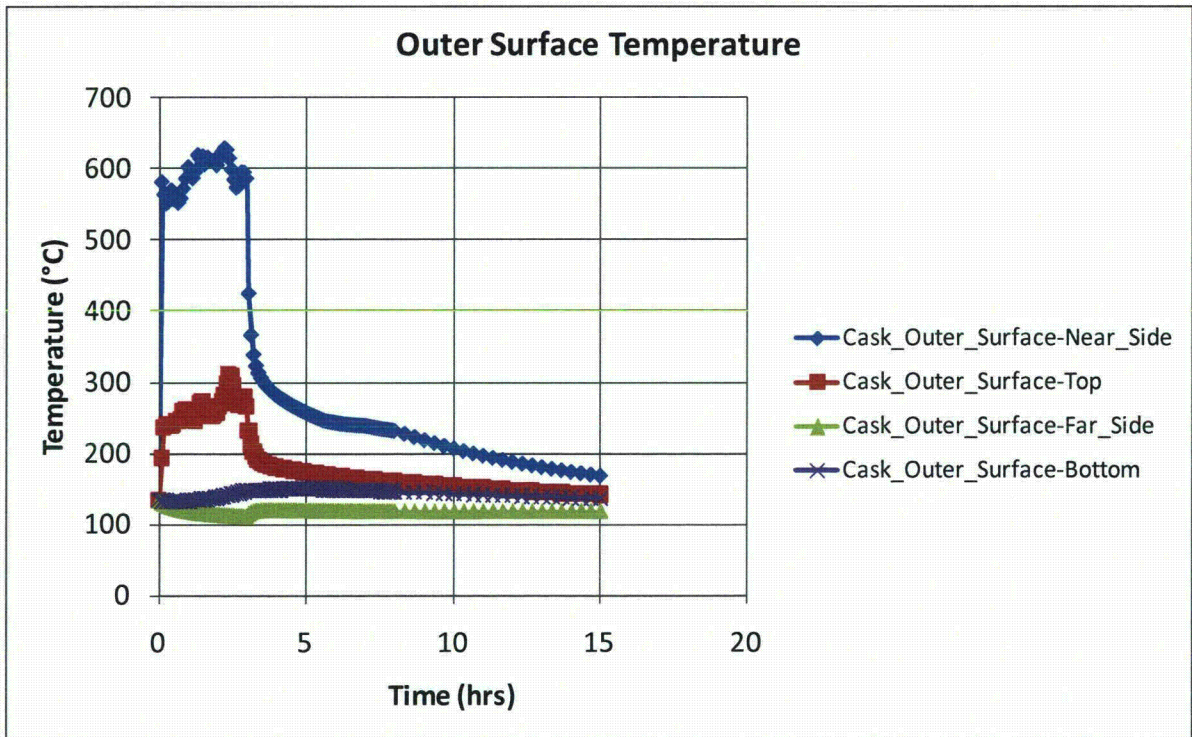
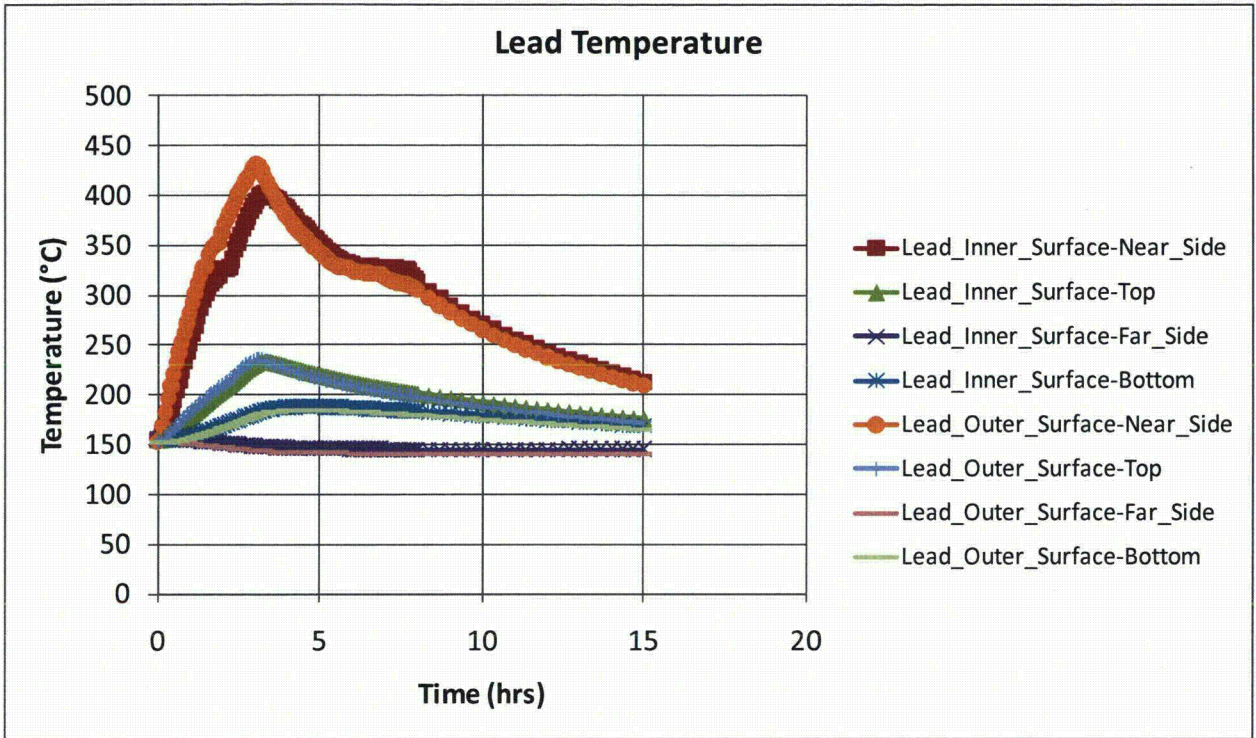


Figure IV-22. Rail-Pb cask on ground 3.0m (10ft) from the edge of the pool. - Continue

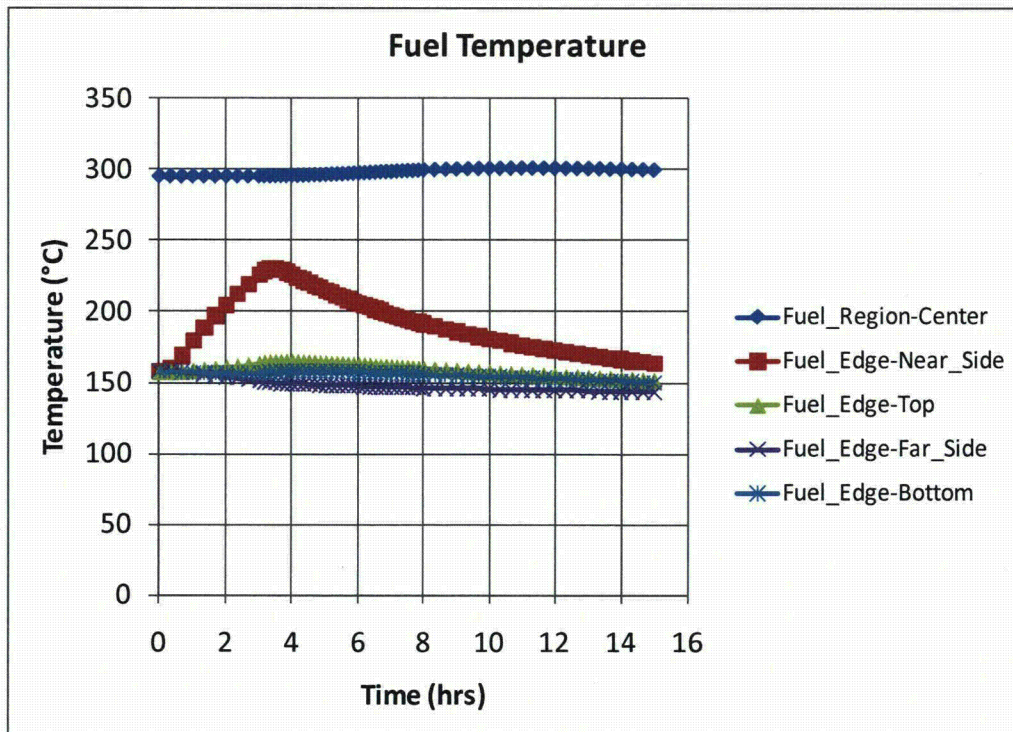
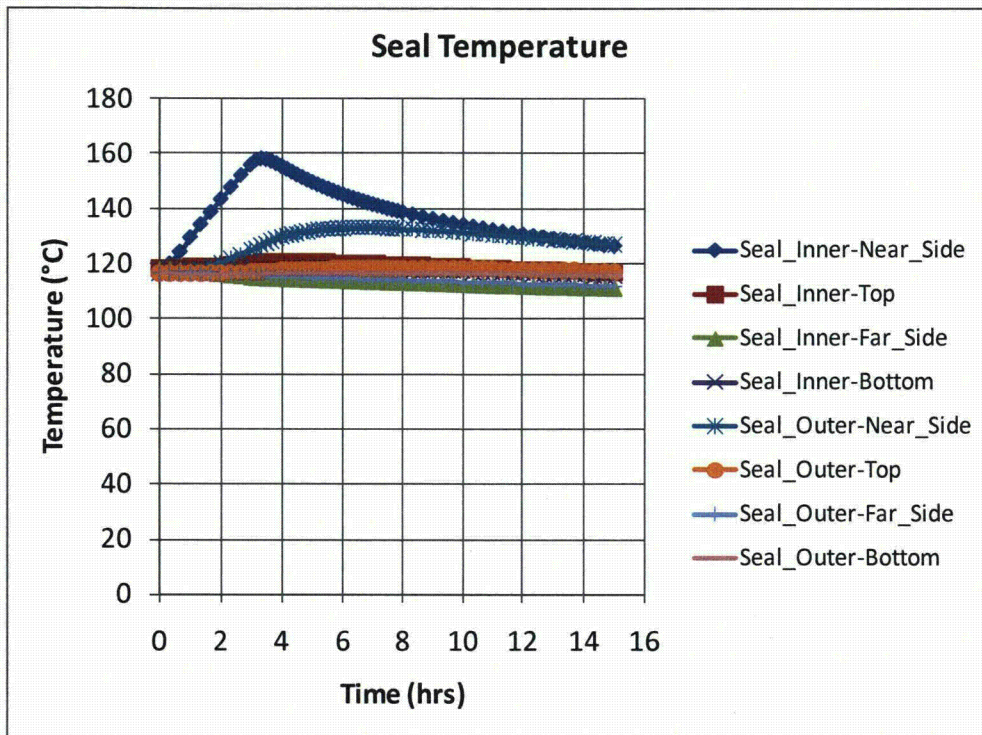


Figure IV-23. Rail-Pb cask on ground 18.3m (60ft) from the edge of the pool.

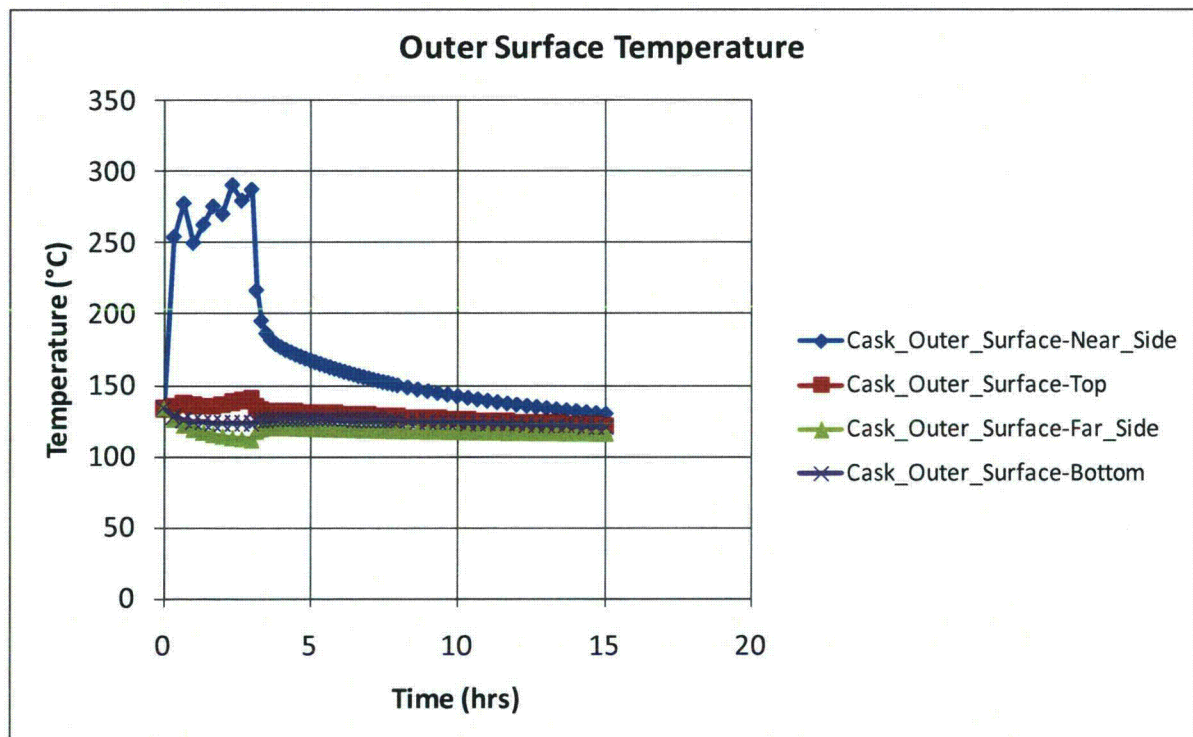
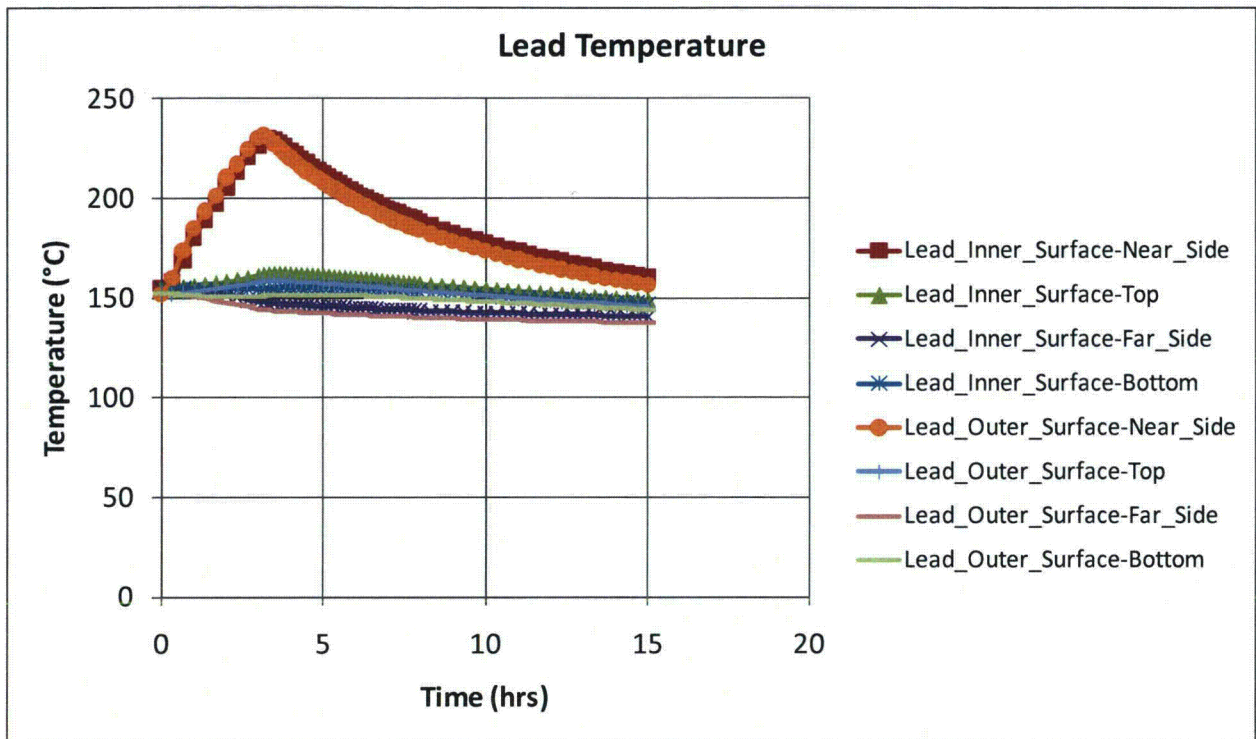


Figure IV-23. Rail-Pb cask on ground 18.3m (60ft) from the edge of the pool. - Continue

IV.5 CAFE Benchmark

Large, fully-engulfed objects have a great impact on the surrounding fire environment. To adequately predict incident heat flux to casks, computational fluid dynamics models must be employed with appropriate boundary conditions. Also, because of the impact that massive objects have on fires, computational fluid dynamics models must be validated against experimental data from test that have similar size objects (Nicolette and Larson, 1989).

Since the development of the CAFE code (del Valle, et. al., 2009; del Valle, 2007; Are et.al., 2005; Lopez et. al., 2003), there has been a continuing effort to benchmark and fine-tune this fire model by making use of relevant empirical data from experiments. Continuing with this effort, prior to running the cases described in Chapter 4, CAFE is benchmarked against experimental data obtained from two fire test series conducted at Sandia National Laboratory Lurance Canyon Burn Site: (1) one using a large calorimeter in the center of the pool (Greiner, 2009; Kramer, 2008), and (2) the other using a smaller diameter calorimeter adjacent to the fire (Lopez et. al., 2003). The large calorimeter is close to the size of the casks analyzed in this study, and had a test setup and conditions that closely matched the regulatory hypothetical fire accident scenario outlined in 10CFR71.73 for certification of nuclear spent fuel transportation packages. The smaller diameter calorimeter test is used to benchmark CAFE's ability to predict heat flux to objects outside the fire plume. This section briefly describes these experiments, and shows benchmark results.

IV.5.1.1 Large Calorimeter Test and Benchmark Results

The large calorimeter is a carbon steel cylindrical pipe approximately 2.43m (96in) in diameter and 4.6m (180in) in length, with nominal 2.54cm (1in) thick walls, and had bolted lids on each end (see Figure IV-24a). The calorimeter is placed on two stands at the center of a 7.93m (26ft) diameter fuel pool. The stands maintained the calorimeter 1m (39.4in) above the fuel surface. Approximately 2000 gallons of JP8 are used per test. Total burn time vary with tests, but is at least 25 minutes. All tests are conducted in relatively low wind conditions (<5m/s) to assure the calorimeter is fully or partially engulfed (see Figure IV-24b.)

Thermocouples are installed on the interior walls of the calorimeter to measure interior surface temperatures. All TCs are installed in a ring configuration as shown in Figure IV-25. Heat flux gages are placed just outside the round walls of the calorimeter in a ring configuration and outside the lids to measure incident heat fluxes close to the outer walls of the calorimeter. Fuel burn rates are measured using a TC rake. Directional flow probes are installed just outside of the calorimeter walls to measure the flow speed of hot gases near the calorimeter walls. Finally, ultrasonic sensors placed on four towers—two sensor towers aligned with the calorimeter lids and two sensor towers perpendicular to the cylindrical section of the calorimeter, but on opposite sides—are used to measure wind speed and wind direction. Each tower is approximately 24.4m (80ft) from the center of the pool and had three ultrasonic sensors 2, 8 and 10m (6.5, 26.2, and 32.8ft) from the ground.



(a)



(b)

Figure IV-24. Large calorimeter fire test: (a) test setup and (b) fire fully engulfing the calorimeter.

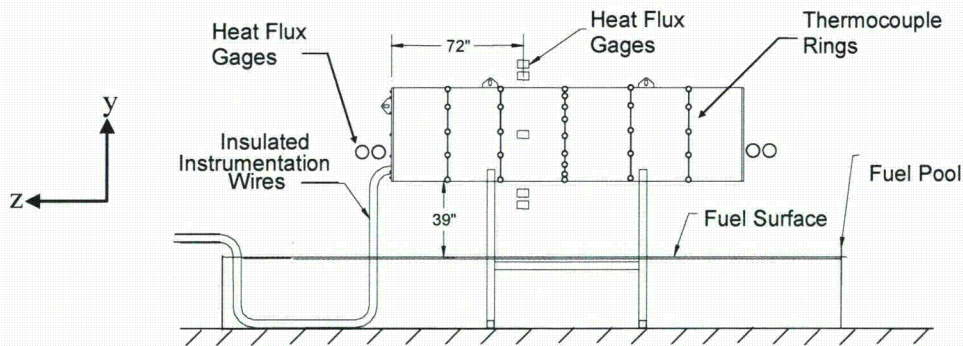


Figure IV-25. Side view (looking from the north) of calorimeter and test setup. Note: the calorimeter is centered with the pool. This drawing is not to scale.

Figure IV-26a shows average temperatures along the four circumferential sides of the calorimeter obtained from Test 1 and from the CAFE benchmark run. Data from Test 1 is chosen because the wind conditions and fire characteristics of this test best matched the regulatory conditions specified in 10CFR71.73 and the fire scenarios analyzed in this study. The test readings are taken from thermocouples located at 0 (north side, i.e., pointing out of the page), 90 (top side), 180 (south side, i.e., pointing into the page) and 270 (underneath) degrees. This plot illustrates that average temperature predictions obtained from CAFE envelope the average temperatures readings from the test. From this perspective, however, CAFE over predicts temperatures underneath and on the south side of the calorimeter, and under predicts temperatures on the top of the calorimeter. Figure IV-26b shows a plot of average temperatures over each thermocouple ring starting from the left side of the calorimeter and moving along the negative z-axis as shown in Figure IV-25. From this perspective CAFE predicts the average

temperatures over the rings reasonably well.

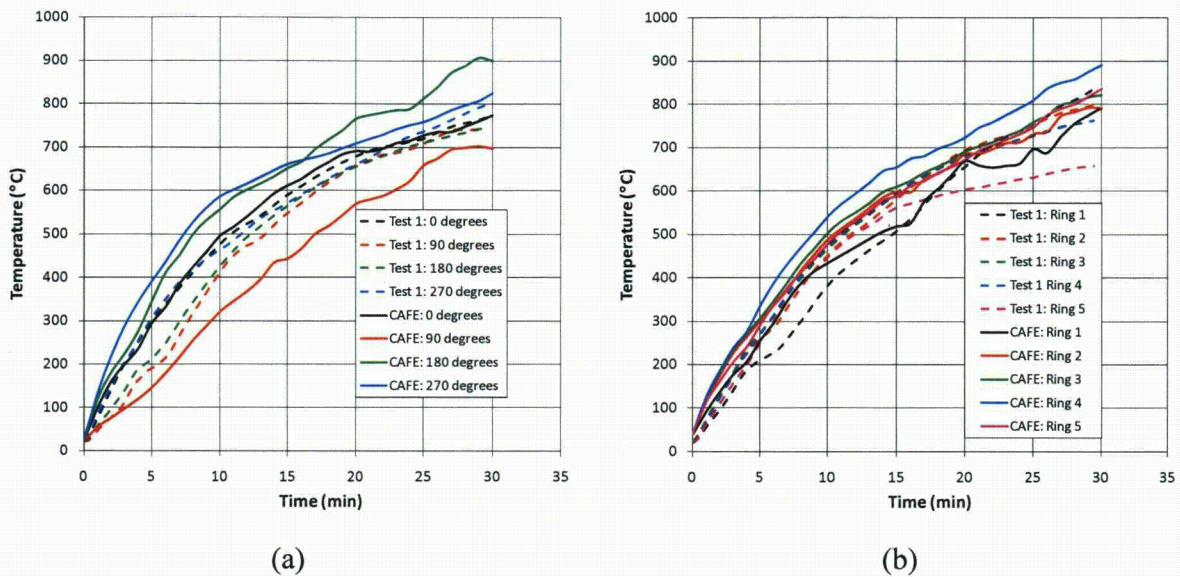


Figure IV-26. CAFE benchmark results using fully engulfed large calorimeter: (a) temperatures average along the 0, 90, 180, and 270 degree side looking at the calorimeter from the negative z-direction, and (b) temperatures averaged over each ring starting from Ring 1 located on the positive side of the z-axis.

Closer inspection of the temperatures histories obtained from CAFE at each of the nodes corresponding to thermocouple locations revealed excellent agreement with test data over most of the cask, except at locations where the wind effects are strongest, the last two rings to the right of Figure IV-25 at 90 (top side), 180 (south side) and 270 (underneath) degrees. Temperatures at 180 and 270 degrees are higher than expected, while temperatures at 90 degrees are under predicted. Differences rapidly diminished going from the rings on the right side of the calorimeter to the rings on the left side as shown in Figure IV-25. Part of the reason for these discrepancies is the way in which the wind boundary conditions are applied in the computational fluid dynamics model. In the large calorimeter test series, wind speeds are obtained only at four locations around the pool, and at three heights. These height dependent data are applied uniformly over the corresponding cross sections of the domain, which does not necessarily reflect the actual conditions in the test. This leads to wind speeds being higher than expected in some locations around the casks such as the south side of the cask near the ring 5 (rightmost ring in Figure IV-25).

IV.5.1.2 Small Calorimeter Test and Benchmark Results

Experimental data from a smaller pipe calorimeter is used to benchmark the view factor method used in CAFE (Lopez et al., 2003). The CAFE model for thermal radiation transport within and near large hydrocarbon fires is divided into two types, diffusive radiation inside the flame zone

and clear air or view factor radiation outside the flame zone. Outside the flame zone, thermal radiation transport is modeled by the clear air or view factor method. The calculation of the view factor between the fire and an adjacent object is complicated due to the fact that the outer surface of a fire (or smoky region) is dynamically changing due to the puffing and turbulent nature of flames (Lopez et. al., 2003).

In the experiments, a calorimeter is positioned such that its axis is 1.5m (4.9ft) away from the center of the fuel pool. The wind blew the fire away from the calorimeter leaving a significantly larger gap between the pipe calorimeter and the plume. Results from tests and CAFE are presented in Figure IV-27. The temperatures shown are at the center ring of this calorimeter. The blue lines are obtained from experimental data and the black lines are obtained from CAFE. By looking at the temperature distribution of this very long pipe, it can be clearly seen how the external radiation algorithm worked on the far field object.

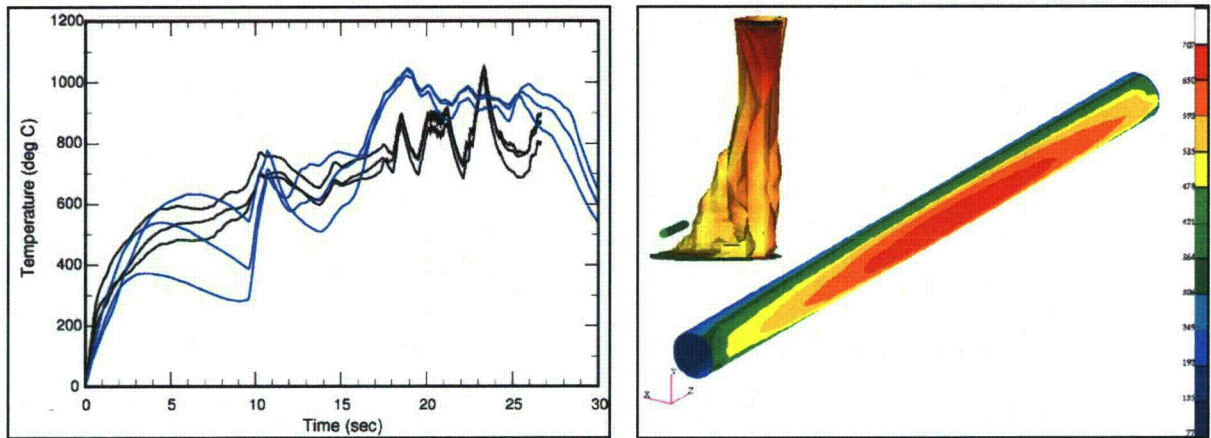


Figure IV-27. CAFE benchmark results using a small calorimeter 1.5m (4.9ft) from the edge of the fire.

APPENDIX V
DETAILS OF TRANSPORTATION ACCIDENTS

TABLE OF CONTENTS

V.1 Types of Accidents and Incidents.....	393
V.2 Accident probabilities.....	393
V.2.1 Historic accident frequencies	393
V.2.2 Development of Conditional Accident Probabilities.....	394
V.3. Accident Risks and Consequences	397
V.3.1 Loss of lead gamma shielding	397
V.3.1.2 Loss of lead shielding with fire	407
V.4 Release of Radioactive Materials in Accidents	411
V.4.1 Spent Fuel Inventory	411

List of Figures

Figure V-1 Event tree for highway accidents (from Mills, et al, 2006).....	395
Figure V-2 . Rail accident event tree (after Volpe, 2006).....	396
Figure V-3. The RADTRAN Loss-of Shielding 2-D Model (O'Donnell, et al, 2005).....	397
Figure V- 4. Dose to the MEI at various distances one to five meters from the cask.....	399
Figure V- 5. Dose to the MEI at various distances 10 to 100 m from the cask.	400
Figure V-6. Event tree branch for a rail fire accident (from Volpe, 2006, Figure 16).....	408

List of Tables

Table V-1. Truck and railcar accidents per km, 1991 through 2007.....	394
Table V-2. Parameters of lead shield slumping from impact.....	398
Table V-3. Fractions of lead shielding lost and conditional probabilities.....	399
Table V-4. Radiation dose (Sv) to the MEI at various distances for the cask. The numbers in bold italics exceed the external dose rate of 10 CFR 71.51..	401
Table V-5. The “conditional dose risk,” the product of dose and conditional probability, in Sv to the maximally exposed individual at distances from the cask from one to five meters.	402
Table V-6. The “conditional dose risk,” the product of dose and conditional probability, in Sv to the maximally exposed individual at distances 10 to 100 meters from the cask.....	403
Table V-7. Collective conditional dose risks in person-Sv in a semicircular area of radius 100 meters around the cask.	404
Table V-8. Average railcar accident frequencies on the routes studied.	405
Table V-9. Conditional collective dose risks (person-Sv) from loss of lead shielding, including conditional probabilities	406
Table V-10. Radiation dose (Sv) to the maximally exposed individual at various distances from a cask that has been in a fire.	407
Table V-11. Events leading to a train fire that could involve a spent fuel cask.....	409
Table V-12. Some parameters used in calculating loss of neutron shielding.....	410
Table V-13. Doses to an emergency responder five meters from the cask.	410
Table V-14. Collective doses (consequences) in person-Sv from loss of neutron shielding. .	410
Table V-16. TBq inventory for the Rail-Pb cask. The ⁶⁰ Co inventory is estimated CRUD. .	412
Table V-17. Parameters for determining release functions for the accidents that would result in release of radioactive material.....	417
Table V-18. Maximally exposed individual doses (consequences) in Sv from accidents that involve a release.	418
Table V-19 Maximally exposed individual conditional dose risks in Sv from accidents that involve a release.	418
Table V-20. Collective conditional inhalation and external dose risks for the 16 routes analyzed.....	419
Table V-21. Total collective dose risks (person-Sv) for each route.....	419

APPENDIX V

DETAILS OF TRANSPORTATION ACCIDENTS

V.1 Types of Accidents and Incidents

Four different types of events can interfere with routine transportation of spent nuclear fuel:

- A minor traffic accident (“fender-bender,” flat tire), resulting in minor damage to the vehicle. These are usually called “incidents.”¹
- An accident which damages the vehicle and or trailer and cask severely enough that the vehicle cannot move from the scene of the accident under its own power, but the accident does not result in any release of radioactive material. This accident type includes train derailments..
- Accidents in which there loss of lead gamma shielding but no release of radioactive material.
- Accidents in which there is a release of radioactive material.

In this analysis the first two types are considered together, since neither type involves a release of radioactive material. The NAC-STC is the only cask studies that uses a lead gamma shield, and is therefore the only cask that could be involved in an accident causing a loss of lead gamma shielding. The shielding could thin or develop a gap in an accident. The HISTAR-100 rail cask is a monolithic steel cask and is loaded with canistered fuel, so that even in an accident there would be no release of radioactive material. Chapter 3 and Appendix III discuss the accident behavior of the GA-4 truck cask, which uses a depleted uranium (DU) gamma shield, and conclude that the GA-4 will not release radioactive material in any achievable accident. Accidents that involve the HISTAR-100 and the GA-4 are limited to “no-release” accidents, discussed in Chapter 5. The NAC-STC could either lose lead shielding or release radioactive material in an accident, and is the only cask of the three whose behavior is discussed in this appendix.

V.2 Accident probabilities

V.2.1 Historic accident frequencies

The probability that a traffic accident happens is based on historic accident frequencies. These have been developed and the statistics validated by the Department of Transportation (DOT). Table V-1 shows truck and railcar accidents from 1991 through 1997 (DOT, 2008). Average accident frequencies for this period are:

¹ In Department of Transportation parlance, an “accident” is an event that results in a death, an injury, or enough damage to the vehicle that it cannot move under its own power. All other events that result in non-routine transportation are called “incidents.” This document uses the term “accident” for both accidents and incidents.

- $1.87 \times 10^{-6}/\text{km}$ for large trucks on interstates and primary highways.
- $1.08 \times 10^{-7}/\text{railcar km}$ for freight rail

Accident frequencies decreased 33.5 percent for trucks and 53.8 percent for railcars between 1991 and 2007. The average is used in this document because there are annual fluctuations. The accident frequency trends are shown in Figure 5.2 in Chapter 5.

Table V-1. Truck and railcar accidents per km, 1991 through 2007.

YEAR	TRUCK ACCIDENTS/KM	ACCIDENTS PER RAILCAR/KM
1991	2.39×10^{-6}	2.08×10^{-7}
1992	1.99×10^{-6}	1.91×10^{-7}
1993	2.19×10^{-6}	1.68×10^{-7}
1994	2.19×10^{-6}	1.64×10^{-7}
1995	2.39×10^{-6}	1.53×10^{-7}
1996	1.90×10^{-6}	1.39×10^{-7}
1997	1.89×10^{-6}	1.32×10^{-7}
1998	2.04×10^{-6}	1.19×10^{-7}
1999	1.84×10^{-6}	1.12×10^{-7}
2000	2.08×10^{-6}	1.12×10^{-7}
2001	1.99×10^{-6}	1.18×10^{-7}
2002	1.83×10^{-6}	1.12×10^{-7}
2003	1.85×10^{-6}	1.02×10^{-7}
2004	1.90×10^{-6}	1.00×10^{-7}
2005	1.73×10^{-6}	1.06×10^{-7}
2006	1.83×10^{-6}	1.04×10^{-7}
2007	1.59×10^{-6}	9.60×10^{-8}

V.2.2 Development of Conditional Accident Probabilities

Each specific accident scenario is described by a conditional probability (“conditional” on an accident happening). Conditional probabilities are derived from event trees, as described below.

V.2.2.1 Conditional probabilities of truck accidents

A transportation accident scenario can be disaggregated into a series of events. The conditional probability of a particular event in the scenario is best illustrated with an event tree: a diagram that includes all possible accident scenarios. Each branch of the tree is the series of events that comprise a particular accident scenario. The conditional probability is the product of the probabilities along a particular branch.

Figure V-1 is an event trees for truck accidents (Mills, et al, 2006). Calculation of the conditional probability of a truck in a collision on a bridge, then falling from the bridge onto a rocky embankment, is illustrative.

$$P_{\text{conditional}} = P_{\text{collision}} * P_{\text{bridge accident}} * P_{\text{fall off bridge}} * P_{\text{rocky soil}}$$

$$P_{\text{conditional}} = (0.054) * (0.064) * (0.02) * (0.046) = 3.18 \times 10^{-6}$$

The conditional probabilities are listed in the right-hand column of Figure V-1.

Truck Event Tree

ACCIDENT	TYPE	OBJECT STRUCK	SPEED DISTRIBUTION	SURFACE STRUCK	PROBABILITY									
Large truck accident on interstate highway	Collision with non-fixed object	Train	Train grade crossing		0.00082									
		0.001	accident speeds											
		Gasoline tanker truck			0.00246									
		0.003												
		Other vehicles (motorcycles, cars, other Trucks)			0.76916									
		0.938												
		Other smaller non-fixed objects (cones, animals, pedestrians)			0.04756									
		0.058												
		Collision with fixed object	Bridge accident	Fall off bridge	0.02	Hard rock	3.45E-06							
						0.050								
	Soft rock, rocky soul					3.18E-06								
	0.046													
	Other soils, clay, silt					5.65E-05								
	Strike bridge structure		Large column	Initial accident speeds	0.03	0.817								
						Railbed, roadbed	5.39E-06							
						0.078								
						Water	6.22E-07							
						0.009								
	0.04													
	Collision with fixed object	Building, wall	Strike bridge structure	0.98	Small columns, abutments, other	Initial accident speeds	0.00010							
0.97								Initial accident speeds	0.00329					
										0.010	Initial accident speeds	0.00054		
													Other fixed objects (trees, signs, barriers, posts, guard rails)	0.03434
		Slide on / into ground, culvert, ditch	0.244											
0.046				Initial accident speeds	0.00014									
						Into slope, embankment	0.00012							
								0.050	0.00222					
										0.895	0.00630			
	0.050	0.11970												
Other non-collision (jack-knife, rollover, mechanical problems)			0.950											
				0.126										

Figure V-1 Event tree for highway accidents (from Mills, et al, 2006)

The construction of the event tree of Figure V-1 is described in detail in Mills, et al (2006). Details of collision accidents are discussed in Appendix III and of fire accidents, in Appendix IV.

V.2.2.2 Conditional probabilities of rail accidents

Figure V-2 is an event tree for rail.

Rail Event Tree

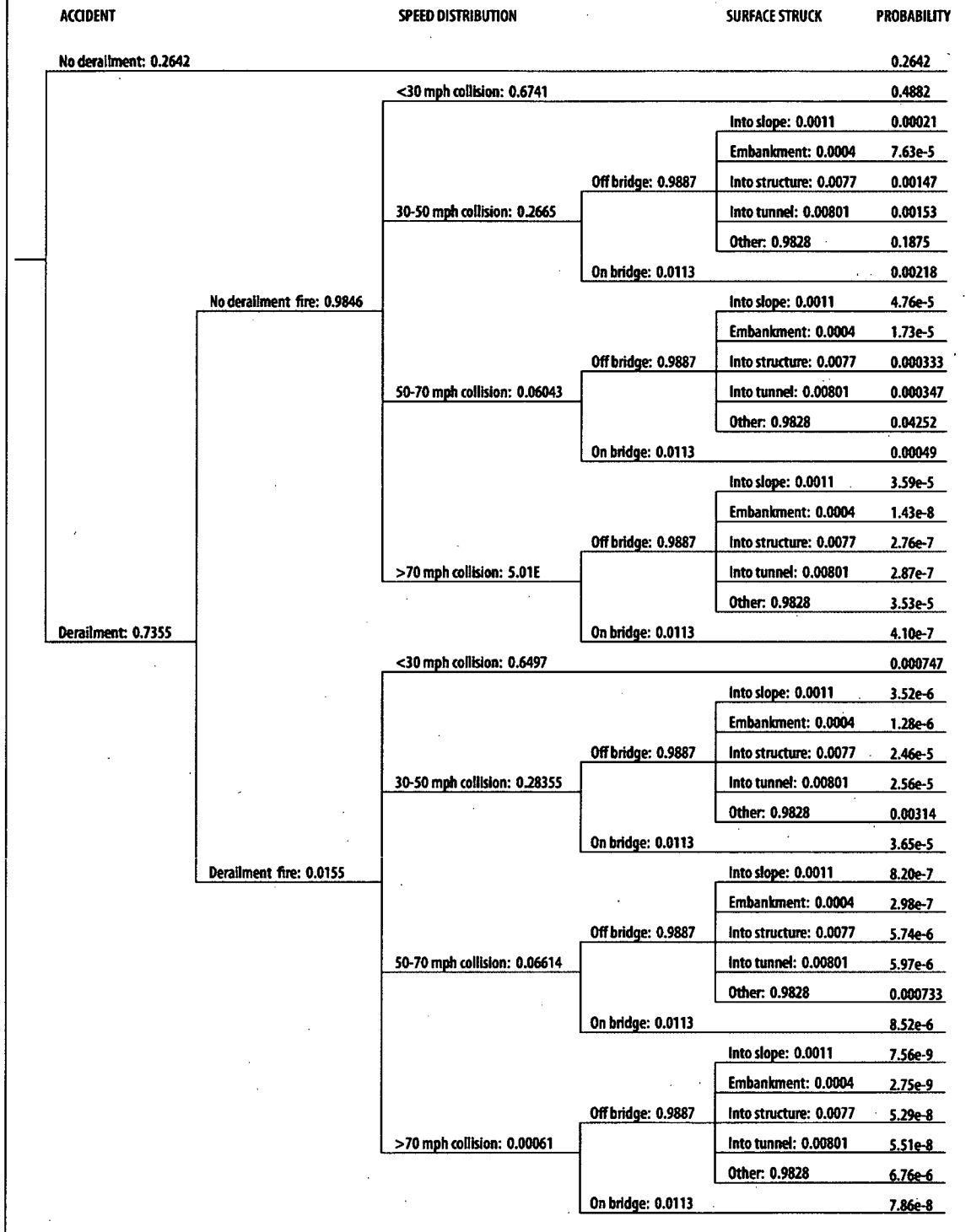


Figure V-2 . Rail accident event tree (after Volpe, 2006)

V.3. Accident Risks and Consequences

V.3.1 Loss of lead gamma shielding

The only cask studied that uses lead as gamma shield is the NAC-STC, a rail cask, so that loss would occur only in rail accidents. The NAC-STC gamma shield is a lead cylinder about 0.127 m. thick. The lead shell can slump in a sufficiently severe impact, leaving a gap in the lead shield which results in increased external gamma radiation. RADTRAN models a gap in the shield from an impact and translates this to an increase in the dose from virtual radiation source (O'Donnell, et al., 2005; Dennis, et al., 2009) that is the basis for the incident-free transportation model (Figure II-1, Appendix II). Figure V-3 is a diagram of the loss-of-shielding model, which recognizes the two-dimensional symmetry of the lead-shielded cask.

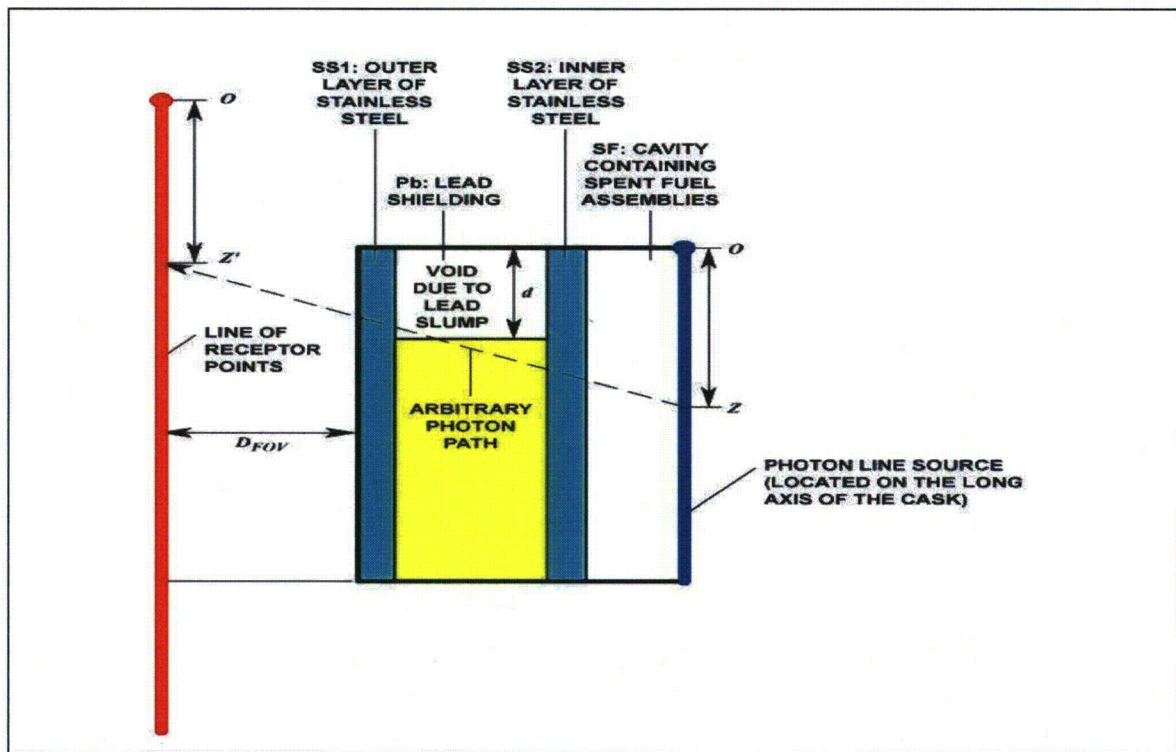


Figure V-3. The RADTRAN Loss-of Shielding 2-D Model (O'Donnell, et al, 2005)

V.3.1.1 Loss of lead shielding from impact

Appendix III (. Section 3.2.2) described the various amounts of lead slump resulting from impact speed and aspect. Table V-2 shows the conditional probabilities of each combination of impact speed and orientation. The conditional probabilities are those of a fall from the bridge into a tunnel, a collision on the bridge, and a fall from a bridge onto hard rock (Mills et al, 2006, Table 9). Table V-3 shows the slump as fractions of the longest dimension of the lead shield and combines the conditional probabilities in Table V-2 for each applicable accident scenario in the rail event tree (Figure V-2). Only the lead-shielded NAC-STC rail cask might lose shielding in an accident.

As Tables V-2 and V-3 show, the lead slump on opposite sides of the cask is different following a corner or side impact. This is particularly noticeable with the side impact. A radiation dose to any exposed person or population would therefore differ depending on the side of the cask to which the receptor was exposed. Table V-4 shows doses to the maximally exposed individual (MEI) at various distances from the cask. Table V-6 shows the population that could be exposed for each of the sixteen routes modeled.

Table V-2. Parameters of lead shield slumping from impact.

Orientation	Impact Speed kph	Event Tree Impact Speed mph	Location (Side 1 or Side 2)	Maximum Slump (mm)	Conditional Probability from Rail Event Tree and 5% >90 mph	Conditional Probability Pc including Orientation ^a
End (Probability = 0.1)	193	>113	1	355.40	1.34E-07	1.34E-08
			2	355.48		
	145	>113	1	83.20	2.54E-06	2.54E-07
			2	82.68		
	97	80 to 113	1	18.28	8.27E-04	8.27E-05
			2	18.21		
48	48 to 80	1	6.43	2.35E-03	2.35E-04	
		2	6.42			
Corner (Probability= 0.6)	193	>113	1	310.48	1.34E-07	8.03E-08
			2	254.56		
	145	>113	1	114.52	2.54E-06	1.53E-06
			2	80.35		
	97	80 to 113	1	25.11	8.27E-04	4.96E-04
			2	20.55		
48	48 to 80	1	1.28	2.35E-03	1.41E-03	
		2	1.65			
Side (Probability= 0.3)	193	>113	1	0.53	1.34E-07	4.01E-08
			2	15.47		
	145	>113	1	0.43	2.54E-06	7.63E-07
			2	20.88		
	97	80 to 113	1	0.00	8.27E-04	2.48E-04
			2	1.37		
48	48 to 80	1	0.06	2.35E-03	7.05E-04	
		2	0.09			

Table V-3. Fractions of lead shielding lost and conditional probabilities

Side Affected	Fraction of Shield. Lost	P _{cond}
1 or 2	0.0725	8.03X10 ⁻⁸
1	0.0634	2.41X10 ⁻⁷
2	0.0520	2.41X10 ⁻⁷
1	0.0234	4.58X10 ⁻⁶
1 or 2	0.0170	7.63X10 ⁻⁷
2	0.0164	4.58X10 ⁻⁶
1	0.00512	0.00149
2	0.00426	2.29X10 ⁻⁶
2	0.00419	0.00149
1 or 2	0.00373	4.96X10 ⁻⁴
2	0.00316	1.20X10 ⁻⁷
2	0.00131	0.00141
2	3.37X10 ⁻⁴	0.00681
1	1.08X10 ⁻⁴	4.01X10 ⁻⁸
1	8.73X10 ⁻⁵	2.29X10 ⁻⁶
2	1.94X10 ⁻⁵	0.00211
1	1.31X10 ⁻⁵	0.00211
1	3.06X10 ⁻⁹	2.13X10 ⁻⁷

Figures V-4 and V-5 show doses to the MEI as a function of the fraction of shielding lost and as a function of distance from the cask.

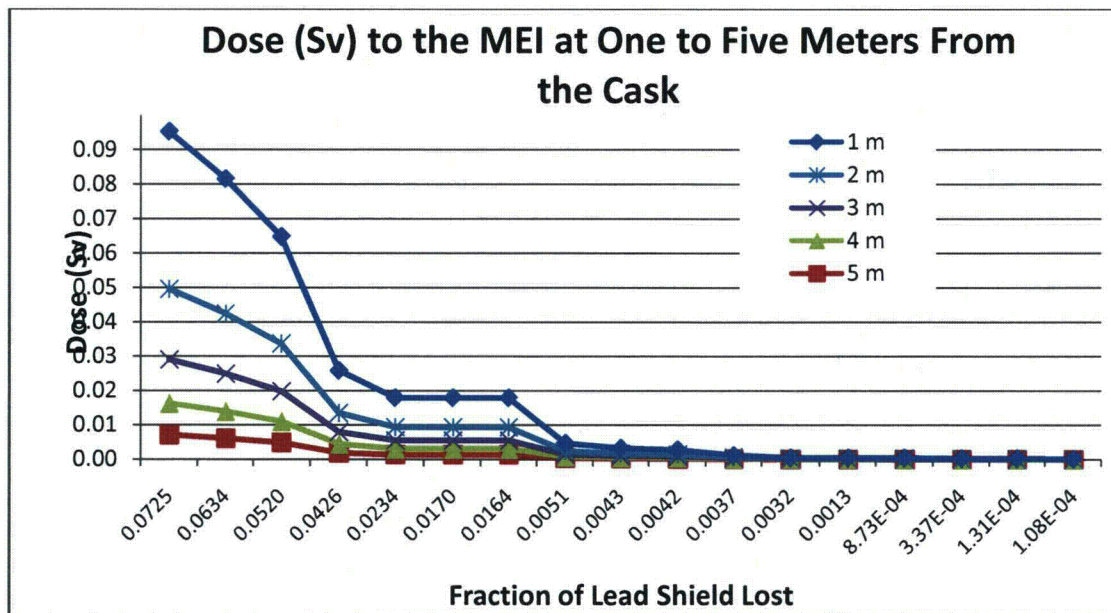


Figure V- 4. Dose to the MEI at various distances one to five meters from the cask.

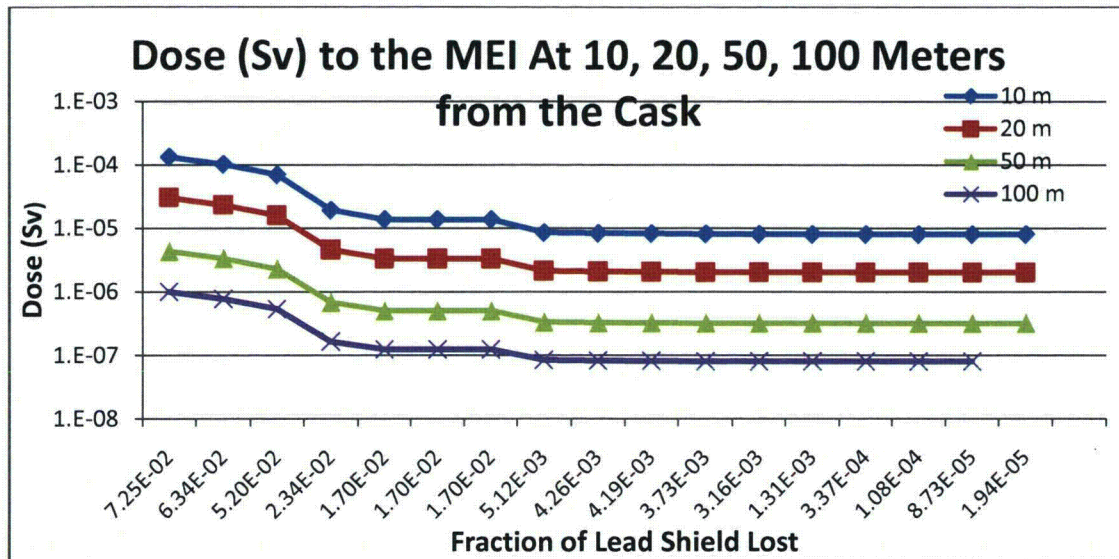


Figure V- 5. Dose to the MEI at various distances 10 to 100 m from the cask.

Table V-5 shows how the dose to the maximally exposed individual (MEI) depends on the fraction of the lead shield lost and distance from the cask, for a ten-hour exposure. Table V-5 includes both sides of the cask, since the doses are to an individual.

The large doses that occur at near the cask (one to five meters from the cask) would be sustained by emergency responders, none of whom would spend all ten hours that close to the cask. The one- to five-meter doses can be considered occupational rather than public doses. If a loss-of-shielding accident occurred on a public right of way – a railroad track in this case – no member of the public would be closer than ten meters (30 feet). The public MEI dose (from the largest gap in the lead shield) would be 1.33 mSv (133 mrem), about 30% larger than the NRC standard for the public.

The “dose risk” combines the probability of a particular accident with the consequence (the dose). It is a risk, not a dose, and is much smaller than the dose. Tables V-6 a and b show the conditional dose risk, the combination of the conditional probability with the consequence, for each fractional loss of lead shielding. This is the risk of a particular accident scenario if there is an accident, and does not include the probability of an accident. The columns in Tables V-6 are in order of descending risk, with the greatest conditional dose risk at the top.

Table V-4. Radiation dose (Sv) to the MEI at various distances for the cask. The numbers in bold italics exceed the external dose rate of 10 CFR 71.51..

Fraction of lead lost	1m	2m	3m	4m	5m	10m	20m	50m
7.25E-02	4.6E-02	2.1E-02	1.3E-02	9.2E-03	7.1E-03	1.3E-04	3.1E-05	4.4E-06
6.34E-02	3.9E-02	1.8E-02	1.1E-02	7.9E-03	6.1E-03	1.0E-04	2.3E-05	3.4E-06
5.20E-02	3.1E-02	1.4E-02	8.7E-03	6.2E-03	4.8E-03	7.0E-05	1.6E-05	2.3E-06
2.34E-02	1.2E-02	5.6E-03	3.5E-03	2.5E-03	1.9E-03	1.9E-05	4.6E-06	6.9E-07
1.70E-02	8.6E-03	3.9E-03	2.4E-03	1.7E-03	1.3E-03	1.4E-05	3.3E-06	5.1E-07
1.70E-02	8.6E-03	3.9E-03	2.4E-03	1.7E-03	1.3E-03	1.4E-05	3.3E-06	5.1E-07
1.70E-02	8.6E-03	3.9E-03	2.4E-03	1.7E-03	1.3E-03	1.4E-05	3.3E-06	5.1E-07
5.12E-03	2.3E-03	1.0E-03	6.4E-04	4.6E-04	3.5E-04	8.5E-06	2.1E-06	3.4E-07
3.73E-03	1.6E-03	7.2E-04	4.5E-04	3.3E-04	2.5E-04	8.3E-06	2.1E-06	3.3E-07
3.16E-03	1.3E-03	6.1E-04	3.8E-04	2.8E-04	2.1E-04	8.2E-06	2.1E-06	3.3E-07
1.31E-03	5.7E-04	2.6E-04	1.7E-04	1.2E-04	9.5E-05	8.1E-06	2.0E-06	3.2E-07
4.26E-04	2.6E-04	1.2E-04	8.0E-05	5.9E-05	4.6E-05	8.1E-06	2.0E-06	3.2E-07
4.19E-04	2.6E-04	1.2E-04	7.9E-05	5.8E-05	4.6E-05	8.1E-06	2.0E-06	3.2E-07
3.34E-04	2.3E-04	1.1E-04	7.2E-05	5.3E-05	4.2E-05	8.1E-06	2.0E-06	3.2E-07
1.08E-04	1.6E-04	8.1E-05	5.3E-05	4.0E-05	3.2E-05	8.1E-06	2.0E-06	3.2E-07
8.73E-05	1.6E-04	7.8E-05	5.2E-05	3.9E-05	3.1E-05	8.1E-06	2.0E-06	3.2E-07
1.94E-05	1.4E-04	7.2E-05	4.8E-05	3.6E-05	2.9E-05	8.1E-06	2.0E-06	3.2E-07

Table V-5. The “conditional dose risk,” the product of dose and conditional probability, in Sv to the maximally exposed individual at distances from the cask from one to five meters.

Conditional Probability	Distance from the cask (m)				
	1	2	3	4	5
8.03E-08	3.7E-09	1.6E-09	1.0E-09	7.4E-10	5.7E-10
2.41E-07	9.4E-09	4.2E-09	2.6E-09	1.9E-09	1.5E-09
2.41E-07	7.5E-09	3.3E-09	2.1E-09	1.5E-09	1.2E-09
7.63E-07	9.5E-09	4.2E-09	2.7E-09	1.9E-09	1.5E-09
1.49E-03	1.3E-05	5.7E-06	3.6E-06	2.6E-06	2.0E-06
4.58E-06	3.9E-08	1.8E-08	1.1E-08	7.9E-09	6.1E-09
4.58E-06	3.9E-08	1.8E-08	1.1E-08	7.9E-09	6.1E-09
2.29E-06	5.1E-09	2.3E-09	1.5E-09	1.0E-09	8.1E-10
1.94E-05	3.1E-08	1.4E-08	8.8E-09	6.3E-09	4.9E-09
8.73E-05	1.2E-07	5.3E-08	3.3E-08	2.4E-08	1.9E-08
1.08E-04	6.2E-08	2.8E-08	1.8E-08	1.3E-08	1.0E-08
1.49E-03	3.8E-07	1.8E-07	1.2E-07	8.7E-08	6.9E-08
4.96E-04	1.3E-07	6.1E-08	3.9E-08	2.9E-08	2.3E-08
3.37E-04	7.7E-08	3.7E-08	2.4E-08	1.8E-08	1.4E-08
1.31E-03	2.2E-07	1.1E-07	7.0E-08	5.2E-08	4.2E-08
3.16E-03	5.0E-07	2.5E-07	1.6E-07	1.2E-07	9.8E-08
3.73E-03	5.3E-07	2.7E-07	1.8E-07	1.3E-07	1.1E-07

Table V-6. The “conditional dose risk,” the product of dose and conditional probability, in Sv to the maximally exposed individual at distances 10 to 100 meters from the cask.

Conditional Probability	Distance from the cask (m)			
	10	20	50	100
8.03E-08	1.1E-11	2.4E-12	3.5E-13	8.0E-14
2.41E-07	2.5E-11	5.6E-12	8.1E-13	1.9E-13
2.41E-07	1.7E-11	3.9E-12	5.6E-13	1.3E-13
7.63E-07	1.5E-11	3.5E-12	5.2E-13	1.3E-13
1.49E-03	2.0E-08	4.9E-09	7.5E-10	1.8E-10
4.58E-06	6.3E-11	1.5E-11	2.3E-12	5.6E-13
4.58E-06	6.3E-11	1.5E-11	2.3E-12	5.6E-13
2.29E-06	1.9E-11	4.9E-12	7.7E-13	1.9E-13
1.94E-05	1.6E-10	4.0E-11	6.4E-12	1.6E-12
8.73E-05	7.2E-10	1.8E-10	2.9E-11	7.1E-12
1.08E-04	8.7E-10	2.2E-10	3.5E-11	8.7E-12
1.49E-03	1.2E-08	3.0E-09	4.8E-10	1.2E-10
4.96E-04	4.0E-09	1.0E-09	1.6E-10	4.0E-11
3.37E-04	2.7E-09	6.8E-10	1.1E-10	2.7E-11
1.31E-03	1.1E-08	2.7E-09	4.2E-10	1.1E-10
3.16E-03	2.5E-08	6.4E-09	1.0E-09	2.5E-10
3.73E-03	3.0E-08	7.5E-09	1.2E-09	3.0E-10

The collective dose risk to an exposed population within a radius r of the cask may be calculated by equation (V-1)

$$(V-1) \quad \text{Dose Risk} = A * 0.5\pi r^2 * PD \sum_i^n P_{ci} * D_{avi}$$

where A is the accident frequency on the route segment under consideration

r is the distance from the cask: 20, 50, 100 and 800 meters

$0.5\pi r^2$ is the area of the semicircle of people around the cask

PD is the population density per km^2 in the semicircle

D_{avi} is the average individual dose from the i^{th} fractional loss of shielding

P_{ci} is the conditional probability of the i^{th} fractional loss of shielding.

The index i indicates a particular fractional shielding loss; these are summarized above in Table V-3. The population along the route is exposed to only one side of the cask. Thus this analysis assumed that half of this population would be exposed to each side of the cask, so that dose risks were calculated separately for exposure to each side of the cask. The summation in equation (V-1) is the conditional dose risk of all of the accidents considered: the “universe” of accidents. Table V-7 shows collective conditional dose risks for the sixteen routes analyzed.

Table V-7. Collective conditional dose risks due to loss of lead shielding in person-Sv in a semicircular area of radius 100 meters around the cask.

		Side 1				Side 2			
		ORNL	DEAF SMITH	HANFORD	SKULL VALLEY	ORNL	DEAF SMITH	HANFORD	SKULL VALLEY
MAINE YANKEE	Rural	9.37E-10	6.91E-10	1.10E-09	8.57E-10	5.09E-09	3.75E-09	5.99E-09	4.66E-09
	Suburb	1.78E-08	1.91E-08	1.77E-08	1.72E-08	9.58E-08	1.03E-07	9.49E-08	9.22E-08
	Urban	1.93E-09	1.99E-09	1.86E-09	1.55E-09	1.03E-08	1.07E-08	1.00E-08	8.34E-09
KEWAUNEE	Rural	9.37E-10	4.61E-10	4.62E-10	5.91E-10	5.09E-09	2.50E-09	2.51E-09	3.21E-09
	Suburb	1.92E-08	2.03E-08	1.78E-08	2.08E-08	1.03E-07	1.09E-07	9.54E-08	1.12E-07
	Urban	2.10E-09	2.10E-09	1.94E-09	1.74E-09	1.13E-08	1.13E-08	1.04E-08	9.36E-09
INDIAN POINT	Rural	7.96E-10	5.72E-10	5.66E-10	6.63E-10	4.32E-09	3.11E-09	3.07E-09	3.60E-09
	Suburb	2.40E-08	1.98E-08	1.89E-08	2.02E-08	1.29E-07	1.06E-07	1.01E-07	1.08E-07
	Urban	2.56E-09	2.19E-09	2.12E-09	1.94E-09	1.37E-08	1.18E-08	1.14E-08	1.04E-08
IDAHO NATIONAL LAB	Rural	5.80E-10	2.40E-10	3.01E-10	5.99E-10	3.15E-09	1.30E-09	1.63E-09	3.26E-09
	Suburb	2.02E-08	2.01E-08	2.02E-08	1.97E-08	1.09E-07	1.08E-07	1.08E-07	1.06E-07
	Urban	1.70E-09	1.56E-09	1.97E-09	2.08E-09	9.13E-09	8.37E-09	1.06E-08	1.11E-08

Population dose risk ultimately depends on the accident frequency as well as on the population along the route where the accident happens. The accident frequency, accidents per km, is equated to the accident probability. The rail accident frequencies used in this analysis are from DOT, 2008. Average railcar accident frequencies for each of the 16 routes are shown in Table V-8. These accident frequencies are combined with the average dose risk integrated over the potentially exposed population.

Table V-9 shows the collective dose risks to populations on each side of the rail cask that has lost lead shielding on impact. These estimates include both the conditional probabilities and the accident frequencies on each route, as in Equation (V-1). Thus the differences in Table V-9 are due to differences in traffic accident frequencies.

Table V-8. Average railcar accident frequencies on the routes studied.

ORIGIN	DESTINATION	AVERAGE ACCIDENTS PER KM
MAINE YANKEE	ORNL	6.5×10^{-7}
	DEAF SMITH	5.8×10^{-7}
	HANFORD	4.2×10^{-7}
	SKULL VALLEY	5.1×10^{-7}
KEWAUNEE	ORNL	4.3×10^{-7}
	DEAF SMITH	3.3×10^{-7}
	HANFORD	2.4×10^{-7}
	SKULL VALLEY	3.7×10^{-7}
INDIAN POINT	ORNL	8.8×10^{-6}
	DEAF SMITH	6.2×10^{-7}
	HANFORD	5.1×10^{-7}
	SKULL VALLEY	5.5×10^{-7}
INL	ORNL	3.6×10^{-7}
	DEAF SMITH	3.5×10^{-7}
	HANFORD	3.2×10^{-7}
	SKULL VALLEY	2.8×10^{-7}

Table V-9. Conditional collective dose risks (person-Sv) from loss of lead shielding, including conditional probabilities

ORIGIN	TYPE	Side 1				Side 2			
		ORNL	DEAF SMITH	HANFORD	SKULL VALLEY	ORNL	DEAF SMITH	HANFORD	SKULL VALLEY
MAINE YANKEE	Rural	3.09E-12	1.35E-12	1.97E-12	9.31E-13	1.70E-11	7.44E-12	1.09E-11	5.13E-12
	Subu	5.87E-11	3.74E-11	3.16E-11	1.87E-11	3.19E-10	2.03E-10	1.72E-10	1.02E-10
	U	6.34E-12	3.89E-12	3.33E-12	1.69E-12	3.45E-11	2.12E-11	1.81E-11	9.18E-12
KEWAU NEE	R	1.22E-12	2.87E-13	3.06E-13	3.06E-13	6.74E-12	1.58E-12	1.69E-12	1.69E-12
	S	2.51E-11	1.26E-11	1.18E-11	1.07E-11	1.36E-10	6.86E-11	6.40E-11	5.85E-11
	U	2.74E-12	1.31E-12	1.28E-12	9.01E-13	1.49E-11	7.11E-12	6.98E-12	4.90E-12
INDIAN POINT	R	3.36E-11	1.09E-12	1.15E-12	4.62E-13	1.85E-10	6.02E-12	6.34E-12	2.55E-12
	S	1.01E-09	3.78E-11	3.83E-11	1.40E-11	5.49E-09	2.06E-10	2.08E-10	7.64E-11
	U	1.08E-10	4.18E-12	4.30E-12	1.35E-12	5.86E-10	2.27E-11	2.34E-11	7.36E-12
IDAHO N. L.	R	2.22E-13	1.61E-13	4.38E-14	5.56E-13	1.23E-12	8.87E-13	2.41E-13	3.07E-12
	S	7.75E-12	1.35E-11	2.94E-12	1.82E-11	4.22E-11	7.35E-11	1.60E-11	9.93E-11
	U	6.52E-13	1.05E-12	2.87E-13	1.92E-12	3.55E-12	5.69E-12	1.56E-12	1.05E-11

V.3.1.2 Loss of lead shielding with fire

Release of radioactive materials in a fire depends on the offset of the cask from the fire.

Lead melts at 330 °C, so that a prolonged high-temperature fire could result in lead slump, leaving a gap in the gamma shield which results in increased external radiation emission. In calculating doses from a loss of lead shielding, RADTRAN models a gap in the shield as an increase in the dose from a virtual radiation source (O'Donnell, et al., 2005; Dennis, et al., 2009). This is the same source as the basis for the incident-free transportation model (Figure II.1, Appendix II).

The loss of lead shielding does not occur during a fire. Lead expands as it melts and can buckle the innermost cask shell. When the melted lead cools and solidifies, it occupies the same volume as before expansion but the volume available between the steel cask shells is larger because of the buckling of the inner shell, leaving a gap. Melting of lead and the formation of a gap in the lead are described fully in Appendix IV. Briefly, if the cask is offset from the fire, the gap would be in the section of lead shield facing the fire. In an engulfing fire, the gap would be at the upper surface of the cask. However, if the cask is turned after the melted lead has solidified, the gap in the lead would be on the side of the cask rather than at the top. Thus, in both cases, anyone facing the side of the cask with the shielding gap could sustain an increased radiation dose.

Two accidental fire scenarios can result in a loss of lead shielding:

- Fire Scenario 1: a sufficiently hot pool fire engulfing a cask on the ground can melt enough lead in three hours to create an 8.14 percent fractional shield loss.
- Fire Scenario 2: a sufficiently hot pool fire offset from the cask, burning for more than three hours, can create an 2.01 percent fractional shield loss.

These scenarios are described fully in Appendix IV. The doses sustained by the maximally exposed individual at various distances from the cask, exposed for an hour, are shown in Table V-10.

Table V-10. Radiation dose (Sv) to the maximally exposed individual at various distances from a cask that has been in a fire.

Fraction of lead lost	1 m	2 m	5 m	10 m	20 m	50 m	100 m
0.0201	7.0E-03	3.1E-03	1.1E-03	1.1E-05	2.6E-06	3.9E-07	9.4E-08
0.0814	3.5E-02	1.6E-02	5.4E-03	1.1E-04	2.6E-05	3.7E-06	8.5E-07

No lead shielding would be lost until the fire was out and the cask had cooled enough for the lead to solidify, since only then would there be a gap in the lead shield. Thus no one would be exposed for many hours after the accident, and with a fire this severe, nearby residents and the public would probably have been evacuated. The maximally exposed individual in this case would be an emergency responder.

Volpe (2006, Figure 16) postulates a chain of events leading to a fire, from which the probability of these scenarios can be calculated. The relevant portion of the Volpe figure is shown in Figure V-6.

Fire Event Tree

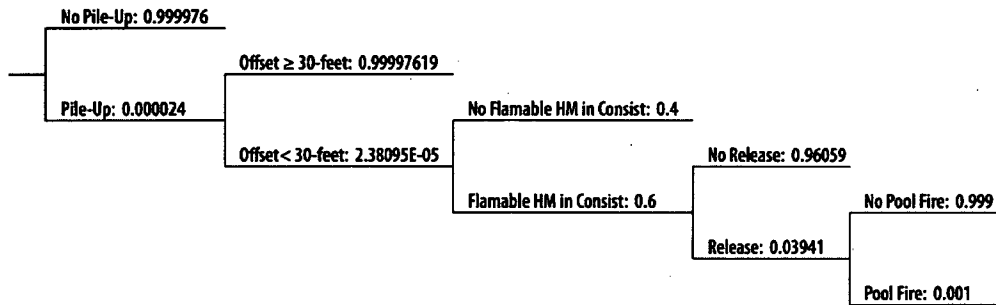


Figure V-6. Event tree branch for a rail fire accident (from Volpe, 2006, Figure 16)

The first of these events is a major derailment, as shown in Table V-11. Volpe estimates that the speed at the time of the accident for such a derailment is at least 80 km/hr (50 mph). If a pileup could occur in any kind of derailment other than in a tunnel, from Figure V-2, the probability of such a major derailment is

$$(0.7355) * (0.0155) * (0.06614 + 0.00061) * (0.0011 + 0.0004 + 0.0077 + 0.0113) = 1.56 \times 10^{-5}$$

Table V-11 lists the other events in the scenario, together with the probability of each event. These events are a pileup, a flammable hazardous cargo within 10 meters (about half a rail-car length), leaking of that hazardous substance, and ignition of a pool fire. The net probability of the sequence of events shown in Table V-11 following a major pileup is 1.35×10^{-14} . However, Volpe's rationale for the pileup probability of 2.4×10^{-5} is not as robust as for the other probabilities. Using the "no pileup" branch, the net probability for the events of Table V-11 is 5.6×10^{-10} .

Thus the conditional probability of Fire Scenario 1, a major derailment leading to a three-hour pool fire that surrounds the cask is then

$$(1.56 \times 10^{-5}) * (5.6 \times 10^{-10}) = 8.8 \times 10^{-15}$$

The conditional probability of Fire Scenario 2, a major derailment leading to a three-hour fire offset from the cask by more than 10 meters is then

$$(1.56 \times 10^{-5}) * (2.36 \times 10^{-5}) = 3.7 \times 10^{-10}$$

Table V-11. Events leading to a train fire that could involve a spent fuel cask

EVENT	PROBABILITY	ALTERNATIVE EVENT	PROBABILITY
Major high speed derailment	1.56×10^{-5}	No major derailment	0.99999
Pileup	2.4×10^{-5}	No pileup	0.99998
Offset < 10 m	2.38×10^{-5}	Offset > 10 m	0.99998
Flammable hazardous material in another railcar	0.6	No flammable material available	0.4
Release of flammable material	0.0394	No release of flammable material	0.9606
Pool fire	0.001	No pool fire	0.999

The average accident frequency for the 16 rail routes studied is 3.9×10^{-3} (the range is from 1.5×10^{-4} to 4.2×10^{-2}). Thus, the average probability of an accidental fire that could cause loss of lead shielding in a rail cask is 3.4×10^{-19} if the cask is concentric with the fire and 1.4×10^{-14} if the cask and fire are offset by 10 meters or more. The largest dose risk would be 4.9×10^{-17} Sv.

V.3.2 Loss of Neutron Shielding

The neutron shield is usually a hydrocarbon or carbohydrate polymer, sometimes borated, since boron and organic polymers are good neutron absorbers. Neutron shielding burns, and could be destroyed in a fire. The neutron dose from loss of shielding in a fire is estimated using the parameters listed in Table V-12. The conditional probability of a truck fire is from Figure V-1. The conditional probability of a rail fire is a combination of the fire probability in Figure V-2 and the following steps from Figure V-5.

- A pileup
- Flammable cargo on the train
- Release of the flammable cargo

The neutron TI for the Truck-DU cask is from General Atomics, 1998; the TI for the Rail-Pb cask, from NAC International, 2002; and the TI for the Rail-Steel cask, from Holtec International, 2004. The RADTRAN external dose rate is modeled as entirely neutron emission. The other parameters are the same as those used in calculating doses from an accident in which there is no release of radioactive material and no loss of lead shielding (Chapter 5, Section 5.4).

Table V-12. Some parameters used in calculating loss of neutron shielding.

Parameter	Truck-DU	Rail-Pb	Rail-Steel
Conditional probability of a fire	0.0063	8.9×10^{-8}	8.9×10^{-8}
Dose rate at one meter from the cask in mSv/hour (mrem/hour)	1.78 (178)	1.81 (181)	1.82 (182)
Shielding of residents.	none	none	none
Time until the cask is removed (hours)	10	10	10

The neutron doses to emergency responders (five meters from the cask) are shown in Table V-13, the collective doses on the 16 routes are shown in Table V-14, and the total collective dose risks, including accident frequency, are shown in Table V-15.

Table V-13. Doses to an emergency responder five meters from the cask.

Cask	Dose in Sv	Ten-hour 10 CFR 71.51 dose in Sv
Truck-DU	0.00729	1.00
Rail-Pb	0.00761	1.00
Rail-Steel	0.00763	1.00

Table V-14. Collective doses (consequences) in person-Sv from loss of neutron shielding.

FROM	TO	Truck-DU	Rail-Pb	Rail-Steel
MAINE YANKEE	ORNL	7.49E-04	7.17E-04	7.40E-04
	DEAF SMITH	7.01E-04	6.71E-04	6.93E-04
	HANFORD	6.23E-04	5.96E-04	6.15E-04
	SKULL VALLEY	6.38E-04	6.11E-04	6.31E-04
KEWAUNEE	ORNL	6.87E-04	6.57E-04	6.78E-04
	DEAF SMITH	6.41E-04	6.13E-04	6.33E-04
	HANFORD	5.98E-04	5.72E-04	5.91E-04
	SKULL VALLEY	6.17E-04	5.91E-04	6.10E-04
INDIAN POINT	ORNL	7.28E-04	6.97E-04	7.20E-04
	DEAF SMITH	6.95E-04	6.65E-04	6.87E-04
	HANFORD	6.38E-04	6.11E-04	6.31E-04
	SKULL VALLEY	6.63E-04	6.34E-04	6.55E-04
INL	ORNL	5.78E-04	5.53E-04	5.71E-04
	DEAF SMITH	6.16E-04	5.89E-04	6.08E-04
	HANFORD	3.78E-04	3.62E-04	3.73E-04
	SKULL VALLEY	6.41E-04	6.13E-04	6.33E-04

Table V-15. Collective dose risks in person-Sv from loss of neutron shielding.

FROM	TO	Truck-DU	Rail-Pb	Rail-Steel
MAINE YANKEE	ORNL	4.7E-06	6.4E-11	6.6E-11
	DEAF SMITH	4.4E-06	6.0E-11	6.2E-11
	HANFORD	3.9E-06	5.3E-11	5.5E-11
	SKULL VALLEY	4.0E-06	5.4E-11	5.6E-11
KEWAUNEE	ORNL	4.3E-06	5.8E-11	6.0E-11
	DEAF SMITH	4.0E-06	5.5E-11	5.6E-11
	HANFORD	3.8E-06	5.1E-11	5.3E-11
	SKULL VALLEY	3.9E-06	5.3E-11	5.4E-11
INDIAN POINT	ORNL	4.6E-06	6.2E-11	6.4E-11
	DEAF SMITH	4.4E-06	5.9E-11	6.1E-11
	HANFORD	4.0E-06	5.4E-11	5.6E-11
	SKULL VALLEY	4.2E-06	5.6E-11	5.8E-11
INL	ORNL	3.6E-06	4.9E-11	5.1E-11
	DEAF SMITH	3.9E-06	5.2E-11	5.4E-11
	HANFORD	2.4E-06	3.2E-11	3.3E-11
	SKULL VALLEY	4.0E-06	5.5E-11	5.6E-11

V.4 Release of Radioactive Materials in Accidents

V.4.1 Spent Fuel Inventory

A Rail Pb-cask is the only cask studied that would release any radioactive material in an accident. Since there is no traffic accident that would result in a release from the Truck-DU or Rail-Steel cask, the inventory of those casks is not relevant to this analysis. The fuel used in this analysis is PWR fuel, 45,000 MWD/MTU burnup, the maximum burnup that a Rail-Pb cask would transport, and has cooled for nine years before transport. The radionuclide inventory of this fuel was determined using ORIGEN (Croff, 1980).² The radionuclide activities in the inventory were “normalized” by dividing each activity by the A_2 value for that radionuclide. The A_2 value—the amount of the radionuclide that could be transported in a Type A container, and thus theoretically released to the environment without damage—is an indication of the radiotoxicity; the larger the A_2 value, the smaller the radiotoxicity of that nuclide. The normalized radioactivities were then sorted and added until 99.99 percent of the total normalized radioactivity was reached.³ The radionuclides selected this way are listed in Table V-16, together with their actual radioactivities (not the normalized radioactivities).

² The preparers are indebted to J.D. Smith of Sandia National Laboratories for the ORIGEN run.

³ The “total normalized activity” referred to here is not the total A_2 value as calculated by the formula in 10 CFR Part 71 Appendix A.

Table V-16. TBq inventory for the Rail-Pb cask. The ⁶⁰Co inventory is estimated CRUD.

Radionuclide	TBq
	26 Assemblies
²⁴⁰ Pu	2.20E+05
²³⁹ Pu	5.16E+03
¹³⁷ Cs	1.23E+06
²³⁸ Pu	2.02E+03
²⁴³ Cm	7.04E+02
⁶⁰ Co	3.39E+04
¹⁵⁴ Eu	2.53E+04
¹³⁴ Cs	1.13E+04
⁸⁵ Kr	6.36E+04
²⁴¹ Am	4.45E+00
²⁴² Cm	2.81E+01
¹⁵⁵ Eu	7.38E+03
²³¹ Pa	8.77E-01
¹⁰⁶ Ru	2.11E+02
²³⁶ U	5.39E+00
²³³ U	2.53E+04
²⁴¹ Pu	1.62E+01
^{113m} Cd	1.72E+01

V.5.3 Dispersion of Released Radionuclides

The public is exposed to radioactive material accidentally released from a cask if that material is dispersed through the air. Experimental work reviewed by Sprung et al (2000, pp.7-30 et seq) indicates that only very small particles with analytic mean aerodynamic diameter (AMAD)⁴ ten microns or less would be released from a cask in an accident, because the only release path is through the seals at the ends of the cask. In addition, particles larger than this are filtered by larger particles inside the cask. Ten microns is generally considered the upper limit of respirability. Thus particles accidentally released from a cask will be released as a respirable aerosol.

The discussion below is an abbreviated discussion of air dispersion, a subject that is treated extensively and in detail in textbooks like Wark and Warner (1981).

The basic equation for atmospheric dispersion of an aerosol is the Gaussian dispersion equation: Equation (V.2) (Turner, 1994, Chapter 2).

$$(V-2) \quad \frac{CHI}{Q} = \frac{1}{2\pi u \sigma_y \sigma_z} \exp\left[\frac{-y^2}{2\sigma_y^2}\right] \exp\left[\frac{-z^2}{2\sigma_z^2}\right]$$

⁴ The AMAD is the diameter of a sphere of density 1 gm/cm³ that has the same inertial properties as the actual particle.

where CHI^5 = the concentration of particles in the air
 Q = the radioactivity or mass of airborne particles
 u = the wind speed
 σ_y, σ_z are meteorological constants and are functions of the downwind distance x .

The wind direction is traditionally along the x axis of a Cartesian coordinate system, the crosswind direction is y , and z represents the altitude above ground. When the plume of released material rises buoyantly to a height H , the Gaussian equation becomes

$$(V-3) \quad \frac{CHI}{Q} = \frac{1}{2\pi u \sigma_y \sigma_z}$$

where H is the height to which the plume rises before being blown downwind. For a ground-level release along the plume centerline, Equations (V.2) and (V.3) reduce to

$$(V-4) \quad \frac{CHI}{Q} = \frac{1}{2\pi u \sigma_y \sigma_z} \exp\left[\frac{-y^2}{2\sigma_y^2}\right] \exp\left[\frac{-H^2}{2\sigma_z^2}\right]$$

Radioactive gases released in accident will disperse in the air according to Equations (V.1) and (V.3). Particles, however, have mass and will settle on the ground. The settling velocity V_t —the terminal velocity of a particle in the indicated size range—is given by Equation (V.5)

$$(V-5) \quad V_t = \frac{g\rho d^2}{18\mu}$$

where g = gravitational acceleration
 d = particle aerodynamic diameter
 ρ = particle density
 μ = air viscosity at ambient temperature

Ground deposition rate is then described by Equation (V.6) (Wark and Warner, 1981, Chapter 5)

$$(V-6) \quad \frac{w_p}{Q} = \frac{V_t}{2\pi u \sigma_y \sigma_z} \exp\left[\frac{-y^2}{2\sigma_y^2}\right] \exp\left[\frac{-\left(H - \frac{xV_t}{u}\right)^2}{2\sigma_z^2}\right]$$

⁵ The Greek letter χ is traditionally used to represent air concentration, but is so easily confused in typescript with the 24th letter of the alphabet that it is often written phonetically ("chi").

where w_p is the particle deposition rate. These equations are programmed in RADTRAN.

Both wind and air temperature profiles affect the dispersion of airborne material. The predominant motion of airborne material is downwind, while crosswind motion is diffusive. Light winds, stable air, and temperature inversions result in less dispersion and higher airborne and ground concentrations of radionuclides. Strong winds and turbulent air are good conditions for dispersion and result in lower airborne and deposited radionuclides concentration and consequently result in lower radiation doses to the public, even though the plume of radioactive material may spread over a large area.

RADTRAN calculates external doses from deposited material (“groundshine”) and from material that remains suspended in the air (“cloudshine”). The code also calculates internal committed doses from airborne material that is inhaled, and from material that becomes resuspended in the air. The doses reported are the sums of the groundshine, cloudshine, inhaled, and resuspended inhaled doses, unless otherwise indicated. Adding these doses to sum to a “total effective dose equivalent” is NRC practice in determining public exposure, as discussed in 10 CFR 20.1301. RADTRAN accommodates a number of atmospheric dispersion conditions.

V.5.4 Release fractions

Release of radionuclides into the environment from a cask depends on releases from the fuel rods into the cask and from the cask to the environment. If the cask contains canistered fuel, no Radioactive material can exit the cask in a traffic accident. In the present study, therefore, only the NAC-STC transporting uncanistered could release any radioactive material in addition to CRUD as a consequence of a traffic accident. Only PWR spent fuel is considered in this section.

V.5.4.1 CRUD

Radioactive material available for release comes from both spent fuel and Chalk River Unidentified Deposits (CRUD). CRUD is a corrosion product that forms on the outside of the fuel rods; its source is not the inventory but other metallic structures in the reactor. In a PWR reactor its radioactive constituents are ^{60}Co , ^{58}Co , ^{54}Mn , ^{51}Cr , ^{59}Fe , ^{95}Zr , ^{125}Sb , and ^{65}Zn . ^{60}Co is the only CRUD constituent sufficiently long-lived to be part of any accidental release. Although CRUD deposits on the outside of fuel rods, cask seals would have to be breached for CRUD to be released. Thus the only cask from which CRUD would be released in an accident is the NAC-STC. Sprung, et al (2000, Page 7-49) and Hanson et al (2010) estimate the amount of CRUD per fuel rod for PWR and BWR spent fuel. The estimates include the following assumptions:

- CRUD forms on the outside rods of the assemblies
- Thirteen percent of the rod area is covered with a CRUD layer. The layer is between 33 and 100 microns thick. The total amount of CRUD was thus assumed to be 8.5 microns thick over the entire surface of the outside rods. The density of the CRUD layer was assumed to be one gram per cm^3 for the CRUD that could be airborne in the cask (Einziger and Beyer, 2007)
- CRUD was assumed to be entirely ^{60}Co , and the activity was calculated using Equation (V-7).

$$(V-7) \quad \text{Activity (Bq)} = \frac{(\ln 2)(6.02 \times 10^{23})(\text{mass (gm)})}{(\text{half-life (sec)})(\text{atomic mass (gm)})}$$

Einzigler and Beyer estimate that, with certain conservative assumptions, about 15 percent of the CRUD formed could remain airborne in the cask and available to be swept from the cask in the event of cask depressurization. Using these estimates, the CRUD activity in the NAC-STC would be:

- 268 TBq (7075 Ci) in a cask carrying twenty-six 17x17 PWR assemblies

And the airborne fraction in the cask would be 40.2 TBq (1061 Ci). If fuel rods are undamaged, no CRUD would be released in an accident because there would be no depressurization even if the cask seals are compromised. If fuel rods are damaged, material from the spent fuel will be released along with CRUD. Therefore, there is no accident in which only CRUD would be released.

The fraction of airborne particles that could be swept from the cask depends on the pressure differential between the cask and the environment:

$$F_{CE} = (1 - f_{\text{deposited}})(p_{\text{atm}}/p_{\text{inp}}) \quad (V-6)$$

Where F_{CE} is the fraction released from the cask to the environment, $f_{\text{deposited}}$ is the fraction of airborne material in the cask deposited on its inner surface, p_{atm} is the atmospheric pressure and p_{inp} is the cask internal pressure. The only release path that would be available is through the seals at the end of the cask. Therefore, $p_{\text{atm}}/p_{\text{inp}} = 0.667$. From Figure 7.5 of Sprung et al (2000), about one percent of the 15 percent of the CRUD that has spalled from the rods; or about 0.15 percent, would be respirable (10 microns or less aerodynamic diameter). Thus, from Equation (V-6) the fraction of CRUD that would be released is 0.001. The dose calculations done with RADTRAN applied the 15 percent to the ^{60}Co inventory and the other factors to the release fraction.

V.5.4.2 Spent Fuel Radionuclides

When fuel rods are fractured in an impact, they depressurize rapidly, and the consequent overpressure sweeps fuel particles out of the cask if there is a breach in the seal. The depressurization and release of material from the rod is described very clearly in Hanson, et al, 2008,

When commercial spent nuclear fuel (CSNF) is handled in a dry environment, whether as fuel assemblies, canned, or within a container, one possible mechanism for radionuclide release is from oxidation of the CSNF exposed to air.... in a drop accident scenario, it is possible that the cladding could fracture, and cans or containers could breach, allowing oxygen to contact the fuel (Sprung et al. 2000). Upon clad breach, it is expected that the rod would rapidly depressurize, releasing its fill gas (e.g., He) and fission gases (e.g., Kr, Xe) that have been released from the fuel matrix, depending on the size of the cladding defect and fuel burnup characteristics (Einzigler and Beyer 2007..... It is also possible for fuel fines to be ejected as the high-pressure fill and fission gases rapidly escape through the defect. As the fuel oxides and forms U_3O_8 , it swells and causes further clad unzipping, potentially releasing the fine-powdered U_3O_8 and allowing additional fission gas release. (Hanson, et al, 2008, Section 1)

These authors examined the behavior of relatively high burnup fuel. The release fractions from the rods to the cask, under the described conditions, are developed from the data of Hanson, et al for 45

GWD/MTU spent fuel. Einziger (2007) describes the formation of a rim on the fuel pellet that has a higher porosity than the body of the pellet. This porosity results in reduced hardness of the pellet (Hanson et al, Figures 1.6 and 1.7)). However, the pellet rim is toughened by grain refinement, suggesting that release of fine particles from the fuel rods could be smaller than releases from lower-burnup fuel. Figure V-6 shows the difference between a rim and the pellet interior.

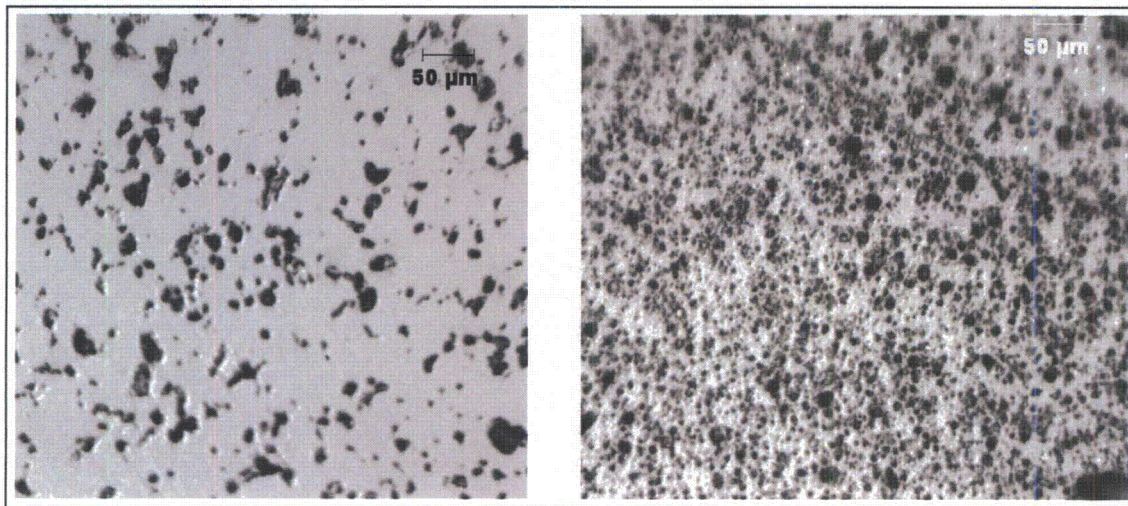


Figure V-6. Electron micrographs of the fuel pellet interior (left-hand picture) and the fuel pellet rim (right-hand picture). (Courtesy of Dr. R. E. Einziger, NRC)

Figure 1.10 of Hanson et al. suggests a release fraction for fission gases (^{85}Kr in the fuel in this analysis) of 0.5 percent. These authors suggest that volatile fission products like ^{137}Cs and ^{134}Cs exhibit release behavior like fission gases. However, cesium would be released as the oxide or chloride, and would therefore behave more like particulate matter than like fission gases. Because the volatiles tend to migrate to the fuel rim and Einziger (2007) recommends 3×10^{-5} as an appropriate release fraction for rim material, this release fraction is for volatiles in the present analysis. Ruthenium was grouped with cesium as a volatile,

Hanson et al. describe a number of mechanical tests performed on unoxidized fuel of varying burnup. Page 4.12 of Hanson et al. summarizes release fractions from these tests for the fuel that appears to be the most appropriate. A release fraction of 4.8×10^{-6} is used in this analysis for release of fine particles from the rod to the cask.

Figure 7.11 of Sprung et al (2000) presents release fractions of several compounds as functions of the available leak area. The compounds studied represent the physical/chemical groups present in spent nuclear fuel: gas, volatiles, and particulate matter. This figure served as the basis for estimating the cask-to-environment release fractions of the physical/chemical groups studied.

Table V-17 summarizes the parameters from which release fractions were developed.

Table V-17. Parameters for determining release functions for the accidents that would result in release of radioactive material.

	Cask Orientation	End	Corner	Side	Side	Side	Side	Corner
	Impact Speed (kph)	193	193	193	193	145	145	145
	Seal	metal	metal	elastomer	metal	elastomer	metal	metal
Cask to Environment Release Fraction	Gas	0.800	0.800	0.800	0.800	0.800	0.800	0.800
	Particles	0.70	0.70	0.70	0.70	0.70	0.70	0.64
	Volatiles	0.50	0.50	0.50	0.50	0.50	0.50	0.45
	Crud	0.001	0.001	0.001	0.001	0.001	0.001	0.001
Rod to Cask Release Fraction	Gas	0.005	0.005	0.005	0.005	0.005	0.005	0.005
	Particles	4.80E-06	4.80E-06	4.80E-06	4.80E-06	4.80E-06	4.80E-06	2.40E-06
	Volatiles	3.00E-05	3.00E-05	3.00E-05	3.00E-05	3.00E-05	3.00E-05	1.50E-05
	Crud	1.00	1.00	1.00	1.00	1.00	1.00	1.00
	Conditional Probability	2.68E-08	1.61E-07	8.02E-08	8.02E-08	8.02E-08	8.02E-08	3.06E-06

The release from these potential accidents is not at ground level but at about 1.5 meters above ground, and the gas flowing from the cask is warmer than ambient, so that the plume of material will be lofted slightly, and the maximum air concentration and ground deposition would be at 21 meters downwind from the cask. The maximally exposed individual would be located at this point. Table V-14 shows the radiation dose (consequence) from each accident that would result in a release of radioactive material from the spent fuel cask. The total doses, 1.6 Sv and 0.73 Sv (160 rem and 73 rem), are significant but not acute or lethal.

Table V-18. Maximally exposed individual doses (consequences) in Sv from accidents that involve a release.

Gask Orientation	Impact Speed (kph)	Seal	Inhalation	Resuspension	Cloudshine	Groundshine	Total
End	193	metal	1.6E+00	1.4E-02	8.8E-05	9.4E-04	1.6E+00
Corner	193	metal	1.6E+00	1.4E-02	8.8E-05	9.4E-04	1.6E+00
Side	193	elastomer	1.6E+00	1.4E-02	8.8E-05	9.4E-04	1.6E+00
Side	193	metal	1.6E+00	1.4E-02	8.8E-05	9.4E-04	1.6E+00
Side	145	elastomer	1.6E+00	1.4E-02	4.5E-06	3.6E-05	1.6E+00
Side	145	metal	1.6E+00	1.4E-02	8.8E-05	9.4E-04	1.6E+00
Corner	145	metal	0.7270	0.0063	0.0001	0.0009	0.7340

When the doses in Table V-18 are multiplied by the probabilities in Table V-17, the “conditional dose risks” of Table V-19 result.

Table V-19 Maximally exposed individual conditional dose risks in Sv from accidents that involve a release.

Gask Orientation	Impact Speed (kph)	Seal	Inhalation	Resuspension	Cloudshine	Groundshine	Total
End	193	metal	4.26E-08	3.67E-10	2.35E-12	2.52E-11	4.29E-08
Corner	193	metal	2.56E-07	2.21E-09	1.41E-11	1.52E-10	2.58E-07
Side	193	elastomer	1.28E-07	1.10E-09	7.04E-12	7.55E-11	1.28E-07
Side	193	metal	1.28E-07	1.10E-09	7.04E-12	7.55E-11	1.28E-07
Side	145	elastomer	1.27E-07	1.10E-09	3.63E-13	2.90E-12	1.28E-07
Side	145	metal	1.28E-07	1.10E-09	7.04E-12	7.55E-11	1.28E-07
Corner	145	metal	2.22E-06	1.93E-08	1.57E-10	2.82E-09	2.25E-06

Population doses are calculated by integrating the rural, suburban, and urban population densities, respectively, over the largest plume footprint in the dispersion calculation: 1420 km² for neutral meteorological stability. Collective dose risks are calculated by multiplying each population dose by the appropriate conditional probability. Collective doses are presented in Table V-20 for the end impact, 193 kph impact speed accident, as an example.

Table V-20. Collective conditional inhalation and external dose risks for the 16 routes analyzed.

	Collective Inhalation Dose Risk (person-Sv)				Collective External Dose Risk (person-Sv)			
	ORNL	DEAF SMITH	HANFORD	SKULL VALLEY	ORNL	DEAF SMITH	HANFORD	SKULL VALLEY
MAINE YANKEE								
RURAL	2.81E-14	1.23E-14	1.80E-14	8.49E-14	2.37E-17	1.03E-17	1.51E-17	7.14E-18
SUBURB	5.54E-13	3.53E-13	2.98E-13	1.76E-13	4.66E-16	2.97E-16	2.51E-16	1.48E-16
URBAN	9.66E-12	5.93E-12	5.08E-12	2.57E-12	8.10E-15	4.98E-15	4.26E-15	2.16E-15
KEWAUNEE								
RURAL	1.11E-14	2.62E-15	2.79E-15	2.79E-15	9.37E-17	2.20E-17	2.35E-18	2.35E-18
SUBURB	2.37E-13	1.19E-13	1.11E-13	1.01E-13	1.99E-16	1.00E-16	9.34E-17	8.53E-17
URBAN	4.18E-12	1.99E-12	1.95E-12	1.37E-12	3.50E-15	1.67E-15	1.64E-15	1.15E-15
INDIAN POINT								
RURAL	3.06E-13	9.96E-15	1.05E-14	4.21E-14	2.57E-17	8.38E-17	8.82E-18	3.54E-18
SUBURB	9.52E-12	3.57E-13	3.61E-13	1.33E-13	8.01E-16	3.00E-16	3.04E-16	1.12E-16
URBAN	1.64E-10	6.37E-12	6.55E-12	2.06E-12	1.38E-15	5.34E-15	5.49E-15	1.73E-15
IDAHO NATIONAL LAB								
RURAL	9.03E-06	3.60E-07	4.01E-10	1.20E-10	9.03E-13	3.60E-13	4.01E-10	1.20E-08
SUBURB	1.23E-08	2.37E-10	3.43E-13	2.21E-13	1.23E-16	2.37E-16	3.43E-13	2.21E-11
URBAN	4.43E-07	2.06E-08	2.38E-11	7.52E-11	4.43E-14	2.06E-14	2.38E-11	7.52E-10

Inhalation doses include doses from direct inhalation and from material resuspended in air. External doses include cloudshine and groundshine. The NRC cites the total effective dose equivalent (TEDE) which includes both inhalation (internal) doses and external doses. The complete collective dose risk is the product of the collective dose risk as shown in Table V-21 and the accident frequency along the route. Average accident frequencies for each route are in Table V-8.

Table V-21 shows the total dose risk for each route.

Table V-21. Total collective dose risks (person-Sv) for each route

	ORNL	DEAF SMITH	HANFORD	SKULL VALLEY
MAINE	2.47E-08	5.97E-10	1.06E-10	9.81E-11
KEWAUNEE	8.85E-07	4.12E-08	8.80E-11	1.53E-09
INDIAN POINT	3.40E-09	1.31E-10	1.35E-10	4.29E-11
INL	2.09E-11	3.36E-11	9.08E-12	6.07E-11

V.6. Summary

The more important technical observations for the analysis of accidents are:

- Event trees based on current accident statistics show that the probability of a severe accident for either truck or rail is small.

- The probability of a fire that would damage a cask on a railcar enough to cause loss of gamma shielding or release of radioactive material is negligible.
- The analyses in Appendices III and IV demonstrate that the only cask that would suffer a loss of lead shielding or release of radioactive material is the Rail-Pb cask. This is the only cask whose behavior in loss of shielding or release accidents is analyzed.
- The fraction of accidents that do not lead to either a release of radioactive material or a loss of lead gamma shielding is 0.999991.
- Loss of more than two percent of the lead shield results in a dose that exceeds the limits of 10 CFR 71.51 for a person within four meters of the cask.
- If the fuel rods are not breached in an accident, there would be no net flow of gas out of the cask, and nothing would be released.
- Weather conditions that result in poor dispersion, very stable Pasquill Stability Class F and wind speed at 0.5 m/sec, resulted in doses very little different from those for neutral, more average weather conditions, and are therefore not reported.

BIBLIOGRAPHY

Code of Federal Regulations (CFR) 2009, Volume 10, Part 20 and Part 71

Adkins, H.E., Cuta, J.M., Koepfel, B.J., Guzman, A.D., Bajwa, C.S. 2006. *Spent Fuel Transportation Package Response To The Baltimore Tunnel Fire Scenario*, NUREG/CR-6886, Rev. 1, PNNL-15313, Pacific Northwest National Laboratory, Richland, WA.

American Society for Testing Materials (ASTM). 2008. *E 2230, Standard Practice for Thermal Qualification of Type B Packages for Radioactive Material*, ASTM International.

Ammerman, D.J. and K. Gwinn. 2004. *Collapse of the Cypress Street Viaduct – Effect on a Postulated Spent Fuel Truck Cask*, Proceedings of the INMM 45th Annual Meeting, Orlando, FL.

Ammerman, D., D. Stevens, and M. Barsotti. 2005. *Numerical Analyses of Locomotive Impacts on a Spent Fuel Truck Cask and Trailer*, PVP2005-71729, Proceedings of the ASME Pressure Vessels and Piping Conference, Denver, CO.

BEIR VII (National Research Council Committee on the Biological Effects of Ionizing Radiation Phase 2). 2006. *Health Effects From Exposure to Low Levels of Ionizing Radiation* National Academy Press, Washington, DC.

Bonzon, I.L. and Schaumann, J.T. 1976. *Container Damage Correlation with Impact Velocity and Target Hardness*, IAEA-SR-10/21, Transport Packaging for Radioactive Materials, IAEA, Vienna, Austria,

Croff, A.G. 1980. *ORIGEN2 - A Revised and Updated Version of the Oak Ridge Isotope Generation and Depletion Code*, ORNL-5621, Oak Ridge National Laboratory, Oak Ridge, TN.

del Valle, M.A., Kramer, M.A., Lopez, C., Suo-Anttila, A., Greiner, M.. 2007, "Temperature Response of a Rail-Cask-Size Pipe Calorimeter in Large-Scale Pool Fires", Proceedings of the 15th International Symposium on the Packaging and Transportation of Radioactive Materials (PATRAM), Miami, FL

del Valle, M.. 2009. *Benchmark And Sensitivity Study Of The Container Analysis Fire Environment (CAFE) Computer Code Using A Rail-Cask-Size Pipe Calorimeter In Large-Scale Pool Fires*,. Thesis, University Of Nevada, Reno, NV

Dennis, M.L., Osborn, D. O., Weiner, R. F., Heames, T.J. 2008. *Verification and Validation of RADTRAN 6.0* SAND2008-4556, Sandia National Laboratories, Albuquerque, NM.

- Dennis, M.L., Weiner, R.F., Osborn, D.M., Heames, T.J. 2009. "Dose Estimates in a Loss-of-Lead-Shielding Truck Accident" SAND2009-5107, Sandia National Laboratories, Albuquerque, NM.
- Einziger, R.E.. 2007. "Source Terms for Spent fuel Transportation and Storage Cask Evaluation" Proceedings of the 15th International Symposium on the Packaging and Transportation of Radioactive Materials, PATRAM 2007, Miami, Florida.
- Einziger, R.E. and Beyer, C. 2007. Effect of High-Burnup Fuel on Source Term In Cask Accidents," *Nuclear Technology* v. 199, pp 134-146.
- Federal Register, Vol. 65, No. 203, Thursday, October 19, 2000, Rules and Regulations, page 62597.
- Fischer, L.E.; Chou, C.K.; Gerhard, M.A.; Kimura, C.Y.; Martin, R.W.; Mensing, R.W.; Mount, M.E.; Witte, M.C. 1987. *Shipping Container Response to Severe Highway and Railway Accident Conditions*, NUREG/CR-4829, Lawrence Livermore National Laboratory, Livermore, CA.
- General Atomics. 1998. *Safety Analysis Report for Packaging*, General Atomics Project 4439, San Diego, CA
- Gonzales, A. 1987. *Target Effects on Package Response: An Experimental and Analytical Evaluation*, SAND86-2275, Sandia National Laboratories, Albuquerque, NM
- Greiner, M., del Valle, M., Lopez, C., Figueroa, V., and Abu-Irshaid, E.. 2009. "Thermal Measurements of a Rail-Cask-Size Pipe-Calorimeter in Jet Fuel Fires," ASME 2009 Summer Heat Transfer Conference, HT2009-88520, July 19-23, 2009, San Francisco, California USA
- Griego, N.R.; Smith, J.D.; Neuhauser, K.S. 1996. "Investigation of Radtran Stop Model Input Parameters for Truck Stops," SAND96-0714C. Sandia National Laboratories. Albuquerque, NM.
- Haire, M.J. and Swaney, P.M. 2005. "Cask Size and Weight Reduction Through the Use of DUO₂-Steel Cermet Material" *Waste Management '05*, Tucson, AZ.
- Hanson, B.D., Daniel, R.C., Casella, A.M., Wittman, R.S., Wu, W., MacFarlan, P.J., Shimskey, P.J. 2008. *Fuel-In-Air FY07 Summary Report Rev. 1* PNNL-17275, Pacific Northwest National Laboratory, Richland, WA.
- Hibbit, Karlsson and Sorensen. 1998. *ABAQUS/Standard User's Manual* (Hibbit, Karlsson and Sorensen, Inc., HKS, 1080 Main Street, Pawtucket, RI, 02860 4847) Version 5.8 edition (1998).
- Hoffman, E. L. and Attaway, S. W. 1991. *Structural Analysis Of The Source Term Transportation Cask*, SAND91-1543, Sandia National Laboratories, Albuquerque, NM,

- Holtec International. 1997. *HI-STAR 100 System Cask Thermal Design Package*, Report No. HI-951325.
- Holtec International. 1999 *Effective Property Evaluations of HI-STAR 100 and HI-STORM Dry Cask System Multi-Purpose Canisters*, Report No. HI-971788.
- Holtec International. 2004. *Safety Analysis Report for the HI-STAR* Holtec Report 951251.
- Husek, H.J. 1986. *Structural Alloys Handbook*, Battelle Memorial Institute, Columbus, OH
- Incropera, F.P. and Dewitt, D.P. 1996. *Fundamentals Of Heat And Mass Transfer*, John Wiley & Sons, New York.
- Interagency Steering Committee on Radiation Standards (ISCORS). 2002. *A Method for Estimating Radiation Risk from TEDE*, ISCORS Technical Report No. 1, USDOE Office of Environmental Policy and Guidance, Washington, DC.
- Johnson, P.E. and Michelhaugh, R.D. 2003. *Transportation Routing Analysis Geographic Information System (TRAGIS) User Manual*, ORNL/NTRC-006, Oak Ridge National Laboratory, TN.
- Kalan, R. J., C.J.R Clutz, and D.J. Ammerman. 2005. "Analysis of a 17 x 17 Pressurized Water Reactor (PWR) Fuel Assembly," letter report to DOE-RW, August 2005
- Kelley, K.K.. 1960. "Enthalpy plots DWG K38745" U. S. Bureau of Mines 584
- Kramer, M.A., del Valle, M., Greiner, M. 2008. "Measurement and Uncertainty of Heat Flux to a Rail-Cask Sized Pipe Calorimeter in a Pool Fire," PVP2008-61600, Proceedings of the 2008 ASME Pressure Vessels and Piping Conference, PVP2008, July 27-31, 2008, Chicago, Illinois.
- Livermore Software Technology Corporation, LS-DYNA User's Manual, 7374 Las Positas Road, Livermore, CA 94550 US
- Lopez, C., Koski, J., Suo-Anttila, A. 2003. "Development and Use of the CAFE-3D Code for Analysis of Radioactive Material Packages in Fire Environments," INMM Conference, Orlando, FL.
- Lorenz, R.A. et al. 1980. *Fission Product Release from Highly Irradiated LWR Fuel*, NUREG/CR-0722, Oak Ridge National Laboratory, Oak Ridge, TN, February 1980.
- Lorenz, R.A., et al., 1978. *Fission Product Release from Simulated LWR Fuel*, NUREG/CR-0274, Oak Ridge National Laboratory, Oak Ridge, TN, July 1978.
- McAdams, W.H. 1954. *Heat Transmission*, 3rd. Ed
- Mills, G.S., Sprung, J.L., Osborn, D.M. 2006. *Tractor/Trailer Accident Statistics SAND2006-7723*, Sandia National Laboratories, Albuquerque, NM.

- Nakos, J.T. 2005. *Uncertainty Analysis of Steady State Incident Heat Flux Measurements in Hydrocarbon Fuel Fires*, SAND2005-7144 Sandia National Laboratories, Albuquerque, NM
- Nicolette, V.F. and Larsen, D.W. 1989. "Influence Of Large, Cold Objects On Engulfing Fire Environments", SAND89-2175C, Sandia National Laboratories, Albuquerque, NM.
- Nuclear Acceptance Corporation (NAC) International. 2002. *Safety Analysis Report for the NAC Universal Multi-Purpose Canister System*, NRC Docket 71-9235, Atlanta, GA.
- Neuhauser, K.S., Kanipe, F.L., Weiner, R.F. 2000. *RADTRAN 5, Technical Manual*, Sandia National Laboratories, Albuquerque, NM.
- Nuclear Acceptance Corporation (NAC) International. 2004. *Safety Analysis Report for the NAC Storage Transport Cask*, NRC Docket 71-9235, Atlanta, GA.
- O'Donnell, B., James, S., Weiner, R.F. 2005. "Calculations for Loss of Shielding Resulting From Transportation Accidents," Institute for Nuclear Materials Management, Annual Meeting, Fort Lauderdale, FL.
- Perry, J.H. 1963. *Chemical Engineering Handbook*, 4th Ed
- Petersen, H. 1970. *The Properties of Helium*, Riso Report No. 224, Danish Atomic Energy Commission
- Pierce, J.D., P.J. Gronewald, J. Mould, R. Oneto. 2003. Radiant heat test of Perforated Metal Air Transportable Package (PMATP), SAND2003-2750, Sandia National Laboratories, Albuquerque, NM
- Pierron, O.N., Koss, D.A., Motta, A.T. 2003. Tensile Specimen Geometry and Constitutive Behavior of Zircaloy-4, *Journal of Nuclear Materials*, 312, 257-261
- Ross, S.S., Weiner, R.F., Best, R.E., Maheras, S., McSweeney, T. 2002. *Transportation Health and Safety Calculation/Analysis Documentation in Support of the Final EIS for the Yucca Mountain Repository* CAL-HSS-ND-000003, USDOE Office of Civilian Radioactive Waste Management, Las Vegas, NV.
- Sanders, T.L., Seager, K.D., Rashid, Y.R., Barrett, P.R., Malinauskas, A.P., Einziger, R.E., Jordan, H., Duffey, T.A., Sutherland, S.H., Reardon, P.C. 1992. *A Method for Determining the Spent-Fuel Contribution to Transport Cask Containment Requirements*, SAND90-2406, Sandia National Laboratories, Albuquerque, NM
- Sandoval, R.P., Einziger, R.E., Jordan, H., Malinauskas, A.P., Mings, W.J. 1988. *Estimate of CRUD Contribution to Shipping Cask Containment Requirements* SAND88-1358. Sandia National Laboratories, Albuquerque, NM.
- Schorsch, R.H. 1966. *Engineering Properties Of Selected Metals*.

- Shleien, B., Slaback, L.S., Birky, B.K. 1998. *Handbook of Health Physics and Radiological Health, Third Edition*. Williams and Wilkins, Baltimore, MD.
- SIERRA Solid Mechanics Team. 2009. *Presto 4.11 User's Guide*. SAND2009-3213, Sandia National Laboratories, Albuquerque, NM, November 2009 Sandia National Laboratories, Albuquerque, NM.
- SIERRA Solid Mechanics Team. 2009. *Presto 4.14 User's Guide*. SAND2009-7401, Sandia National Laboratories, Albuquerque, NM, November 2009 Sandia National Laboratories, Albuquerque, NM.
- Soo-Haeng, C., D. Jae-Bum, R. Seung-Gy, D. Chun-Ho. 1996. "Fabrication and Characteristics of Resin-Type Neutron Shielding Materials for Spent Fuel Shipping Cask," *Journal of Industrial and Engineering Chemistry*, Vol. 7, No. 3, June 1996, 597-604
- Stabin, M.G. 2009. "Doses from Medical Radiation Sources," Health Physics Society Topical Articles, <http://www.hps.org/hpspublications/articles/dosesfrommedicalradiation.html>
- Sprung, J.L., Ammerman, D. J., Breivik, N.L., Dukart, R.J., Kanipe, F.L., Koski, J. A., Mills, G.S., Neuhaiuser, K.S., Radloff, H.D., Weiner, R.F., Yoshimura, H.R.. 2000. *Re-Examination of Spent Fuel Risk Estimates* NUREG/CR-6672, Sandia National Laboratories, Albuquerque, NM.
- Steinman, R. L., Weiner, R.F., Kearfott, K. 2002. . "Comparison of Transient Dose Model Predictions and Experimental Measurements." *Health Physics* v. 83 (2002), p.504 et seq
- Suo-Antilla, A., C. Lopez, and I. Khalil. 2005. *User Manual for CAFE-3D: A Computational Fluid Dynamics Fire Code*, SAND2005-1469, Sandia National Laboratories, Albuquerque, NM.
- Taylor, J.M. and Daniel, S.L 1977. *RADTRAN: A Computer Code to Analyze Transportation of Radioactive Material*, SAND76-0243, Sandia National Laboratories, Albuquerque, NM.
- Thermophysical Properties Research Laboratory Inc. 2001. *Thermophysical Properties of Kaowool, Honeycomb, Foam and Cork*, Report No. 2649, August 2001
- Turner, D.B. 1994. *Workbook of Atmospheric Dispersion Estimates* Lewis Publishers, New York, NY
- Tubiana, M. and Aurengo, A. 2005, "Dose-effect relationship and estimation of the carcinogenic effects of low doses of ionizing radiation: the Joint Report of the Académie des Sciences (Paris) and the Académie Nationale de Médecine" *Int. J. Low Radiation*, V 2, pp. 1-19
- U.S. Bureau of the Census. 2008. <http://www.census.gov>

- U.S. Department of Energy (DOE). 1986 *Environmental Assessment Yucca Mountain Site, Nevada Research and Development Area, Nevada*. DOE/RW-0073. U.S. Department of Energy, Office of Civilian Radioactive Waste Management, Washington, D.C.
- U.S. Department of Energy (DOE). 2002 *Final Environmental Impact Statement for a Geologic Repository for the Disposal of Spent Nuclear Fuel and High-Level Radioactive Waste at Yucca Mountain, Nye County, Nevada*. DOE/EIS-0250F, Washington, DC, Chapter 6 and Appendix J..
- U.S. Department of Transportation (DOT). 2004a. "Maximum Posted Speed Limits by Type of Road," (Table 2-9) Bureau of Transportation Statistics Research and Innovative Technology Administration, Washington, DC
- U.S. Department of Transportation (DOT). 2004b. "Rail freight Average Speeds, Revenue Ton-Miles, and Terminal Dwell Times" (Table 2-9) Bureau of Transportation Statistics Research and Innovative Technology Administration, Washington, DC
- U.S. Department of Transportation (DOT). 2005. State Transportation Statistics 2004, Bureau of Transportation Statistics , Research and Innovative Technology Administration, Washington, DC
http://www.bts.gov/publications/state_transportation_statistics/state_transportation_statistics_2005/pdf/entire.pdf
- U.S. Department of Transportation (DOT). 2007. "Traffic Safety Facts 2007" (Tables 1-32, 2-03, 2-04, 2-09, 2-28, 2-37) Bureau of Transportation Statistics Research and Innovative Technology Administration, www.bts.gov, Washington, DC
- U.S. Department of Transportation (DOT). 2009. "Commodity Flow Survey: Shipment Characteristics by Mode of Transportation for the U.S., 2007" (Table1) Bureau of Transportation Statistics Research and Innovative Technology Administration, Washington, DC
- U.S. Department of Transportation (DOT). 2008. National Transportation Statistics 2008, Bureau of Transportation Statistics , Research and Innovative Technology Administration, Washington, DC
http://www.bts.gov/publications/national_transportation_statistics/html/table_02_23.htm
- U.S. Nuclear Regulatory Commission (NRC). 1975. *Reactor Safety Study*, WASH-1400, Washington, DC.
- U. S. Nuclear Regulatory Commission (NRC). 1977. *Final Environmental Statement on the Transportation of Radioactive Material by Air and Other Modes*, NUREG-0170, U.S. Nuclear Regulatory Commission, Washington, DC.
- U. S. Nuclear Regulatory Commission (NRC). 1978. *Safety Analysis Report for the Plutonium Air Transportable Package, Model PAT-1*, NUREG-0361, U.S. Nuclear Regulatory Commission, Washington, DC.

- U. S. Nuclear Regulatory Commission (NRC). 2003a. *Safety of Spent Fuel Transportation*, NUREG/BR-0292, U.S. Nuclear Regulatory Commission, Washington, DC.
- U. S. Nuclear Regulatory Commission (NRC). 2003b. *United States Nuclear Regulatory Commission Package Performance Study Test Protocols, Draft Report for Comment*, NUREG-1768, U.S. Nuclear Regulatory Commission, Washington, DC.
- U. S. Nuclear Regulatory Commission (NRC). 2008. *State of the Art Reactor Consequence Analysis – Reporting Offsite Health Consequences*, SECY-08-0029, and Commission Voting Record on SECY-08-2009, U.S. Nuclear Regulatory Commission, Washington, DC.
- Volpe Center. 2006. *Spent Nuclear Fuel Transportation Risk*, Draft Report, Volpe National Transportation Systems Center, Cambridge, MA (Document available from Sandia National Laboratories)
- Waddoups, I.G. 1975. *Air Drop Test of Shielded Radioactive Material Containers*, SAND75-0276, Sandia National Laboratories, Albuquerque, NM,
- Wark, K. and Warner, C.F. 1981. *Air Pollution: Its Origin and Control*, Harper and Row, New York, NY.
- Weast, R.C. 1966. *Handbook of Chemistry and Physics*, 47th Ed
- Weiner, R.F., LaPlante, P.A., Hageman, J.P. 1991. “Risks of Incident-Free Transportation of Radioactive Materials by Highway” *Risk Analysis* v. 11, pp.660-666.
- Weiner, R. F. and. Tenn, H. F. 1999. *Transportation Accidents and Incidents Involving Radioactive Materials (1971-1998)*, Sandia National Laboratories, Albuquerque, NM
- Weiner, R.F., Dennis, M.L. Hinojosa, D., Heames, T.J., Penisten, J.J., Marincel, M.K., Osborn, D.M. 2009. *RadCat 3.0 User Guide*, SAND2009-5129P. Sandia National Laboratories, Albuquerque, NM
- Wellman, G. W., and Salzbrenner, R. 1992. *Quasistatic Modeling and Testing of Exclusion Region Barrier Mock-Ups*, SAND92-0024, Sandia National Laboratories, Albuquerque, NM.
- Wooden, D.G. 1986. *Railroad Transportation of Spent Nuclear Fuel* SAND86-7083, Sandia National Laboratories, Albuquerque, NM
- Yafei, S., T. Yongjun, S. Jing, N. Dongjie, 2009. *Effect of Temperature and Composition of Thermal Properties of Carbon Steel*, Chinese Control and Decision Conference, Guilin, China